Seismic and Newtonian noise modeling for Advanced Virgo and Einstein Telescope

Maria Karolina Margit Bader

Promotor:	prof.dr. J.F.J. van den Brand
Copromotor:	dr. H.J. Bulten
Other members:	prof.dr. A. Freise
	prof.dr. J. Harms
	prof.dr. F.L. Linde
	dr. G. Losurdo
	prof.dr. G. Raven
	dr. J. Steinlechner
	dr.ir. B.L. Swinkels
Paranymphs:	Akash Raj Komarlu Narendra Gupta
	Zhanna Khabanova

Printed by Gildeprint
Cover picture by Jonathan Borba
ISBN: 978-94-6419-093-9

This work is part of the research programme *Silent sensors for stellar echos and seismic surveys* with project number 13338, which is financed by the Dutch Research Council (NWO). This work has been carried out at Nikhef.

VRIJE UNIVERSITEIT

Seismic and Newtonian noise modeling for Advanced Virgo and Einstein Telescope

ACADEMISCH PROEFSCHRIFT

ter verkrijging van de graad Doctor of Philosophy
aan de Vrije Universiteit Amsterdam,
op gezag van de rector magnificus
prof.dr. V. Subramaniam,
in het openbaar te verdedigen
ten overstaan van de promotiecommissie
van de Faculteit der Bètawetenschappen
op dinsdag 9 februari 2021 om 15.45 uur
in de aula van de universiteit,
De Boelelaan 1105

door

Maria Karolina Margit Bader

geboren te München, Duitsland

promotor: prof.dr. J.F.J. van den Brand

copromotor: dr. H.J. Bulten

Für meine liebe Oma, die immer sagte:

Lern so viel du kannst,
denn du trägst nicht schwer

Contents

Preface

There is a theory which states that if ever anyone discovers exactly what the Universe is for and why it is here, it will instantly disappear and be replaced by something even more bizarre and inexplicable.

There is another theory which states that this has already happened.

Douglas Adams

Gravitational wave physics is a branch of science, where research is conducted on extreme scales of the scientific spectrum: While fluctuations that are smaller than the size of atomic nuclei are observed in the separation between two test masses, these fluctuations originate from the most violent cosmic events, such as stellar explosions and colliding black holes. At this point the paths of scientists part. Where theorists and data analysts indulge in perfecting the cosmic models and methods that lead to a deep understanding of the structure and composition of our Universe, instrumentalists are driven to push state-of-the-art technology to its limits to measure fainter fluctuations in distance than ever imagined.

The simultaneous operation of a global ground-based network of gravitational wave detectors is the result of the combined effort of a worldwide collaboration of scientists. As the current detectors are slowly heading towards their design sensitivity, the scientists are preparing to embark on the next endeavor: a new generation of detectors that will overcome inevitable restrictions set by the existing infrastructure. This so called third generation will open a window that will allow a deeper understanding of our entire Universe to times as early as the Dark Ages, an era before the formation of the first stars.

Ground-based detectors are now reaching a point where technological optimizations are exploited to a degree where fundamental, site-specific factors start to limit the detection performance. Local ground vibrations that are for example caused by human activity cannot be eliminated completely and pose a threat to the quality of the measured gravitational wave signals. To determine the effect of ground vibrations on existing infrastructure and to facilitate the optimal site choice for the future detector locations, sophisticated techniques to model the seismic displacement field and the resulting detector disturbance at various sites are necessary. This is the quest the dissertation is set on.

This thesis is structured in the following way: In the first chapter, a brief review of the mathematical expression for gravitational waves is given. This will allow to motivate laser interferometers as the preferred detector choice to measure gravitational waves. A brief introduction of laser optics and feedback control systems that are relevant for Advanced Virgo will allow to understand the technical noise sources of current detectors especially for low frequency noise.

Technical noise, most notably angular control noise, at the Advanced Virgo detector will be addressed in the second chapter. Control noise at low frequencies is one of the remaining technical noise sources that needs to be overcome in order to operate the current detectors at their fundamental limits in the full frequency range.

In the third chapter, the foundation of seismic wave propagation is reviewed, which includes numerical solving techniques for the wave equation in complex geologies. Modeling seismic fields in realistic geological environments allows us to understand the direct coupling between seismic fluctuations and detector signal, the fundamental Newtonian noise. Furthermore, a numerical integration method for making site-based Newtonian noise estimates, that takes into consideration the seismic field at a specific detector site, is introduced and its advantages with respect to analytical modeling techniques are carved out.

To derive Newtonian noise at a specific detector site, knowledge of the local geology is required. In the fourth chapter, seismic studies with large arrays of surface sensors are introduced as a tool to measure the set of subsurface parameters which allows to model the seismic field at any given detector site.

In the fifth chapter, Newtonian noise for Advanced Virgo is estimated with a realistic seismic field that is generated in a layered subsurface geology. The geological parameters of this model are derived from a seismic sensor array study and are specific to the site at EGO in Italy.

Finally, in the sixth chapter, Newtonian noise is estimated for the Belgian-German-Dutch Einstein Telescope candidate site. The seismic displacement field is specific for the layered subsurface geology that is representative for the region. The site-specific geological parameters are obtained from field trials with sensor arrays and from borehole measurements.

Chapter 1

Theory and background

Here the mathematical foundations are laid which pave the way towards the main concepts of this work. This encompasses in the first section a brief discussion of Einstein's field equations within the theory of general relativity, gravitational waves as a consequence of these field equations, their cosmic sources and a synopsis of present day gravitational wave detections. In the second section, the detection principle of interferometric gravitational wave detectors are presented together with their fundamental noise sources and a summary of the global detector network with a focus on the Advanced Virgo and Einstein Telescope detectors is given. The third section elaborates on fundamental principles of Gaussian beams and their properties in resonant cavities. This lays the foundation for the stability control of gravitational wave detectors and principles of feedback control systems that are summarized in the fourth section.

1.1 Gravity, general relativity and gravitational waves

The theory of gravity is not new to physics, where pioneering work came from Newton in 1687 by stating the first law of gravity. Since then, Einstein has revolutionized the field with his description of gravity with the theory of general relativity in 1915. Gravitational waves, a direct consequence of Einstein's field equations, have long been believed to be unobservable, even though indirect evidence for their emission existed [1]. However in 2015, one hundred years after the formulation of general relativity, the first direct measurement of gravitational waves from a binary-black hole merger was achieved by the LIGO-Virgo Collaboration [2].

1.1.1 The Einstein field equations

The pioneer in the field of gravitation is Isaac Newton with his formulation of the universal law of gravity in 1687 [3]. It states that a mass m_1 exerts a force $\vec{F}_{21}$ on m_2 as

$$\vec{F}_{21} = -G \cdot \frac{m_1 m_2}{|\vec{r}|^2} \hat{r}, \tag{1.1.1}$$

where the two masses are separated by a distance $\vec{r} = \vec{r}_2 - \vec{r}_1$, $\hat{r}$ represents the normalized vector pointing in the direction of $\vec{r}$ from m_1 towards m_2 and G is the universal gravitational constant. Even though Newton could not provide any explanation of the origin of the gravitational force and its mediator, the universal law of gravity allowed the successful formulation of Kepler's laws of the planetary motion and the explanation of gravitational effects on Earth. Despite these

known limitations, the universal law of gravity was widely accepted for more than two centuries for the lack of a more elaborate theory.

The understanding of gravitation was revolutionized when Albert Einstein published his theory of general relativity in 1915 [4], a generalization of the theory of special relativity that he formulated in 1905 [5]. The theory of special relativity is centered around the assumption that time and the three dimensions of space, unified to the four-dimensional coordinate called *spacetime*, are relative and that the speed of light is constant in any reference frame. The constance of the speed of light was widely accepted as a result of the Michelson-Morley experiment [6]. In special relativity, the laws of physics are covariant in flat spacetime and for reference frames that are not accelerated. In the theory of general relativity Einstein establishes the concept of covariance for accelerated frames, where the gravitational acceleration of masses towards each other is a result of curved spacetime and the curvature is a consequence of the presence of mass.

In the theory of relativity, spacetime is modeled as a 4-dimensional Lorentzian manifold, which is a special case of a pseudo-Riemannian manifold. A pseudo-Riemannian manifold is a differentiable manifold, which is locally similar to Euclidean space and has a non-degenerate metric tensor **g**. In a Lorentzian manifold, one dimension, notably the time, has an opposite sign with respect to that of the spatial dimensions. The metric tensor allows to formulate a coordinate-independent measure of the distance ds between two points in spacetime coordinates as

$$ds^2 = g_{\mu\nu} dx^\mu dx^\nu, \tag{1.1.2}$$

where $(\mu, \nu) \in \{0, 1, 2, 3\}$ are the indices referring to the spacetime coordinates $(x^0, x^1, x^2, x^3) = (ct, x, y, z)$ and $g_{\mu\nu}$ are the components of the metric tensor. In this section the Einstein summation convention is used, which means that indices that appear twice, once as a subscript and once as a superscript, are summed over. The explicit form of the metric tensor depends on the geometry and the coordinate system.

In special relativity, where space is assumed to be Euclidean, free falling particles move along straight lines. The equivalent to straight lines in multi-dimensional, curved geometries are called *geodesics*. A geodesic is defined as a curve along which the tangent vector $\vec{U}$, with elements $\frac{\partial x^\alpha}{\partial \lambda}$ where λ is a parameter of the curve, is parallel transported. The geodesic equation in any arbitrary geometry is derived from the assumption that free falling particles are not accelerated along straight lines and is written as

$$\nabla_{\vec{U}} \vec{U} = 0 \rightarrow \frac{d^2 x^\alpha}{d\lambda^2} = -\Gamma^\alpha_{\mu\beta} \frac{dx^\mu}{d\lambda} \frac{dx^\beta}{d\lambda}, \tag{1.1.3}$$

where $\Gamma^\alpha_{\mu\beta}$ represent the *Christoffel symbols*. The Christoffel symbols are a set of coefficients that describe the change of the basis vectors in curved spacetime and in terms of the metric tensor they are defined as as

$$\Gamma^\alpha_{\mu\nu} = \frac{1}{2} g^{\alpha\beta} \left(\frac{\partial}{\partial x^\nu} g_{\beta\mu} + \frac{\partial}{\partial x^\mu} g_{\beta\nu} + \frac{\partial}{\partial x^\beta} g_{\mu\nu} \right). \tag{1.1.4}$$

A measure for the curvature of spacetime is given by the Riemann curvature tensor. It assigns a tensor to each point in the manifold that expresses the deviation of the local geometry from Euclidean space and is given by

$$R^\beta_{\alpha\mu\nu} = \frac{\partial \Gamma^\beta_{\alpha\nu}}{\partial x^\mu} - \frac{\partial \Gamma^\beta_{\alpha\mu}}{\partial x^\nu} + \Gamma^\gamma_{\alpha\nu} \Gamma^\beta_{\gamma\mu} - \Gamma^\gamma_{\alpha\mu} \Gamma^\beta_{\gamma\nu}. \tag{1.1.5}$$

From the Riemann curvature tensor $R^{\beta}_{\alpha\mu\nu}$ the Ricci curvature tensor $R_{\alpha\nu}$ can be calculated by contracting the Riemann tensors's first and third index. The contraction of the last two remaining indices gives the scalar curvature R.

The density and flux of energy and momentum are expressed by the energy-momentum tensor $T_{\alpha\beta}$ and spacetime is curved as a result of the presence of energy (or mass). This interplay between curved geometry and the mass-energy content is described by the *Einstein field equations* (EFEs), that connect the metric tensor and the energy-momentum tensor in a set of coupled, non-linear differential equations as

$$G_{\alpha\beta} = R_{\alpha\beta} - \frac{1}{2}Rg_{\alpha\beta} = \frac{8\pi G}{c^4}T_{\alpha\beta}, \tag{1.1.6}$$

where $G_{\alpha\beta}$ is called the Einstein tensor, c is the speed of light and G refers to the universal gravitational constant. The Einstein field equations depend on the metric tensor, a symmetric 4×4 tensor. Taking into account energy-momentum conservation, the EFEs represent a set of 6 independent, coupled, non-linear differential equations. By specifying the energy-momentum tensor of a given geometry, the corresponding metric tensor can be derived from Eq. (1.1.6). Using this metric tensor in Eq. (1.1.3) the motion of any particle in spacetime can be derived.

1.1.2 Gravitational waves

The linearized field equations

Analytical solutions of the Einstein field equations only exist in special cases, like for the flat-space Minkowski metric [7]. The metric of weakly curved spacetime can be derived from a Taylor expansion to the first order as

$$g_{\alpha\beta} \approx \eta_{\alpha\beta} + h_{\alpha\beta}, \tag{1.1.7}$$

where the dominating term is the flat spacetime metric $\eta_{\alpha\beta}$ and $|h_{\alpha\beta}| \ll 1$ is the small, first order perturbation representing the disturbance of the gravitational field. Using the expressions

$$h \equiv \eta^{\alpha\beta}h_{\alpha\beta}, \tag{1.1.8}$$

$$\bar{h}_{\alpha\beta} \equiv h_{\alpha\beta} - \frac{1}{2}\eta_{\alpha\beta}h, \tag{1.1.9}$$

in Eq. (1.1.6), allows to formulate the linearized Einstein field equations as

$$\Box\bar{h}_{\alpha\beta} + \eta_{\alpha\beta}\partial^{\nu}\partial^{\mu}\bar{h}_{\nu\mu} - \partial^{\nu}\partial_{\beta}\bar{h}_{\alpha\nu} - \partial^{\nu}\partial_{\alpha}\bar{h}_{\beta\nu} = -\frac{16\pi G}{c^4}T_{\alpha\beta}, \tag{1.1.10}$$

where $\Box = \partial_{\nu}\partial^{\nu}$ is the d'Alembertian operator. By specifying the Minkowski metric in Euclidean space as $\eta = \text{diag}(-1, 1, 1, 1)$ and introducing the Lorentz gauge $\partial^{\beta}\bar{h}_{\alpha\beta} = 0$, the linearized field equations reduce to

$$\Box\bar{h}_{\alpha\beta} = -\frac{16\pi G}{c^4}T_{\alpha\beta}, \tag{1.1.11}$$

where the d'Alembertian operator is defined as $\Box \equiv -\frac{\partial}{c^2\partial t^2} + \frac{\partial^2}{\partial x^2} + \frac{\partial^2}{\partial y^2} + \frac{\partial^2}{\partial z^2}$.

Our interest is in the propagation of a gravitational field far away from the source, which implies $T_{\alpha\beta} = 0$. This means that Eq. (1.1.11) becomes $\Box\bar{h}_{\alpha\beta} = 0$, which has the plane-wave solution

$$\bar{h}_{\alpha\beta} = A_{\alpha\beta}\cos(k^{\nu}r_{\nu}), \tag{1.1.12}$$

where $A_{\alpha\beta}$ represents a constant 4×4 matrix, $k = (\omega, k_x, k_y, k_z)$ the spacetime wave vector and $r = (ct, x, y, z)$ the spacetime position vector. Eq. (1.1.12) represents a plane wave traveling at the speed of light in the spatial direction $\vec{k} = (k_x, k_y, k_z)$ with the wave amplitude in the plane perpendicular to the direction of propagation. These solutions to the wave equation are called *gravitational waves*.

By introducing the transverse-traceless gauge as

$$h_{0\beta} = 0,\ h^{\nu}_{\ \nu} = 0,\ \partial^{\nu} h_{\alpha\nu} = 0, \tag{1.1.13}$$

the number of degrees of freedom is further reduced from 6 to 2. It can then be shown that a wave propagating in the positive z-direction is expressed as

$$h_{\alpha\beta}(t,z) = \left(h_+ \begin{bmatrix} 0 & 0 & 0 & 0 \\ 0 & 1 & 0 & 0 \\ 0 & 0 & -1 & 0 \\ 0 & 0 & 0 & 0 \end{bmatrix} + h_\times \begin{bmatrix} 0 & 0 & 0 & 0 \\ 0 & 0 & 1 & 0 \\ 0 & 1 & 0 & 0 \\ 0 & 0 & 0 & 0 \end{bmatrix} \right) \cdot \cos(kz - \omega t), \tag{1.1.14}$$

where the two remaining degrees of freedom h_+ and $h_\times$ correspond to the *plus* and *cross* polarization amplitudes of the gravitation wave, respectively.

Observable effects of gravitational waves

To study the effect of a gravitational wave on matter, consider the distance ds between any two points starting from Eq. (1.1.2) and by using Eq. (1.1.7) and Eq. (1.1.14) as

$$\begin{aligned} ds^2 &= g_{\alpha\beta} dx^\alpha dx^\beta \\ &= -c^2 dt^2 + dz^2 + 2h_\times \cos(k^\nu r_\nu) dx dy \\ &\quad + [1 + h_+ \cos(kz - \omega t)] dx^2 + [1 - h_\times \cos(kz - \omega t)] dy^2. \end{aligned} \tag{1.1.15}$$

Consider two test masses with the spacetime coordinates $(ct, 0, 0, 0)$ and $(ct, l, 0, 0)$, where l is the distance between the test masses and τ the proper time. The proper distance between the two test masses is probed by a photon that is sent out at the first test mass and then reflected back by the second towards its initial position. This photon moves along the x-axis, thus $y = z = 0$. Furthermore, a photon is moving along a light-like world line, which means $ds^2 = 0$, and therefore Eq. (1.1.15) becomes

$$c^2 dt^2 = [1 + h_+ \cos(\omega t)] dx^2. \tag{1.1.16}$$

This shows that for two test masses positioned along the x-axis, only the plus polarized gravitational wave amplitude has an influence on their separation. From this the distance s, that the photon has traveled in time t, can be calculated by integrating as

$$\begin{aligned} ct = c \int_0^t dt &= \int_0^s \sqrt{1 + h_+ \cos(\omega t)} dx \\ &\approx \int_0^s 1 + \frac{1}{2} h_+ \cos(\omega t) dx \\ &= s[1 + \frac{1}{2} h_+ \cos(\omega t)], \end{aligned} \tag{1.1.17}$$

where in the second step it was assumed that the amplitude of the gravitational wave is very small and that the wavelength is much larger than the distance that the photon traveled, meaning that the amplitude h_+ can be assumed to be constant. If no gravitational wave is present, then the traveled distance is given by $s = 2l$. If a wave passes, then the distance between the test masses is squeezed and stretched by an amplitude $\Delta l = \frac{1}{2}h_+ l$. A measure for the strength of this deformation of spacetime by the gravitational wave is called *strain* and it is defined as the ratio $\Delta l/l$ of the fluctuation induced by the gravitational wave and the unperturbed distance. The effect on a ring of test masses of a gravitational wave traveling perpendicular to the plane spanned by the test masses can be calculated in an similar manner (see Fig. 1.1).

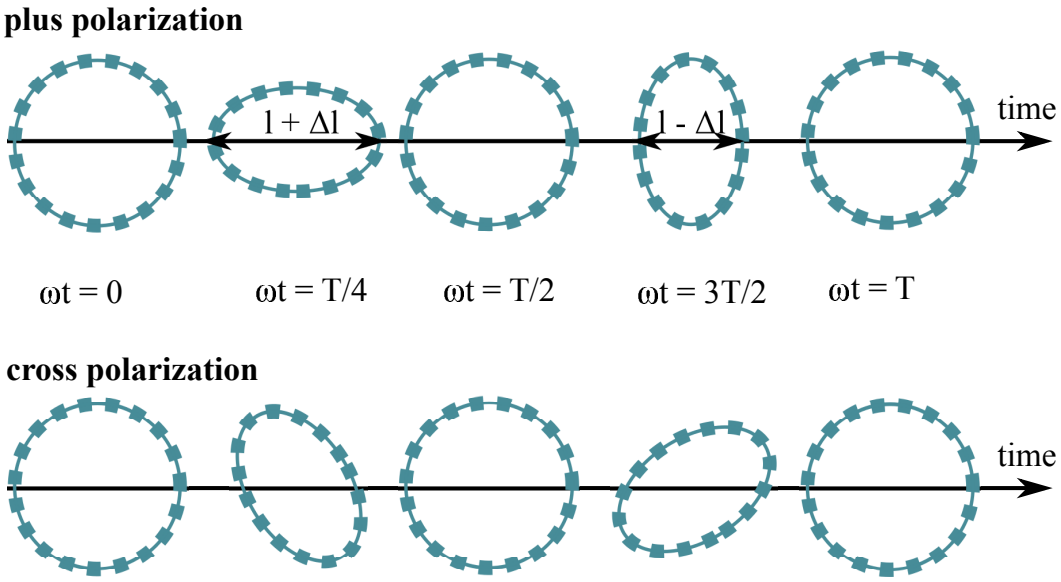

Figure 1.1: *Effect of the plus and cross polarization, top and bottom panel respectively, of a gravitational wave propagating into the plane on a ring of test masses. The period of the wave is denoted with T.*

1.1.3 Sources of gravitational waves

In the above section the effect of gravitational waves far away from the source has been considered. Next, it is of interest to study the conditions that lead to the generation of gravitational waves. In that case the energy-momentum tensor $T_{\alpha\beta}$ is not negligible and its explicit form depends on the mass and energy content of the source. At the source location, where mass and energy are abundant, curvature effects are high. The resulting gravitational field can be studied with a multipole expansion of the energy-momentum tensor [7], which leads in first order to a formulation of the gravitational wave amplitude in the transverse-traceless gauge as

$$h_{\alpha\beta}(t, r) = \frac{1}{r}\frac{2G}{c^4}\ddot{Q}_{\alpha\beta}(t - r/c), \tag{1.1.18}$$

where r is the location of the source and the $\ddot{}$ refers to the second derivative of the elements of the mass quadrupole moment tensor Q with elements $Q_{\alpha\beta}$ with respect to time. This equation implies that gravitational radiation is emitted by sources whose motion involves acceleration,

provided that the motion is not spherically or rotationally symmetric. Such sources are listed in the following and can for example be two objects that are orbiting each other, a spinning non-axisymmetric planetoid or a supernova.

Compact binary inspiral systems

Such a system is characterized by a pair of massive, compact objects which are orbiting each other. For stellar objects in binary systems to emit gravitational waves that are strong enough to be measurable by ground-based detectors, their components need to be of the heaviest and densest objects that are found in our Universe, such as white dwarfs, neutron stars or black holes. Depending on the mass and spin composition of the components, each binary system emits gravitational waves with a characteristic waveform. As binary systems are mathematically relatively easy to describe, these waveforms are to high accuracy predictable by numerical relativity [8]. The evolution of an inspiraling binary system goes through three phases. During the *inspiral* phase, the objects orbit each other up to billions of years while emitting gravitational radiation. Due to the loss of energy through gravitational waves, the inspiral radius gets smaller. The motion of the objects is then accelerated as they orbit faster and faster around each other, while the strength of the gravitational wave increases. This process continues until both objects collide and it is during this *merger* phase that the gravitational radiation power reaches a maximum. The resulting object is in a highly excited state and slowly relaxes to a state of low energy by further emitting gravitational waves. This final phase is called the *ringdown*. The first indirect evidence of the emission of gravitational waves in 1981 originates from a fourteen-year long observation of a binary pulsar system [1, 9] and the most frequent sources of gravitational waves detected with laser interferometers have been binary black hole systems (see Section 1.1.4).

Continuous gravitational wave emission

A single, massive spinning object can emit a continuous gravitational wave signal if it has non-axisymmetric deformations [10]. Such objects can for example be rotating neutron stars with 'mountains' and 'valleys'. These surface imperfections lead to a quadrupole moment that changes in time. As a result the object emits gravitational waves at a quasi-constant frequency and amplitude. Current models estimate that our Galaxy contains more than 500 000 active pulsars, from which only about 2000 have been discovered [11]. Based on the expected population, as well as their distance and mass distribution, an upper limit of the maximum strain that can be detected in the frequency band from 50 Hz to 2 kHz has been estimated to be of the order of $h_0 \approx 4 \cdot 10^{-24}$ [12]. This is within the sensitivity range of next generation gravitational wave detectors such as Einstein Telescope (see Fig. 1.10).

Burst gravitational wave emission

Bursts are short-duration events from unknown or unexpected sources, which may be accompanied by electromagnetic radiation such as intense gamma-ray bursts. As sources are either unknown or poorly understood, modeling waveforms from burst events is highly challenging and contains many degrees of freedom. Gamma-ray bursts may be accompanied by gravitational waves originating from a range of events: they are emitted by matter interacting with an accreting black hole [13], core-collapsing supernovae [14] or even neutron star binaries [15]. The various generation mechanisms underline the importance of multi-messenger astronomy when searching for gravitational waves from burst signals.

Stochastic gravitational wave background

It is assumed that a background of gravitational radiation is present in the Universe [16]. This radiation may consist of gravitational waves emitted from many independent, weak and unresolved sources or of gravitational waves that have been stochastically generated during the Big Bang, very much like the cosmic microwave background. This radiation is thought to have been produced a fraction of a second after the Big Bang, much earlier than the generation of the cosmic microwave background. Due to the expected low amplitudes, measuring this type of gravitational radiation will be challenging, but would allow to probe the Universe to the earliest moments of its existence.

1.1.4 Direct detections of gravitational waves

Direct gravitational wave events are measured with a global network of detectors, currently with main contributions from the Advanced LIGO detectors in Hanford and Livingston, US, and the Advanced Virgo detector in Italy, Europe (see Section 1.2.4). The operation periods of gravitational wave detectors can be split into two parts; a commissioning and upgrade phase, and an observation run phase. During the commissioning and upgrade phase the sensitivity of the detector is improved by implementing hardware and software upgrades, and by fine-tuning the performance of existing structures. The goal is to minimize technical noise from within the detector to achieve its best state-of-the-art response to gravitational wave signals. Gravitational wave data is taken during observation runs, during which the detector soft- and hardware state is frozen. The observational periods are synchronized between all detectors in the network, such that times of parallel data acquisition are maximized. Three observation runs, labeled O1, O2 and O3, have been completed by the network [17].

During observation runs, three independent algorithms search the data for gravitational wave events. Two matched-filter searches, called PyCBC [18] and GstLAL [19], are based on a bank of gravitational wave template waveforms that have been derived from relativistic gravitational wave models. An unmodeled search for short-duration or burst signals, called coherent WaveBurst (cWB) [20], aims to identify gravitational wave events with unknown waveforms. These three algorithms target overlapping, but different search spaces, where they apply independent methodologies. They complement each other, but can also serve to cross-check individual search results.

All three search methods lead to event triggers and the identification of possible gravitational wave events. Their statistical significance is classified via a term called False-Alarm-Rate probability (FAR). The FAR expresses the probability that a pipeline wrongly labels a non-astrophysical event with the same statistical significance as the candidate event under question [21]. A sample of events, all with a FAR less than 1 event per 30 days, contains less than 50% noise triggers. It has therefore been chosen as threshold to separate confident gravitational wave detections from event triggers [17]. Key source parameters, such as mass and spin of the components involved in the merger process, source distance or parameters of the equation of state, are derived from Bayesian inference [22]. Sky localization, which is crucial for the search of electromagnetic counterparts in multi-messenger astronomy, and event rate estimates are improved by increasing the numbers of detectors in the network [23, 24].

Since O3, an additional pipeline called Multi-Band Template Analysis (MBTA) identifies events with matched filtering and archives them in the publicly available GraceDB database [25]. MBTA generates a probability sky map that communicates information such as sky localization

of events with electromagnetic counterparts with a latency of up to 40 min to electromagnetic follow-up partners [26].

Highlights of the first three observation runs will be given in the following. For a full catalogue of all gravitational wave events during O1 and O2 the reader is referred to [17, 27] and citations in these references.

First observation run (O1): 12.09.2015 - 19.01.2016

During the first observation run the two Advanced LIGO detectors in Handford (LHO) and Livingstone (LLO) were operational for a total of 130 days, where they collected 51.5 days of coincident data. In this period LLO had a sensitivity corresponding to the binary neutron star (BNS) range of about 60 Mpc and LHO of about 80 Mpc. During the first observation run, three confidence gravitational wave detections from stellar-mass binary black hole mergers were made [2, 17, 28]. The very first detection of gravitational waves, called GW150914, was also the event with the highest signal-to-noise ratio (SNR) during O1 (Fig. 1.2) [2]. The signal emerged from a binary-black hole merger (BBH) at a luminosity distance of 440^{+150}_{-170} Mpc, which has been localized to an area of about 182 deg^2 towards the southern hemisphere. In the source frame, the initial component masses have been estimated to be $35.6^{+4.7}_{-3.1}$ $M_\odot$ and $30.6^{+3.0}_{-4.4}$ $M_\odot$, with a final black hole mass of $63.1^{+3.4}_{-3.0}$ $M_\odot$, where a total energy of $3.1^{+0.4}_{-0.4}$ $M_\odot c^2$ has been radiated in gravitational waves. Considering only O1 data, their FAR is less than one event per 203 000 years.

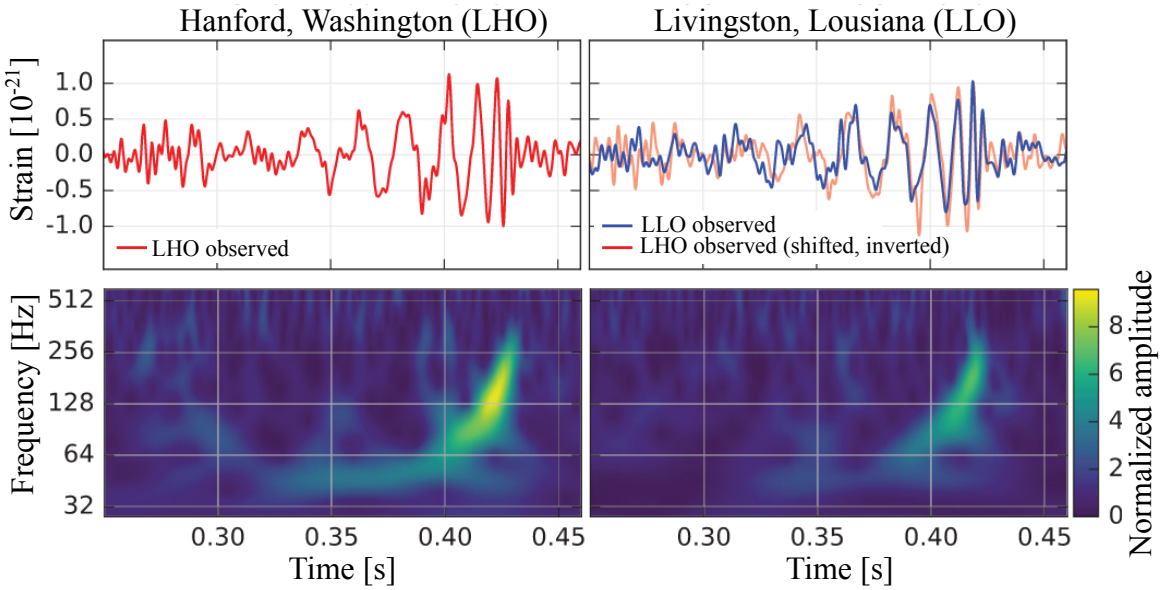

Figure 1.2: *Gravitational wave event GW150914 observed at LHO (left column) and LLO (right column). In the top right plot, the LHO data has been shifted by about* 7 ms *and inverted to account for the travel time and the orientation of the detectors with respect to each other. The first row shows the almost unfiltered, raw time-domain signal in terms of the detector strain. It is remarkable that the gravitational wave signal is visible with the bare eye. The second row shows the same data in the time-frequency domain, where an increase in amplitude and frequency can be related to the chirp signal of the merging black holes. Figure adapted from [2].*

Second observation run (O2): 30.11.2016 - 25.08.2017

During the second observation run, the two Advanced LIGO detectors were operational for 269 days, during 118 of which they collected coincident data. In this period LLO reached a maximum BNS range of 100 Mpc, while LHO reached a BNS range of about 80 Mpc. On 01.08.2017 the Advanced Virgo detector joined the network with a BNS range of 25 Mpc. The three-detector network collected 15 days of coincident data. During the second observation run 11 confident gravitational wave detections were made, 10 of which originated from binary black hole mergers and one from the first measurement of gravitational waves from a binary neutron star inspiral [17, 29–32]. Next to being the first observed BNS event, GW170817 was the event with the highest network SNR during O1 and O2 combined (Fig. 1.3) [32]. Due to the three-detector network the event was localized within a sky region of 16 deg^2 in the southern hemisphere at a luminosity distance of 40^{+7}_{-15} Mpc, which makes it the closest event detected so far. Employing an equation of state that includes tidal effects and spins, the component masses were estimated to be $1.46^{+0.12}_{-0.10}$ $M_\odot$ and $1.27^{+0.09}_{-0.09}$ $M_\odot$ and the energy radiated in gravitational waves was constrained to a lower limit of 0.04 $M_\odot c^2$. Furthermore, the event could be associated with a short γ-ray burst measured with the FERMI and INTEGRAL satellites, which made it the first gravitational wave event in an era of multi-messenger astronomy [33].

Third observation run (O3): 01.04.2019 - 27.03.2020

The third observation run started with a three-detector network consisting of the two Advanced LIGO and the Advanced Virgo detector and lasted until 27.03.2020. The detectors reached BNS ranges of about 130 Mpc for LLO, 115 Mpc for LHO and 60 Mpc for Advanced Virgo [34]. During this observation period a second binary neutron star merger, GW190425, was detected by the LIGO Livingston detector [35]. The system was located at a luminosity distance of 159^{+69}_{-71} Mpc and was with an observed total mass of $3.4^{+0.3}_{-0.1}$ $M_\odot$ larger than any known BNS system. On 25.02.2020 the KAGRA detector in Japan joined the network for the first time, where it reached a sensitivity of about 1 Mpc at the end of the run. Further upgrades will allow its contribution to future observational runs [36]. Since O3, observations and event triggers are publicly accessible through the GraceDB database [25]. Post-processing analysis of these events will lead to a further classification of the events. Results and updates on parameter estimates

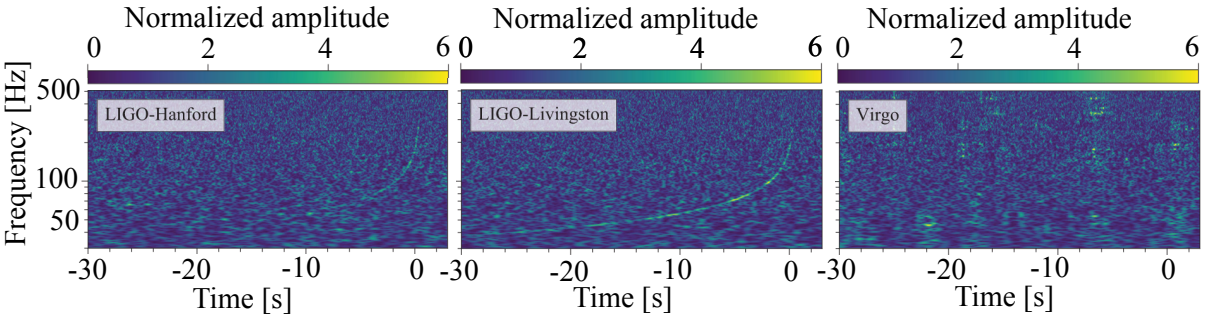

Figure 1.3: *Time-frequency representation of coincident data during the BNS inspiral GW170817. The event was loudest in the LLO detector, followed by the LHO detector, while it has not been observed in the Virgo detector. The lack of signal in the Virgo detector is a result of the event's orientation in the sky coinciding with the Virgo detector's blind spot. Figure adapted from [32].*

can be expected soon after the conclusion of the observation run.

1.2 Gravitational wave detection

The observable effect of a gravitational wave is the change in distance between two free falling test masses, which is proportional to the gravitational wave's amplitude. The differential displacement that a gravitational wave has on two perpendicular directions can be measured across a wide frequency band with a laser interferometer. All laser interferometers that are built for gravitational wave detection are derived from the basic setup used by Michelson and Morley in their attempt to prove the existence of the luminiferous aether in 1887 [6]. This section derives the working principle of this device for gravitational wave detection and how the basic setup needs to be upgraded in order to reach a sensitivity that allows gravitational wave detection on Earth. Many fundamental noise sources limit the performance of ground based detectors and overcoming these noise sources leads to the advanced gravitational wave detectors that are currently operational in a global network.

1.2.1 Interferometric detection principle

The Michelson interferometer is the basis configuration for today's laser interferometers that are designed for gravitational wave detection [6]. In a Michelson interferometer a laser beam with amplitude E_{in} is split into two separate paths that enter the *interferometer arms* after a beam splitter (BS) (Fig. 1.4, left panel). The beam splitter has amplitude reflection and transmission coefficients r_s and t_s, respectively. At the end of the arms, mirrors with amplitude reflection coefficients r_a and r_b reflect the light back towards the beam splitter, where both beams are recombined. At Advanced Virgo the amplitude transmission and reflection coefficients of the beam splitter are $r_s = t_s = \sqrt{0.5} \approx 0.7$ and the amplitude transmission of the end mirrors is smaller than 0.0001 % [37]. The intensity of the recombined beam is monitored with a photodetector (PD) [38]. If the initial beam at a time t_0 is denoted with

$$E_{in} = E_0 e^{i(kx-\omega t_0)}, \tag{1.2.1}$$

where E_0 represents the initial amplitude right before the beam splitter, ω the angular frequency, k the wave number and x the propagation distance, then the recombined beam is represented as

$$E_{out} = r_s t_s E_0 (r_a e^{2ika} + r_b e^{2ikb}), \tag{1.2.2}$$

where the factor $e^{-i\omega t_0}$ has been absorbed into the amplitude E_0. The power on the PD is then

$$P(t) = \left|E_{out}\right|^2 = r_s^2 t_s^2 |E_0|^2 \left(r_a^2 + r_b^2 + 2 r_a r_b \cos(2k(a-b))\right). \tag{1.2.3}$$

Now assume a gravitational wave is passing the detector such that one arm is extended while the other one is compressed by a small distance $\delta x(t)$. In this case

$$a \to a + \delta x(t) \text{ and } b \to b - \delta x(t), \tag{1.2.4}$$

where the variation in distance $\delta x(t)$ is much smaller than the wavelength of the laser beam. This means that the gravitational wave leads to a dephasing in the single arms as

$$e^{2ika} \to e^{2ika} + e^{2ik\delta x(t)} \text{ and } e^{2ikb} \to e^{2ikb} + e^{-2ik\delta x(t)} \tag{1.2.5}$$

and with Eq. (1.2.3) the power on the photodiode becomes

$$\begin{aligned} P(t) &= r_s^2 t_s^2 |E_0|^2 \Big(r_a^2 + r_b^2 + 2 r_a r_b \cos\big(2k(a-b) + 4k\delta x(t)\big) \Big) \\ &= r_s^2 t_s^2 |E_0|^2 \Big(r_a^2 + r_b^2 + 2 r_a r_b \{\cos\big(2k(b-a)\big)\cos(4k\delta x(t)) + \sin(2k(b-a))\sin(4k\delta x(t))\} \Big) \\ &\approx r_s^2 t_s^2 |E_0|^2 \Big(r_a^2 + r_b^2 + 2 r_a r_b \cos\big(2k(b-a)\big) + 4k r_a r_b \delta x(t) \sin\big(2k(b-a)\big) \Big) \\ &= P_{DC} + \Delta P(t), \end{aligned} \tag{1.2.6}$$

where small angle approximations with $\delta x(t) \ll \lambda$, where λ is the wavelength of the laser beam, were used to split the signal into a static part P_{DC} and a time varying part $\Delta P(t)$. The static part

$$P_{DC} = r_s^2 t_s^2 P_0 (r_a^2 + r_b^2 + 2 r_a r_b \cos\alpha), \tag{1.2.7}$$

where $P_0 = |E_0|^2$ is the laser power, is dependent on the tuning $\alpha = 2k(b-a)$ of the interferometer, which allows to change the interference condition. If $\alpha = (2n+1)\pi$ then $P_{DC} \propto (r_a - r_b)^2$ is minimal and the interferometer is in the *dark fringe* configuration.

To quantify the detection efficiency of a Michelson interferometer in the dark fringe operation, the signal-to-noise ratio needs to be specified. The amplitude of the differential arm length modulation from the gravitational wave signal, depending on the laser power P_0, is given by $\Delta P(t)$. For the signal-to-noise ratio in terms of the power spectrum this is converted to the frequency domain and squared to obtain the power spectrum of the gravitational wave signal as

$$S_{GW}(f) = \big|\Delta P(f)\big|^2 = k^2 r_a^2 r_b^2 P_0^2 \big|\delta x(f)\big|^2, \tag{1.2.8}$$

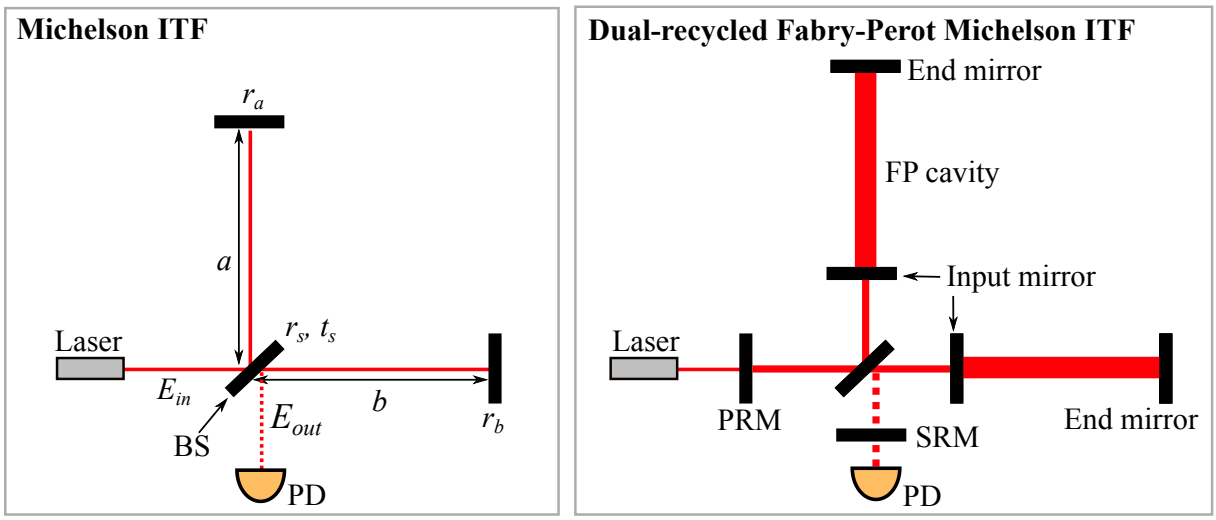

Figure 1.4: *Left: Configuration of a Michelson interferometer (ITF), where an incoming laser beam E_{in} is split at a beam splitter (BS) and directed into two arms of length a and b. The BS has reflection and transmission coefficients r_s and t_s. After being reflected at the mirrors at the end of the arms, the two beams are recombined and the output power is measured with a photodiode (PD). Right: Configuration of a dual-recycled Fabry-Perot Michelson ITF. Two Fabry-Perot cavities in both interferometer arms increase the effective arm length, the power recycling mirror (PRM) leads to an increase of laser power in the interferometer and the signal recycling mirror (SRM) increases the signal amplitude by recirculating a possible gravitational wave signal in the detector.*

where $\delta x(f)$ is the Fourier transform of the time domain signal $\delta x(t)$ and where a balanced beam splitter with $r_s = t_s = \frac{1}{\sqrt{2}}$ has been assumed. If a constant power impinges on a photodiode, the average number of photons arriving at the sensor is fixed, but their arrival time is determined by a Poissonian distribution. The time dependence of the photon arrivals leads to a white noise signal by the diode, the so called shot noise. Its power spectrum is

$$S_{SN}(f) = 2h_P\nu P_{DC} = \frac{1}{2}h_P\nu P_0(r_a + r_b)^2 \tag{1.2.9}$$

where h_p is Planck's constant and ν is the laser frequency. Assuming further that $r_a = r_b = 1$, the signal-to-noise ratio in power becomes

$$SNR = \frac{S_{GW}(f)}{S_{SN}(f)} = P_0\frac{\left|\delta x(f)\right|^2}{2h_P\nu}\left(\frac{2\pi}{\lambda}\right)^2, \tag{1.2.10}$$

where the wave number has been replaced by the wavelength as $k = \frac{2\pi}{\lambda}$. For an $SNR = 1$, the detector strain $h(f) = \frac{\delta x(f)}{L}$, where $L \approx a \approx b$ is the arm length, is then

$$h(f) = \frac{\lambda}{4\pi L}\sqrt{\frac{2h_P\nu}{P_0}}. \tag{1.2.11}$$

Assuming a laser power of $P_0 = 20$ W, a wavelength of $\lambda = 1.064$ μm and an arm length of $L = 3$ km the minimum detectable strain from a gravitational wave signal is about 10^{-20} $\frac{1}{\sqrt{\text{Hz}}}$. The peak strain observed with the loudest gravitational wave event so far was about $1 \cdot 10^{-21}$ [2], which would have not been detected by this idealized Michelson interferometer, not to speak of more quiet gravitational wave events. Main limitations of the sensitivity of the Michelson interferometer originate from its arm length and laser power. Changes to overcome these obstacles have been implemented (see Fig. 1.4, right panel) [39] and are listed in the following.

Fabry-Perot arm cavities

Physically it is difficult to extend the arm length of the ground based interferometers to more than 3 or 4 km, but the effective arm length can be increased by introducing a Fabry-Perot cavity in each detector arm. These cavities are tuned to be resonant with the fundamental mode of the laser beam, leading to an increase of power between the cavity mirrors (for details on Fabry-Perot cavities see Section 1.3.2). The statistical expression for the number of round trips $\mathcal{N}$ a photon can take in a cavity before it leaks out can be related to the finesse $\mathcal{F}$ as

$$\mathcal{N} = \frac{2\mathcal{F}}{\pi} \text{ with } \mathcal{F} = \frac{\pi\sqrt{r_1 r_2}}{1 - r_1 r_2}, \tag{1.2.12}$$

where r_1 represents the amplitude reflection coefficient of the partly reflective input mirror and r_2 the amplitude reflection coefficient of the highly reflective output mirror of the cavity [38]. For a Michelson interferometer the dephasing due to a gravitational wave is $\delta\phi = 2k\delta x(t)$ (see Eq. (1.2.5)), whereas the dephasing in a Fabry-Perot Michelson interferometer is enhanced by $\mathcal{N}$ as

$$\delta\phi = \mathcal{N} \cdot 2k\delta x(t) = 2k\frac{2\mathcal{F}}{\pi}\delta x(t). \tag{1.2.13}$$

The Fabry-Perot arms of the Advanced Virgo detector have a finesse of about 450 [37], which means that the number of round trips is about 285, resulting in an effective arm length of about 860 km.

It may seem that maximizing the finesse of the Fabry-Perot cavities is the ideal way to maximize the dephasing from a gravitational wave signal. However, maximizing the finesse comes with a cost. The higher the finesse, the more power is built up in the cavity and losses due to scattering or absorption increase. In addition, the line width of the reflected light is decreased, which makes it more difficult to control the cavity length and keep the cavity at resonance. The goal is therefore to determine the highest possible finesse to maximize the dephasing from a gravitational wave while minimizing effects from losses and maintaining a stable length control of the cavity [39].

The response of a Michelson interferometer with Fabry-Perot arm cavities $h_{FPM}(f)$, where shot noise is the only noise source, can then be written as [40]

$$h_{FPM}(f) = \frac{\lambda}{8\mathcal{F}L}\sqrt{\frac{2h_P\nu}{\eta P_0}}\sqrt{1+\left(\frac{f}{f_c}\right)^2}, \tag{1.2.14}$$

where η represents the photodiode detection efficiency and f_c the cavity pole frequency, which is related to the effective photon storage time τ as $f_c = \frac{1}{4\pi\tau}$. If $f < f_c$, then the detector response can be assumed to be frequency independent, if $f > f_c$ it increases linearly with f. The cavity pole frequency at Advanced Virgo is about 56 Hz [41].

Power recycling

The signal-to-noise ratio of the Michelson interferometer (see Eq. (1.2.10)) is proportional to the laser power. As increasing the laser power directly to hundreds of Watt is technically not feasible, the power recycling technique is used to increase the effective power in the detector. If the interferometer is operated in dark fringe condition, then the beams from both arms interfere destructively at the beam splitter and no light reaches the PD, as the light is reflected back towards the laser source. By placing a semi-transparent mirror between laser source and beam splitter, this light is guided back into the interferometer, leading to a power build up in the Michelson interferometer and the Fabry-Perot cavities. This additional mirror comes at the cost of an additional degree of freedom that needs to be controlled, the power recycling cavity length. For Advanced Virgo in the final configuration the optical power at the input of the interferometer is foreseen to be 125 W, which will lead to a power of 650 kW on the test masses [37].

Signal recycling

The differential change in path length from a gravitational wave introduces a dephasing of the recombined laser beam. For this dephased beam, the destructive interference condition does not hold anymore and it leaks through towards the PD. By placing an additional semi-transparent mirror, the signal recycling mirror, between the PD and the beam splitter, this signal is reflected back into the interferometer, where the dephasing is increased. Signal recycling allows to shape the response of the interferometer via the length of the signal recycling cavity and the transmissivity of the mirror in three ways. In the *broad-band* configuration the interferometer's detection bandwidth is maximized at the cost of sensitivity. In the *tuned* configuration the sensitivity is increased by about one order of magnitude, but in return the detection bandwidth is decreased by the same factor. In the *detuned* configuration the sensitivity and frequency response are

at an intermediate level, but the sensitivity peaks to the value of the tuned configuration for a small, selected frequency range [39]. These three configurations allow to reshape the response of the interferometer to certain source types, for example for a dedicated search of interesting astrophysical sources such as pulsars.

1.2.2 Fundamental noise sources of ground based interferometers

For gravitational wave detection it is crucial that the residual motion of the mirror is lower than the signal amplitude that is to be observed and that the mirror positions can be read out to high accuracy without introducing any additional noise. These two requirements lead to a set of fundamental noise sources, which ultimately restrain the sensitivity of the detector. In comparison to technical noise sources, which are to be removed during commissioning and by improving the electronic devices in the detector, fundamental noise source are related to the infrastructure and the detector site and cannot be eliminated. Fundamental noise therefore determines the ultimate sensitivity of the detector.

Seismic noise

Vibration of the test mass from direct coupling to ambient seismic vibrations is the most powerful noise source at low frequencies in ground based gravitational wave detectors. A general expression for the mirror displacement $x_{seis}(f)$ due to seismic noise is

$$x_{seis}(f) = \frac{\alpha}{f^2} \left[\frac{\mathrm{m}}{\sqrt{\mathrm{Hz}}}\right], \tag{1.2.15}$$

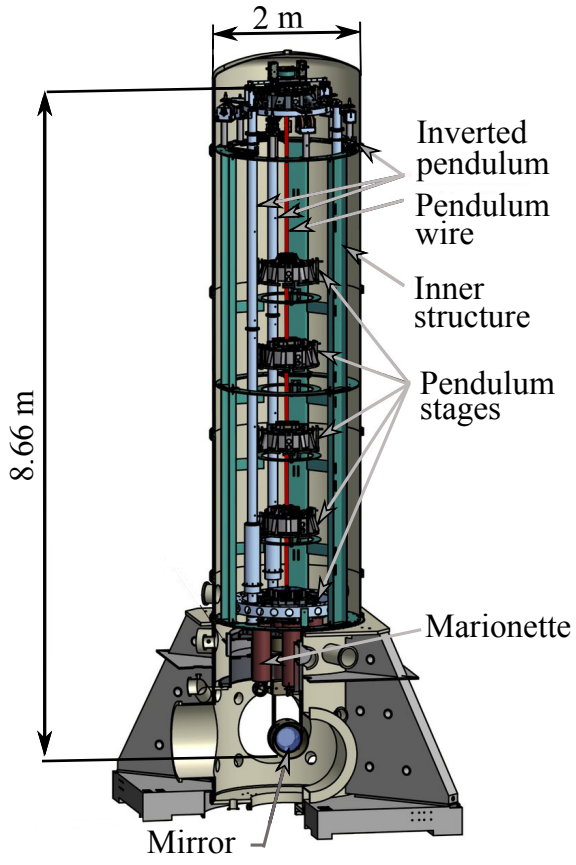

Figure 1.5: *Schematic drawing of the Superattenuator for seismic isolation of each of the mirrors at the Advanced Virgo detector. It consists of a five-stage,* 8.66 m *long pendulum that suppresses coupling of horizontal ground motion to the mirror. Each pendulum stage is replaced by a mechanical filter system, which reduces the coupling to vertical ground motion. At the bottom stage of the cascaded filters, the marionette and the mirror are suspended. Ground motion is suppressed by more than a factor* 10^{10} *by this system. Figure adapted from [42].*

where α depends on the seismic displacement at the location of the detector site and ranges from about 10^{-6} to 10^{-9} m $\cdot$ Hz$^{3/2}$ [39]. This seismic noise needs to be suppressed by at least a factor of 10^{10} to reach sensitivity to gravitational wave signals in the 10 Hz range, where displacements of the order of 10^{-23} $\frac{\text{m}}{\sqrt{\text{Hz}}}$ have to be detected.

In the advanced detectors, seismic noise is actively and passively suppressed through a system of multi-stage horizontal and vertical pendula. The so called Superattenuator of Advanced Virgo [37] consists of a five-stage pendulum, supported by a three-leg elastic inverted-pendulum structure (Fig. 1.5). The transfer function between the top and the bottom stage of a pendulum with N stages drops with $1/f^{2N}$ above the resonant frequencies [43]. With a pendulum length of 8.66 m, the resonant modes of the pendulum in the Superattenuator are shifted to frequencies below 2.5 Hz.

To suppress vertical displacement noise, mechanical filters are used, that consist of a set of concentric blade-springs and magnetic anti-springs. Each stage of the pendulum is connected to the next through a metal wire. At the last stage of the pendulum the optical payload is attached; it comprises the marionette from which the mirror is suspended by four fused silica wires. Coil-magnet actuators on the marionette allow to actively control the mirror position and orientation. The active control of the absolute and relative mirror position with respect to the ground and to the other mirrors in the interferometer is crucial for the stable operation of the detector (see Section 1.2.3).

Seismic noise can also be reduced by carefully selecting a detector site with low seismic noise performance. For seismic noise reduction, next generation detectors such as Einstein Telescope are foreseen to be operated several hundred meters underground.

Newtonian noise

Another noise source related to the seismic field at the detector location is Newtonian or gravity gradient noise. Newtonian noise is the direct interaction of a free falling test mass with time varying density fluctuations of the seismic field (Fig. 1.6). Contrary to seismic noise, this interaction is direct and cannot be suppressed with a filter system. With the improvement of the low frequency sensitivity of advanced gravitational wave detectors in the last years, the scientific effort in modeling site-dependent Newtonian noise that comprises realistic geologies, local sources and full solutions of the wave equation has increased; see for example [44, 45] and Section 3.4, 5.3 and 6.3 of this work.

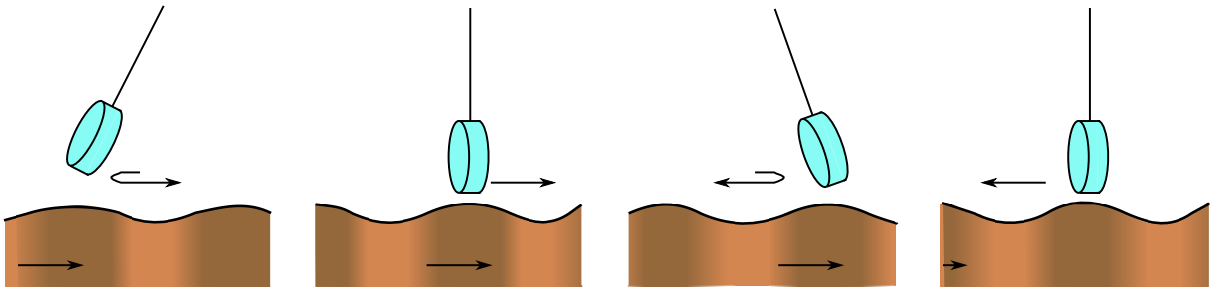

Figure 1.6: *Schematic of the effect of a seismic wave traveling from left to right on a suspended test mass, where denser regions are indicated in dark brown. The test mass is attracted to the most dense regions of the seismic field, which induces a signal in the detector that cannot be distinguished from a gravitational wave signal.*

As Newtonian noise is directly correlated with the seismic noise level of the site, Einstein Telescope aims to be situated in a location that minimizes Newtonian noise. This means that seismically quiet locations are assessed and that the detector will be installed underground. Furthermore, ambient Newtonian noise cancellation schemes, based on large networks of seismic sensors, are under investigation [45, 46] and will allow for real-time subtraction of Newtonian noise.

Next to seismically induced Newtonian noise, atmospheric density fluctuations can lead to Newtonian noise for gravitational wave detectors [47]. However, these fluctuations are not the focus of this work and will not be discussed.

Thermal noise

Thermal noise is present in the mirror bulk, coating and suspensions. It originates from Brownian motion and thermoelastic effects, which affect the material's properties, for instance the refraction index, with temperature. The basis of thermal noise modeling is the fluctuation-dissipation theorem, which states that any mechanical oscillator experiences a motion due its thermodynamic temperature [39]. It relates the power spectrum $S_F(\omega)$ of the force, that induces the thermal fluctuation, to the system impedance $Z(\omega)$ as

$$S_F(\omega) = 4k_B T \mathfrak{Re}\big(Z(\omega)\big), \tag{1.2.16}$$

where k_B represents the Boltzmann constant, T the temperature and where the real value of the impedance is related to the heat dissipation of the system.

The mirrors of Advanced Virgo are made of fused silica that combines low optical absorption, low mechanical losses, negligible birefringence and high homogeneity. The loss angle represents the phase delay that is induced in the laser beam due to the noise source. For the mirror bulk it is of the order of 10^{-10}, which is negligible with respect to the loss angle of the highly reflective coating materials [48].

The coating is a few micrometer thick multilayer of alternating materials with high and low refraction index, tantalum pentoxide and silica, respectively. Their loss angle is of the order of 10^{-4} [49], which makes coating thermal noise the main noise source of the mirror system. The displacement of the mirror surface due to coating thermal noise $x_{th}(f)$ is given by [50]

$$\begin{aligned} x_{th}(f) &= \frac{4k_B T}{\pi f}(\phi_c U_c + \phi_s U_s), \text{ with} \\ U_s = \frac{1-\sigma^2}{2\sqrt{\pi} w Y}&, \text{ and } U_c = \delta_c \frac{(1+\sigma)(1-2\sigma)}{\pi Y w^2}\Omega, \end{aligned} \tag{1.2.17}$$

where U_s and U_c are the strain energy, ϕ_s and ϕ_c are the loss angles of the substrate and coating, respectively, and δ_c is the thickness of the coating. The strain energies depend on the Poisson ratio σ, the beam radius w on the mirror, the Young's modulus Y and a correction factor Ω, where $\Omega = 1$ if the mechanical properties of the alternating substrates are the same. It is apparent from Eq. (1.2.17) that thermal noise can be reduced by decreasing the temperature, increasing the beam spot size or by using different materials for the substrate. For an efficient thermal noise suppression by reducing the system temperature, the detector needs to be operated in cryogenic conditions. Next to the technical challenges of cooling a mirror that is radiated with a high power laser in vacuum, fused silica becomes more 'lossy' with lower temperatures. As a result cryogenic operation requires new mirror bulk materials. The KAGRA experiment is the first

cryogenic gravitational wave detector that employs sapphire mirrors and for Einstein Telescope silicon mirrors are under investigation. Increasing the spot size on the mirror is technically relatively easy to implement, and a thermal compensation system is already in use at Advanced Virgo to counteract deformation due to the uneven heat distribution across the mirror surface (see Section 1.2.3). Finally it is an ongoing challenge to investigate new coating materials and mixtures that combine low losses, allow for cryogenic operation and that can homogeneously be deployed across large surfaces.

At Advanced Virgo, the mirror suspensions are made of fused silica fibers, the same material as the mirror bulk. Still, thermal noise in the suspension system leads to a non-negligible test mass motion. The main origin of thermal noise occurs at the attachment points of the suspension to the metal of the top stage. It has been shown that both ends of the fiber add to the thermal noise depending on the exact shape of the endings [48].

Quantum noise

Two fundamental noise sources arise due to the quantum nature of light. For a laser beam with constant power, the mean number of photons N arriving at the photodetector within an observation time T is fixed and as a result the average power measured by the photodiode is given by $P_0 = \frac{Nh_P\nu}{T}$, where h_P is the Planck constant and ν is the frequency of the laser beam. However, the individual arrival times of the photons within that observation time follow a Poisson distribution, which has a standard deviation of $\sqrt{N}$ for a large number of photons. This means that a fluctuation of the mean power is observed in the photodiode, which is referred to as shot noise. From the signal-to-noise ratio of shot noise with respect to a gravitational wave signal in a Michelson configuration, the strain sensitivity due to shot noise can be derived as (see Eq. 1.2.11)

$$h_{SN}(f) = \frac{\lambda}{4\pi L}\sqrt{\frac{2h_P\nu}{P_0}} \propto \sqrt{\frac{1}{P_0}}. \tag{1.2.18}$$

Furthermore, a laser beam impinging and reflecting from a mirror with mass m exerts a pressure on that mirror. Again, the pressure fluctuates as photon arrivals follow a Poissonian probability distribution, which induces a stochastic force on the mirror. The resulting fluctuation is called radiation pressure noise and its detector strain is [39]

$$h_{RP}(f) = \frac{1}{mf^2L}\frac{1}{2\pi^2}\sqrt{\frac{h_PP_0}{c\lambda}} \propto \frac{\sqrt{P_0}}{f^2}. \tag{1.2.19}$$

Radiation pressure limits the detector performance at low frequency, while shot noise limits the performance at high frequency. Furthermore, increasing the laser power to reduce shot noise at high frequencies comes at the cost of an increased radiation pressure noise at low frequencies and vice versa.

For each frequency there exists a laser power for which shot noise and radiation pressure noise are equal and thus the combined radiation pressure and shot noise, the so called quantum noise, is minimal. These optimal conditions generate a curve across the full frequency band and all optical powers, that is called the Standard Quantum Limit, which is considered as the ultimate sensitivity limit of classical interferometers [39]. To overcome the Standard Quantum Limit, advanced detectors in their final configuration will make use of quantum non-demolition techniques such as injecting squeezed light, which effectively increases the signal-to-noise ratio.

Residual gas noise

The arms of laser interferometers are kept under vacuum at pressures of the order of 10^{-9} mbar to suppress noise from coupling of acoustic excitation to the test masses and to reduce fluctuations in the refractive index due to the statistical variation of the density of gas molecules along the interferometer arms [37]. Reduction in the residual gas noise level is achieved by increasing the performance of the vacuum pumping system. As Advanced Virgo represents one of the world's most sophisticated vacuum installations with a volume of about 7000 m^3, this is an effort of ongoing research.

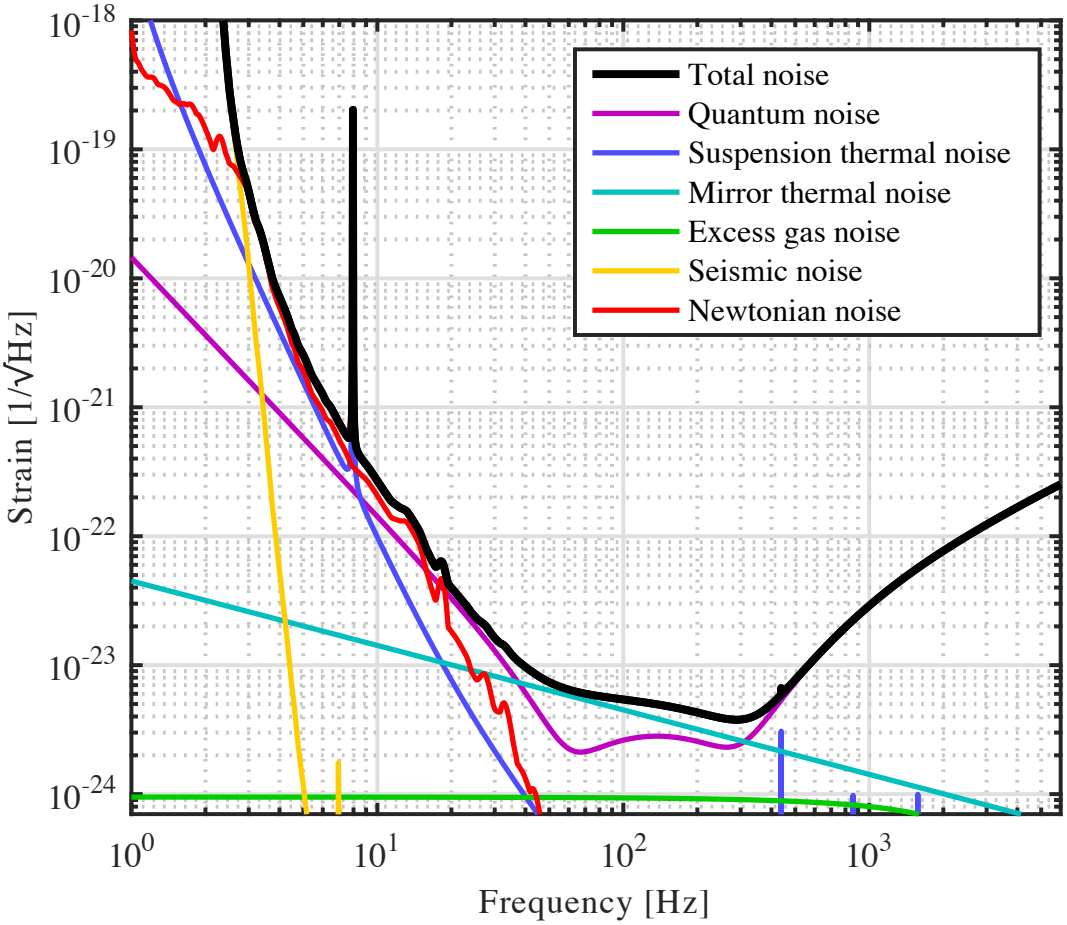

Figure 1.7: *Design sensitivity of the dual-recycled Advanced Virgo gravitational wave detector with an input laser power of* 125 W. *Below* 20 Hz *seismically induced Newtonian noise dominates the performance, while above* 20 Hz *mirror thermal noise and quantum noise determine the shape of the sensitivity curve. The spike at about* 8 Hz *corresponds to a bounce mode of the suspension fiber [51]. The average range for detecting coalescing binary neutron star systems is about* 140 Mpc *and about* 1 Gpc *for stellar-mass binary black hole systems.*

The design sensitivity of the dual-recycled Advanced Virgo interferometer with a laser power of 125 W is displayed in Fig. 1.7 [52,53]. Seismic noise limits the sensitivity at low frequencies, but is negligible above about 2 Hz due to Virgo's efficient seismic isolation. Seismically induced Newtonian noise is the dominating noise source between 2 and 20 Hz, closely followed by the thermal noise from the suspensions. In the intermediate frequency band between 20 and 300 Hz, quantum and mirror thermal noise limit the sensitivity while above 300 Hz only shot noise limits the detector performance. Excess gas noise is almost flat across the whole frequency band and does not limit the sensitivity of Advanced Virgo. In this configuration the parameters of the signal recycling mirror and cavity are chosen to maximize the detection range to about 140 Mpc for coalescing binary neutron star events of mass 1.4 $M_\odot$ and to about 1 Gpc for binary black hole systems with component masses of 30 $M_\odot$.

1.2.3 The Advanced Virgo detector

Advanced Virgo (AdV) in its final configuration is a dual-recycled Fabry-Perot Michelson laser interferometer, where the cavity arms measure a length of 3 km (Fig. 1.8). The main optical components of the detector, that is the Fabry-Perot cavity mirrors, the beam splitter, the power recycling and the signal recycling mirror as well as the optical benches housing the input mode cleaner, the laser injection system and the detection diodes are seismically isolated in Superattenuators.

Parameter	Advanced Virgo
Arm length	3 km
Laser type	Nd:YAG
Laser power at input	125 W
Laser power at the mirror	650 kW
Carrier	1064 nm
Sidebands	$f_1 = 6\,270\,771$ Hz
	$f_2 = 56\,436\,993$ Hz
	$f_3 = 8\,361\,036$ Hz
Mirror material	Fused silica
Mirror weight	42 kg
Mirror diameter	35 cm
Mirror flatness	0.5 nm rms
Input mirror reflectivity	$R = 0.986$
End mirror transmissivity	$T < 1$ ppm
Arm cavity finesse	443
Beam radius at input/end mirror	48.758 mm
beam splitter reflectivity	$R = 0.5$
Power recycling reflectivity	$R = 0.95$
Signal recycling reflectivity	$R = 0.80$
Vacuum pressure	10^{-9} mbar
Best strain sensitivity	$3.4 \cdot 10^{-24}\ \frac{1}{\sqrt{\text{Hz}}}$ (at 300 Hz)
BNS range	140 Mpc

Table 1.2.3: *Main design parameters for the final configuration of the dual-recycled Advanced Virgo interferometer [37].*

The remaining optical benches have less stringent seismic isolation requirements and are suspended through a 1 m long wire in MultiSAS minitowers, which consists of a dual-stage pendulum for vertical and an inverted pendulum followed by two normal pendula for horizontal noise suppression. Before the laser beam enters the interferometer, it passes through the injection system that is housed on a single-stage EIB-SAS bench [37], while the bench hosting the laser is not isolated. For the most relevant parameters see Table 1.2.3.

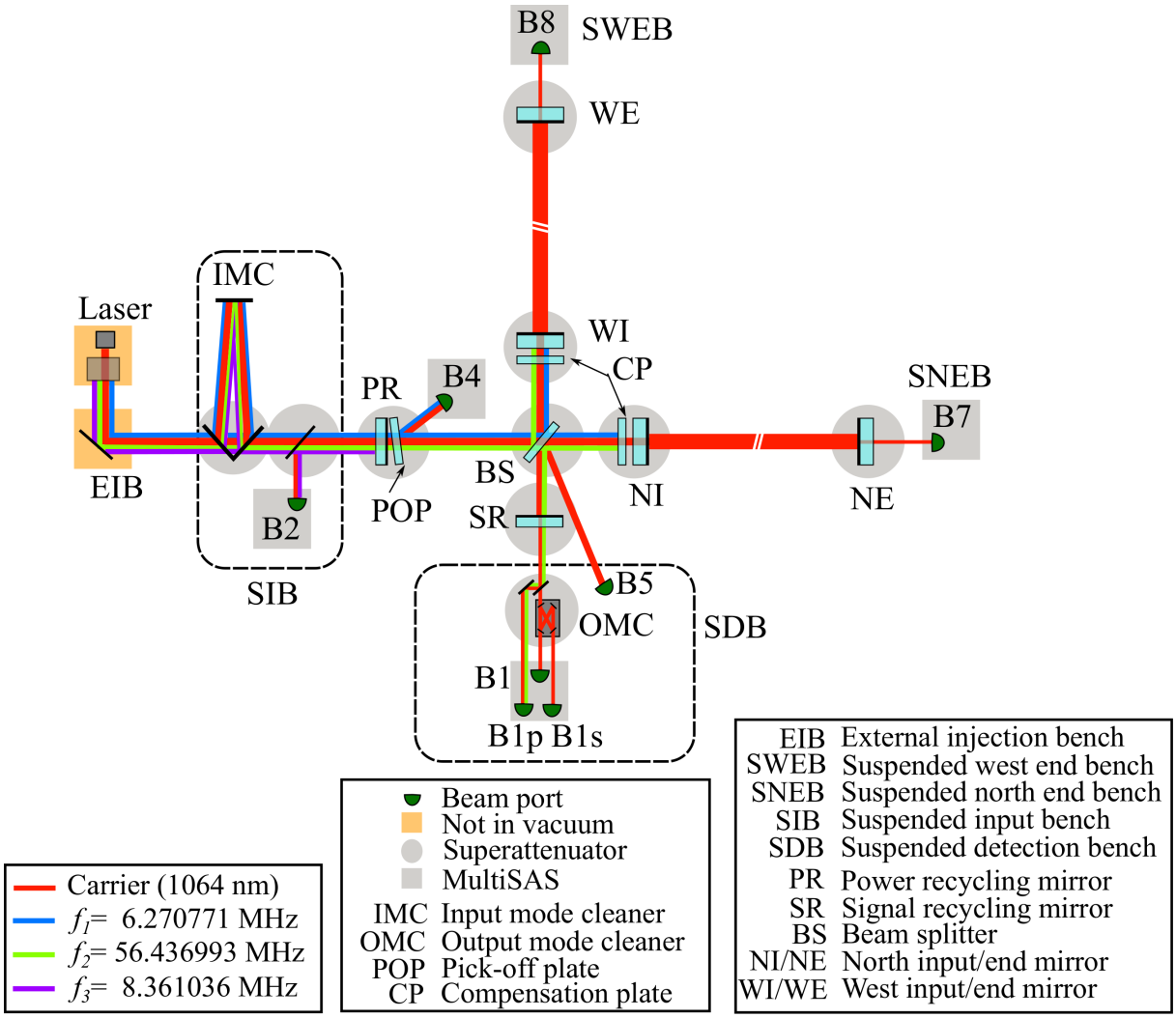

Figure 1.8: *Optical layout of Advanced Virgo in its configuration as dual-recycled Fabry-Perot Michelson laser interferometer. The carrier is indicated in red while the sidebands f_1, f_2 and f_3 are indicated in blue, green and purple, respectively.*

The interferometer is operated with a Nd:YAG laser as carrier with a wavelength of 1064 nm in the fundamental mode. It will have an input power of 125 W in the interferometer's final configuration. The Fabry-Perot cavities are designed such that the fundamental mode of the laser light is resonant in these cavities. In practice, laser light is not completely clean as it may contain higher order modes and suffer from frequency fluctuations. The input mode cleaner (IMC) is an additional cavity that serves as a filter to remove higher order modes and beam jitter from the beam before it enters the interferometer. Similarly, the output mode cleaner (OMC) removes higher order modes or sidebands from the laser beam before it reaches the diodes used for grav-

itational wave detection. The laser light can leave the interferometer at several output ports. These ports and the corresponding extracted beams are characterized as follows:

- Before the OMC, light is extracted at the B1p port, the transmission of the OMC is picked up at the B1 port and the reflection of the OMC is picked up at the B1s port. The reflected field contains all sidebands and higher order modes generated in the interferometer, while the transmitted field contains only the fundamental carrier field. In the dark fringe operation, almost no light should be on the B1 port except when a gravitational wave passes. The B1 port is therefore the detection port of the interferometer,

- At the B2 port, which is also referred to as the symmetric port, part of the beam that is reflected by the interferometer towards the laser is extracted,

- The pickoff from the power recycling mirror is extracted at the B4 port. This signal is used during lock acquisition and it indicates whether the power recycling cavity is at resonance,

- At the B5 port the pickoff of the beam coming from the North arm being reflected of a small wedge on the beam splitter is extracted,

- The B7 and the B8 port contain the signals that are transmitted by the end mirrors of the Fabry-Perot cavities. These signals are used during the process of lock acquisition as they indicate the resonance of the arm cavities.

At each output port one longitudinal photodiode and two quadrant photodiodes are located; they measure DC and RF signals from the interferometer. The longitudinal photodiodes enable the length control of the interferometer, where five degree's of freedom (DOFs) need to be kept under stable length conditions. The DARM degree of freedom corresponds to the differential and the CARM to the common length of the West and North arm Fabry-Perot cavity. The MICH degree of freedom corresponds to the length of the Michelson interferometer at the central part of the interferometer, PRCL to the length of the power recycling cavity. The SRCL degree of freedom corresponds to the signal recycling cavity length. The quadrant photodiodes allow the angular control of the mirrors of the Fabry-Perot cavities, of the beam splitter, and of the signal and the power recycling mirror. There are eight cavity degrees of freedom that need to be controlled. For the pitch and yaw motion of the mirrors these can be identified to be the differential (common) tilt of both cavities that leads to a recombination of both beams on opposite (the same) sides of the beam splitter and the differential (common) shift of both cavities that leads to a recombination of both beams on opposite (the same) sides of the beam splitter (for a detailed treatment see Section 2.3).

Information about the interferometer's longitudinal and angular state is obtained through auxiliary laser beams, which are derived from the fundamental carrier mode. Through phase modulation, three sidebands are derived just before the IMC (Table 1.2.3), where sidebands are laser beams that are in the fundamental mode as the carrier, but oscillate at a predefined frequency offset from the carrier. These sidebands are required to fulfil the following conditions (Fig. 1.8):

- All sidebands have to be resonant in and pass through the IMC,

- As the Fabry-Perot cavities are controlled with the Pound-Drever-Hall technique (see Section 1.3.3), all sidebands need to be reflected by the arm cavities,

- As a result, the first sideband at f_1 needs to be resonant in the power recycling cavity,
- The second sideband at f_2 needs to be resonant in the signal recycling cavity and to be reflected by the arms, also in the power recycling cavity,
- A third sideband at f_3 is used as phase reference and should not resonate in the power recycling cavity, and therefore not enter the interferometer.

In the final configuration the laser power on the test masses will reach up to 650 kW. The heating of the test mass will cause distortions of the optical path length such as thermal lensing and aberration, deform the profile of the highly reflective surface and change the radius of curvature of the test mass due thermal expansion. As a result, the matching between fundamental mode and the cavity is spoiled, which leads to a power loss in the carrier of up to 50 % [53]. To reduce these losses a thermal compensation system, comprising of complementary measurement and correction techniques, is in place at several places in the interferometer. Thermally induced distortions are measured independently on each optical component with a Hartmann Wavefront Sensor and a probe beam, the wavefront of which contains information about the distortion. Additional information can be obtained from the phase camera that measures the spatial intensity and phase distribution of the carrier and sideband in the recycling cavity [54]. To correct the radius of curvature, ring heaters are placed around each of the four test masses as well as around the power and the signal recycling mirror. With a CO_2 laser, compensation plates in front of the input test masses are illuminated with a heat pattern that allows to correct for thermal lensing, aberration and deformation of the substrate.

The Advanced Virgo Plus upgrade

To reach the design sensitivity goal shown in Fig. 1.7 and to surpass the targeted binary neutron star detection range of about 140 Mpc, an upgrade of the Advanced Virgo detector has been initiated. This project is called Advanced Virgo Plus and it aims for a detection range in excess of 200 Mpc. The upgrade consists of two phases, Phase I will be implemented between O3 and O4 and will mainly focus on the permanent reduction of quantum noise by facilitating frequency-dependent squeezing [55]. Furthermore, the signal recycling technique will be integrated, the laser input power will gradually be increased from 26 W to 40 W, a permanent seismic sensor array will be installed at the central building and both end buildings to develop online Newtonian noise subtraction schemes and environmental noise will be reduced by improving the infrastructure of local air-conditioning. Phase II will be integrated between O4 and O5 and is focused on the reduction of mirror thermal noise [56]. Therefore the beam diameter at the end mirrors will be enlarged to about 20 cm, while it is kept unchanged in the central interferometer. This means that the end test masses need to be to replaced by mirrors with a diameter of 55 cm and a mass of 105 kg. Due to the changed beam divergence, input test masses, signal and power recycling mirrors need to be replaced as well. This upgrade requires to adjust the Superattenuator and suspension system, as well as coating and mirror polishing infrastructures.

1.2.4 A global detector network

Since May 2007, the study of gravitational waves with laser interferometers is embedded in a global collaboration (see Fig. 1.9), where a joint effort is made to coordinate data taking periods and to share data and hardware expertise between the individual experiments. This association

of detectors and work force across the globe has several scientific advantages. First, considering coincident events in all detectors of the network allows to reject single-detector environmental noise events or glitches, that might otherwise mimic gravitational wave detections. Second, the accuracy of the sky localization of gravitational wave events with triangulation techniques improves with the number of detectors in the network. This is relevant from a cosmological point of view, but also allows for electromagnetic follow-up studies with optical telescopes. This multi-messenger astronomy embeds the network of gravitational wave detectors in a global effort to push forward the understanding of the fundamental composition and dynamics of the Universe. Currently, five gravitational wave detectors are operational, whereof four are part of the global detection network; a brief overview of their status is listed in the following (see Fig. 1.10).

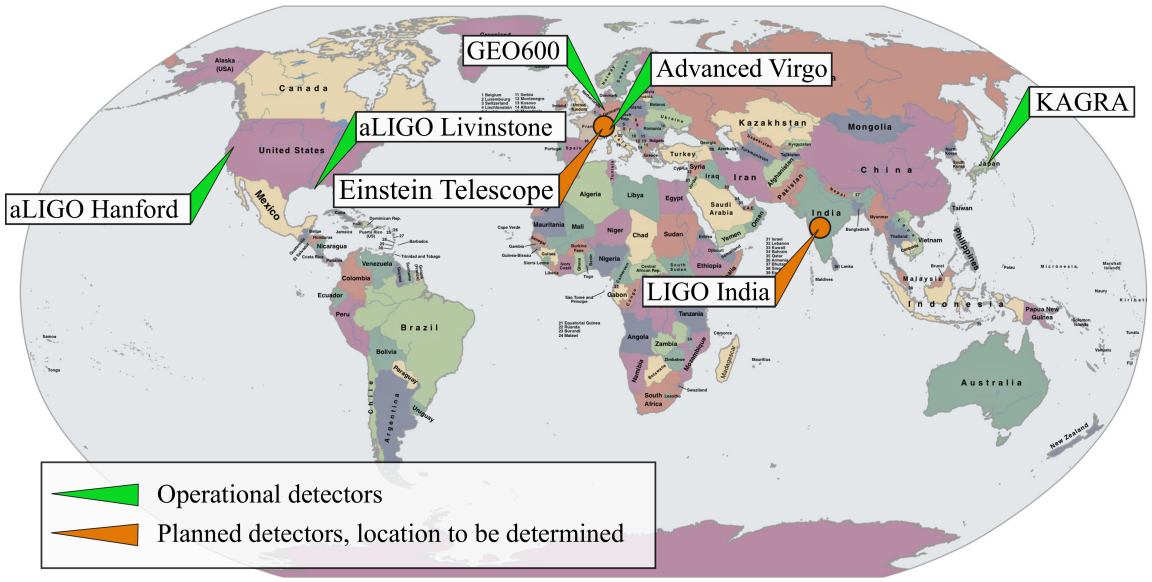

Figure 1.9: *Global gravitational wave detector network with the Advanced Virgo detector in Italy, two Advanced LIGO (aLIGO) detectors in the USA, KAGRA in Japan, GEO600 in Germany, LIGO-India in India and Einstein Telescope in Europe. The two aLIGO detectors, Advanced Virgo and KAGRA are part of the detection network, GEO600 is embedded in the Astrowatch programme, and LIGO-India and Einstein Telescopes are future detectors in the planning phase.*

Advanced LIGO

The LIGO Scientific Collaboration analyses data from two gravitational wave detectors with a 4 km baseline operation, where H1 is located in Hanford, Washington, and L1 in Livingston, Louisiana [57]. A third detector (H2) used to be operated alongside the Hanford detector, but will be employed in India [58]. The first joined operation of the initial LIGO detectors started in 2002 and after several phases of upgrades, commissioning and intermediate science runs the Advanced LIGO detectors started O1 in 2015. They were sensitive in a frequency range from about 10 Hz to 10 kHz. Currently, the Advanced detectors are in their mid design phase where they reach a BNS range of about 120 Mpc, with the goal to reach the final design sensitivity of up to about 180 Mpc in late 2022 [59]. Both facilities will be further upgraded within their

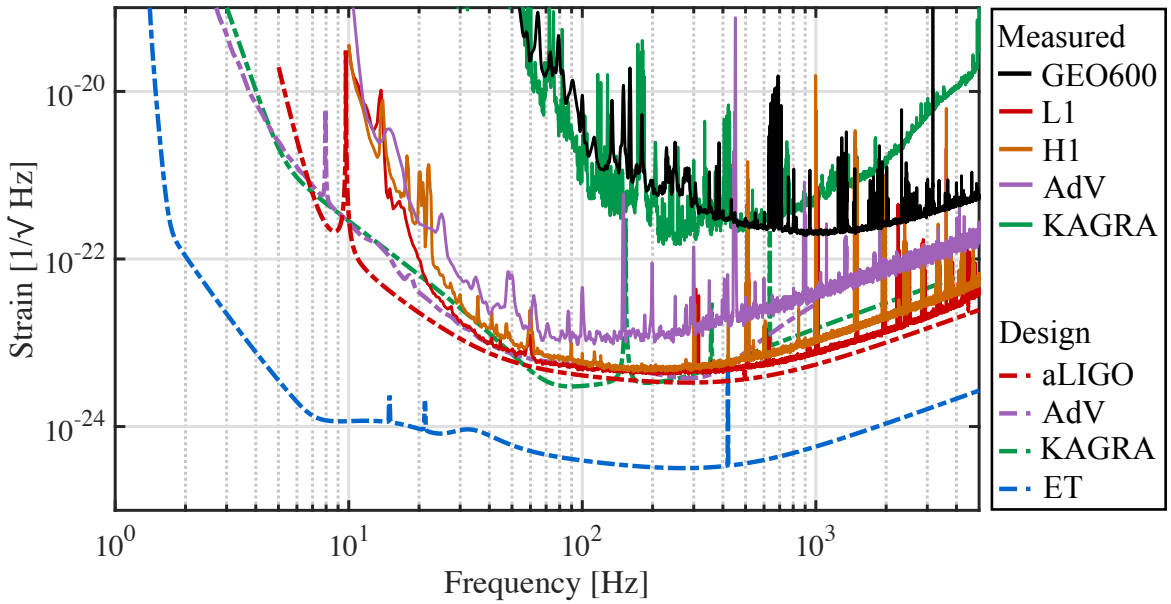

Figure 1.10: *Measured sensitivities of the GEO600, aLIGO Hanford (H), aLIGO Livingston (L) and Advanced Virgo (AdV) detector at the end of O3, together with the design sensitivity curves of AdV, aLIGO, KAGRA and Einstein Telescope (ET).*

existing infrastructure for a sensitivity improvement of a factor two by integrating among others cryogenic mirrors and 40 km long arms.

Advanced Virgo

Advanced Virgo has a baseline of 3 km length and is located in Cascina near Pisa in Italy [60]. Advanced Virgo is sensitive in a frequency range from about 10 Hz to 10 kHz and joined the Advanced LIGO detectors for its first scientific run during O2. Virgo reached a maximum sensitivity of 61 Mpc during O3 and will be further commissioned and upgraded to reach its final design sensitivity of 115 Mpc.

KAGRA

The KAGRA detector has a baseline of 3 km and is located in central Japan. It is the first gravitational wave detector that is constructed underground and it uses mirrors that are cryogenically cooled to 20 K. KAGRA's construction started in 2014 and the detector joined the global network at the end of O3 with an operational Fabry-Perot Michelson interferometer at a sensitivity of about 1 Mpc [61]. In the next years the detector will be further commissioned and upgraded to reach its design sensitivity of about 130 Mpc [62].

GEO600

The GEO600 detector became operational in the early 2000s and is located south of the city Hanover in Germany [63]. Its 1200 m long arms are folded inside a 600 m long beam tube, thus the detector does not have Fabry-Perot arm cavities. GEO600 serves as test bed for new and more risky technologies that may eventually be deployed in its long base-line counterparts. Examples

of technologies that have already been integrated at Advanced LIGO and Advanced Virgo are the multi-stage suspension systems with monolithic final stage, the signal recycling technique and the injection of squeezed light. GEO600 is sensitive from about 100 Hz to about 10 kHz and has a peak design sensitivity of about $2 \cdot 10^{-22} \frac{1}{\sqrt{\text{Hz}}}$ at 1 kHz. During the upgrade periods of the LIGO and Virgo detectors, GEO600 dedicates time to the collection of Astrowatch data. Other test facilities as GEO600 are AIGO in Western Australia [64] and ET Pathfinder in the south of the Netherlands [65]. With their shorter baselines these detectors are dedicated solely to serve as Astrowatch and test facilities for the advanced and next generation instruments.

1.2.5 Einstein Telescope - a European third generation observatory

Existing infrastructures like Advanced Virgo and Advanced LIGO will be further upgraded to optimize their performance until site and infrastructure constraints, such as the detector arm length, vacuum system size, or local seismic conditions prohibit further sensitivity improvement. Advanced Virgo and Advanced LIGO already measure BNS events up to a redshift of $0.03^{+0.01}_{-0.02}$ [35] and stellar mass BBH to a redshift of $0.49^{+0.19}_{-0.21}$ [17]. Next generation detectors will overcome the fundamental technical and infrastructural restrictions and will surpass the strain sensitivity of these detectors by one order of magnitude and extend the low frequency limit as low to as 2 Hz. To reach these sensitivity goals, the European Einstein Telescope project (ET) aims for an underground facility at a yet to be chosen site [66].

The high sensitivity of next generation detectors will significantly improve the detection distance and rate of gravitational wave signals. At design sensitivity, ET is expected to measure BNS events of redshift higher than 10, and stellar-mass BBH systems up to a redshift of about 100 [67], thus probing the Universe up to the Dark Ages where star formation just began. Event rates for these systems will increase by at least a factor 10^4, which will change the perspective on the observation of gravitational waves transients. Observation of the inspiral of an astrophysical system several days before the merger will allow for a preselection of the most exciting events as well as the establishment of an early warning system for the search for electromagnetic counterparts in the context of multi-messenger astronomy. With large numbers of gravitational wave signals, valuable information about the neutron star equation of state can be derived from the coalescence of BNS systems, and the mass and spin distribution of BNS and BBH systems can be refined to unprecedented precision. Furthermore, the high signal-to-noise ratio of nearby events will lead to better constraints on general relativity and the detection of new phenomena like gravitational waves from core-collapse supernovae become more likely.

Design and infrastructure

The baseline geometry of Einstein Telescope consists of three pairs of 10 km long nested, triangular shaped Michelson interferometers (Fig. 1.11, left panel). Traditional L-shaped detectors can only measure a linear combination of the two distinct polarizations of a gravitational wave signal. The triangular design of several nested detectors allows to fully reconstruct both polarizations with two detectors, while the third detector adds to the sensitivity and allows for the rejection of false candidate events through null-streams [68].

Each detector consists of a set of two interferometers, one optimized for high- (HF) and one for low-frequency (LF) operation (Fig. 1.11, right panel). This nested design gives rise to the name *xylophone configuration*. Splitting each detector into two independent interferometers is key to the reduction of quantum noise in the full frequency band. Shot noise at high frequency

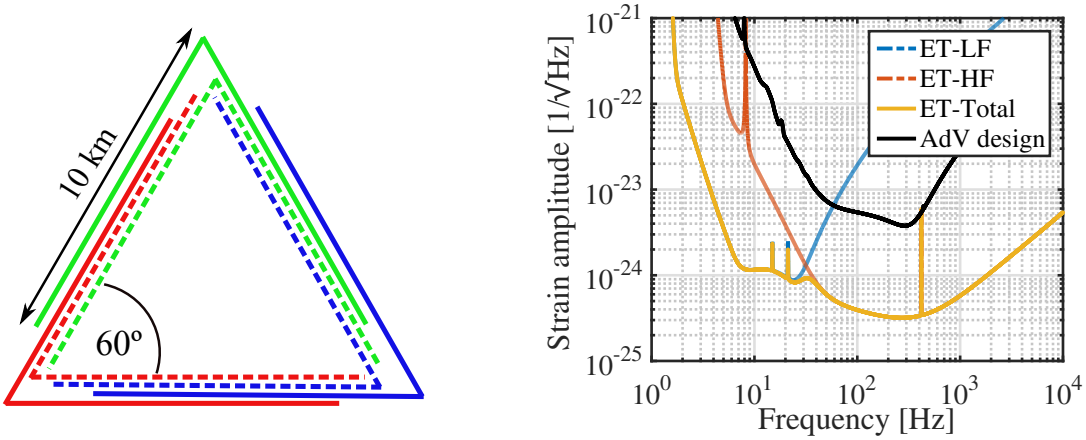

Figure 1.11: *Left: Xylophone configuration of three nested, triangular-shaped Michelson detectors. At each detector orientation an interferometer optimized for low-frequency operation (dashed lines) and one for high-frequency operation (full lines) is located. Right: The total ET sensitivity curve is derived from two interferometers which are optimized at low- and high-frequencies respectively with the cross-over frequency at* 35 Hz*. The sensitivity curve corresponds to one pair of interferometers and the signal polarization being aligned with the interferometer arms. The sensitivity of the full configuration with three nested detectors as shown on the left is dependent on the polarization of the incident signal [69].*

is reduced by increasing the laser power, which leads to a simultaneous increase of radiation pressure noise at low frequencies. The xylophone design allows to achieve a low radiation pressure in a second interferometer with significantly lower laser power with respect to that of the other interferometer. The HF interferometer will be operated at room temperature with high laser power incident on fused silica test masses as in Advanced Virgo. The LF interferometer will be operated under cryogenic conditions with relatively low laser power. To allow for cryogenic mirrors, the test mass bulk material will be silicon and the laser will feature a wavelength of 1550 nm. Additional characteristics of both interferometers are listed in Table 1.2.5.

	ET-LF	ET-HF
Frequency range	1-250 Hz	10-100 kHz
Input laser power	3 W	500 W
Laser power in arms	18 kW	3 MW
Laser wavelength	1550 nm	1064 nm
Beam shape	TEM_{00}	TEM_{00}
Beam radius	9 cm	12 cm
Temperature	10 K	290 K
Mirror material	silicon	fused silica
Mirror diameter	>45 cm	62 cm
Mirror mass	211 kg	200 kg
Suspension length	17 m	8 m
Vacuum pressure	10^{-10} mbar	10^{-10} mbar

Table 1.2.5: *Design parameters for the low- and high-frequency optimized Einstein Telescope nested detectors [37, 70].*

Except for seismic noise, the noise sources that limit the detector performance are mostly due to the detector infrastructure and design. The seismic noise level of the detector is determined by the seismic conditions of the site. To reduce seismic noise at low frequencies, Einstein Telescope will be constructed at a depth of 200 to 300 m below the surface.

Sensitivity curve

The fundamental noise sources contributing to the sensitivity curves of the high- and low frequency ET detectors are displayed in Fig. 1.12 [69]. Quantum noise, that is shot noise at high and radiation pressure noise at low frequencies, is a main noise contribution to both interferometers. In the HF-detector a high laser power suppresses shot noise, while a low laser power reduces radiation pressure in the LF-detector. In both detectors frequency dependent squeezing will be applied to obtain an additional broadband quantum noise reduction of 10 dB.

Thermal noise of suspension and mirrors is most significant at frequencies below 10 Hz. This can be overcome by cooling the optics, which motivates the cryogenic operation of the LF interferometer. For the HF interferometer it is sufficient to spread the heat by an increased spot size.

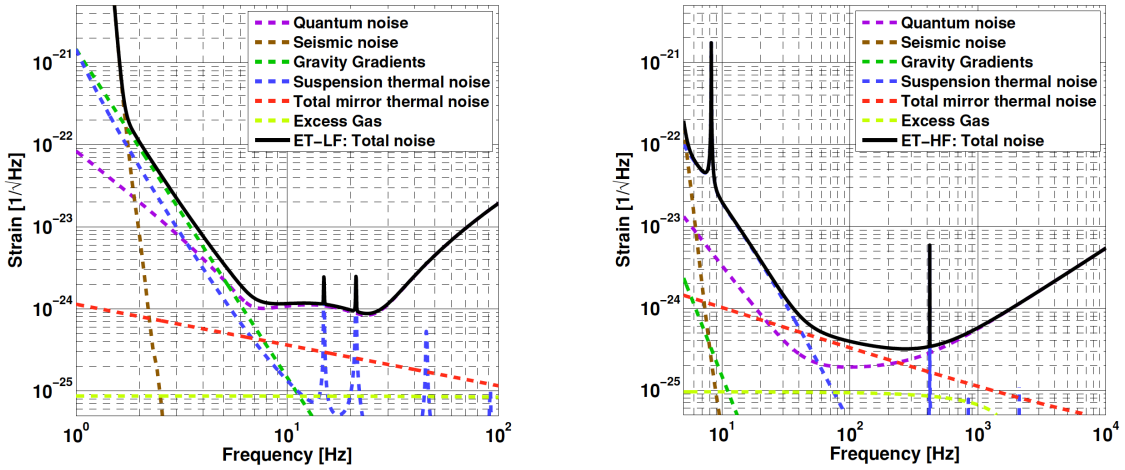

Figure 1.12: *Left: The dominating noise source of the LF interferometer is Newtonian, or gravity gradient noise. It is closely related to the seismic field at the detector site, which itself depends on the local geology and source distribution. Right: The HF interferometer is limited by mirror thermal noise between the cross-over frequency and* 200 Hz*, at high frequency the only fundamental noise source is shot noise.*

The most significant noise sources for the LF interferometer are seismic and Newtonian noise. Seismic noise will be well suppressed by mechanical isolation through a pendulum filter system of 17 m length. Nevertheless, a low seismic noise level of the site is necessary to reach the low noise target set by the design sensitive curve. The seismic noise requirement for the Einstein Telescope site amounts to $4 \cdot 10^{-16} \frac{(\mathrm{m/s^2})^2}{\mathrm{Hz}}$ between 1 and 10 Hz [45]. Such low seismic noise levels can be observed at underground sites or in remote locations, motivating the underground construction of Einstein Telescope.

Closely related to the seismic noise is the site characteristic Newtonian noise. The underground seismic and therefore its Newtonian noise level depends on the local seismic wave field, geology and seismic noise source distribution. To suppress Newtonian noise further than the site

specific noise level, active noise cancellation based on seismic sensor networks is anticipated. By closely monitoring the seismic field in the vicinity of the test masses, Newtonian noise will be predicted and suppressed online from the interferometer output with (Wiener) filtering algorithms.

Candidate sites

The site selection for Einstein Telescope aims at an acceptable seismic and Newtonian noise at the prospective detector site. Seismic studies have been conducted at 14 locations in Europe to derive an understanding about which site characteristic geological and seismic conditions are suitable to reach the design sensitivity targets [45]. It has been found that hard rock geologies exhibit the desired low seismic noise level, however, these sites also showed a negligible attenuation of surface amplitudes at several hundreds of meters depth below 20 Hz. In contrast, geologies of soft materials exhibit the highest seismic noise levels at the surface, but feature a fast attenuation of wave amplitudes with depth. Two sites with varying seismic and geological conditions are currently considered in the site selection process: Sardinia in Italy and Limburg in the Belgian-German-Dutch (BGN) border region (Fig. 1.13). The following will give an overview of the characteristics of each location and the status of the local site characterization efforts.

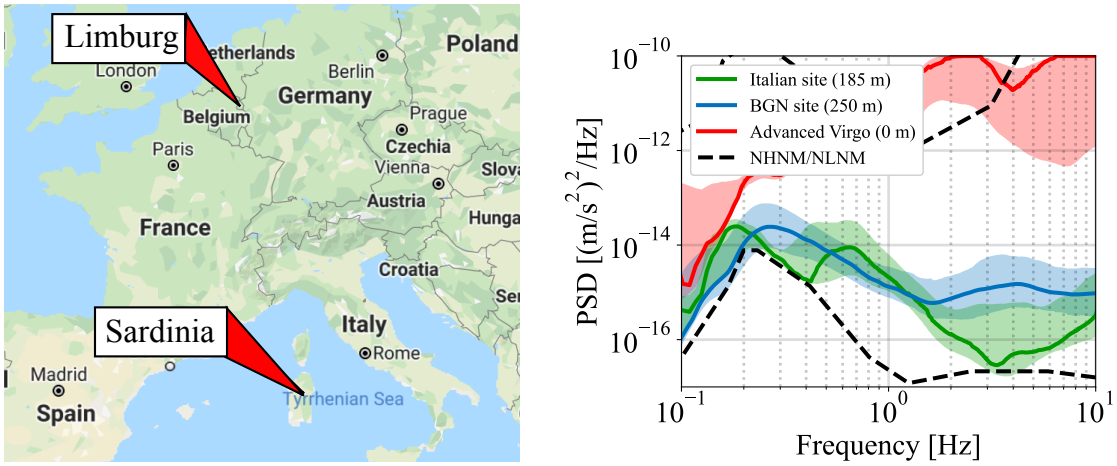

Figure 1.13: *Left: Geographical location of Einstein Telescope candidate sites in Italy and the Belgian-German-Dutch (BGN) border region. Right: Underground power spectral density (PSD) measured at the candidate sites in Italy in* 2013 *and the BGN site in* 2019 *in comparison to the surface PSD at the Advanced Virgo site. The transparent band encloses the* 10^{th} *and* 90^{th} *percentiles of the spectrum and the full curve indicates the mode. Underground PSD values decrease significantly with respect to surface data. The black dashed curves refer to Peterson's new high and new low noise model (see Section 4.1), that place an averaged upper and lower bound on seismic noise observed on Earth.*

Sardinia, Italy The Italian candidate site is located near the Sos Enattos mine close to the village Lula, 40 km from the coast in the north-eastern part of Sardinia [71]. Due to its central

location on the European tectonic plate, the island is less affected by the geo-dynamics of the Mediterranean domain, making it a seismically quiet location. The region is nearly vertically stratified with hard rock materials such as granite and schist [72]. Seismic spectra at a depth of 189 m have been recorded during a measurement period of two weeks in 2012 [45]. In addition to the microseismic peak common to all measurements, the spectrum also exhibits a tertiary microseismic peak between 0.4 and 0.8 Hz, which is characteristic for the Tyrrhenian sea. Around 3 Hz the seismic noise level almost reaches that of Peterson's low noise model.

Limburg, BGN border region The BGN candidate site is located close to the village Terziet in the southernmost part of the Netherlands, within 20 km range of the cities Maastricht and Aachen in the Belgian and German border region. The geology of this area consists of a layer of soft clay material, with a thickness ranging from a few up to about 200 m, laying on hard rock such as sandstone and sandstone conglomerates. Terziet is a remote and seismically quiet location. Near surface, longterm seismic data 10 m below ground are made available by the Royal Dutch Meteorological Institute (KNMI) [73]. Furthermore, the site has been extensively studied with standard techniques of exploration geology since 2017: two passive [74] and one active seismic surface study, based on large arrays of seismic sensors allowed to determine the characteristic seismic noise source distribution and subsurface geology [75]. Underground rock samples have been collected during a borehole study to 135 m depth to determine subsurface material properties. A borehole seismometer at 250 m depth allows to take longterm measurements of seismic spectra at subsurface level. In this work, Newtonian noise at the BGN candidate site has been estimated for a depth of 250 m with a novel approach that takes into consideration the full solution of the wave equation in a geology based on the measured site-specific parameters (see Section 6.3).

These site characterization efforts show a strong motivation to determine the most suitable location for Einstein Telescope in terms of geology, seismic and Newtonian noise. Both candidate sites show low underground seismic noise levels, but have different geological characteristics. As Newtonian noise is the main limit to the low frequency sensitivity of Einstein Telescope it is crucial to not only compare PSD, but also site-based Newtonian noise levels at candidate sites. These Newtonian noise estimates must incorporate realistic geology models that are based on measured subsurface composition of the candidate site, an ambient seismic field model that is based on the local seismic noise source distribution and that represents the full solution of the elastodynamic wave in this geology model. This work presents a possible method to achieve this objective.

1.3 A short introduction to optics

The main detection signal and all control signals of interferometric gravitational wave detectors are derived from laser beams resonating in the cavities of the detector. The mode content of a beam, its frequency composition and whether it is reflected or transmitted by a cavity gives valuable information about the state of the system. The following section aims to summarize the basic properties of Gaussian beams and optical resonators, which are relevant to understand how to control the state of such a system.

1.3.1 Gaussian beams

Electromagnetic waves $\vec{\Psi}(\vec{x},t)$ are solutions to the three dimensional wave equation

$$(\nabla^2 - \frac{1}{v^2}\frac{\partial^2}{\partial t^2})\vec{\Psi}(x,y,z,t) = 0, \tag{1.3.1}$$

where $\nabla^2 \equiv \frac{\partial^2}{\partial x^2} + \frac{\partial^2}{\partial y^2} + \frac{\partial^2}{\partial z^2}$ represents the Laplace operator and v the velocity of the wave in the medium of propagation [76]. The fundamental solution is of the form

$$\vec{\Psi}(x,y,z,t) = \hat{x}\ \tilde{E}(x,y,z)e^{-i(kz-\omega t)} + \hat{x}\ \tilde{E}^*(x,y,z)e^{i(kz-\omega t)}, \tag{1.3.2}$$

which is a harmonic wave propagating in the z-direction with spatial amplitude $\tilde{E}(x,y,z)$, that is transverse polarized in the $\hat{x}$-direction, where $\hat{x}$ represents a vector in the plane perpendicular to the direction of propagation, and where * denotes the complex conjugate. The wave is characterized by its wave number $k = \frac{2\pi}{\lambda}$, with wavelength λ, and its angular frequency $\omega = kv$. Using this expression in Eq. (1.3.1) allows to formulate the time-independent *Helmholtz equation* for the spatial amplitude as

$$(\nabla^2 + k^2)\ \tilde{E}(x,y,z)e^{-ikz} = 0, \tag{1.3.3}$$

where the complex conjugate expression and polarization direction are omitted for convenience without loss of generality. For a laser beam, the amplitude $\tilde{E}$ varies less in the direction of propagation than in the transverse direction. In this case Eq. (1.3.3) reduces to the *paraxial wave equation*

$$(\frac{\partial^2}{\partial x^2} + \frac{\partial^2}{\partial y^2} + 2ik\frac{\partial}{\partial z})\tilde{E}(x,y,z) = 0. \tag{1.3.4}$$

A complete solution of this equation is given in terms of the *Hermite-Gauss modes* E_{nm} of a laser beam

$$\tilde{E} = \sum_{n=0}^{\infty}\sum_{m=0}^{\infty}\tilde{E}_{nm}, \text{ with}$$
$$\tilde{E}_{nm}(x,y,z) = \frac{A}{w(z)}H_m\left(\frac{\sqrt{2}x}{w(z)}\right)H_n\left(\frac{\sqrt{2}y}{w(z)}\right)e^{-\frac{x^2+y^2}{w(z)^2}}e^{ik\frac{x^2+y^2}{2R(z)}}e^{-i(n+m+1)\phi(z)}, \tag{1.3.5}$$

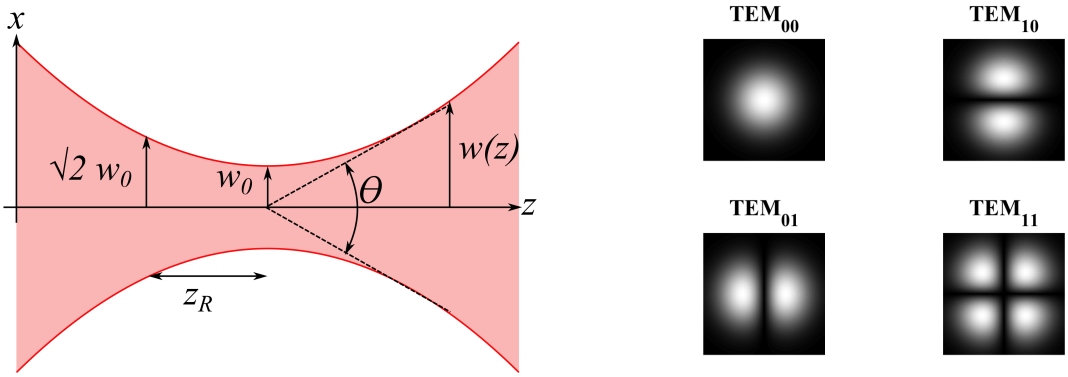

Figure 1.14: *Left: Schematics of a Gaussian beam with radius $w(z)$ (w_0 at the waist), and Rayleigh length z_R. Right: Spatial amplitude of a Gaussian beam of the fundamental* TEM_{00} *mode and the first three higher order modes which are denoted as* TEM_{10}, TEM_{01}, *and* TEM_{11}.

where each index pair n and m corresponds to a so called transverse electromagnetic mode of the order nm, or short TEM_{nm} mode. The amplitude factor is defined as $A = (\frac{2^{1-(n+m)}}{\pi n!m!})^{1/2}$ and the following beam parameters are introduced (Fig. 1.14, left panel):

- The beam radius $w(z) = w_0\sqrt{1 + (\frac{z}{z_R})^2}$ with w_0 being the radius at the waist, and $z_R = \frac{\pi w_0^2}{\lambda}$ the Rayleigh distance. The Rayleigh distance is defined such that at z_R the diameter of the beam is a factor $\sqrt{2}$ larger than the diameter at the waist
- The beam divergence $\Theta = \lim_{z\to\infty} \arctan(\frac{w(z)}{z}) \approx \frac{\lambda}{\pi w_0}$ is a measure for the opening angle of the beam
- The evolving radius of curvature of the beam $R(z) = z\big(1 + (\frac{z_R}{z})^2\big)$. It is infinite at the waist ($z = 0$) and at large distances from the waist ($z \to \pm\infty$), which corresponds to a flat wavefront
- The Gouy phase $\phi(z) = \arctan(\frac{z}{z_R})$, which is a phase shift that occurs when a Gaussian beam propagates through the waist. It accounts for the phase delay between a curved and a plane wave front at a distance z from the focus
- The Hermite polynomials $H_j(x)$ of order j, where $H_0(x) = 1$ and $H_1(x) = 2x$ are the Hermite polynomials of the first and second order.

Laser beams of this form are called *Gaussian beams*, because their intensity profile perpendicular to the direction of propagation follows the Gaussian function. The TEM_{00} mode is called the *fundamental mode* while all other modes are referred to as *higher order modes* (HOM). The spatial amplitude of the fundamental mode and the first three higher order modes are displayed in Fig. 1.14, right panel. The main laser beam in current advanced interferometric gravitational wave detectors is in the fundamental mode. HOMs can occur, but they point towards a misalignment or deformation effect in the optics of the interferometer. We will see in a later chapter how HOM modes can be used to determine the state of the alignment in the detector.

1.3.2 Fabry-Perot cavities

The simplest form of an optical resonator is the Fabry-Perot (FP) cavity (Fig. 1.15) [77]. It consists of two parallel mirrors M_1 and M_2, separated by a distance L. The highly reflective mirror planes with reflection coefficients r_1 and r_2 are facing each other, allowing a standing electromagnetic field to build up in the cavity. The transmission coefficients of the mirrors are denoted by t_1 and t_2. FP cavities are typically used in laser interferometers to increase the optical path length of the carrier field and therefore the sensitivity of the detector.

The electromagnetic fields at different points in a FP cavity can be written in terms of the input field E_{in}, where $E_{in} = \tilde{E}(x, y, z)e^{-ikz}$ corresponds to the spatial amplitude as derived in the previous section, as

$$\begin{aligned}
&\bullet \quad E_{c1} = t_1 E_{in} + r_1 E_{c4} && \bullet \quad E_{c3} = r_2 E_{c2} \\
&\bullet \quad E_{c2} = E_{c1} e^{ikL} && \bullet \quad E_{c4} = E_{c3} e^{ikL} \\
&\bullet \quad E_{tr} = t_2 E_{c2} && \bullet \quad E_{refl} = -r_1 E_{in} + t_1 E_{c4},
\end{aligned} \tag{1.3.6}$$

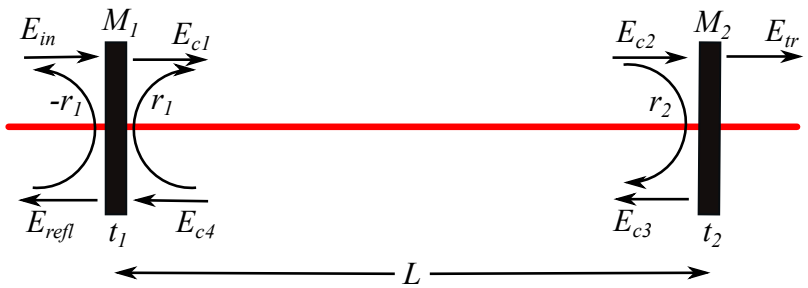

Figure 1.15: *Schematics of a Fabry-Perot cavity of length L, where the amplitude reflection and transmission coefficients, r_i and t_i respectively, are the same on both sides of the mirror M_i. Note that this is not the case at Advanced Virgo.*

where k is the wave number of the electromagnetic wave. Here the convention is used that the reflection of the beam inside the cavity is positive, whereas a reflection from the back side of the mirror generates a phase shift of π [78]. The expressions above allow to derive equations for the transmitted (E_{tr}) and reflected (E_{refl}) fields as

$$\begin{aligned} E_{refl} &= E_{in} \cdot \frac{-r_1 + r_2(r_1^2 + t_1^2)e^{2ikL}}{1 - r_1 r_2 e^{2ikL}} = E_{in} \cdot \tilde{r} \\ E_{tr} &= E_{in} \cdot \frac{t_1 t_2 e^{ikL}}{1 - r_1 r_2 e^{2ikL}} = E_{in} \cdot \tilde{t}, \end{aligned} \tag{1.3.7}$$

where $\tilde{r}$ and $\tilde{t}$ are the reflection and transmission coefficients of the cavity. In practice we measure the power of the transmitted or reflected light. It can be calculated as

$$\begin{aligned} P_{refl} &= P_{in} \cdot \frac{r_1^2 + r_2^2(r_1^2 + t_1^2)^2 - 2r_1 r_2 \cos(2kL)}{1 + r_1^2 r_2^2 - 2r_1 r_2 \cos(2kL)} = P_{in} \cdot R \\ P_{tr} &= P_{in} \cdot \frac{t_1^2 t_2^2}{1 + r_1^2 r_2^2 - 2r_1 r_2 \cos(2kL)} = P_{in} \cdot T, \end{aligned} \tag{1.3.8}$$

where $R = |\tilde{r}|^2$ is the frequency dependent reflectance and $T = |\tilde{t}|^2$ is the frequency dependent transmittance of the cavity. The amount of transmitted and reflected power of a cavity depends on the accumulated round trip phase $\Delta\phi = 2kL$ and the reflection and transmission coefficients of the mirrors. Fig. 1.16, left panel, shows the intra-cavity power of different lossless cavities, where $r_i^2 + t_i^2 = 1$ holds. It is maximal when the cavity is on resonance, which means that the accumulated roundtrip phase of the laser beam is an integer multiple of 2π,

$$\phi = 2kL = n \cdot 2\pi. \tag{1.3.9}$$

The frequency separation between two resonant modes of a cavity is called the *free spectral range* δf_{FSR}. For a cavity of length L, the frequency spacing between two successive optical intensity maxima is

$$\delta f_{\text{FSR}} = \frac{c}{2L}\ [\text{Hz}]. \tag{1.3.10}$$

The linewidth δf of the transmittance peaks, the *full width at half maximum*, depends on the reflection and transmission coefficients of the cavity mirrors. For a cavity of a given length L it

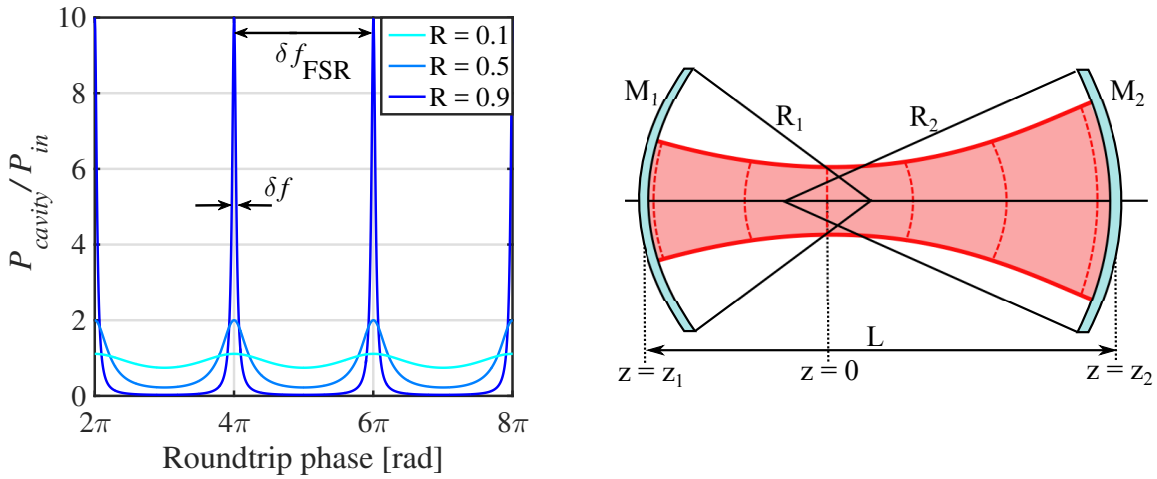

Figure 1.16: *Left: Intra-cavity power P_{cavity} depending on the input power P_{in} with high, intermediate and low reflection coefficients of the mirrors. The peaks of the roundtrip phase are separated by the free spectral range δf_{FSR}, the full width of half maximum is indicated with δf. Right: A stable resonator hosting a Gaussian beam needs to have mirrors that are curved as the laser wavefront and has to fulfil the stability equation $0 < g_1 g_2 < 1$ where $g_i = 1 - \frac{L}{R_i}$.*

can be obtained from $T(\omega = 0) \cdot 1/2 = T(f_{1/2})$ and with Eq. (1.3.8) as

$$\delta f = 2 \cdot f_{1/2} = \frac{\delta f_{\text{FSR}}}{\pi} \arccos\left(-\frac{1 + r_1^2 r_2^2 - 4 r_1 r_2}{2 r_1 r_2}\right), \tag{1.3.11}$$

where $f_{1/2}$ is the frequency at which the transmitted power drops to $1/2$ of its total value. For cavities with high reflection coefficients ($r_1 r_2 \approx 1$) a Taylor expansion of the arccos allows to simplify the linewidth to

$$\delta f = \frac{\delta f_{\text{FSR}}}{\pi} \frac{1 - r_1 r_2}{\sqrt{r_1 r_2}}. \tag{1.3.12}$$

The ratio between free spectral range and linewidth of a cavity is called the *finesse* $\mathcal{F}$ and for a cavity with high reflective mirrors it is

$$\mathcal{F} = \frac{\delta f_{\text{FSR}}}{\delta f} \approx \frac{\pi \sqrt{r_1 r_2}}{1 - r_1 r_2}. \tag{1.3.13}$$

For Advanced Virgo with an arm length of 3 km and reflection coefficients as displayed in Table 1.2.3, the finesse is $\mathcal{F} \approx 450$, the free spectra range is $\delta f_{FSR} \approx 50$ kHz and the full width at half maximum is $\delta f \approx 110$ Hz.

For a FP cavity to be a stable resonator for a Gaussian beam, the mirrors need radii of curvature that are the same as the curvature of the wavefront of the beam at the position of the mirror (Fig. 1.16, right panel). If a resonator with mirrors M_1 and M_2 at locations z_1 and z_2 and radii of curvature R_1 and R_2 is given, then a resonating Gaussian beam in the cavity needs to fulfil the following requirements

$$R(z_1) = z_1 + \frac{z_R^2}{z_1} = -R_1, \quad R(z_2) = z_2 + \frac{z_R^2}{z_2} = R_2, \quad L = z_2 - z_1. \tag{1.3.14}$$

Making use of the cavity parameters $g_i = 1 - \frac{L}{R_i}$, the Rayleigh length z_R and the mirror locations z_1 and z_2 can be expressed as

$$z_R^2 = \frac{g_1 g_2 (1 - g_1 g_2)}{(g_1 + g_2 - 2 g_1 g_2)^2} L^2, \quad z_1 = \frac{-g_2 (1 - g_1)}{(g_1 + g_2 - 2 g_1 g_2)} L, \quad z_2 = \frac{g_1 (1 - g_2)}{(g_1 + g_2 - 2 g_1 g_2)} L. \tag{1.3.15}$$

In order to obtain real and finite solutions of the Gaussian beam resonating in the cavity, the parameters g_1 and g_2 need to be confined to the *stability range* $0 < g_1 g_2 < 1$ [76]. In the FP cavities of Advanced Virgo the input test mass has a radius of curvature of about 1420 m and the end test mass of about 1683 m. The resulting combined cavity parameter is then $g_1 g_2 \approx 0.87$ and it fulfils the stability condition.

1.3.3 The Pound-Drever-Hall technique

The Pound-Drever-Hall (PDH) technique has initially been developed to stabilize the frequency of a laser beam by locking to a stable Fabry-Perot cavity [79, 80]. However, if a stable laser is available, the PDH technique can be used to measure the optical length of a cavity. It is therefore a prominent technique for longitudinal length control in laser interferometers.

Phase modulation

For the PDH technique, a laser beam is phase modulated with an electro-optic modulator (EOM), that is driven by a local oscillator (see Fig. 1.17). In practice this means that power from the incoming field is shifted to different frequency components of the field. The part of the resulting field that has the same frequency as the incoming beam is called the *carrier*, whereas other frequency components are called the *sidebands*. Mathematically, the phase modulation of a carrier field $\Psi(\vec{x}, t) = \tilde{E}_{00} e^{i\omega t}$, where for simplicity the spatial amplitude has been abbreviated

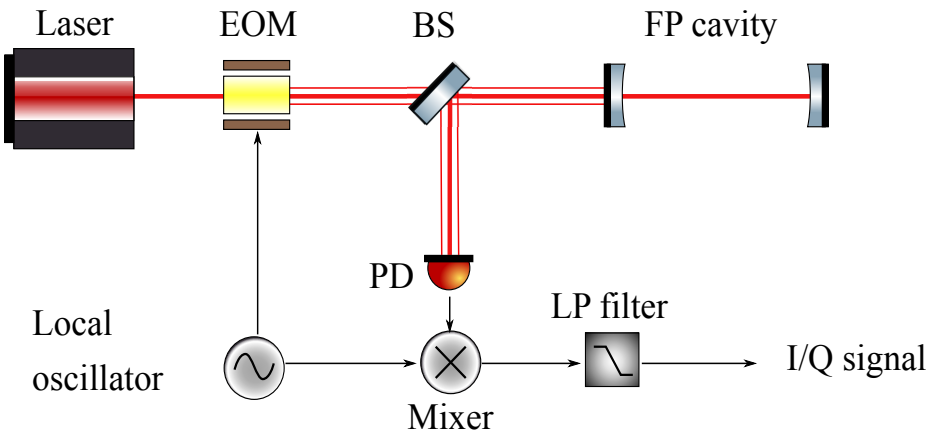

Figure 1.17: *For the PDH technique sidebands are added to a laser beam with an electro-optic modulator (EOM) such that the carrier is resonant in the FP cavity, while the sidebands are anti-resonant. If the cavity is slightly off resonance, a beat signal between the partially reflected carrier and the sidebands can be measured at the photodiode (PD). Demodulating the measured signal at the mixer followed by low-pass (LP) filtering gives an error signal for the length control of the cavity.*

as $\tilde{E}_{00}(\vec{x}) = E_{00}(\vec{x})e^{-ikz}$ (see Eq. (1.3.5)) and where the direction of the polarization has been omitted, can be expressed as

$$\Psi(\vec{x},t) = \tilde{E}_{00}(\vec{x})e^{i(\omega t + m\cos\Omega t)}, \tag{1.3.16}$$

where m represents the modulation depth and Ω the frequency offset between carrier and sideband and called the modulation frequency. Making use of the Jacobi-Anger identity,

$$e^{im\cos(\Omega t)} = \sum_{k=-\infty}^{\infty} i^k J_k(m)e^{ik\Omega t}, \tag{1.3.17}$$

where the $J_k(m)$ are Bessel functions of the first kind, Eq. (1.3.16) can be written as

$$\Psi(\vec{x},t) = \tilde{E}_{00}(\vec{x})e^{i\omega t}\sum_{k=-\infty}^{\infty} i^k J_k(m)e^{ik\Omega t}. \tag{1.3.18}$$

For small modulation indices ($m \ll 1$), higher order Bessel functions decrease rapidly and only the first order terms have to be taken into account. The resulting field is then

$$\Psi(\vec{x},t) = \tilde{E}_{00}(\vec{x})(J_0(m)e^{i\omega t} - iJ_{-1}(m)e^{i(\omega-\Omega)t} + iJ_1(m)e^{i(\omega+\Omega)t}), \tag{1.3.19}$$

where $J_0(m)$ corresponds to the amplitude of the carrier at frequency ω, $J_{-1}(m)$ is the lower sideband amplitude oscillating at $\omega - \Omega$ and $J_1(m)$ is the upper sideband amplitude oscillating at $\omega + \Omega$.

Signal sensing

The modulated beam, consisting of the carrier and sideband fields, is now sent to a Fabry-Perot cavity to probe its response. While the carrier resonates in the cavity, the sideband frequencies are chosen such that they are anti-resonant and reflected from the input mirror. According to Eq. (1.3.9), a laser resonates in a cavity if its length is an integer multiple of the wavelength. For a cavity where the reflection coefficients of both mirrors are the same, and that is slightly off resonance, a part of the carrier field is reflected by the input mirror as well.

The carrier and the sidebands can be seen as three independent beams where the cavity responds to each of them in a different way due to their difference in frequency. The response of a beam reflected by a FP cavity is given by the frequency dependent reflection coefficient $\tilde{r}$ in Eq. (1.3.7). The total reflected field is then the sum of the individual reflected beams

$$\Psi_{refl} = \tilde{E}_{00}[\tilde{r}(\omega)J_0(m)e^{i\omega t} + i\tilde{r}(\omega+\Omega)J_1(m)e^{i(\omega+\Omega)t} + i\tilde{r}(\omega-\Omega)J_1(m)e^{i(\omega-\Omega)t}], \tag{1.3.20}$$

where the relation $J_{-k}(m) = (-1)^k J_k(m)$ was used and where coordinate dependencies have been dropped for readability. The PD then measures the reflected power $P_{refl} = |\Psi_{refl}|^2$ which is

$$\begin{aligned} P_{refl} =& P_c|\tilde{r}(\omega)|^2 + P_s(|\tilde{r}(\omega+\Omega)|^2 + |\tilde{r}(\omega-\Omega)|^2) + \\ & 2\sqrt{P_c P_s}[\cos(\Omega t)\cdot \mathrm{Im}\big(\tilde{r}(\omega)\tilde{r}^*(\omega+\Omega) - \tilde{r}^*(\omega)\tilde{r}(\omega-\Omega)\big) \\ & - \sin(\Omega t)\cdot \mathrm{Re}\big(\tilde{r}(\omega)\tilde{r}^*(\omega+\Omega) - \tilde{r}^*(\omega)\tilde{r}(\omega-\Omega)\big)] + \\ & + \mathcal{O}(2\Omega), \end{aligned} \tag{1.3.21}$$

where $P_c = |\tilde{E}_{00}|^2 J_0^2(m)$ and $P_s = |\tilde{E}_{00}|^2 J_1^2(m)$ are the individual powers of the carrier and the sideband, respectively. The first line of Eq. (1.3.21) corresponds to the static DC part of the signal, the terms in the second and third line with the frequency Ω are the interference (beat) between carrier and the first order sidebands and the last line with frequency terms of 2Ω or higher contains the interference between the sidebands themselves, and the beat between carrier and higher order sidebands.

Demodulation

The PD measures the power of the reflected beam, where the information about the cavity length is embedded in the amplitude reflection coefficient (see Eq. (1.3.7)). This information can be extracted by demodulating the beat signal between carrier and sideband at a demodulation frequency Ω' by electronically mixing it with the signal from a local oscillator. Mathematically, this means to multiply Eq. (1.3.21) with $\cos(\Omega' t)$. Making use of the identities

$$\begin{aligned}\cos(\Omega t)\cos(\Omega' t) &= \frac{1}{2}[\cos((\Omega-\Omega')t) + \cos((\Omega+\Omega')t)] \xrightarrow{\Omega'=\Omega} \frac{1}{2}[1+\cos(2\Omega t)],\\ \sin(\Omega t)\cos(\Omega' t) &= \frac{1}{2}[\sin((\Omega-\Omega')t) + \sin((\Omega+\Omega')t)] \xrightarrow{\Omega'=\Omega} \frac{1}{2}\sin(2\Omega t),\end{aligned} \tag{1.3.22}$$

it can be seen that in the case of $\Omega' = \Omega$ only one DC term remains from the beat between carrier and sideband, the rest of the signal is shifted to 2Ω. The other parts of the signal in Eq. (1.3.21) are shifted to Ω, 2Ω or 3Ω. Isolating the DC part with a low pass (LP) filter, we can obtain the *in-phase* error signal (P_I). By demodulating with a $\pi/2$ phase shifted signal ($\sin(\Omega' t)$), the complementary *quadrature* error signal (P_Q) is obtained

$$\begin{aligned}P_I &= 2\sqrt{P_c P_s}\cdot \mathrm{Im}\big(\tilde{r}(\omega)\tilde{r}^*(\omega+\Omega) - \tilde{r}^*(\omega)\tilde{r}(\omega-\Omega)\big),\\ P_Q &= 2\sqrt{P_c P_s}\cdot \mathrm{Re}\big(\tilde{r}(\omega)\tilde{r}^*(\omega+\Omega) - \tilde{r}^*(\omega)\tilde{r}(\omega-\Omega)\big).\end{aligned} \tag{1.3.23}$$

Now consider a Fabry-Perot cavity with high finesse ($1-r_1 r_2 \ll 1$), low losses ($r_1^2+t_1^2 \approx 1$) and a highly reflective end mirror ($r_2 \approx 1$) close to resonance [78]. On resonance the phase of the carrier $\phi_\omega = 2\pi n$ is derived from the resonance condition (see Eq. (1.3.9)) and the phase of the anti-resonant sidebands is $\phi_{\omega\pm\Omega} = 2\pi(n \pm \frac{1}{2})$. Assuming a small deviation from resonance $\phi \to \phi + \delta\phi$, where $\delta\phi \ll 1$, the reflection coefficients for the carrier and the sidebands from the cavity, $\tilde{r}(\omega)$ and $\tilde{r}(\omega\pm\Omega)$ respectively, can be derived from Eq. (1.3.7) as

$$\begin{aligned}\tilde{r}(\omega) &\approx \frac{-r_1 + r_2(r_1^2+t_1^2)(1+i\delta\phi)}{1-r_1 r_2(1+i\delta\phi)} \approx \frac{(1-r_1+i\delta\phi)(1-r_1+ir_1\delta\phi)}{(1-r_1-ir_1\delta\phi)(1-r_1+ir_1\delta\phi)}\\ &= 1 + i\delta\phi\frac{1+r_1}{1-r_1},\end{aligned} \tag{1.3.24}$$

$$\begin{aligned}\tilde{r}(\omega\pm\Omega) &\approx \frac{-r_1 - (1+i\delta\phi)}{1+r_1(1+i\delta\phi)} \approx \frac{(-r_1-1-i\delta\phi)(1+r_1-ir_1\delta\phi)}{(1+r_1+ir_1\delta\phi)(1+r_1-ir_1\delta\phi)}\\ &= -1 - i\delta\phi\frac{1-r_1}{1+r_1}.\end{aligned} \tag{1.3.25}$$

This means that the product $\tilde{r}(\omega)\tilde{r}^*(\omega+\Omega) - \tilde{r}^*(\omega)\tilde{r}(\omega-\Omega)$ in Eq. (1.3.23) is purely imaginary and that P_Q is zero. In order to use the reflected signal as error signal, it needs to be demodulated with a cosine. The resulting in-phase error signal is then

$$P_I = 64\sqrt{P_c P_s}\frac{r_1}{1-r_1^2}\frac{\pi}{\lambda}\delta L, \tag{1.3.26}$$

where the relation $\delta\phi = \frac{4\pi}{\lambda}\delta L$ has been used to convert phase to length. Close to resonance P_I drops with a slope of $64\sqrt{P_c P_s}\frac{r_1}{1-r_1^2}\frac{\pi}{\lambda}$ and vanishes at $\delta L = 0$, it is therefore used as error signal to stabilize the length of a cavity on resonance for the carrier.

For the angular alignment of a Fabry-Perot cavity a similar method, that exploits the beat signal between a sideband and a higher order mode, is used. If the error signal is generated from the transmission of the cavity it is called the Anderson-Giordano technique [81] and if it is generated from the reflection of the cavity it is called the Ward technique [82] (see Section 2).

1.4 Feedback control systems

Feedback and control systems are essential in all branches of technology and engineering. Typically, the output of a system is desired to stay as close as possible to a predefined value, while the system undergoes disturbances and fluctuations. To keep the system close to the predefined value, its input is manipulated through a feedback loop that constantly monitors the difference between output signal and set-point. This section summarizes the basic principles of linear control theory that are employed in laser interferometers. Furthermore, the method of noise projection that allows to measure transfer functions and control loop performance, will be introduced.

1.4.1 Control theory

The most simple model of a physical system is the one where a single input $u(t)$ is related to a single output $y(t)$ by a linear transformation $h(t)$ as

$$y(t) = (h * u)(t) = \int_0^\infty h(\tau)u(t-\tau)\mathrm{d}\tau, \tag{1.4.1}$$

where $*$ denotes convolution. Eq. (1.4.1) is the most general expression that describes a *linear time-invariant system* (LTI), where time invariance implies that the output does not change if the input to the system is applied at t_1 or t_2, except for a time delay of $t_1 - t_2$. Most processes in laser interferometers can be well described by LTI systems [39].

It is common practice to carry out the analysis in the frequency domain by means of the Laplace transform $\mathcal{L}$, which is defined as

$$\mathcal{L}[f(t)] = F(s) \equiv \int_0^\infty f(t)e^{-st}dt, \tag{1.4.2}$$

where $s = \sigma + i\omega$ is a complex variable with real numbers σ and ω, where ω represents the angular frequency. The Laplace transform can be considered an extension of the Fourier transform, which can be recovered for $\sigma = 0$. When applying the Laplace transform the convolution theorem applies and Eq. (1.4.1) becomes

$$Y(s) = H(s)U(s), \tag{1.4.3}$$

where $H(s)$ is called the *transfer function* (TF) of the linear system and it is the ratio of the system output $Y(s)$ over the system input $U(s)$.

Dynamic systems are mathematically represented by differential equations, which become polynomials in s in the Laplace domain. This allows to express the TF of an LTI system as a rational function as

$$\begin{aligned} \mathrm{TF}(s) &= \frac{Y(s)}{U(s)} \\ &= \frac{b_M s^M + b_{M-1} s^{M-1} + ... + b_1 s + b_0}{a_N s^N + a_{N-1} s^{N-1} + ... + a_1 s + a_0} \qquad (1.4.4) \\ &= k \cdot \frac{\Pi_{m=0}^{M}(s - z_m)}{\Pi_{n=0}^{N}(s - p_n)} \qquad (1.4.5) \end{aligned}$$

where a_N and b_M are the coefficients of the polynomials, which are of order M and N. In the last step the polynomials in the numerator and denominator have been factorized and k is the gain, the z_m are the zeros and the p_n are the poles of the system. The expression of the transfer function as in Eq. (1.4.4) can be derived from the state-space model, while the representation as in Eq. (1.4.5) is called the zpk-model.

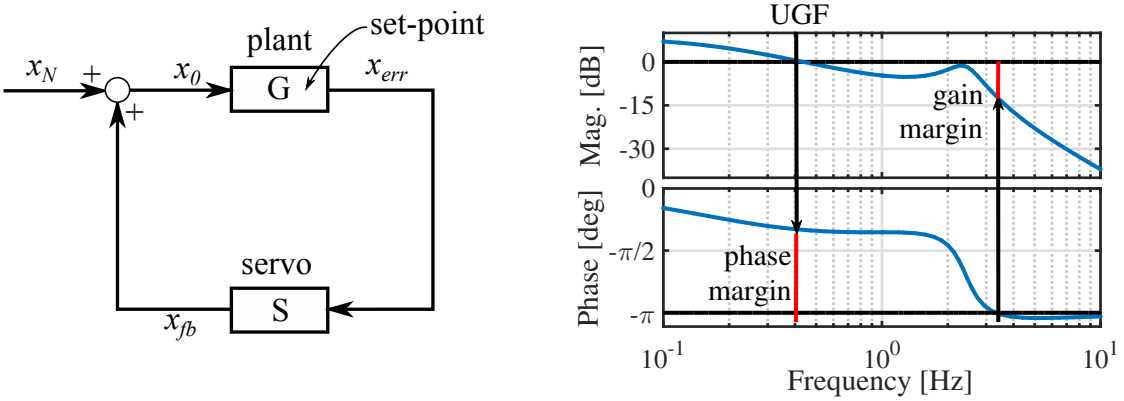

Figure 1.18: *Left: Block scheme of a feedback control loop with single in- and output. The input to the plant is denoted with x_0 and the output of the plant is the error signal x_{err}, which describes the deviation of the plant from the set-point due to the noise x_N in the system. In the servo, the feedback signal x_{fb} is generated. It is sent back to the input of the plant, where it corrects for the noise in the system. Right: Magnitude and phase of the open-loop transfer function of a closed-loop system, indicating the gain and phase margin within which the system is stable. The larger both margins, the wider the stable range with respect to gain or phase variations.*

In control theory the object of interest is called the plant, which is an LTI system that can have multiple inputs and outputs (Fig. 1.18, left panel) [83]. The goal is to keep a physical parameter of the plant as close as possible to a predefined value called the set-point. The parameter is continuously monitored with a sensor in the plant. If its value deviates from the set-point, then an error signal x_{err} proportional to this deviation is sent to the servo system. In the servo, a feedback signal x_{fb} proportional to the error signal is generated and sent via actuators back to the input of the plant, where it corrects for the noise x_N that disturbs the plant. An example of a plant is a Fabry-Perot cavity, where the arm length is kept constant with a feedback control loop by monitoring the reflection of a laser beam from the cavity with the PDH method (see Section 1.3.3).

If the s-domain transfer function of the plant is denoted with G and the transfer function of the servo with S, then the input signal and the feedback signal are expressed as

$$x_0 = x_N + x_{fb} \text{ and } x_{fb} = \text{TF}_{OL} \cdot x_0, \tag{1.4.6}$$

where $\text{TF}_{OL} = G \cdot S$ is the product of the transfer function of the plant and the servo, and called the open-loop transfer function of the feedback loop. The input and feedback signal, depending on the noise x_N, are then

$$x_0 = \frac{1}{1 - \text{TF}_{OL}} x_N = \text{TF}_{CL} \cdot x_N \text{ and } x_{fb} = \frac{\text{TF}_{OL}}{1 - \text{TF}_{OL}} x_N, \tag{1.4.7}$$

where TF_{CL} is called the closed-loop gain. If the open-loop gain is very large ($|\text{TF}_{OL}| \gg 1$), then $\text{TF}_{CL} \to 0$ and the noise is suppressed at the input of the plant. It seems as if the limit is only defined by the gain of the plant and the feedback filter. However, in a real gravitational wave detector the noise of sensors and actuators ultimately determines the loop performance and stability.

The closed-loop system loses stability if its transfer function converges towards infinity. As TF_{OL} is a complex function of the frequency, this occurs when the magnitude of the open-loop transfer function approaches 1 and its phase to $\pm\pi$. The frequency at which the magnitude open-loop transfer function reaches 1 is called the *unity-gain frequency* (UGF). To evaluate the stability range of a system two parameters are relevant (Fig. 1.19, right panel):

- The **gain margin** gives the range of gain between 0 dB and the magnitude at the $-\pi$ cross-over frequency. It gives information about how sensitive the loop is to gain changes in the system. Gain changes can for example originate from temperature fluctuations.

- The **phase margin** is the range of phase between $-\pi$ and the phase at the unity-gain frequency. It gives information how much delay can be added to the system before it loses stability. Delay can be for example due to the speed of the computer the servo is running on.

The larger the phase and gain margin of a system, the wider the range of stability.

1.4.2 Method of noise projection

In complex systems like gravitational wave detectors, the plant can be disturbed by many different noise sources x_{N_i} that may enter the system at any point [84,85]. First, consider an open-loop configuration where only noise is propagating through the system. Each noise source has then an individual transfer function TF_i to the error signal x_{err} (Fig. 1.19, left panel). The power spectrum of the total error signal is then the quadratic sum of the individual noise contributions as

$$x_{err}^2 = \sum_i \text{TF}_i^2 \cdot x_{N_i}^2, \tag{1.4.8}$$

where for readability the frequency dependence of the transfer function and the noise have been dropped. By injecting a large, known signal along the path of the j^{th} noise source in the frequency range of interest, its contribution to Eq. (1.4.8) will be dominant and all other noise sources will be negligible. This method is called *noise injection* and it allows to obtain the

j^{th} transfer function as the ratio of the cross-power spectral density between the error and the noise signal and the auto-power spectral density of the noise signal as (see Section 3.2)

$$\mathrm{TF}_j = \sqrt{\left| \frac{\langle x_{err} x_{N_j}^* \rangle}{\langle x_{N_j} x_{N_j}^* \rangle} \right|_{x_{N_j}}}, \tag{1.4.9}$$

where * refers to the complex conjugate, $\langle . \rangle$ denotes an average over several data segments, $|.|$ denotes the absolute value and the subscript $|_{x_{N_j}}$ indicates that the j^{th} noise source is dominant during the time of injection. The contribution of the j^{th} noise source x_{N_j} to the error signal during nominal operation is obtained by multiplying the measured noise during nominal operation with the transfer function from the noise injection as

$$M_j = \mathrm{TF}_j|_{x_{N_j}} \cdot x_{N_j}, \tag{1.4.10}$$

where M_j is called the noise projection. This method is repeated for all noise sources and the sum of all projections is called the *noise budget* of channel x_{err}. The noise budget gives information about the most dominant noise source contributing to x_{err} and if $\sum_i M_i \neq x_{err}$, it allows to conclude that not all noise sources that form the error signal are taken into account and that the system is not fully understood yet. Hence, noise budgets are an important tool to understand the composition of a noise floor of a given control system.

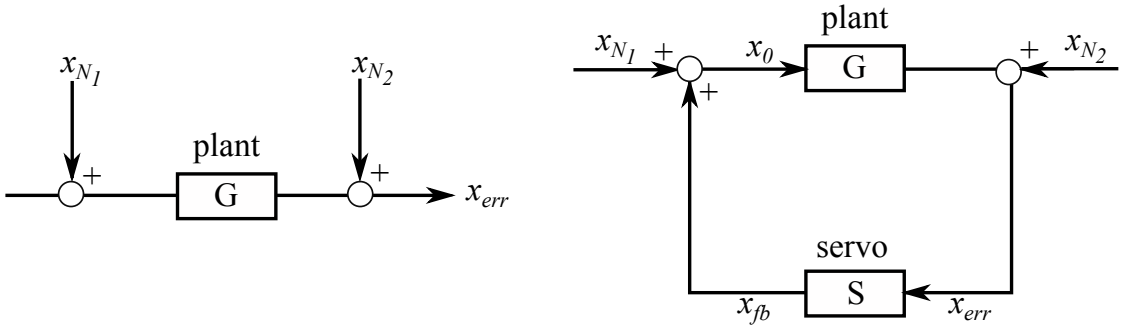

Figure 1.19: *Left: Block scheme of an open control system where only noise propagates through the system. The noises x_{N_i} are contributing before and after the plant to the error signal x_{err}. Right: Block scheme of a closed control loop, where noises x_{N_i} are contributing before and after the plant to the error signal x_{err} that is sent to the servo, where a feedback signal x_{fb} is sent back to the plant to correct for the disturbances.*

During nominal operation the control loops of an interferometer are closed and it is of interest to determine in which frequency range the projection of noise x_{N_1}, which is added to the loop before the plant, on the error signal is valid in the presence of a noise source x_{N_2}, that is added after the plant (see Fig. 1.19, right panel). The input and error signal are then expressed as

$$\begin{aligned} x_0 &= x_{N_1} + x_{fb} = \mathrm{TF}_{CL}(x_{N_1} + S \cdot x_{N_2}) \text{ and} \\ x_{err} &= G \cdot x_0 + x_{N_2} = \mathrm{TF}_{CL}(G \cdot x_{N_1} + x_{N_2}), \end{aligned} \tag{1.4.11}$$

where the feedback signal is given by $x_{fb} = G \cdot x_0 + x_{N_2}$ and where the closed-loop transfer function is $\mathrm{TF}_{CL} = \frac{1}{1-G \cdot S}$ (see Eq. (1.4.7)).

If the noise source x_{N_1} is dominating the system, the closed-loop transfer function from input to error signal is

$$\mathrm{TF}_1^{CL} = \left.\frac{x_{err}}{x_0}\right|_{x_{N_1}} = G \tag{1.4.12}$$

and the resulting noise projection of the input channel on the error signal is

$$M = \mathrm{TF}_1^{CL} \cdot x_0 = G \cdot \mathrm{TF}_{CL}(x_{N_1} + S \cdot x_{N_2}). \tag{1.4.13}$$

The individual contributions of x_{N_1} and x_{N_2} to the noise budget can be obtained equivalently breaking the loop at specific points and weighing the obtained open-loop projections with the closed-loop gain TF_{CL} as

$$M_1^{OL} = \mathrm{TF}_{CL} \cdot G \cdot x_{N_1} \text{ and } M_2^{OL} = \mathrm{TF}_{CL} \cdot x_{N_2}. \tag{1.4.14}$$

To evaluate the validity of the closed-loop projection M in Eq. (1.4.13), it is compared to the open-loop projections of Eq. (1.4.14). As long as x_{N_1} is dominant, $M = M_1^{OL}$ and M is a valid projection of the noise on x_{err}. However, if a noise source x_{N_2} after the plant is dominating the system, the apparent projection becomes $L = \mathrm{TF}_{OL} \cdot \mathrm{TF}_{CL} \cdot x_{N_2}$, where the contribution of x_{N_2} to the error signal is overestimated by the open loop gain TF_{OL}. L thus represents an upper limit for the noise source x_{N_2}.

Real control loops have frequency dependent loop gain and noise contributions. To visualize the validity range of a closed-loop noise projection for a noise x_{N_1} dominating the system, consider a loop with G and S as displayed in Fig. 1.20, left panel. When a noise source x_{N_1} is dominating the system, a closed-loop projection of x_0 on x_{err} is valid for frequencies above the UGF (see Fig. 1.20, right panel). Below the UGF the projection is an overestimate of the actual contribution due to the pollution with x_{N_2}, and the overestimate can be as high as L. In gravitational wave detectors the control loops are usually designed such that the unity-gain frequencies

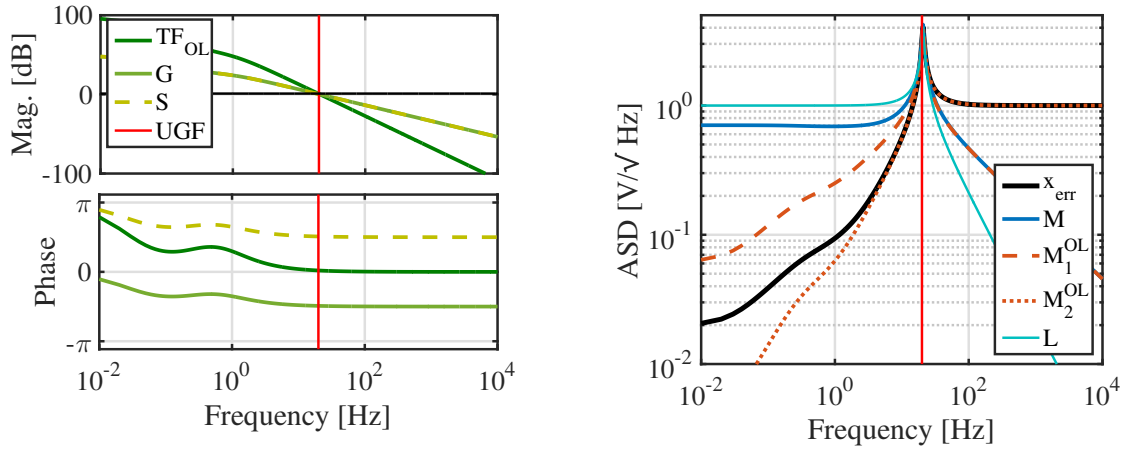

Figure 1.20: *Left: Magnitude and phase of the plant gain G and servo gain S together with the open-loop transfer function* TF_{OL}. *The unity-gain frequency (UGF) is* 20 Hz. *Right: Above the UGF, the closed-loop projection M is equal to the open-loop projection M_1^{OL} if the x_{N_1} is dominating the system, below the UGF it is polluted by the contribution of x_{N_2}. The upper limit that the overestimate can reach below the UGF is defined by L. For a noise source x_{N_2} that is dominating the system M represents an upper limit to the noise contribution.*

are around 1 Hz, which allows that the noise contributions of noise sources before the plant in the frequency band of interest can be well understood through closed-loop projections.

The control system of Advanced Virgo is based on digital control loops as described in this section. The plants are the longitudinal and angular degree's of freedom, the error signals are measured with special photodiodes and a feedback signal is digitally generated, which is then sent to the mirrors to correct their position. To measure the performance of the control loops noise injections are performed on a regular basis. For more information the reader is referred to Section 2.

Chapter 2

Angular control at Advanced Virgo

The purpose of the control system of an interferometer is to keep the beams circulating in the interferometer coupled to the fundamental gaussian mode of the laser. A stable, fundamental mode in the Fabry-Perot arms of the laser interferometer allows to increase the path length that the light travels by resonating in the cavity, and therefore enhances the sensitivity of the interferometer. Seismic motion below 50 Hz, which is not fully filtered by the seismic isolation system, and radiation pressure from the high power laser beams resonating in the Fabry-Perot cavities, couple to the mirrors [37]. Hence, an active control scheme is required to suppress the remaining mirror motion such that the fundamental mode stays resonant in the cavities. The behavior of the interferometer needs to be controlled for two types of drift: the longitudinal and the angular motion of the mirrors. Both form independent sets of degrees of freedom and can be controlled separately. Here, we will focus on the angular alignment of the mirrors with respect to the laser beam at Advanced Virgo, the implemented control scheme and the noise sources that limit the performance of the control loops. For mathematical details on feedback control loops, the reader is referred to Section 1.4.1 and for details on noise projections to Section 1.4.2.

2.1 The alignment of Fabry-Perot cavities

The angular degrees of freedom (DOFs) of a laser interferometer are complex. To gain a first understanding of angular alignment, it is instructive to study the effect of a misaligned beam on a Fabry-Perot (FP) cavity. Two types of misalignment can be distinguished: the tilt and the shift of the cavity axis with respect to the axis of the input beam [81] (Fig. 2.1). In a perfectly aligned system, only the fundamental mode of the laser resonates in the cavity, while if misalignment occurs, higher order modes (HOMs) resonate in the system as well. Together with the fundamental mode they leak out of the misaligned cavity where they can be measured and used for the angular control of the system.

First, consider a well aligned input beam propagating in the z-direction in the fundamental mode, expanded in terms of Hermite-Gauss polynomials as derived in Section 1.3.1. The general components of the complex wave field are assumed to be of the form

$$\Psi(x, y, z) = \tilde{E}(x, y, z)e^{i\omega t} = E_{nm}(x, y, z)e^{-ikz}e^{i\omega t}, \tag{2.1.1}$$

where n and m correspond to the transverse electromagnetic mode in the x- and y-direction. Without loss of generality, we consider the beam at the waist where $z = 0$ and misalignment

only in the xz-plane. The spatial amplitudes of the fundamental and first higher order mode of such a laser beam, $E_{00}(x, y, z = 0)$ and $E_{10}(x, y, z = 0)$ respectively, are expressed as

$$E_{00}(x, y, z = 0) = \sqrt{\frac{2}{\pi}} \frac{1}{w_0} e^{-\frac{x^2+y^2}{w_0^2}}$$
$$E_{10}(x, y, z = 0) = \sqrt{\frac{2}{\pi}} \frac{1}{w_0} \frac{2x}{w_0} e^{-\frac{x^2+y^2}{w_0^2}} = \frac{2x}{w_0} \cdot E_{00}(x, y, z = 0). \tag{2.1.2}$$

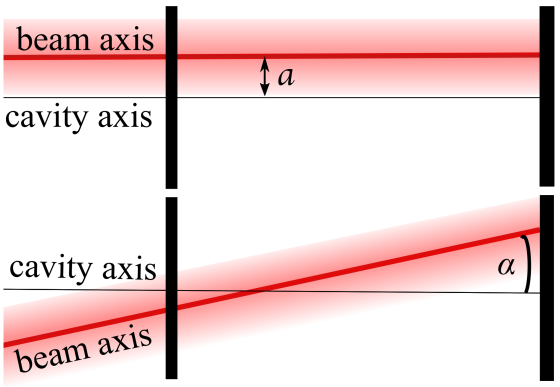

Figure 2.1: *For Fabry-Perot cavities two types of misalignment can be distinguished, the shift (top panel) of the beam with respect to the cavity axis by a and the tilt (bottom panel) of the beam axis with respect to the cavity axis by α.*

Misalignment due to shift

A shift a of the optical axis with respect to the cavity axis can be described by the transformation $x \to x - a$ and $z \to z = 0$ and hence only influences the spatial amplitude of the wavefield. The spatial amplitude of the shifted beam described in the cavity frame is then

$$\begin{aligned} \tilde{E}(x, y, z = 0) &= E_{00}(x - a, y, z = 0) \\ &\approx \sqrt{\frac{2}{\pi}} \frac{1}{w_0} \left(1 + 2a\frac{x}{w_0^2}\right) e^{-\frac{x^2+y^2}{w_0^2}} \\ &\approx E_{00}(x, y, z = 0) + \frac{a}{w_0} E_{10}(x, y, z = 0), \end{aligned} \tag{2.1.3}$$

where the Taylor expansion of the exponential in the second line is based on the assumption that the shift is smaller than the beam waist, $a/w_0 \ll 1$. Thus, a misalignment due to a shift of the optical axis with respect to the cavity axis results in the in-phase coupling of the first higher order mode to the fundamental mode.

Misalignment due to tilt

In the second type of misalignment the beam axis is rotated by a small angle α with respect to the cavity axis. The rotation angle is assumed to be small with respect to the beam divergence ($\alpha \ll \frac{\lambda}{\pi w_0}$). The coordinate transformation for a small rotation is $x \to x - z\alpha$ and $z \to x\alpha + z$ and at the waist where $z = 0$ this becomes $x \to x$ and $z \to x\alpha$. This means that for small

rotations the spatial amplitude at the waist does not change, whereas it induces a phase change in the direction of propagation as $e^{ikz} \xrightarrow{z=0} e^{ik\alpha x} \approx (1 + ik\alpha x)$ and the resulting field is then

$$\begin{aligned}\tilde{E}(x, y, z = 0) &\approx \sqrt{\frac{2}{\pi}}\frac{1}{w_0}\left(1 + i\pi\frac{\alpha\omega_0}{\lambda}\frac{2x}{\omega_0}\right)e^{-\frac{x^2+y^2}{w_0^2}} \\ &\approx E_{00}(x, y, z = 0) + \frac{\alpha w_0 \pi}{\lambda}E_{10}(x, y, z = 0) \cdot e^{i\frac{\pi}{2}}. \end{aligned} \tag{2.1.4}$$

The tilt of the input beam axis with respect to the cavity axis hence introduces the coupling to the first off-axis mode, together with a phase shift of $\pi/2$ with respect to the fundamental mode E_{00}.

Sensing misalignment with the Ward technique

Misalignment between laser beam and cavity axis leads to the generation of higher order modes. When adding sidebands to the laser beam with an electro-optic modulator (see Section 1.3.3), the beat between the sideband and the HOM can be detected if the cavity is misaligned (Fig. 2.2). Determining the misalignment by means of this beat signal, that is reflected by the cavity, is called the *Ward technique* [82] and it is used to generate an error signal for the angular alignment of the Advanced Virgo detector [86]. Another method, called the Anderson-Giordano technique, determines the error signal from the transmission of a misaligned cavity [81]. However, this method requires the first higher order mode of the upper sideband to be resonant in the cavity, which imposes an additional condition on the sideband frequency. As the Ward techniques exploits the already existing sideband for length control of the interferometer, it is used as the strategy of choice to generate the error signal for angular misalignment at Advanced Virgo.

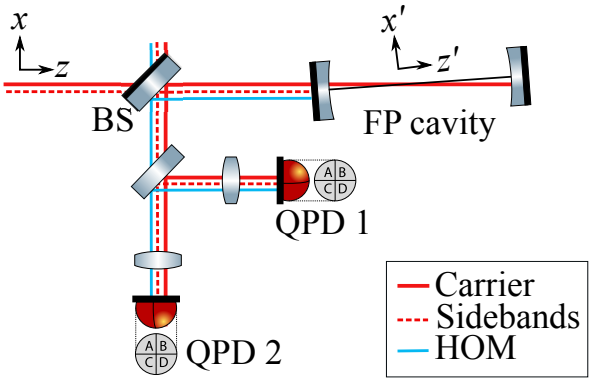

Figure 2.2: *At the Advanced Virgo detector the error signal for the angular control of the arm cavities is obtained from the reflection of the beat between a sideband and a HOM that is generated when the cavity is misaligned. One quadrant photodiode (QPD) in the near field around the waist and one QPD in the far field several Rayleigh distances from the waist of the beam, realized with lenses in front of the QPDS, allow to disentangle the tilt and shift alignment of the cavity.*

The incoming complex wave field of the carrier is then according to Eq. (2.1.1) expressed in the frame of the misaligned cavity (x', y', z') as

$$\Psi_{in,car}(x', y', z') = \left[E_{00}(x', y', z') + CE_{10}(x', y', z')\right]e^{-ikz'}e^{i\omega t}, \text{ with} \tag{2.1.5}$$
$$\Psi_{00}(x', y', z') = E_{00}(x', y', z')e^{-ikz'}e^{i\omega t} \text{ and } \Psi_{10}(x', y', z') = \frac{2x}{w_0}\Psi_{00}(x', y', z')e^{-i\phi(z')},$$

where $\Psi_{00}(x', y', z')$ and $\Psi_{10}(x', y', z')$ represent the fundamental and first higher order mode of the carrier field, $\phi(z')$ represents the Gouy phase shift between the modes (see Eq. (1.3.5)), E_{00}

represents the spatial amplitude (see Eq. (2.1.2)) and $C = C_1 + iC_2$ represents the general term for the misalignment in the $x'z'$-plane with $C_1 = \frac{a}{w_0}$ for a shift and $C_2 = \pi\frac{\alpha w_0}{\lambda}$ for a tilt of the beam. The reflected carrier field can then be expressed as

$$\Psi_{refl,car}(x', y', z') = \Psi_{00}(x', y', z') - C\Psi_{10}(x', y', z'), \tag{2.1.6}$$

where a phase shift of π occurs between terms that are on and off resonance (see Section 1.3.3). If the cavity is tilted (shifted) upwards with respect to the frame of the incoming beam, then the frame of the incoming beam is tilted (shifted) downwards with respect to the cavity frame. The transformations from the cavity to the beam frame (x, y, z) are then

$$\begin{aligned}&\Psi_{00}(x', y', z') \rightarrow \Psi_{00}(x, y, z) - C\Psi_{10}(x, y, z) \text{ and}\\ &\Psi_{00}(x', y', z') + C\Psi_{10}(x', y', z') \rightarrow \Psi_{00}(x, y, z)\end{aligned} \tag{2.1.7}$$

and as a result the expression for the reflected carrier in the frame of the misaligned beam becomes

$$\Psi_{refl,car}(x, y, z) = \Psi_{00}(x, y, z) - 2C\Psi_{10}(x, y, z). \tag{2.1.8}$$

With Eq. (1.3.19) and the approximation $J_\alpha(m) = \frac{1}{\alpha!}\left(\frac{m}{2}\right)^\alpha$, where $J_\alpha(m)$ represents the Bessel function of order α with the modulation index m as argument, the fields of the incoming sidebands in the frame of the incoming beam are expressed as

$$\Psi_{in,lsb} \approx i\frac{m}{2}e^{i(\omega-\Omega)t}\Psi_{00} \text{ and } \Psi_{in,usb} \approx i\frac{m}{2}e^{i(\omega+\Omega)t}\Psi_{00}, \tag{2.1.9}$$

where $\Psi_{00} = E_{00}e^{-ikz}e^{i\omega t}$ is the fundamental mode in the beam frame, where the subscript lsb (usb) refers to the lower (upper) sideband and where for simplicity the coordinate dependency has been dropped. The sidebands are fully reflected by the cavity and experience a phase shift of π with respect to the incoming beam so that

$$\Psi_{refl,lsb} = -i\frac{m}{2}e^{i(\omega-\Omega)t}\Psi_{00} \text{ and } \Psi_{refl,usb} = -i\frac{m}{2}e^{i(\omega+\Omega)t}\Psi_{00}. \tag{2.1.10}$$

The total reflected field is derived from the sum of the individual contributions as

$$\Psi_{refl} = \Psi_{refl,car} + \Psi_{refl,lsb} + \Psi_{refl,usb} \tag{2.1.11}$$

and the power of the total reflected field contains a static DC-term, a term that describes the interference of the two sidebands at 2Ω, an interference term of the carrier with the sidebands - the Pound-Drever-Hall error signal for the length control of the cavity (see Section 1.3.3), and an interference term of the sidebands with the higher order mode term of the misaligned carrier in the beam frame. The last term, the beat between sidebands and higher order mode, is the error signal of the Ward technique for the angular misalignment of the cavity and this part of the reflected power can be expressed as

$$\begin{aligned}P_{Ward} &= -2\Big[C\Psi_{10}(\Psi^*_{refl,lsb} + \Psi^*_{refl,usb}) + C^*\Psi^*_{10}(\Psi_{refl,lsb} + \Psi_{refl,usb})\Big]\\ &= 2\frac{xm}{w_0}|E_{00}|^2\Big[C^*e^{i\phi_z}(ie^{i\Omega t} + ie^{i\Omega t}) - Ce^{-i\phi_z}(ie^{i\Omega t} + ie^{-i\Omega t})\Big]\\ &= 4\frac{xm}{w_0}|E_{00}|^2\cos(\Omega t)\Big[-\sin\phi_z(C + C^*) - i(C - C^*)\cos\phi_z\Big]\\ &= 8\frac{xm}{w_0}|E_{00}|^2\cos(\Omega t)\Big[\mathfrak{Im}(C)\cos\phi_z - \mathfrak{Re}(C)\sin\phi_z\Big],\end{aligned} \tag{2.1.12}$$

where * denotes the complex conjugate and where in the third step the expression $e^{i\gamma} = \cos\gamma + i\sin\gamma$ has been used to reformulate the Gouy-phase term. Demodulating Eq. (2.1.12) with a cosine gives the quadrature term as the error signal for the angular control. By placing one photodiode in the near field at the waist, where $z < z_R$ and as a result $\sin\phi_z = 0$ and $\cos\phi_z = 1$, the tilt is probed, whereas a photodiode in the far field several Rayleigh distances from the waist, where $z > z_R$ and as a result $\sin\phi_z = 1$ and $\cos\phi_z = 0$, probes the shift of the beam (see Fig. 2.3, left panel). For a waist of $w_0 \approx 1$ cm [37], the far field at Advanced Virgo begins at about 300 m. This optical distance is realized in a compact design with a pair of lenses in front of both quadrant photodiodes, which are tuned to ensure a Gouy phase separation of $\frac{\pi}{2}$.

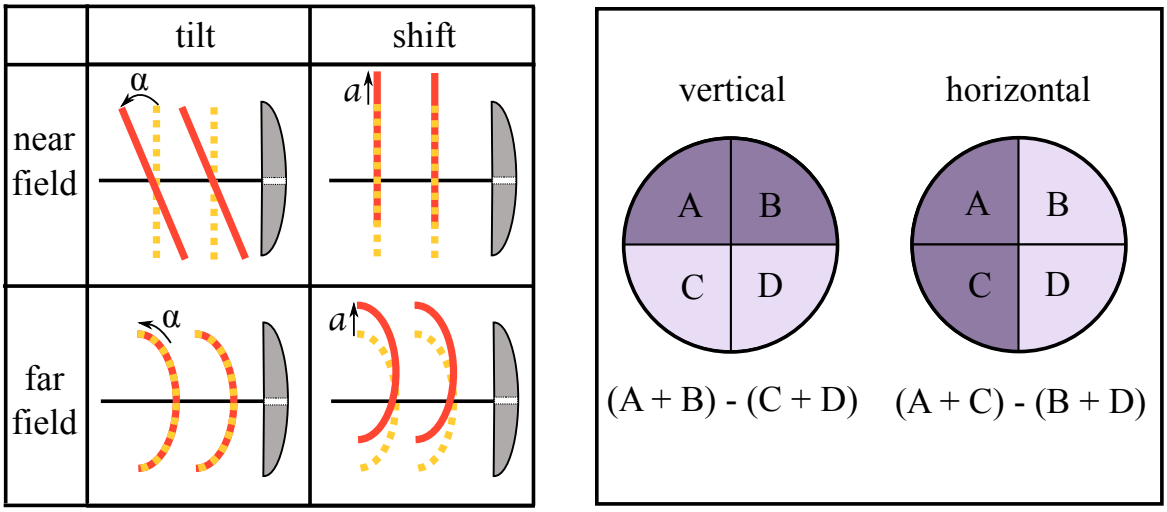

Figure 2.3: *Left: Well aligned (orange dashed) and misaligned beam front (red) in the near field around the waist and the far field several Rayleigh distances away from the waist, measured with a quadrant photodiode sensor. Misalignment due to tilt is measured in the near field, while misalignment due to shift is measured in the far field of the laser beam. Right: Schematic of the four sensing elements of a quadrant photodiode that can be used to distinguish a horizontal pitch from a vertical yaw motion of the cavity.*

Mathematically, the total power measured by the photodiode is obtained by integrating over the area of the photodiode. Assuming that the spot size of the laser beam is much smaller than the area of the photodiode, the integration bounds are $\pm\infty$. The spatial amplitude $E_{00} = E_{00}(x, y, z)$ of the beam that is misaligned in the xz-plane is proportional to e^{-x^2} and thus the integrand xe^{-x^2}, which is an odd function, would vanish if measured with a regular photodiode. Special *quadrant photodiodes* (QPDs), where the area is split into four equal segments, are required to extract the error signal for the misaligned cavity from the power of the reflected beam (Fig. 2.3, right panel). The segments of the QPD allow to split the measured power in a horizontal part, which corresponds to the pitch rotation of the cavity, and a vertical part, which corresponds to the yaw rotation of the cavity (see Fig. 2.4, right panel). On each beam port, four error signals for the angular control are available. For horizontal misalignment, that is in the xz-plane, the error signals are derived from

$$P^h_{near} = (A_{near} + B_{near}) - (C_{near} + D_{near}), \tag{2.1.13}$$

$$P^h_{far} = (A_{far} + B_{far}) - (C_{far} + D_{far}), \tag{2.1.14}$$

and for the vertical misalignment, that is in the yz-plane, the error signals are

$$P^v_{near} = (A_{near} + C_{near}) - (B_{near} + D_{near}), \tag{2.1.15}$$
$$P^v_{far} = (A_{far} + C_{far}) - (B_{far} + D_{far}), \tag{2.1.16}$$

where the A_i, B_i, C_i and D_i refer to the individual areas of the quadrant photodiode that is either placed in the near or the far field of the laser beam.

2.2 Interferometer alignment coordinates

If there is no light in the Fabry-Perot cavity of a laser interferometer, the mirrors can exhibit an independent torsional oscillation, originating from the natural restoring force of the wires by which they are suspended. Once there is light inside the cavity, the motion of both cavity mirrors is not independent anymore. The radiation pressure of the laser couples to the motion of the two mirrors, which is called an *optical spring* [87]. Consider a Fabry-Perot cavity with mirror radii of curvature R_1 and R_2, where the mirrors are separated by a distance L (Fig. 2.4, left panel). The optical axis of the cavity is defined as the line through the centers of the curvature radii of both mirrors. The z-axis is defined as normal to the reflecting surface of the mirror, pointing in the direction of propagation of the laser beam. The x- and y-axis are normal to the direction of propagation, where the x-axis is defined to be parallel to the ground, so that $\vec{z} = \vec{x} \times \vec{y}$ is a right-handed system. The *yaw* angle is then defined as the right-handed rotation around the y-axis, the *pitch* angle is the right-handed rotation around the x-axis and the *roll* angle is the right-handed rotation around the z-axis (Fig. 2.4, right panel). Since the mirrors at Advanced Virgo are spherically shaped, only a pitch and yaw rotation has an effect on the light in the cavity for a well centered beam. Pitch and yaw motion are independent and hence the following calculation will focus on yaw only; the calculations for pitch are analogous.

Based on the approach from Sigg and Sidles [88, 89] the equation of motion of a cavity with

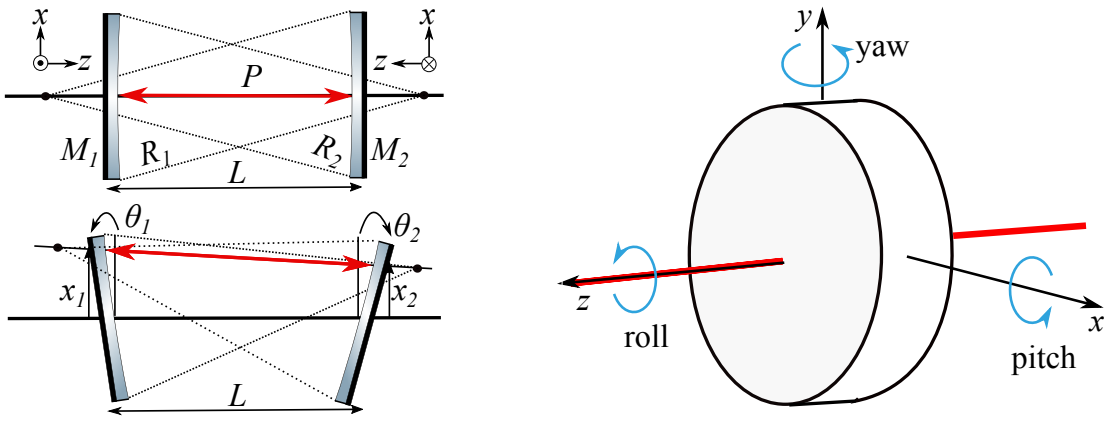

Figure 2.4: *Left, top: Perfectly aligned cavity of length L with mirrors M_1 and M_2, and radii of curvature R_1 and R_2, with a stored laser beam of power P. For M_1 the y-axis is pointing into the plane, while it is pointing out of the plane for M_2. The red arrow indicates the optical axis of the cavity. Left, bottom: Yaw rotations θ_1 and θ_2 result in a shift and tilt of the optical axis in the cavity with respect to the well aligned optical axis. Right: Definition of pitch θ_x, yaw θ_y and roll θ_z angle.*

two rotating mirrors is described via the harmonic oscillator equation as

$$\frac{\partial^2\vec{\theta}}{\partial t^2} = -\omega^2\vec{\theta}, \tag{2.2.1}$$

where ω is the eigenfrequency of the angular mirror rotation, and $\vec{\theta} = (\theta_1, \theta_2)$ with θ_i being the independent mirror rotation angles (Fig. 2.4, right bottom panel). The restoring torque $\vec{\tau}_{rest}$ of such a system is

$$\vec{\tau}_{rest} = I\omega^2\vec{\theta} = -I\frac{\partial^2\vec{\theta}}{\partial t^2}, \tag{2.2.2}$$

where I is the moment of inertia. If a laser beam with power P is resonating in the cavity, the radiation pressure exerts an additional force on the mirrors. The torque corresponding to this force is

$$\vec{\tau}_{rad} = \vec{x}\frac{2P}{c}, \tag{2.2.3}$$

where $\vec{x} = (x_1, x_2)$, and x_i is the distance of the beam from the center of mirror M_i and c is the speed of light. The beam offset x_i on the mirror in terms of the rotation angles θ_i can be derived from geometrical considerations [76] as

$$\begin{bmatrix} x_1 \\ x_2 \end{bmatrix} = L \begin{bmatrix} \frac{g_2}{1-g_1g_2} & \frac{1}{1-g_1g_2} \\ \frac{1}{1-g_1g_2} & \frac{g_1}{1-g_1g_2} \end{bmatrix} \begin{bmatrix} \theta_1 \\ \theta_2 \end{bmatrix}, \tag{2.2.4}$$

where $g_i = 1 - L/R_i$. Using Eq. (2.2.4) in Eq. (2.2.3), and with the total torque of the system $\vec{\tau} = \vec{\tau}_{rest} + \vec{\tau}_{rad}$ the modified equation of motion can be formulated as

$$\frac{\partial^2\vec{\theta}}{\partial t^2} = -(\mathbf{\Omega}^2 + \omega^2\mathbf{1})\vec{\theta}, \text{ where} \tag{2.2.5}$$

$$\mathbf{\Omega}^2 = -\frac{2PL}{Ic}\begin{bmatrix} \frac{g_2}{1-g_1g_2} & \frac{1}{1-g_1g_2} \\ \frac{1}{1-g_1g_2} & \frac{g_1}{1-g_1g_2} \end{bmatrix} \text{ and } \mathbf{1} = \begin{bmatrix} 1 & 0 \\ 0 & 1 \end{bmatrix}. \tag{2.2.6}$$

The eigenvalues ω_s and ω_h and eigenvectors $\vec{v_s}$ and $\vec{v_h}$ of $\mathbf{\Omega}^2$ are

$$\begin{aligned} \omega_h &= -\omega_0 \cdot (g_1 + g_2 - \sqrt{4 + (g_1 - g_2)^2}), \quad \vec{v_h} = \begin{bmatrix} \frac{\omega_0}{\omega_0 g_1 + \omega_h} \\ -1 \end{bmatrix} \\ \omega_s &= -\omega_0 \cdot (g_1 + g_2 + \sqrt{4 + (g_1 - g_2)^2}), \quad \vec{v_s} = \begin{bmatrix} 1 \\ \frac{-\omega_0}{\omega_s + \omega_0 g_2} \end{bmatrix}, \end{aligned} \tag{2.2.7}$$

where $\omega_0 = \frac{PL}{Ic(1-g_1g_2)}$ and where the subscript s (h) refers to the soft (hard) mode of the cavity. In a stable cavity the relation $0 < g_1g_2 < 1$ holds (see Section 1.3.2), and therefore $\omega_0 > 0$. It follows that $\omega_s < 0$ and $\omega_h > 0$. This means that ω_s reduces the overall spring constant to a smaller value, making the system softer, whereas ω_h increases the spring constant, making the system harder. These two eigenvectors correspond to two resonance modes of the cavity. This can be understood by looking at the sign of the eigenvector entries

$$\text{sign}(\vec{v_h}) = (1, -1) \text{ and } \text{sign}(\vec{v_s}) = (1, 1), \tag{2.2.8}$$

where opposite signs of θ_1 and θ_2 correspond to the hard mode of the cavity, resulting in a pure tilt of the optical axis (Fig. 2.5, left top panel). In this case the radiation pressure works in

conjunction with the original restoring force, pushing the mirrors back to their original position. The stronger restoring torque corresponds to a stiffer total spring constant of the system. Equal signs of θ_1 and θ_2 correspond to the soft mode of the cavity, resulting in a pure shift of the optical axis (Fig. 2.5, left bottom panel). The radiation pressure works against the original restoring force, hence making the system softer. If the laser power in the arm cavities of Advanced Virgo is higher than a few tens of kW, then the soft mode can lead to instability of the cavity, making an active control of the angular motion via an external force necessary [90, 91].

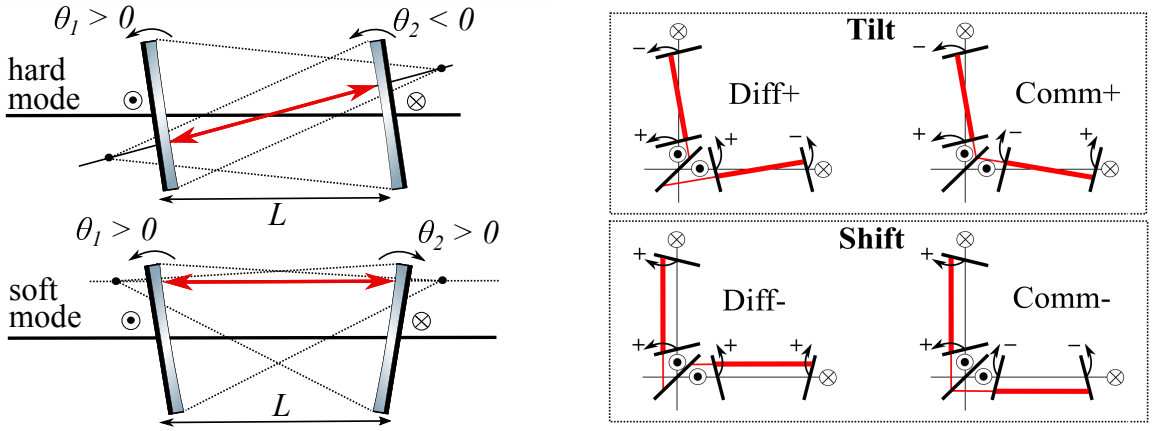

Figure 2.5: *Left top: Hard mode of a cavity, leading to a pure tilt of the optical axis. Left bottom: Soft mode of a cavity, leading to a pure shift of the optical axis. Right: The four interferometer arm degrees of freedom for yaw, depending on a common (differential) tilt and shift of the individual FP cavities. The sign of each mirror rotation is derived from the right-handed rotation around the y-axis, which is indicated in standard vector notation pointing in- and out of the plane.*

The tilt (hard) and shift (soft) mode are the fundamental modes of a cavity. The long arms of a laser interferometer consist of two Fabry-Perot cavities, which are coupled via the beam splitter in the central interferometer. In total eight degree's of freedom of the arm cavities (four in pitch and four in yaw) can be defined (Fig. 2.5, right panel):

- **Diff+**: The differential tilt of both FP cavities, which results in a recombination of the optical axes on opposite sides of the BS,
- **Comm+**: The common tilt of both FP cavities, which results in a recombination of the optical axes on the same side of the BS,
- **Diff-**: The differential shift of both FP cavities, which results in a recombination of the optical axes on opposite sides of the BS,
- **Comm-**: The common shift of both FP cavities, which results in a recombination of the optical axes on opposite sides of the BS.

The pitch and yaw motions of the power recycling mirror, the beam splitter and the signal recycling mirror in the central interferometer lead to an additional six angular DOFs. Since the power in the central interferometer is low we do not expect the motion of these mirrors to be coupled via radiation pressure, which allows to control their motions individually. This means that for a full control of the angular motion of a Michelson-Fabry-Perot laser interferometer in

total 14 mirror DOFs need to be taken into consideration. In practice, two additional degrees of freedom are added due to the shift and tilt of the laser beam from the laser injection system. However, for the scope of this work it will be assumed that the plane of the interferometer and that all optics are well aligned with respect to the input beam.

2.3 The angular control scheme

During the steps of lock acquisition procedure of a laser interferometer, different control schemes with varying accuracy and scope of operation are employed [86]. The initial scheme focuses on the stabilization of the longitudinal degrees of freedom of the interferometer and the centering of the beam on the mirrors. Mechanical modulation of the mirrors in pitch and yaw, referred to as *dithering technique*, ensures that the laser is well centered on the mirrors. If the beam is well centered, a pitch and yaw rotation of the spherical mirrors have no effect on the transmitted power. If the beam is miscentered and the mirror is mechanically modulating the beam, then lines at the dither frequency appear in the transmitted spectrum of the mirror [92]. By minimizing the dither lines in the transmitted spectrum, beam centering can be achieved within an accuracy of 0.5 mm, which translates to an angular accuracy of about 0.5 µrad [86].

The beam spot location that minimizes the lines in the transmitted spectrum then gives the set-point of the mirror location for the *local control* (LC) system. The local control is a ground-

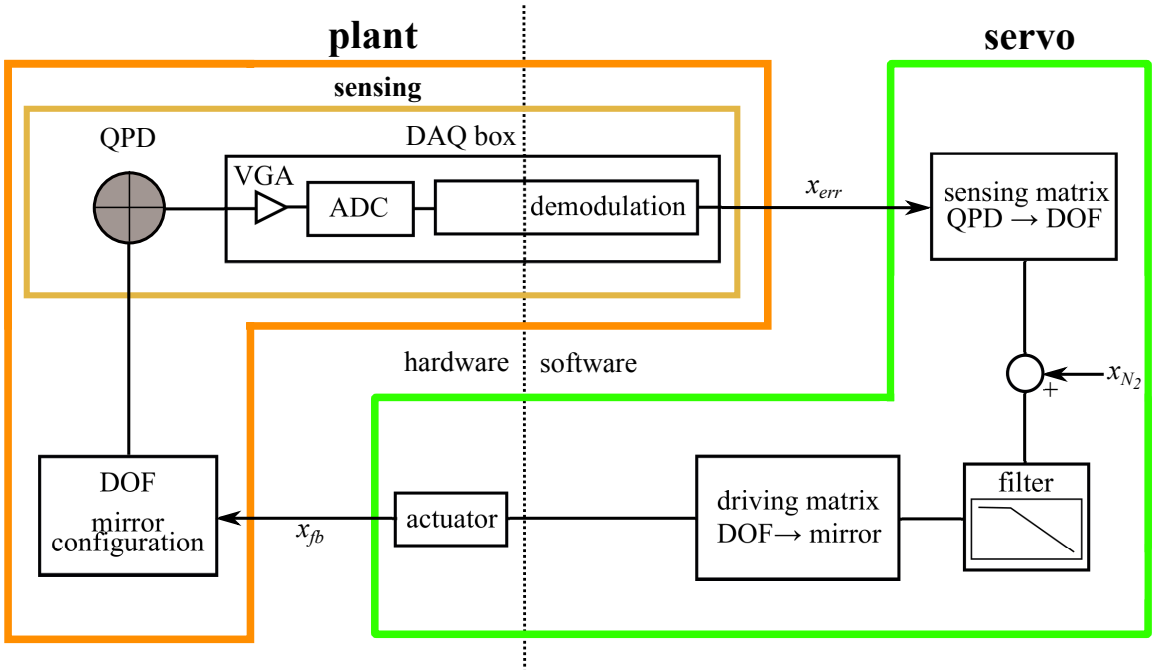

Figure 2.6: *Block schematic of the Automatic Alignment control loop: The plant is an angular DOF, where the corresponding optical configuration of the mirrors is to be controlled. The error signal is measured with a quadrant photodiode (QPD) and is derived after demodulation from the beat between the higher order mode, generated from the misalignment, and a side-band. After demodulation, the error signal is attributed to the DOF via the sensing matrix, converted to a feedback signal through a filter and sent to the individual mirrors of the DOF via the driving matrix. The correction of the mirror position is achieved with actuators on the mirror marionette.*

based reference system, which uses an optical lever on the marionette of each mirror to sense its deviation from the set-point [93]. The LC allows to keep the mirrors stable in the range of several μrad per hour; however long term drifts and a high electronic noise floor of the sensors limit the performance.

Dither lines and local control ensure that the position of the mirrors with respect to each other does not change, but they cannot ensure an angular alignment of the mirrors. The overall control of the angular DOFs is achieved with the *Automatic Alignment* (AA) system. It is a global feedback-loop servo system, that derives an error signal directly from the interferometer [94–96]. The control loops of the Automatic Alignment system consist for each angular DOF of two main parts (Fig. 2.6):

- **The plant**: The parameter to be controlled is an angular DOF and relates to the optical configuration of the mirrors of the PF cavities. Misalignment of the cavities results in higher order modes, which generate a beat signal with the sideband (see Section 2.1). This beat signal is sensed with a quadrant photodiode (QPD) and serves, after being digitized and demodulated, as error signal for the DOF. Sensing noise can enter as shot noise from the diode and electronic noise from its readout circuit, which are digitization noise from the ADC and noise from the demodulation electronics. The configuration with the maximum laser power in the interferometer has been designed such that sensing noise will be dominated by shot noise [37]. Other noise sources such as the residual seismic motion of the benches can be neglected.

- **The servo**: In the servo system, the error signal from the plant is attributed to the corresponding DOF through the sensing matrix. The sensing matrix is an online operation that maps an input vector, containing the error signals of QPDs at different points in the interferometer, on a vector with the angular DOFs of the interferometer. For Advanced Virgo this matrix is diagonal, which means that each error signal corresponds to a single DOF. Control filters then derive a feedback signal for each DOF, which is distributed across the mirrors via the driving matrix. The driving matrix is an operation that maps the input vector of interferometer DOFs on the individual mirrors. This matrix is not diagonal for Advanced Virgo, since the individual mirrors can contribute to different DOFs in the interferometer. The position of the individual mirrors is then corrected through magnetic coil actuators on the marionette of each mirror. The actuators can induce electronic noise on the plant, however their noise level has been measured and does not exceed the expected sensing noise from the QPDs [97, 98]. This means that the loop performance can be measured with in-loop noise projections of sensing noise above the unity-gain frequency (see Section 1.4.2).

Two control topologies are employed within the Automatic Alignment system: The *fast control* derives the error signal only from the QPD sensors and has a control bandwidth of several Hz. Since this topology gets the error signal directly from the interferometer it is also called the global control. Ideally, all angular DOFs should be controlled in full bandwidth by the fast control. However, in the real interferometer, the DOFs are coupled due to the presence of the power recycling mirror. To decouple DOFs, the *drift control* is used to mix global and local control signals: the global control is used with a small bandwidth of a few mHz at low frequencies up to a few 100 mHz depending on the DOF, to ensure the overall alignment of the mirrors, and the local control is used to control the mirrors with respect to a local set-point. This allows to avoid the long term drifts that otherwise limit the performance of the local control. The

choice of the drift control bandwidths depends on the coupling of the DOF to the dark fringe. The stronger the DOF couples to the dark fringe, the wider the bandwidth of the fast topology should be to allow for a fast correction of any disturbances in the dark fringe signal. Adjusting the drift control depending on the dominance of the DOF is referred to as *hierarchical control*.

2.4 Control noise and the O3 noise budget

To validate the performance of the Automatic Alignment system, the noise projection of angular misalignment onto the Advanced Virgo detection channel is of relevance as it determines the instantaneous sensitivity of the detector. In Section 1.2.2 the design sensitivity of the Advanced Virgo detector has been introduced as the incoherent sum of the fundamental noise sources that limit the performance of the detector. While this is the target sensitivity for the final configuration of the detector, its present sensitivity is limited by technical noise sources. Overcoming the technical limitations of a detector and moving towards the target sensitivity where only fundamental noise sources limit the performance is the ongoing work of commissioning and upgrading. An important tool for this process is the analysis of the online noise budget of Advanced Virgo's sensitivity, which allows to identify and eliminate the dominant technical noise sources that limit the present detector performance. In this section, the first measurement of the angular control noise contribution to the Advanced Virgo sensitivity is presented.

Angular DOFs during O3

In Section 2.2 the angular interferometer DOFs were introduced in their final configuration; reaching this configuration is part of ongoing commissioning of the Automatic Alignment system at Advanced Virgo. During O3 the Diff+, PR, and BS DOFs were controlled in full bandwidth with the fast loop and with error signals that were generated by the QPDs. The global control error signals were derived from the beat of the HOM with the 56 MHz sideband by using the beam at the B5 and B1p port (see Fig. 1.8 in Section 1.2.3). The Comm+ DOF is the first DOF where the full control via four mirrors in the fast control loop has been achieved. Its error signal is derived from the position of the laser beam on the B5 DC diode and a mitigation

Signal channel	DOF	BS	PR	WE	WI	NE	NI
B5, 56 MHz, Q	BS	1	0	0	0	0	0
B5, 56 MHz, I	PR	0	1	0	0	0	0
B1p, 56 MHz, I	Diff+	0	0	$1/2$	$1/2$	0	0
B5, DC	Comm+	0	0	$1/2$	$1/2$	$1/2$	$1/2$
Optical levers West arm	Diff-	0	0	$1/2$	$-1/2$	0	0
Optical levers North arm	Comm-	0	0	0	0	$1/2$	$1/2$

Table 2.4: *Combined sensing and driving matrix for the angular DOFs during O3. In the signal channel, 'Q' refers to the quadrature signal of the demodulated beam whereas 'I' refers to the in-phase signal. For pitch the vertical and for yaw the horizontal quadrant signal is used. The BS, PR, and cavity tilt DOFs are controlled via the fast loop in full bandwidth, while the cavity shift DOFs are under drift control. Note that the cavity DOFs are constructed from the individual input and end mirrors of the west and north arm, referred to as WI, WE, NI, NE, respectively.*

to a demodulated QPD signal is foreseen in the future. The Comm-and Diff- DOFs were kept under drift control as their full implementation into the fast control loop was still work in progress [99]. A combined sensing and driving matrix for all DOFs as employed during O3 is displayed in Table 2.4.

Angular noise injections

To measure the performance of the fast control loops, in-loop projections of sensing noise have been carried out for all DOFs. The unity-gain frequencies of the control loops lie between 3 and 4 Hz for all DOFs [100] and the dither lines are at frequencies between 6 and 8 Hz [37]. Previous measurements indicated that above 60 Hz, angular control noise will be well below the Advanced Virgo sensitivity and negligible with respect to other noise sources [94]. Therefore, noise with a flat amplitude that ensures that the error signal is at least one order of magnitude above the nominal level during quiet times from about 10 to 100 Hz has been injected (Fig. 2.7, left panel). The amplitude has been determined by stepwise increasing the noise power until a clear effect of the injection was observed in the DARM channel (Fig. 2.7, right panel).

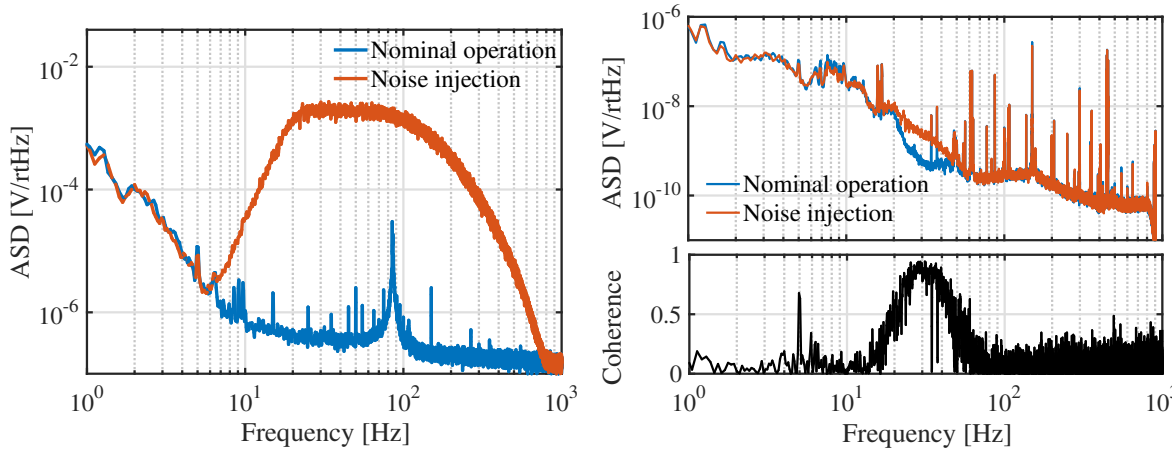

Figure 2.7: *Left: Spectrum of the Comm+ pitch error signal during nominal operation and during noise injection. The shape of the noise filter, with a flat amplitude between* 10 *to* 100 Hz *and more than two orders of magnitude above the nominal signal, is clearly visible. Above* 100 Hz *the roll-off of the injected signal is visible. Similar injections were carried out for all DOFs. Right, top: Signal in DARM during nominal operation and during noise injections in the Comm+ pitch DOF. Right, bottom: Coherence between DARM and the injection channel is visible between* 15 *and* 70 Hz.

The DARM channel measures the differential arm length of the West and North arm, and is directly linked to the detection channel for a gravitational wave signal. Angular misalignment results in a variation in the cavity length and thus the performance of the Automatic Alignment is directly related to sensitivity of the detector. The coupling between angular misalignment and cavity length is non-linear, which has as a result that even though the noise injection band ranges from about 10 to 100 Hz, coherence to DARM has only been (if at all) observed between about 15 and 70 Hz. The absence of coherence at frequencies within the noise injection band thus indicates that other noise sources dominate DARM. To avoid unknown, non-linear effects, the amplitude of the injection has not been raised further after an effect of the injection was visible in the DARM channel.

Angular control noise projection on the gravitational wave detection channel

For the noise projection of the angular DOFs onto the Advanced Virgo sensitivity, the transfer functions are derived with the gravitational wave detection channel as error signal channel and the injected noise amplitudes as noise channels as expressed in Eq. (1.4.9) during times of noise injection. The noise injections have been carried out during two independent measurement times: first the noise projection of the BS and PR mirror control loop have been measured and at a later time the noise projection of the control loops of the cavity DOFs were determined. This was necessary as not all control loops were in their optimized, final configuration at the same time. For the frequency range of the transfer function, only frequency bins were consid-

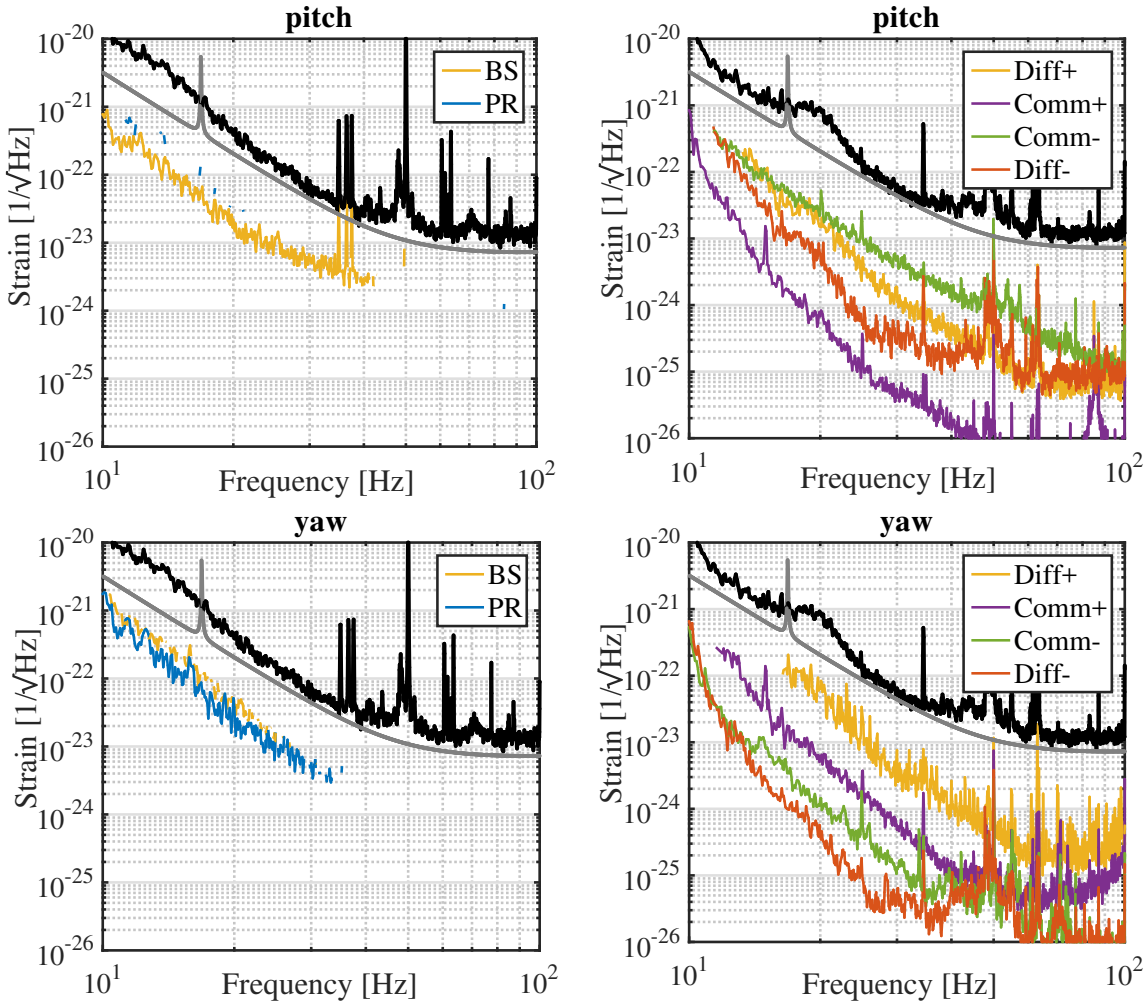

Figure 2.8: *Noise projection of the angular DOFs on the Advanced Virgo sensitivity for pitch and yaw. The O3 target sensitivity with a BNS range of* 85 Mpc *[101] is depicted in grey, the unperturbed Advanced Virgo sensitivity at the time of the noise injection is depicted in black. The noise projections, except for the yaw motion of BS, PR and Diff+, are at least one order of magnitude below the measured sensitivity and the target sensitivity for O3, hence fulfilling the noise requirement [37]. The performance of the remaining DOFs has been improved during ongoing commissioning. The spikes at about* 35 Hz *and* 60 Hz *correspond dominantly to calibration lines, but also show contributions from dark, environmental, demodulation and longitudinal control noise (see Fig. 2.9).*

ered where the injected noise amplitude surpassed the amplitude of the noise channel during nominal operation by about a factor 10. For the BS and PR mirror control loop this confined the transfer function to the frequency range from about 10 to 40 Hz, while for the cavity DOF this range had an upper limit of about 100 Hz. Finally, the noise projection of the individual DOFs onto the Advanced Virgo sensitivity curve was derived according to Eq. (1.4.10) by multiplying the transfer function with the signal in the noise channel during nominal operation (Fig. 2.8). At the time of the measurement, the projected angular control noise of almost all DOFs was at least one order of magnitude below the measured Advanced Virgo sensitivity and the O3 target sensitivity. During the ongoing commissioning effort the noise filters of all DOFs have been improved and the noise projections have been remeasured [102, 103], such that all DOFs are compliant with the O3 sensitivity requirement set for the Automatic Alignment system [37].

The Advanced Virgo noise budget

The online noise budget of Advanced Virgo, that encompasses the full list of known technical noise sources, is a Simulink-framework, that models in real-time the interferometer noise budget based on measured and theoretical transfer functions [98, 104]. The noise sources of the Advanced Virgo noise budget during early stages of O3 can be grouped into eleven categories (see Fig. 2.9):

(a) the total angular control noise is the incoherent sum of the noise projections of the 12 angular DOFs as shown in Fig. 2.8. Furthermore, this noise category includes the control noise in the alignment of the input beam to the interferometer,

(b) the calibration lines are signals of known frequency and amplitude that are injected manually into the detector to determine the conversion from detector signal to strain,

(c) the actuator noise is the electronic noise of the actuators on the marionette that convert the digital feedback signal for the mirror control to an analog signal,

(d) the dark noise is the electronic noise of the photodiodes and their readout circuit, when no light impinges on the diodes,

(e) the demodulation noise encompasses quantization noise and numerical noise from digital filters, as well as jitter in the demodulation phase due to errors in the signal timing, which causes a coupling between the in-phase and quadrature signal,

(f) the environmental noise refers to acoustic and magnetic noise that couples directly to the test masses,

(g) the longitudinal control noise is the incoherent sum of the noise projection of four longitudinal DOFs - excluding the signal recycling cavity length, as the signal recycling mirror was not installed during O3,

(h) the quantum noise is the shot noise of the photodiodes and radiation pressure,

(i) the frequency stabilization noise refers to the control noise of the loop that aims to stabilize the frequency of the laser beam through an external reference cavity,

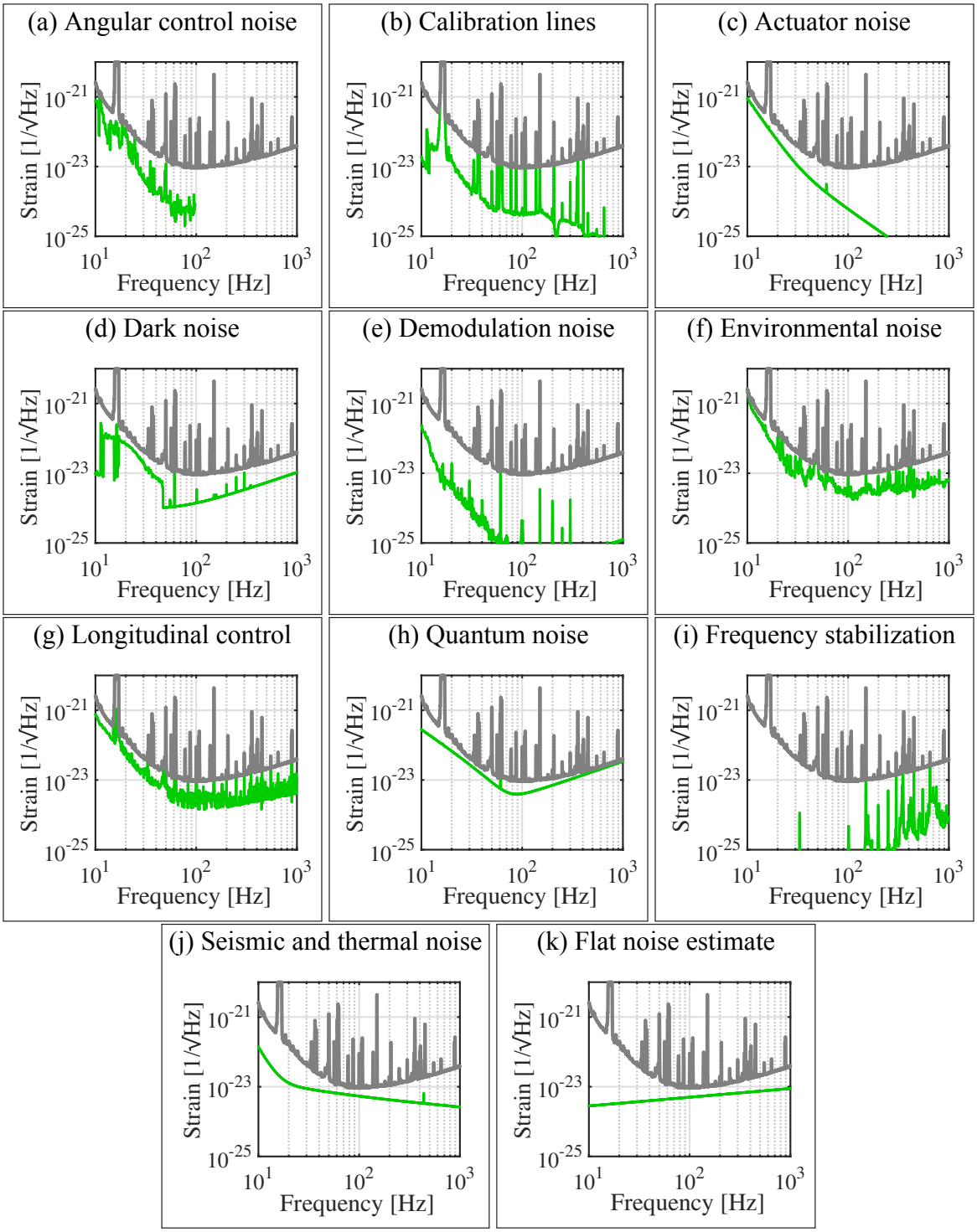

Figure 2.9: *The Advanced Virgo noise budget during O3. At low frequencies angular control, actuator, environmental, longitudinal control, quantum and dark noise from scattered light dominate. At high frequencies only shot noise contributes, which means that here the interferometer has reached its fundamental performance limit. The calibration lines contribute at selected frequencies to the sensitivity, while other noise sources like demodulation, frequency stabilization, as well as seismic and thermal noise are mostly negligible. A flat noise of unknown origin is dominating the mid frequency band and its identification is the focus of ongoing commissioning work.*

(j) the seismic noise refers to the remaining noise that enters the system after the filtering of the pendulum system and thermal noise refers to the thermal noise of the suspension that induces a motion on the test mass,

(k) the flat noise estimate corresponds to a flat noise that is assumed to be non-negligible between about 50 to 100 Hz. The origin of this noise source is unknown and its identification is part of the commissioning before the start of O4.

The transfer functions of all noise sources have been measured through noise injections, except for seismic, thermal and quantum noise, where the transfer functions have been derived from theoretical considerations. At high frequencies the noise budget is dominated by shot noise, while at low frequencies a variety of noise sources such as angular and longitudinal control noise, environmental, actuator and quantum noise contribute to a comparable level to the noise budget.

If all noise sources in the interferometer were understood, then the incoherent sum of all technical noise terms would be equal to the measured sensitivity in the detector. At low frequencies, a deviation between the sum of the noise contributions and the measured sensitivity leads to the conclusion that unidentified noise sources are present in the detector (see Fig. 2.10). It is furthermore visible that technical noise across the full frequency band, including angular control noise at low frequencies, need to be further reduced by at least one order of magnitude to reach the Advanced Virgo and the Advanced Virgo Plus design sensitivity. For the angular control noise this includes engaging a four-mirror based, fast control of all cavity DOFs, the derivation of all error signals from the beat between HOM and sidebands with QPDs, optimizing

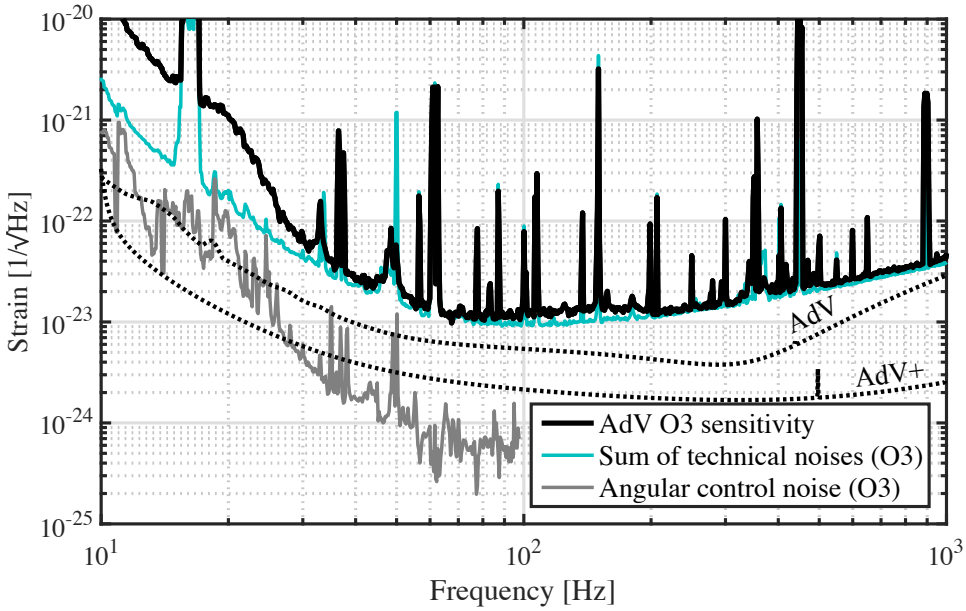

Figure 2.10: *The measured Advanced Virgo sensitivity and sum of technical noise sources during O3 are in reasonable agreement at high frequencies, while at low frequencies unknown technical noises still need to be identified and eliminated. In the mid frequency band an unknown, flat noise source contributes to the noise budget, but its origin and exact form still needs to be determined. To reach the Advanced Virgo and Advanced Virgo Plus design sensitivity, technical noise need to be reduced by at least an order of magnitude across the whole frequency band, including the angular control noise at low frequencies.*

noise filters and the possible mitigation from the 56 MHz to the more sensitive 8 MHz sideband frequency.

Chapter 3

Seismic and Newtonian noise modeling

The performance of terrestrial interferometric gravitational wave detectors at frequencies below 20 Hz is limited by seismic noise. This noise couples to the test masses in two ways, mechanically by moving the mirror suspensions and directly by gravitational attraction. The mechanical coupling of the ground motion can efficiently be suppressed by several orders of magnitude through advanced vibration isolation systems [37]. However, the Newtonian force on the test mass, created by seismically induced mass density fluctuations, cannot be suppressed. This effect on the detector sensitivity is referred to as *Newtonian noise*.

In the following we restrict our consideration to Newtonian noise from the seismic field near the site, assuming that 'trivial' noise generated by local equipment like pumps and air conditioning can be mitigated. Furthermore, we neglect the effect of Newtonian noise from atmospheric pressure variations, which is treated for example in [47]. Estimates of the seismic Newtonian noise for a given detector rely on a model of the geology and on the seismic field near the test masses.

Here we will first introduce seismic wave propagation in both, half-space and horizontal layered geologies, and consider full solutions to the elastodynamic wave equation that are obtained with numerical solver software. The results are used to model an ambient seismic field and to estimate Newtonian noise at a specified detector site, based on measured geology and seismic source distribution.

3.1 Seismic wave propagation

The behavior of soil under dynamic loading conditions is typically complex, anisotropic and non-linear. If the forces that excite a soil profile are small, then it can be assumed that the soil behaves like an elastodynamic medium. This means that the soil obeys Hooke's law and that a force on the medium results in its pure displacement, neglecting irreversible deformation effects. When studying the soil response to ambient noise, a given soil profile can be approximated as a homogeneous half-space or as a horizontally layered medium. In this section we first derive the equations governing wave propagation in homogenous media. If the soil profile is simple, for example in the case of a uniform half-space, then the solutions of the wave equation can be derived analytically. For more complex geologies, standard numerical solving techniques have been derived in seismology. They are discussed in the second part of this section.

3.1.1 The elastodynamic wave equation

Elasticity is the property that enables fluids or solid bodies to resist changes in size and shape when an external force is applied or to return to their original size and shape when the force is removed [105]. The theory of elasticity is a major building block of seismology, as it uses concepts known from classical mechanics such as stress and strain and their connection via Hooke's law to derive the principles of seismic wave propagation through solids such as rocks.

The entity describing the motion of a volume element at location $\vec{x} = (x_1, x_2, x_3)$ inside a medium at time t is a vector field, the so called *displacement field* $\vec{u}(\vec{x}, t)$. If the position of the element changes by an infinitesimal amount with respect to the initial position $\vec{x}_0$, then the displacement field can be Taylor-expanded as [106]

$$\vec{u}(\vec{x},t) = \vec{u}(\vec{x}_0,t) + \left[\begin{matrix} \frac{\partial u_1}{\partial x_1} & \frac{\partial u_1}{\partial x_2} & \frac{\partial u_1}{\partial x_3} \\ \frac{\partial u_2}{\partial x_1} & \frac{\partial u_2}{\partial x_2} & \frac{\partial u_2}{\partial x_3} \\ \frac{\partial u_3}{\partial x_1} & \frac{\partial u_3}{\partial x_2} & \frac{\partial u_3}{\partial x_3} \end{matrix}\right]\Bigg|_{\vec{x}_0} \cdot \begin{bmatrix} d_1 \\ d_2 \\ d_3 \end{bmatrix} = \vec{u}(\vec{x}_0,t) + \mathbf{J}\vec{d}, \tag{3.1.1}$$

where $\vec{d} = (d_1, d_2, d_3) = \vec{x} - \vec{x}_0$ is the distance to the initial position. The matrix $\mathbf{J} = \boldsymbol{\epsilon} + \boldsymbol{\Omega}$ can be further expanded into the symmetric *strain tensor* $\boldsymbol{\epsilon}$ with components

$$\begin{aligned} \epsilon_{ij} &= \begin{bmatrix} \frac{\partial u_1}{\partial x_1} & \frac{1}{2}(\frac{\partial u_1}{\partial x_2} + \frac{\partial u_2}{\partial x_1}) & \frac{1}{2}(\frac{\partial u_1}{\partial x_3} + \frac{\partial u_3}{\partial x_1}) \\ \frac{1}{2}(\frac{\partial u_2}{\partial x_1} + \frac{\partial u_1}{\partial x_2}) & \frac{\partial u_2}{\partial x_2} & \frac{1}{2}(\frac{\partial u_2}{\partial x_3} + \frac{\partial u_3}{\partial x_2}) \\ \frac{1}{2}(\frac{\partial u_3}{\partial x_1} + \frac{\partial u_1}{\partial x_3}) & \frac{1}{2}(\frac{\partial u_3}{\partial x_2} + \frac{\partial u_2}{\partial x_3}) & \frac{\partial u_3}{\partial x_3} \end{bmatrix} \\ &= \frac{1}{2}(\frac{\partial u_j}{\partial x_i} + \frac{\partial u_i}{\partial x_j}), \end{aligned} \tag{3.1.2}$$

and the asymmetric *rotation tensor* $\boldsymbol{\Omega}$ with components

$$\begin{aligned} \Omega_{ij} &= \begin{bmatrix} 0 & \frac{1}{2}(\frac{\partial u_1}{\partial x_2} - \frac{\partial u_2}{\partial x_1}) & \frac{1}{2}(\frac{\partial u_1}{\partial x_3} - \frac{\partial u_3}{\partial x_1}) \\ \frac{1}{2}(\frac{\partial u_2}{\partial x_1} - \frac{\partial u_1}{\partial x_2}) & 0 & \frac{1}{2}(\frac{\partial u_2}{\partial x_3} - \frac{\partial u_3}{\partial x_2}) \\ \frac{1}{2}(\frac{\partial u_3}{\partial x_1} - \frac{\partial u_1}{\partial x_3}) & \frac{1}{2}(\frac{\partial u_3}{\partial x_2} - \frac{\partial u_2}{\partial x_3}) & 0 \end{bmatrix} \\ &= \frac{1}{2}(\frac{\partial u_j}{\partial x_i} - \frac{\partial u_i}{\partial x_j}). \end{aligned} \tag{3.1.3}$$

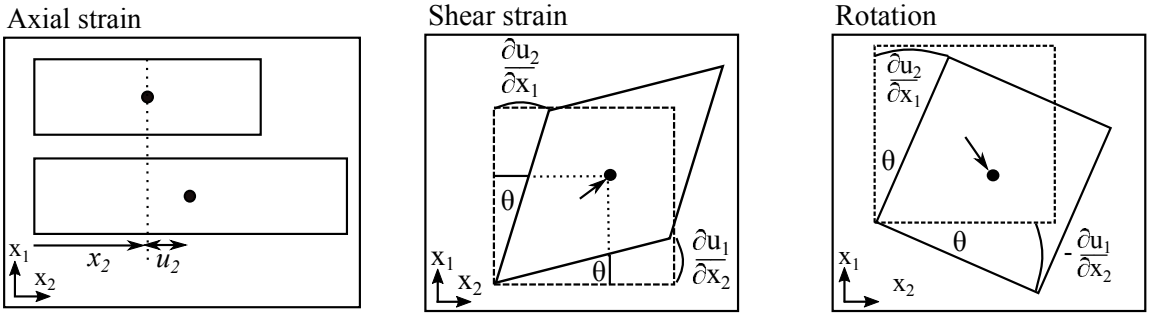

Figure 3.1: *Left: The axial strain is the deformation of an object parallel to the axis of the displacement, $\frac{\partial u_2}{\partial x_2}$ for this example. Middle: The shear strain as the rate of change in an object's angles in a two-dimensional plane. Right: If both derivatives $\frac{\partial u_1}{\partial x_2}$ and $\frac{\partial u_2}{\partial x_1}$ have an opposite sign, the shape of the volume element does not change and a pure rotation occurs.*

Strain describes how positions of points in a continuum are changed through a displacement field $\vec{u}(\vec{x}, t)$. The diagonal elements of the tensor are called the *axial strain* and they describe the ratio of change in deformation parallel to the direction of displacement with respect to the original form of the object (Fig. 3.1, left panel). The off-diagonal elements of the strain tensor are called the *shear strain* and they are the ratio in change of deformation in the direction perpendicular to the axis of the displacement acting on the object. For a more intuitive understanding consider the two-dimensional case with $x_3 = 0$, where the axial strain is zero ($\frac{\partial u_i}{\partial x_i} = 0$) and where both derivatives $\frac{\partial u_1}{\partial x_2}$ and $\frac{\partial u_2}{\partial x_1}$ are equal (Fig. 3.1, central panel). Since we are considering infinitesimal small displacements, the deformation angles can be expressed as

$$\theta \approx \tan(\theta) = \frac{\partial u_1}{\partial x_2} = \frac{\partial u_2}{\partial x_1}. \tag{3.1.4}$$

The sum of both deformation angles are then the elements of the shear tensor and its elements therefore represent the deformed object's angles with respect to the initial angles. In contrast the elements of the rotation tensor $\mathbf{\Omega}$ cause a pure rotation, which is represented by the opposite signs of the derivatives (Fig. 3.1, right panel) and in Eq. (3.1.3).

The force per unit area, acting on an infinitesimal small plane that is characterized by the normal vector $\hat{n}$, is called the *traction* $\vec{t}$ (Fig. 3.2). This definition, which is common in seismology, means that a compressional force is negative and an extensional force is positive [106]. A force on a plane of the medium leads to internal forces, which are called *stress*. The i^{th} component of the traction, t_i, across the plane with normal vector $\hat{n}$, with components n_j, is then represented by the element σ_{ij} of the *stress tensor* $\boldsymbol{\sigma}$, so that the expression $t_i = \sigma_{ij} n_j$ holds.

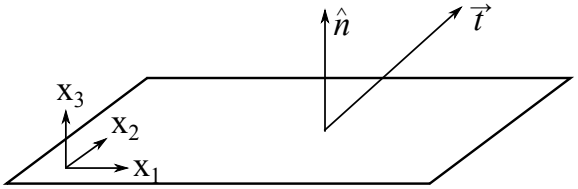

Figure 3.2: *The traction $\vec{t}$ is a force per unit area on the surface with normal vector $\hat{n}$, where an extensional force is positive, while a compressional force is negative.*

External forces on the medium lead to displacement and deformation and hence stress and strain are inevitably linked to each other. Hooke's law states that stress and strain are proportional as

$$\sigma_{ij} = \sum_{kl} C_{ijkl} \epsilon_{kl}, \tag{3.1.5}$$

where the proportionality C_{ijkl} is given by the *elasticity tensor*. For an isotropic medium the elasticity tensor can be expressed in terms of the so called Lamé parameters μ and λ, which are defined as

$$\mu \equiv \frac{E}{2(1+\nu)}, \quad \lambda \equiv \frac{E\nu}{(1+\nu)(1-2\nu)}, \tag{3.1.6}$$

where E represents the Young's modulus and ν the Poisson ratio. As the Lamé parameters relate to material properties, they can be used to describe the elastic restoring force of a medium as

$$C_{ijkl} = \lambda \delta_{ij} \delta_{kl} + \mu(\delta_{ik}\delta_{jl} + \delta_{ik}\delta_{jl}), \tag{3.1.7}$$

where δ_{ij} denotes the Kronecker delta. This allows to re-express Eq. (3.1.5) as

$$\sigma_{ij} = \sum_{k} \lambda \epsilon_{kk} \delta_{ij} + 2\mu \epsilon_{ij}. \tag{3.1.8}$$

The total force $\partial\vec{F}$ per infinitesimal volume element $\partial V = \partial x_1 \partial x_2 \partial x_3$ can then be derived by multiplying the individual traction vectors $\vec{t_j}$ with the surface area they are acting on as

$$\frac{\partial \vec{F}}{\partial V} = \frac{\partial \vec{t_1} \cdot \partial A_{23}}{\partial x_1 \partial x_2 \partial x_3} + \frac{\partial \vec{t_2} \cdot \partial A_{13}}{\partial x_1 \partial x_2 \partial x_3} + \frac{\partial \vec{t_3} \cdot \partial A_{12}}{\partial x_1 \partial x_2 \partial x_3} = \sum_{j=1}^{3} \frac{\partial \vec{t_j}}{\partial x_j}, \tag{3.1.9}$$

where $\partial A_{kl} = \partial x_k \partial x_l$, with $j \neq k \neq l$, represents the infinitesimal surface that the traction $\vec{t_j}$ is defined across. Using this in Eq. (3.1.9) allows to formulate the i^{th} component of the force density $\frac{\partial F_i}{\partial V} = \rho \cdot \frac{\partial^2 u_i}{\partial t^2}$ as

$$\frac{\partial F_i}{\partial V} = \sum_{j=1}^{3} \frac{d\sigma_{ij}}{dx_j} = \rho \frac{\partial^2 u_i}{\partial t^2}, \tag{3.1.10}$$

where $\rho = \frac{\partial m}{\partial V}$ represents the density of the medium. In addition to external forces, internal forces called body forces can act on the volume element. Body forces encompass for example gravity and electromagnetic fields. They are typically small in comparison to those in seismic wave fields and are therefore neglected in this treatment.

Making use of Eq. (3.1.8) and the relation between strain and displacement (Eq. (3.1.2)) allows to reformulate Eq. (3.1.10) for the i^{th} vectorial component in terms of the displacement field as

$$\sum_{j=1}^{3} \left((\lambda + \mu) \frac{\partial^2 u_j}{\partial x_i \partial x_j} + \mu \frac{\partial^2 u_i}{\partial x_j \partial x_j} \right) = \rho \frac{\partial^2 u_i}{\partial t^2}, \tag{3.1.11}$$

which is called the *elastodynamic wave equation*. The vectorial expression of the elastodynamic wave equation is written as

$$(\lambda + \mu) \nabla (\nabla \cdot \vec{u}) + \mu \nabla^2 \vec{u} = \rho \frac{\partial^2 \vec{u}}{\partial t^2}, \tag{3.1.12}$$

where $\nabla = (\frac{\partial}{\partial x_1}, \frac{\partial}{\partial x_2}, \frac{\partial}{\partial x_3})$ represents the Nabla operator and where $\nabla \vec{u}$, $\nabla \cdot \vec{u}$ and $\nabla \times \vec{u}$ denote the gradient, the divergence and the curl of the vector field $\vec{u}$.

3.1.2 Analytical solutions of the elastodynamic wave equation

Solutions of the elastodynamic wave equation depend on the composition of the medium and on the imposed boundary conditions. Analytical solutions only exist in very special cases, for example for two-dimensional, uniform problems. For all other types of problems, for example for the solution in multilayered three-dimensional media, special analysis techniques and numerical solutions and methods need to be employed to solve the wave equation. Nevertheless, it is instructive to study the analytical solutions as they give an overview of the fundamental wave types that exist. The analytical solutions of the wave equation are extensively treated in standard literature for seismology [106–108] and in the following a short derivation of the different solutions based on this literature will be given.

Two types of boundary conditions are used in seismology [107]: *kinematic boundary conditions* refer to the study of motion and therefore restrict the displacement field. For a boundary between two solid materials it is required that the displacement field is continuous for all three components throughout the boundary. Discontinuity for example in the horizontal components

means that slip is possible between the two materials, which is not the case for the solid rock geologies that are considered in this work. *Dynamic boundary conditions* refer to the study of forces on a system and therefore require continuity of the traction vector. As the vector normal to the surface of a medium is by definition pointing outward of the medium, this means that the stresses across an interface are equal in magnitude, but opposite in sign, which is only true if the horizontal stress components across the surface are continuous.

Body waves

At first an unbound, homogeneous medium is considered. Since the differential equation given by Eq. (3.1.11) is not trivial to solve, solutions are typically obtained as a sum of solutions of simpler equations. One method, which is common practice in seismology, is to decompose the displacement vector field $\vec{u}$ via the *Helmholtz decomposition* [109] in terms of the scalar potential Φ and the vector potential $\vec{\Psi} = (\Psi_1, \Psi_2, \Psi_3)$ as

$$\vec{u} = \nabla\Phi + \nabla \times \vec{\Psi} = \begin{bmatrix} \frac{\partial\Phi}{\partial x_1} + \frac{\partial\Psi_3}{\partial x_2} - \frac{\partial\Psi_2}{\partial x_3} \\ \frac{\partial\Phi}{\partial x_2} + \frac{\partial\Psi_1}{\partial x_3} - \frac{\partial\Psi_3}{\partial x_1} \\ \frac{\partial\Phi}{\partial x_3} + \frac{\partial\Psi_2}{\partial x_1} - \frac{\partial\Psi_1}{\partial x_2} \end{bmatrix}, \tag{3.1.13}$$

where $\nabla\Phi$ represents a curl-free field and $\nabla \times \vec{\Psi}$ a divergence-free vector field and where the curl has been calculated in a right-handed coordinate system. This decomposition allows to rewrite the elastodynamic wave equation in terms of two uncoupled equations as

$$\nabla^2\Phi = \frac{1}{v_P^2}\frac{\partial^2}{\partial t^2}\Phi \rightarrow v_P = \sqrt{\frac{\lambda + 2\mu}{\rho}}, \tag{3.1.14}$$

$$\nabla^2\vec{\Psi} = \frac{1}{v_S^2}\frac{\partial^2}{\partial t^2}\vec{\Psi} \rightarrow v_S = \sqrt{\frac{\mu}{\rho}}, \tag{3.1.15}$$

where v_P and v_S are the velocities of the fundamental waves, which are solutions to the corresponding equations. For simplicity plane wave solutions in Cartesian coordinates are assumed. In Cartesian coordinates, plane waves are especially simple since all coordinate contributions which are perpendicular to the direction of propagation are constants. Two types of waves are solutions to the above set of equations (Fig. 3.3, left panel). First, consider a wave propagating in x_1-direction, where the particle displacement is parallel to the direction of motion. This type of wave is called a *pressure* (P)-wave and the displacement field is of the form

$$\vec{u}_P(\vec{x}, t) = \big(f(t - \frac{x_1}{v_P}), 0, 0\big) = \big(\frac{\partial\Phi}{\partial x_1}, 0, 0\big), \tag{3.1.16}$$

where f is some function describing the amplitude of the displacement. This is a solution of Eq. (3.1.14), which is called the wave equation for P-waves and $\nabla\Phi$ is the P-wave contribution of the displacement field. A plane wave propagating in the x_1-direction with particle motion perpendicular to the direction of motion is called a *shear* (S)-wave and it can be defined in two ways

$$\begin{aligned} \vec{u}_{SV}(\vec{x}, t) &= \big(0, f(t - \frac{x_1}{v_S}), 0\big) = \big(0, -\frac{\partial\Psi_3}{\partial x_1}, 0\big), \\ \vec{u}_{SH}(\vec{x}, t) &= \big(0, 0, f(t - \frac{x_1}{v_S})\big) = \big(0, 0, \frac{\partial\Psi_2}{\partial x_1}\big), \end{aligned} \tag{3.1.17}$$

where all derivatives other than in the direction of propagation are zero. Both equations are independent solutions to Eq. (3.1.15), and they are referred to as the two polarizations of the S-wave. Their polarization is determined by the plane that is spanned by the particle motion and propagation direction. If it is parallel to a surface or interface in the medium it is called the horizontally polarized shear (SH) wave and if the plane is perpendicular to an interface or surface the wave is called a vertically polarized shear (SV) wave. The term $\nabla \times \vec{\Psi}$ in the displacement field is referred to as the S-wave contribution to the displacement field.

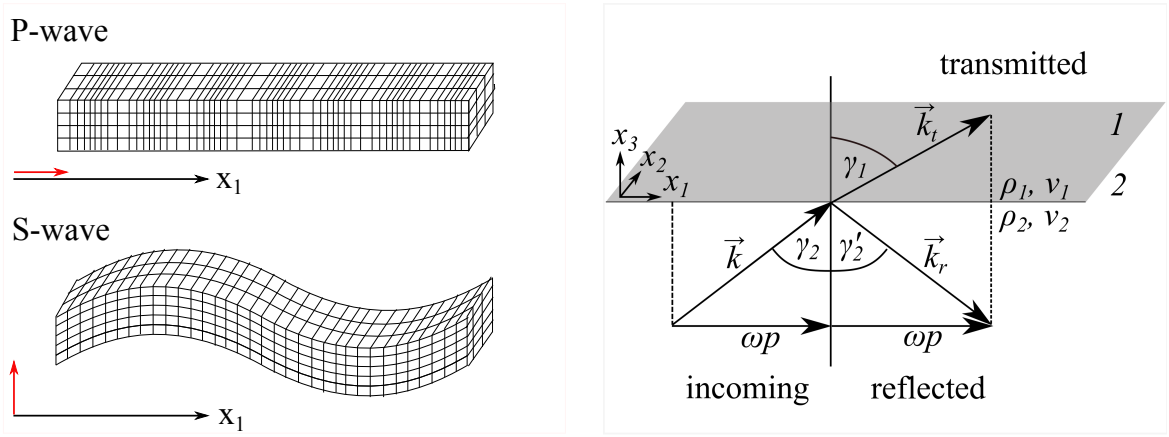

Figure 3.3: *Left: Plane P- and S-wave propagation in an unbounded medium. The direction of propagation is along x_1 and the direction of particle displacement is indicated with a red arrow. Right: Visualization of Snell's law for seismic waves at an interface with two media of density ρ_1 and ρ_2, and velocities v_1 and v_2. The wave vectors of the incoming, reflected and transmitted wave are denoted by $\vec{k}$, $\vec{k}_r$ and $\vec{k}_t$. The horizontal component of the wave vector is ωp, where p is called the slowness.*

Interactions at material boundaries

A realistic soil model consists of layers with different material properties. If body waves encounter an interface between two different materials, then transmission, reflection and mode conversion can occur. To study these phenomena, consider in medium 2 an incoming plane wave, where the wave vector $\vec{k}$ is confined to the x_1x_3-plane (Fig. 3.3, right panel). For such a wave the displacement field is given by

$$\vec{u}(\vec{x},t) = \vec{u}_0(\vec{x}) \cdot e^{i(\omega t - \vec{k}\cdot\vec{x})} = \vec{u}_0(\vec{x}) \cdot e^{i\omega\left(t - \frac{1}{v_2}(x_1 \sin\gamma_2 + x_3 \cos\gamma_2)\right)}, \tag{3.1.18}$$

where the wave vector is $\vec{k} = \frac{2\pi f}{v_2}(\sin\gamma_2, 0, \cos\gamma_2)$ with wave oscillation frequency f, wave speed v_2 in the direction of propagation at the location $\vec{x} = (x_1, x_2, x_3)$ and where $|\vec{k}| = \frac{\omega}{v_2}$ holds for the wave vector. The reflected and transmitted displacements are, respectively,

$$\begin{aligned} \vec{u}_r(\vec{x},t) &= \vec{u}_{r,0}(\vec{x}) \cdot e^{i\omega\left(t - \frac{1}{v_2}(x_1 \sin\gamma_2' - x_3 \cos\gamma_2')\right)}, \\ \vec{u}_t(\vec{x},t) &= \vec{u}_{t,0}(\vec{x}) \cdot e^{i\omega\left(t - \frac{1}{v_1}(x_1 \sin\gamma_1 + x_3 \cos\gamma_1)\right)}. \end{aligned} \tag{3.1.19}$$

The kinematic boundary condition requires the horizontal (in this example the x_1-) component of the incoming, reflected and transmitted wave vector to be continuous and as a result Snell's

law for seismic wave propagation in solid media is obtained as

$$p = \frac{\sin\gamma_2}{v_2} = \frac{\sin\gamma_2'}{v_2} = \frac{\sin\gamma_1}{v_1}, \tag{3.1.20}$$

where the inverse surface velocity p, or horizontal *slowness*, is conserved across the interface. Equation (3.1.20) only holds when $\gamma_2 = \gamma_2'$.

Since the wave propagates in the x_1x_3-plane, the displacement field is constant in x_2. This means that derivatives of the potentials with respect to x_2 are zero. The amplitude $\vec{u}_0$ of the incoming field can then be formulated based on Eq. (3.1.13) in terms of the potentials as

$$(u_{0,1}, u_{0,2}, u_{0,3}) = \left(\frac{\partial\Phi}{\partial x_1} - \frac{\partial\Psi_2}{\partial x_3}, \quad \frac{\partial\Psi_1}{\partial x_3} - \frac{\partial\Psi_3}{\partial x_1}, \quad \frac{\partial\Phi}{\partial x_3} + \frac{\partial\Psi_2}{\partial x_1}\right). \tag{3.1.21}$$

It can be seen that the displacements in the x_1x_3-plane are coupled via the wave potentials and that they are completely independent from the displacement $u_{0,2}$. Hence two independent systems can be defined: the system with the horizontally polarized S-wave (SH-system) and the system with a superposition of P-wave and vertically polarized S-wave (P/SV-system).

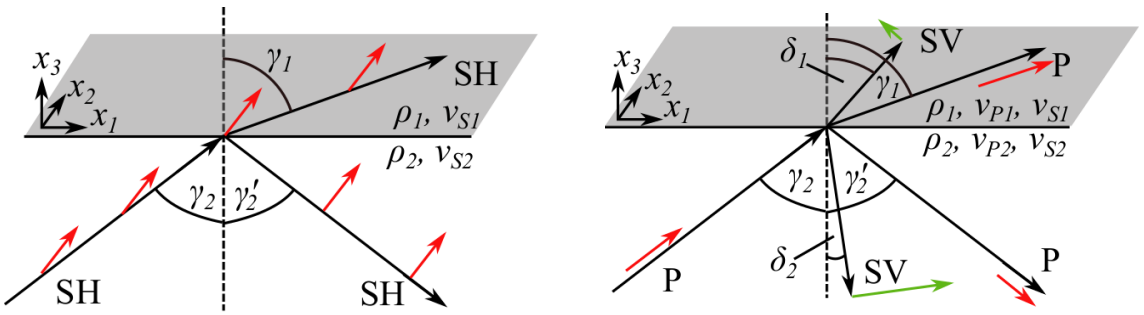

Figure 3.4: *Left: Reflection of an SH-wave on an interface between two layers. The displacement direction (red, parallel to the x_2-axis) is perpendicular to the direction of propagation and does not change direction when interacting with the interface. Right: The displacement of an incoming P-wave changes direction when the P-wave interacts with an interface (red). The direction of displacement on the interface is then only conserved, if an additional SV-wave (green) is generated. This coupling between P- and SV-waves is known as mode conversion.*

If an SH-wave encounters an interface it is reflected and transmitted. The direction of the displacement field remains unchanged even though the propagation direction of the wave may change. The displacement stays unaffected, because it is confined to the plane perpendicular to the direction of propagation (Fig. 3.4, left). Considering the boundary conditions, the amplitude reflection and transmission coefficients of the SH-wave, r_{SH} and t_{SH} respectively, can be derived as [107]

$$r_{SH} = \frac{\rho_1 v_{S1}\cos\gamma_1 - \rho_2 v_{S2}\cos\gamma_2}{\rho_2 v_{S2}\cos\gamma_2 + \rho_1 v_{S1}\cos\gamma_1}, \quad t_{SH} = \frac{2\rho_2 v_{S2}\cos\gamma_2}{\rho_2 v_{S2}\cos\gamma_2 + \rho_1 v_{S1}\cos\gamma_1}. \tag{3.1.22}$$

In the P/SV-system, P- and SV-waves are coupled and conversions between both modes occur when the waves interact with an interface (Fig. 3.4, right panel). Consider an incoming P-wave that interacts with an interface. The displacement of a P-wave is parallel to the direction of propagation, so as the direction of propagation changes for the transmitted (reflected) P-wave, the direction of displacement also changes. The conservation of displacement at the interface

gives rise to a wave with displacement in the SV-direction. Reflection and transmission coefficients for all waves have been derived in [107] (p.139ff). For completeness the P- and SV-wave amplitude reflection coefficients at a free surface for an incoming P-wave will be given here as

$$r_{SV} = \frac{4v_{S2}^2 p \frac{\cos\gamma_2}{v_{P2}}(1-2v_{S2}^2p^2)}{4v_{S2}^4p^2\frac{\cos\gamma_2}{v_{P2}}\frac{\cos\delta_2}{v_{S2}}+(1-2v_{S2}^2p^2)^2}, \quad r_P = \frac{4v_{S2}^4p^2\frac{\cos\gamma_2}{v_{P2}}\frac{\cos\delta_2}{v_{S2}}-(1-2v_{S2}^2p^2)^2}{4v_{S2}^4p^2\frac{\cos\gamma_2}{v_{P2}}\frac{\cos\delta_2}{v_{S2}}+(1-2v_{S2}^2p^2)^2}. \quad (3.1.23)$$

Surface waves

Surface waves attenuate fast with increasing depth and propagate parallel to the surface. The mathematical description of such a singular wave traveling in the x_1-direction is of the form

$$\vec{u}(\vec{x},t) = f(x_3)e^{i\omega(t-\frac{x_1}{v})}, \quad (3.1.24)$$

where v represents the velocity in the direction of propagation. Surface waves are a superposition of body waves at the free surface and under certain boundary conditions, both the SH and the P/SV-system can generate surface waves. The surface waves of the P/SV-system have been studied by J. Rayleigh [110], hence they are called *Rayleigh waves*. He has shown that in a homogeneous half-space, surface waves can exist by interfering P- and SV-waves if the velocities fulfil

$$\left(\frac{v_R^2}{v_S^2}\right)^3 - 8\left(\frac{v_R^2}{v_S^2}\right)^2 + 8\left(\frac{2-\nu}{1-\nu}\right)\left(\frac{v_R^2}{v_S^2}\right) - \frac{8}{1-\nu} = 0 \quad (3.1.25)$$

and obey the condition that $v_R < v_S < v_P$. With this condition the respective horizontal and vertical particle displacements of the Rayleigh wave are obtained as

$$\begin{aligned} u_1(\vec{x},t) &= ik_RA\big(e^{qk_Rx_3} - \frac{2pq}{1+p^2}e^{pk_Rx_3}\big)e^{i(\vec{k_R}\cdot\vec{x}-\omega t)}, \\ u_3(\vec{x},t) &= -qk_RA\big(e^{qk_Rx_3} - \frac{2}{1+p^2}e^{pk_Rx_3}\big)e^{i(\vec{k_R}\cdot\vec{x}-\omega t)}, \end{aligned} \quad (3.1.26)$$

where $k_R = |\vec{k}_R|$ represents the wave vector of the Rayleigh wave, A an arbitrary wave amplitude, and the velocity ratios are defined as

$$q \equiv \sqrt{1-\frac{v_R^2}{v_P^2}}, \quad p \equiv \sqrt{1-\frac{v_R^2}{v_S^2}}. \quad (3.1.27)$$

The particle motion of a Rayleigh wave is elliptical and counter-clockwise at the surface (Fig. 3.5, left panel). At a depth of about $0.2\ \lambda_R$ the sign of the phase between horizontal and vertical motion changes, leading to a change of the particle rotation to the clock-wise direction. The horizontal amplitude of the Rayleigh wave attenuates strongly with depth (Fig. 3.5, right panel). At $0.2\ \lambda_R$ a zero-crossing is reached, which corresponds to the shift in phase. Vertical amplitudes experience a short amplitude increase close below the surface before they attenuate. At the depth of one Rayleigh wavelength, both amplitudes are attenuated to less than 20% of their surface value.

Rayleigh waves also exist if the medium is not a homogeneous half-space, but is composed of layers with different material properties [108]. In this case a similar, but frequency dependent condition for the velocities similar to Eq. (3.1.25) can be formulated. This so called *dispersion curve* depends on the number, thickness and material properties of the subsurface layers. A

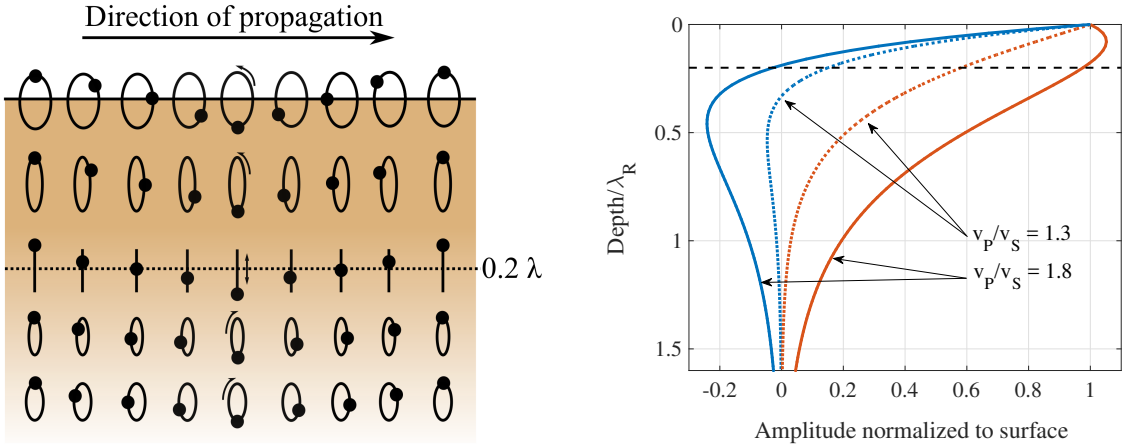

Figure 3.5: *Left: Particle motion of a Rayleigh wave propagating from left to right. One horizontal wavelength λ is shown, and the dots represent all particle locations at the same fixed point in time. On the surface the particle motion is counter-clockwise, changing to a purely vertical motion at about $0.2\ \lambda_R$ and becoming a clockwise rotation at greater depths. The time behavior at a fixed location is given by looking from right to left. Figure adapted from [106]. Right: Attenuation of horizontal (blue) and vertical (red) Rayleigh wave amplitudes with depth. The horizontal motion attenuates faster than the vertical motion and changes sign close to a depth of $0.2\ \lambda_R$ (black dashed line). Vertical particle motion slightly increases before being strongly attenuated with increasing depth. The peak amplitude depends on the ratio of P- and S-wave speeds in the medium. Both types of motion are suppressed to about 20% of their surface value at a depth of one Rayleigh wavelength.*

general, analytical formulation of the dispersion curve is not possible. It is characteristic for a soil profile, a property which is exploited in seismology and exploration geology to image subsurface composition from surface measurements.

Under certain conditions, the SH-system can produce surface waves, called *Love* waves, as well. It can be shown that in a half-space the boundary condition of zero stress on the surface can only be fulfilled if the amplitude of the wave is zero [106]. This means that Love waves cannot exist in a homogeneous half-space geology, but they can exist in a layered medium. It can be shown [106] that in a medium that consists of one layer of thickness d (medium 1) on a half-space (medium 2) the condition for the Love wave speed v_L is

$$\tan\left(\frac{d\cdot\omega}{v_L}\sqrt{\frac{v_L^2}{v_{S1}}-1}\right)=\frac{\rho_2 v_{S2}^2\sqrt{1-\frac{v_L^2}{v_{S2}^2}}}{\rho_1 v_{S1}^2\sqrt{1-\frac{v_L^2}{v_{S1}^2}}}, \tag{3.1.28}$$

where ρ_i represents the density, v_{Si} the S-wave speed in the layer ($i=1$) or half-space ($i=2$), and ω the angular frequency of the wave. To obtain the Love wave dispersion curve, this equation needs to be solved for $v_L = v_L(\omega)$. The tangent is a harmonic function ($\tan(x) = \tan(x+n\pi)$) and therefore the solution of Eq. (3.1.28) is not unique. The solutions of Eq. (3.1.28) are referred to as the modes of the wave, where the solution for $n=0$ is called the *fundamental mode*, and all other solutions with $n>0$ are called *higher order modes*. Fundamental and higher order modes exist and have been measured for Love and for Rayleigh waves [111, 112]. The physical interpretation of higher order modes beyond the mathematical understanding is still de-

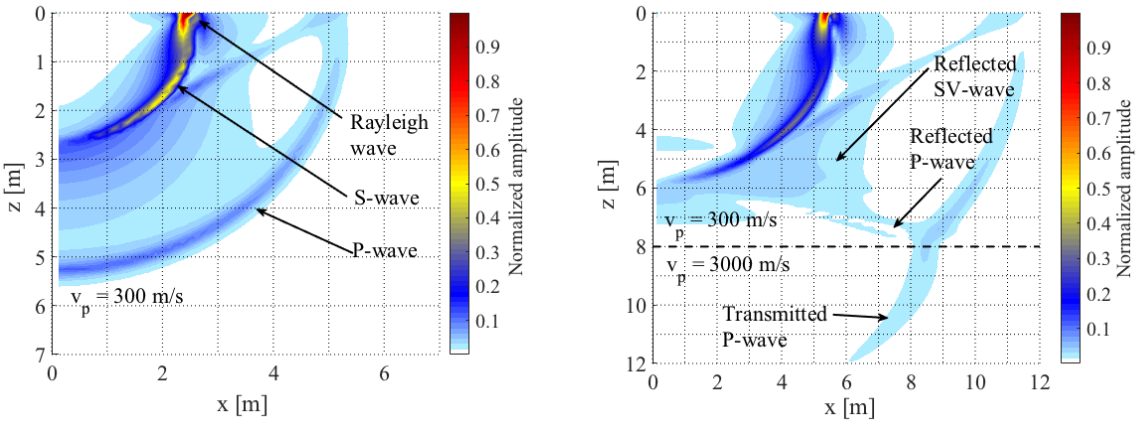

Figure 3.6: *Left: P- and S-waves generated by a point source in a homogeneous half-space spread over the entire volume while the energy of Rayleigh waves is constrained to a circle in the surface plane. Right: The layer interface leads to additional effects like wave reflection, transmission and mode conversion.*

bated within the geophysics community. Most commonly they are interpreted as a phenomenon of constructive interference of waves that are reflected multiple times within the layers of a heterogeneous material [107, 113]. The amplitude and energy distribution of higher order modes depends on many site-specific factors such as geology, layer material properties, source mechanism, type and distance. Typically the fundamental mode is more dominant in geologies where the S-wave velocity increases gradually with depth, while geologies with high velocity contrasts in layers at shallow depths can lead to an increased amplitude of the higher order modes.

Attenuation and energy spreading

Attenuation of seismic waves is connected to the concept of energy loss during propagation. Energy of a seismic wave can be dissipated by geometric or by material damping. *Geometric damping* is a result of energy spreading over an increasing area of the wavefront. In reality, seismic waves are rarely plane waves, but they are emitted by sources and spread equally in all three spatial dimensions (Fig. 3.6). Hence, body waves are spherical waves. With increasing distance r from the excitation point their energy decreases with $1/r^2$ and their amplitude with $1/r$. Surface waves propagate along the two surface dimensions, hence their energy is reduced by $1/r$ and their amplitude by $1/\sqrt{r}$. *Material damping* contributes to energy loss due to inelastic processes and internal friction within the medium during wave propagation. This can for example be attributed to internal heating or to deformation of the material. Material damping of P- and S-waves is described by the wave-dependent quality factors Q_P and Q_S [106]. The quality factor is inversely related to the attenuation: regions with high quality factor exhibit low amplitude attenuation and regions with small quality factor exhibit high amplitude attenuation. For a wave propagating in the $\vec{x}$-direction the amplitude attenuation by material damping is given by

$$u_c(x) = e^{-\frac{\vec{k}\cdot\vec{x}}{2Q_c}}, \tag{3.1.29}$$

where the subscript $c \in (P, S)$ either represents the P- or the S-wave material quality factor, respectively. With Eq (3.1.18) the total wave amplitude of a plane wave with material damping

can then be expressed as

$$\vec{u}(\vec{x},t) = \vec{u}_0(\vec{x}) \cdot u_c(x) \cdot e^{i(\omega t - \vec{k}\cdot\vec{x})}. \tag{3.1.30}$$

3.1.3 The stiffness matrix method for horizontally stratified soil profiles

Analytical solutions of the wave equation for a multilayered medium with arbitrary boundary conditions do not exist. Hence, one needs to rely on finite element analysis or other numerical tools to derive the displacement field and associated stress components of complex soil profiles. Standard methods to solve these type of problems are the *propagator matrix* method by Haskell and Thomson [114,115] and the closely related *direct stiffness* method [116]. The direct stiffness method has several advantages, for instance it involves half the number of degrees of freedom compared to the propagator matrix method. This means that it is computationally twice as fast as the propagator matrix method, hence it is typically integrated in numerical solver software like the Matlab Elastodynamics toolbox (EDT) [117]. Furthermore, the direct stiffness method naturally allows to derive the normal modes of the soil profile from the wave equation and the computation of the dynamic soil response to source excitations, which make it ideal for the purpose of seismic field modeling. The direct stiffness method is based on a transformation of the wave equation from the space-time domain to the wave number-frequency domain, where for each layer a stiffness matrix can be formulated [118, 119]. Superposition of the stiffness matrices from each layer allows the exact mathematical reformulation of the full wave equation as an eigenvalue problem. The numerical solution of the eigenvalue problem and the inverse transformation to the space-time domain gives the displacement field vector and stress components at any specified receiver coordinate.

For a conceptual understanding of the steps in the numerical solving analysis we consider the case of plane wave propagation in a horizontally stratified medium, with the wave vector lying in the x_1x_3-plane, where x_1 indicates the horizontal and x_3 the vertical direction in Cartesian coordinates. This approach is expanded to the three-dimensional representation in spherical coordinates for example in [118, 119]. In this example the displacement in the x_2-direction is constant and all derivatives in Eq. (3.1.12) with respect to $\partial/\partial x_2$ are zero. For simplicity the x_2-component will therefore be dropped in the following.

The Fourier transform allows to transform between the time-domain representation of a function $f(x_1,t)$ and the frequency-domain representation $\hat{f}(x_1,\omega)$ of the function as

$$\hat{f}(x_1,\omega) = \mathcal{F}(f(x_1,t),\omega) = \int_{-\infty}^{\infty} e^{-i\omega t} f(x_1,t)dt \tag{3.1.31}$$

$$f(x_1,t) = \mathcal{F}^{-1}(\hat{f}(x_1,\omega),t) = \frac{1}{2\pi}\int_{-\infty}^{\infty} e^{i\omega t}\hat{f}(x_1,\omega)d\omega, \tag{3.1.32}$$

where $\mathcal{F}$ is the forward and $\mathcal{F}^{-1}$ is the inverse transformation [118]. A transformation between the horizontal space and the horizontal wave number domain is further defined as

$$\tilde{f}(k_{x_1},t) = \mathcal{F}(f(x_1,t),k_{x_1}) = \int_{-\infty}^{\infty} e^{-ik_{x_1}x_1} f(x_1,t)dx_1 \tag{3.1.33}$$

$$f(x_1,t) = \mathcal{F}^{-1}(\hat{f}(k_{x_1},t),x_1) = \frac{1}{2\pi}\int_{-\infty}^{\infty} e^{ik_{x_1}x_1}\tilde{f}(k_{x_1},t)dk_{x_1}, \tag{3.1.34}$$

where k_{x_1} is the horizontal wave number. In case of three-dimensional wave propagation in spherical symmetrical geometries, Hankel transformations are used [118]. For a wave propagating in the x_1x_3-plane, the horizontal wave number k_{x_1} of P- and S-waves are then defined as

$$\vec{k}_P = (k_{x_1}, k_{P,x_3}) \rightarrow |\vec{k_P}| = \frac{\omega}{v_P} = \sqrt{k_{x_1}^2 + k_{P,x_3}^2}, \tag{3.1.35}$$

$$\vec{k}_S = (k_{x_1}, k_{S,x_3}) \rightarrow |\vec{k_S}| = \frac{\omega}{v_S} = \sqrt{k_{x_1}^2 + k_{S,x_3}^2}. \tag{3.1.36}$$

Displacement and stress in a homogeneous medium

The elastodynamic wave equation for a plane wave in the x_1x_3-plane in a homogeneous medium can then be derived from Eq. (3.1.12) in the frequency-wave number domain following [118] as

$$-k_{x_1}^2\mathbf{A}\vec{\mathfrak{u}} - k_{x_1}\mathbf{B}\frac{\partial\vec{\mathfrak{u}}}{\partial x_3} + \mathbf{C}\frac{\partial^2\vec{\mathfrak{u}}}{\partial x_3^2} = -\omega^2\rho\vec{\mathfrak{u}}, \text{ where} \tag{3.1.37}$$

$$\mathbf{A} = \begin{bmatrix} \lambda+2\mu & 0 & 0 \\ 0 & \mu & 0 \\ 0 & 0 & \mu \end{bmatrix}, \mathbf{B} = \begin{bmatrix} 0 & 0 & -(\lambda+\mu) \\ 0 & 0 & 0 \\ \lambda+\mu & 0 & 0 \end{bmatrix}, \mathbf{C} = \begin{bmatrix} \mu & 0 & 0 \\ 0 & \mu & 0 \\ 0 & 0 & \lambda+2\mu \end{bmatrix},$$

where $\vec{\mathfrak{u}} = (u_1(k_{x_1}, x_3, \omega), u_2(k_{x_1}, x_3, \omega), -iu_3(k_{x_1}, x_3, \omega))$ represents the modified displacement vector in the frequency-wave number domain representation (for the derivation see Appendix A). The x_3-component of the displacement vector has been rewritten as $u_3 \rightarrow -iu_3$, to allow for a symmetric formulation of the stiffness matrix later. For readability, all parameter dependencies have been dropped. It can be shown [118] that the solution to Eq. (3.1.37) is of the form

$$\vec{\mathfrak{u}} = \begin{bmatrix} \mathbf{R}_u\mathbf{E}^{-1} & \mathbf{R}_d\mathbf{E} \end{bmatrix} \begin{bmatrix} \vec{\mathfrak{a}}_u \\ \vec{\mathfrak{a}}_d \end{bmatrix}, \text{ where} \tag{3.1.38}$$

$$\mathbf{R}_u = \begin{bmatrix} 1 & 0 & -p \\ 0 & 1 & 0 \\ -q & 0 & 1 \end{bmatrix}, \mathbf{R}_d = \begin{bmatrix} 1 & 0 & p \\ 0 & 1 & 0 \\ q & 0 & 1 \end{bmatrix}, \mathbf{E} = \begin{bmatrix} e^{k_{x_1}qx_3} & 0 & 0 \\ 0 & e^{k_{x_1}px_3} & 0 \\ 0 & 0 & e^{k_{x_1}px_3} \end{bmatrix},$$

where the $\vec{\mathfrak{a}} = (\mathfrak{a}_P, \mathfrak{a}_{SH}, \mathfrak{a}_{SV})$ are the complex wave potential amplitudes of the P-, SH- and SV waves respectively, with the subscript d indicating a wave propagating downward in the negative x_3-direction and the subscript u indicating a wave propagating upward in the positive x_3-direction and where p and q are as defined in Eq. (3.1.27). The modified stress components $\vec{\mathfrak{s}} = (\sigma_{13}, \sigma_{23}, -i\sigma_{33})$ on a horizontal layer that are associated with this displacement are derived from the relationships between displacement, strain and stress, Eq. (3.1.2) and Eq. (3.1.5) respectively. Transforming these equations to the frequency-wave number domain and using Eq. (3.1.38) gives

$$\vec{\mathfrak{s}} = k_{x_1}\mu\begin{bmatrix} -\mathbf{Q}_u\mathbf{E}^{-1} & \mathbf{Q}_d\mathbf{E} \end{bmatrix} \begin{bmatrix} \vec{\mathfrak{a}}_u \\ \vec{\mathfrak{a}}_d \end{bmatrix}, \text{ where} \tag{3.1.39}$$

$$\mathbf{Q}_u = \begin{bmatrix} 2q & 0 & -(1+p^2) \\ 0 & p & 0 \\ -(1+p^2) & 0 & 2p \end{bmatrix}, \mathbf{Q}_d = \begin{bmatrix} 2q & 0 & 1+p^2 \\ 0 & p & 0 \\ 1+p^2 & 0 & 2p \end{bmatrix}.$$

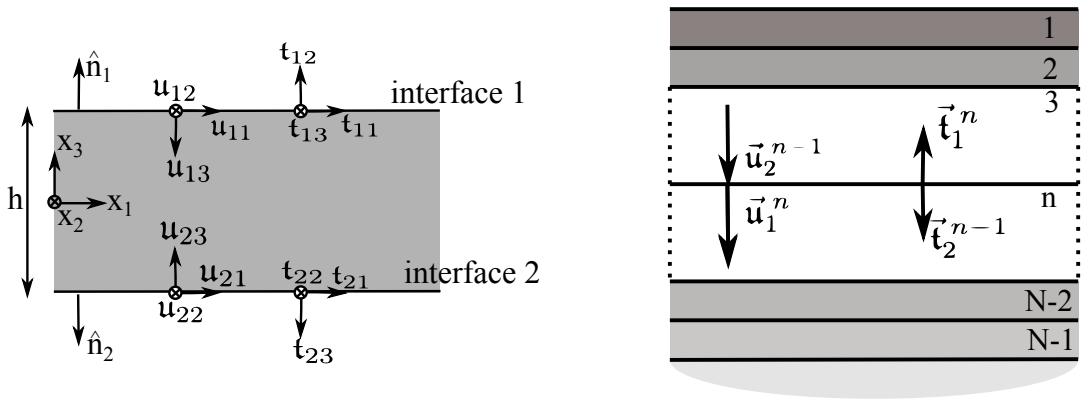

Figure 3.7: *Left: Displacement and tractions on a free layer. The coordinate system is located in the center of the layer and $\hat{n}_1$ and $\hat{n}_2$ are the vectors normal to interface 1 and interface 2, respectively. Right: Horizontally layered medium with $N-1$ layer elements on a half space element.*

Displacement and traction in a single horizontal layer

Next consider a homogeneous, horizontal layer of thickness h where the upper and lower interface are labeled with 1 and 2 following [118], respectively, as in Fig. 3.7, left panel. With the previously derived wavefield (Eq. (3.1.38)), the displacement on interface 1, $\vec{u}_1 = (u_{11}, u_{12}, u_{13})$, and on interface 2, $\vec{u}_2 = (u_{21}, u_{22}, u_{23})$, can be written as

$$\begin{bmatrix} \vec{u}_1 \\ \vec{u}_2 \end{bmatrix} = \begin{bmatrix} \mathbf{R}_u \mathbf{E}^{-1}(x_3 = \frac{h}{2}) & \mathbf{R}_d \mathbf{E}(x_3 = \frac{h}{2}) \\ \mathbf{R}_u \mathbf{E}^{-1}(x_3 = -\frac{h}{2}) & \mathbf{R}_d \mathbf{E}(x_3 = -\frac{h}{2}) \end{bmatrix} \begin{bmatrix} \vec{a}_u \\ \vec{a}_d \end{bmatrix}, \tag{3.1.40}$$

where it has been assumed that the center of the coordinate system is in the center of the layer.

The force per unit area on a horizontal interface of the layer, the so called traction, is related to the elements of the stress tensor that correspond to the vector normal to this interface. In this case $\vec{t}_1 = \vec{s}$ is the traction on interface 1 and $\vec{t}_2 = -\vec{s}$ is the traction on interface 2 and with Eq. (3.1.39) this can be written as

$$\begin{bmatrix} \vec{t}_1 \\ \vec{t}_2 \end{bmatrix} = \begin{bmatrix} -\mathbf{Q}_u \mathbf{E}^{-1}(x_3 = \frac{h}{2}) & \mathbf{Q}_d \mathbf{E}(x_3 = \frac{h}{2})] \\ \mathbf{Q}_u \mathbf{E}^{-1}(x_3 = -\frac{h}{2}) & -\mathbf{Q}_d \mathbf{E}(x_3 = -\frac{h}{2})] \end{bmatrix} \begin{bmatrix} \vec{a}_u \\ \vec{a}_d \end{bmatrix} = \begin{bmatrix} \mathbf{K}_{11} & \mathbf{K}_{12} \\ \mathbf{K}_{21} & \mathbf{K}_{22} \end{bmatrix} \begin{bmatrix} \vec{u}_1 \\ \vec{u}_2 \end{bmatrix}, \text{ with} \tag{3.1.41}$$

$$\begin{aligned} \mathbf{K} &= \begin{bmatrix} \mathbf{K}_{11} & \mathbf{K}_{12} \\ \mathbf{K}_{21} & \mathbf{K}_{22} \end{bmatrix} \\ &= \begin{bmatrix} -\mathbf{Q}_u \mathbf{E}^{-1}(x_3 = \frac{h}{2}) & \mathbf{Q}_d \mathbf{E}(x_3 = \frac{h}{2})] \\ \mathbf{Q}_u \mathbf{E}^{-1}(x_3 = -\frac{h}{2}) & -\mathbf{Q}_d \mathbf{E}(x_3 = -\frac{h}{2})] \end{bmatrix} \begin{bmatrix} \mathbf{R}_u \mathbf{E}^{-1}(x_3 = \frac{h}{2}) & \mathbf{R}_d \mathbf{E}(x_3 = \frac{h}{2}) \\ \mathbf{R}_u \mathbf{E}^{-1}(x_3 = -\frac{h}{2}) & \mathbf{R}_d \mathbf{E}(x_3 = -\frac{h}{2}) \end{bmatrix}^{-1}, \end{aligned}$$

where in the second step Eq. (3.1.40), solved in terms of the wave amplitudes, has been used and where $\mathbf{K}$ is called the symmetric *stiffness matrix* of the layer. The stiffness matrix of an elastic half-space is obtained for $\vec{a}_d = 0$ and $h \to \infty$.

Displacement and traction in a horizontally multilayered medium

Now consider a system with $N-1$ layers and N interfaces on a half-space (Fig. 3.7, right panel). Following [118], the stiffness matrix of the n^{th} layer is then denoted as

$$\mathbf{K}^n = \begin{bmatrix} K_{n,n} & K_{n,n+2} \\ K_{n+1,n} & K_{n+1,n+1} \end{bmatrix}, \tag{3.1.42}$$

and by overlapping the stiffness matrices of all $N-1$ layers, the total stiffness matrix of the system is of the form

$$\begin{bmatrix} \vec{t}_1 \\ \vec{t}_2 \\ \vec{t}_3 \\ \vdots \\ \vec{t}_N \end{bmatrix} = \begin{bmatrix} \mathbf{K}_{1,1} & \mathbf{K}_{1,2} & 0 & \cdots & 0 \\ \mathbf{K}_{2,1} & \mathbf{K}_{2,2} & \mathbf{K}_{2,3} & \cdots & 0 \\ 0 & \mathbf{K}_{3,2} & \mathbf{K}_{3,3} & \ddots & 0 \\ \vdots & \vdots & \ddots & \ddots & \mathbf{K}_{N-1,N} \\ 0 & 0 & \cdots & \mathbf{K}_{N,N-1} & \mathbf{K}_{N,N} \end{bmatrix} \begin{bmatrix} \vec{u}_1 \\ \vec{u}_2 \\ \vec{u}_3 \\ \vdots \\ \vec{u}_N \end{bmatrix}. \tag{3.1.43}$$

For a given traction on an interface, the displacement field is the solution to the matrix inversion problem in Eq. (3.1.43). The traction on the surface represents a source that excites the soil profile. In the context of the dynamic response of a soil to an external source, the displacement field is also referred to as Green's function. In this work we restrict ourselves to harmonic point excitations on the surface of layered soil profiles. Surface point sources allow to model the soil response to anthropogenic sources, which corresponds to seismic noise above 1 Hz that is generated by human activity. Sources at low frequencies are for example microseismic activity, originating from ocean waves interacting with the shore, or earthquakes, which are accompanied by fault slips at great depths below the surface. These type of sources are not of relevance for the analysis of this work. The interested reader can find an overview of modeling techniques for more complex source types and mechanisms in [107].

Even though it is tedious for larger numbers of N, the matrix operation in Eq. (3.1.43) in the frequency-wave number domain may still be derived by hand and a closed-form solution to the above eigenvalue problem may be given. However, the problem further increases in complexity when arbitrary wave propagation in three-dimensional geometries with curved wavefronts are required. Hence, numerical solving tools are required to derive the solution to the eigenvalue problem for a realistic geology.

3.2 Spectral wave analysis

Seismic data are recorded in the time domain, but to extract the spectral components of the seismic field, the analysis is carried out in the frequency domain. To transform the data from the time to the frequency domain, Fourier analysis is used. Since the data points are discrete and to facilitate implementation in software algorithms, Eq. (3.1.31) is modified to the *discrete Fourier transform* (DFT) which maps the elements of the time domain data vector $\vec{x} = (x_0, ..., x_{N-1})$ with N components to its frequency domain counterpart $\vec{y} = (y_0, ...y_{N-1})$ as [120]

$$y_m = \sum_{k=0}^{N-1} x_k \exp(-2\pi i \frac{mk}{N}), \tag{3.2.1}$$

where the index $k = 0, ..., N-1$ refers to the data points in the time domain vector and $m = 0, .., N-1$ denotes the index of the data points in the frequency domain representation. As the x_k are real values, the corresponding frequency domain signal is conjugate symmetric as $y_{N-m} = y_m^*$.

The time domain data are sampled with a sampling frequency f_s, which depends on the data acquisition device. According to the Shannon-Nyquist theorem [121], the maximum frequency f_{Ny} that can be resolved equals half of the sampling frequency, so that $f_{Ny} = f_s/2$. So for a signal that is sampled at 100 Hz, information about its spectral content can be obtained up to 50 Hz. By defining the frequency bin width as $f_{res} = \frac{f_s}{N}$, the frequency values of the N data points in Eq. (3.2.1) are

$$f_m = m \cdot f_{res} - f_{Ny}, \tag{3.2.2}$$

which is a vector of N components ranging from $-f_s/2$ to $f_s/2$.

The DFT implicitly assumes that the time domain signal is periodic. Any discontinuity between the first and the last point in the data vector results in a distortion of the signal across the whole frequency domain. To prevent such distortion effects the time domain data are multiplied by a symmetric *window function* before applying the DFT. Window functions typically increase at the beginning of the interval, then peak in the middle and drop again at the end of the interval, hereby suppressing discontinuities at the boundary of the data array. Many different window functions have been defined for a wide variety of purposes, and an extended list can be found in [120]. A common window function is the Hanning window (Fig. 3.8, left panel) which is defined as

$$w_m = \frac{1}{2}[1 - \cos(\frac{2\pi m}{N})], \text{ where } m = 0, .., N-1, \tag{3.2.3}$$

and for normalization purposes the following sums are defined

$$S_1 \equiv \sum_{m=0}^{N-1} w_m, \quad S_2 \equiv \sum_{m=0}^{N-1} w_m^2. \tag{3.2.4}$$

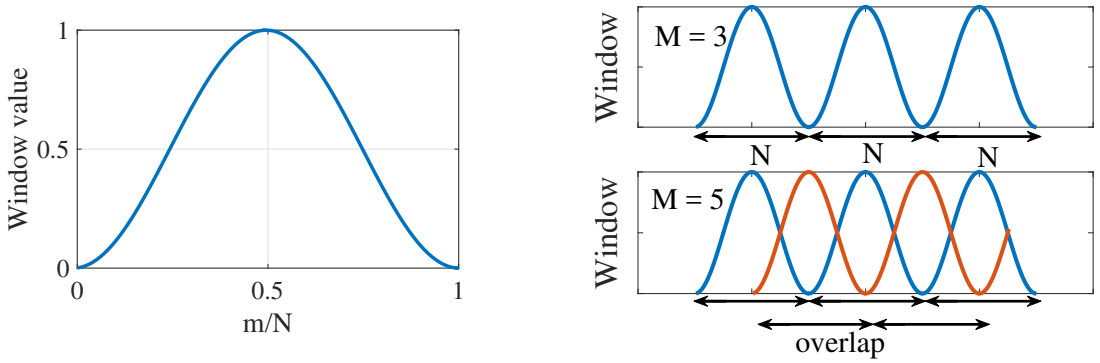

Figure 3.8: *Left: Hanning window function in the time domain normalized by the number of samples N. Right: If a signal is split into m neighboring segments, information is lost at the boundary of the segments due to the window function (top). To avoid information loss, the M windows are chosen to be overlapping.*

The signal power in the frequency domain is obtained by taking the square of the absolute values of y_m (Eq. (3.2.1)). Normalizing it by the window power, the number of frequency bins N

and the bandwidth f_{res} gives

$$PSD(f_{\tilde{m}} = \tilde{m} f_{res}) = \frac{2 \cdot |y_{\tilde{m}}|^2}{N \cdot f_{res} \cdot S_2} = \frac{2 \cdot |y_{\tilde{m}}|^2}{f_s \cdot S_2}, \tag{3.2.5}$$

where $\tilde{m} = \frac{N-1}{2}, ...N-1$ is the index that only regards the positive frequency components of Eq. (3.2.2) and where the second, conjugate symmetric side of the spectrum is taken into account by the factor 2 in the nominator. This is called the one-sided *power spectral density* (PSD). It is also common to display the amplitude spectral density (ASD), which is the square root of the PSD.

To reduce the noise fluctuations in a PSD signal, the data array is split into M segments of N samples length. To each segment the window function is applied and the resulting M PSDs are averaged. This allows to reduce the stochastic noise by a factor $1/\sqrt{M}$. If the signal is split into neighboring segments (Fig. 3.8, right panel), information is lost at the boundaries of each segment. To overcome this relic of the window function, the segments are typically chosen to be overlapping. For a Hanning window the standard overlap between two neighboring windows is 50 % .

Coherence and correlation

The nomenclature on this topic is not used consistently in the literature, so in this work the following definitions based on [122,123] will be used. Consider a seismic signal that is measured simultaneously at two different locations, with $X_1(f)$ and $X_2(f)$ being the frequency domain representation of the signal at sensor 1 and 2, respectively. The similarity between the two signals can then be determined via the *frequency domain cross-spectrum* as

$$K_{12}(f) = \frac{\langle X_1(f) X_2^*(f) \rangle}{\sqrt{\langle X_1(f) X_1^*(f) \rangle \langle X_2(f) X_2^*(f) \rangle}}, \tag{3.2.6}$$

where * denotes the complex conjugate operation and $\langle . \rangle$ denotes an average over M data segments. Eq. (3.2.6) is a complex number, where the magnitude $|K_{12}(f)|$ is called the *coherence* and the real part $\mathfrak{Re}(K_{12})$ is called the *correlation*. If two signals are very similar and related to each other by means of a linear transformation the coherence is one, whereas it tends to zero when both signals are completely unrelated. The correlation also contains information about the similarity of the phase of both signals. It is equal to 1 if both signals are in phase and -1 if both signals are completely out of phase. Assuming a seismic signal that is emitted along the line connecting two measurement locations on the surface, the correlation for that signal is given by

$$\mathfrak{Re}(K_{12}) = \cos(\frac{2\pi}{\lambda(f)} \Delta z), \tag{3.2.7}$$

where $\lambda(f)$ represents the frequency-dependent wavelength and Δz is the distance between the two measurement points. For waves originating uniformly from all azimuth directions θ around the sensor pair, the wavelength that is perceived by that receiver pair is $\lambda = \frac{\lambda(f)}{\cos\theta}$ and the integral over all azimuth angles yields

$$\begin{aligned} \mathfrak{Re}(K_{12}) &= \frac{1}{2\pi} \int_{-\pi}^{\pi} \cos(\frac{2\pi}{\lambda(f)} \Delta z \ \cos\theta) d\theta \\ &= J_0(\frac{2\pi}{\lambda(f)} \Delta z), \end{aligned} \tag{3.2.8}$$

where J_0 is the zero-order Bessel function of the first kind.

3.3 Seismic model with a complete seismic field

The response of a horizontally layered soil profile to source excitations can be obtained by numerically solving the elastodynamic wave equation. A structural overview of the necessary steps that are required to derive an ambient seismic field model in a specified geology is displayed in Fig. 3.9, left panel. The geology at the detector location can be determined with a seismic study by using a dense sensor array. Beam forming is used to determine the seismic source distribution and the dispersion curve of the subsurface, while seismic inversion is carried out to obtain a horizontally layered subsurface model with velocity, density and damping ratio information (for details see Section 4). This section presents how this geological information is used to obtain a model for a seismic field with use of the full solution of the elastodynamic wave equation.

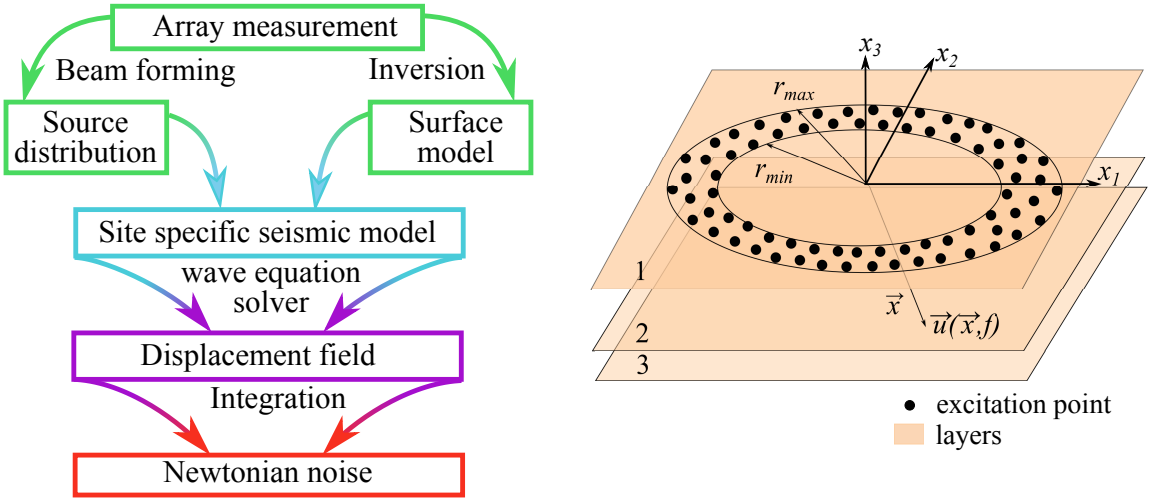

Figure 3.9: *Left: The lithology and source distribution at the site are determined with seismic sensor array measurements (green). Solving the elastodynamic wave equation for the derived seismic model (blue) results in a seismic displacement field that is characteristic for the site (purple). Integrating over the seismic displacements allows to calculate the Newtonian noise on a test mass located in this wave field (red). Right: Schematic layout of the model for an ambient seismic field. Excitation points, where the soil is horizontally and vertically excited, are placed in a ring around a region where the ambient seismic field is calculated.*

The soil response to source excitations is obtained by numerically solving the elastodynamic wave equation with the Matlab Elastodynamics toolbox [117, 119]. The response is a three-dimensional vector field denoted as $\vec{u}(\vec{x}, f) = (u_1(\vec{x}, f), u_2(\vec{x}, f), u_3(\vec{x}, f))$ (Fig. 3.10). It represents the complex amplitude of the seismic displacement at a receiver location $\vec{x}$ to a source oscillating with frequency f. To model an ambient seismic field the soil is vertically excited at N excitation points, which are located within a ring of r_{min} and r_{max} from the center of the geometry (Fig. 3.9, right panel).

The response at the receiver location $\vec{x}$ to the n^{th}-source is denoted as $\vec{u}_n(\vec{x}, f)$. The default strength of a source is 1 N. Due to the linear relationship between traction and displacement (see Eq. (3.1.43)), increasing the source strength directly leads to an increase of the displacement magnitude by the same factor. In a realistic geology, the strength of the sources depends on their cardinal direction. It is for example possible, that source excitations from the northern direction are dominant across the whole frequency band. To take this directional dependence into consideration, a *relative scaling factor* $\tilde{m}_n(f)$ is introduced, where the subscript indicates

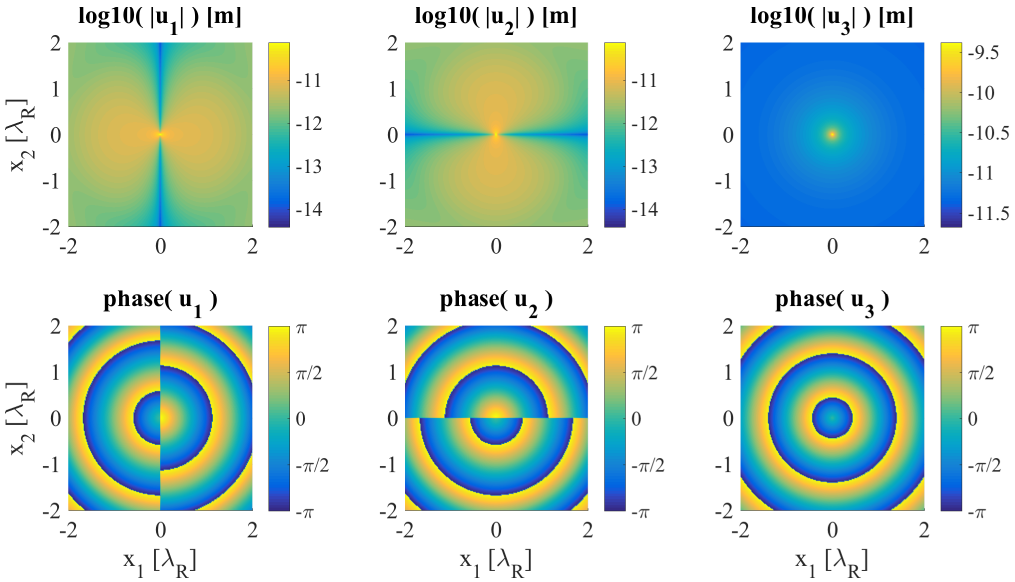

Figure 3.10: *Amplitude, top row, and phase, bottom row, of the three displacement components from a vertical excitation of a half-space in the center of the geometry, where the phase indicates the direction of the displacement. Along the x_1-axis (x_2-axis) the horizontal displacement is purely in the x_1-direction (x_2-direction) and at any other point the radial displacement is a superposition of u_1 and u_2.*

that the scaling factor corresponds to the n^{th}-source. The value of the relative scaling factor is derived from the beam power, a quantity that can be measured with a seismic sensor array. It appoints the main energy content of a seismic field to a cardinal direction (see Section 4.2). The response of the soil to a force $F(f) = \tilde{m}_n^{1/2}(f)$ is then calculated by multiplying the power of the default response $|\vec{u}_n(\vec{x}, f)|^2$ of the n^{th}-source by the relative scaling factor $\tilde{m}_n(f)$.

All sources are assumed to act as incoherent noise sources, which means that for the total ambient seismic field at $\vec{x}$ the individual responses are summed quadratically as

$$|u_i(\vec{x}, f)|^2 \quad = \sum_{n=1}^{N} \tilde{m}_n(f) \cdot |u_{i,n}(\vec{x}, f)|^2 \ [\mathrm{m}^2], \tag{3.3.1}$$

where the index $i = 1, 2, 3$ indicates the i^{th} component of the displacement vector. Modeling the seismic field as a coherent sum is in principle possible as well. However, the seismic field from a coherent sum would rather describe a single, complicated soil excitation, whereas the incoherent sum attributes a transient, individual displacement field from each noise source.

Using the fact that the squared absolute value of the displacement $|u_i(\vec{x}, f)|^2$ is proportional to the PSD, an *absolute scaling factor* $m(f)$ (in units $[1/\mathrm{Hz}]$) can be introduced as the proportionality constant. The absolute scaling factor ensures that the strength of the sources is increased equally such that the resulting simulated PSD is equivalent to the measured PSD as

$$\mathrm{PSD}_i(\vec{x}, f) = m(f) \cdot |u_i(\vec{x}, f)|^2 \ [\mathrm{m}^2/\mathrm{Hz}]. \tag{3.3.2}$$

For a specific geology, the absolute scaling factor can be obtained by solving Eq. (3.3.2) for a PSD that has been measured for example at the surface of the site. The total, scaled wave field is then obtained by multiplying the displacements at all locations with the obtained scaling factor.

3.4 Newtonian noise in a horizontally layered geology

When the seismic displacement field is known at all points of a geology, it can be used to calculate Newtonian noise on a test mass of a gravitational wave detector embedded in this geology. Newtonian noise is the motion of the test mass due to Newtonian interaction with seismically induced density fluctuations in the soil surrounding the detector. To derive the connection between seismic displacement and density fluctuation, first consider a small, cubic volume element of width w in a homogeneous medium where a displacement field moves the volume element at $\vec{x}$ by $\vec{u}(\vec{x}, f) = (u_1(\vec{x}, f), u_2(\vec{x}, f), u_3(\vec{x}, f))$ (Fig. 3.11, left panel). The resulting density fluctuations are assumed to be much smaller than the displacements such that an unperturbed, uniform density ρ_0 can be assumed to first order across the medium. For a displacement only in the x_1-direction, the total change in mass at the location of the original volume element is

$$\delta m_1 = m_{in} - m_{out} = -\rho_0 w^2 \big(u_1(x_1 + w, x_2, x_3) - u_1(x_1, x_2, x_3)\big), \tag{3.4.1}$$

where $m_{in} = \rho_0 w^2 u_1(x_1, x_2, x_3)$ represents the mass that flows into and $m_{out} = \rho_0 w^2 u_1(x_1 + w, x_2, x_3)$ the mass that flows out of the original location of the volume element. For an infinitesimal small volume element the density fluctuation $\delta\rho_1 = \frac{\delta m_1}{w^3}$ from the displacement in the x_1-direction can then be expressed as

$$\delta\rho_1 = -\rho_0 \lim_{w\to 0} \frac{u_1(x_1 + w, x_2, x_3) - u_1(x_1, x_2, x_3)}{w} = -\rho_0 \frac{\partial u_1}{\partial x_1}, \tag{3.4.2}$$

where the partial derivative has been defined as

$$\frac{\partial f(x, y)}{\partial x} = \lim_{a\to 0} \frac{f(x + a, y) - f(x, y)}{a}. \tag{3.4.3}$$

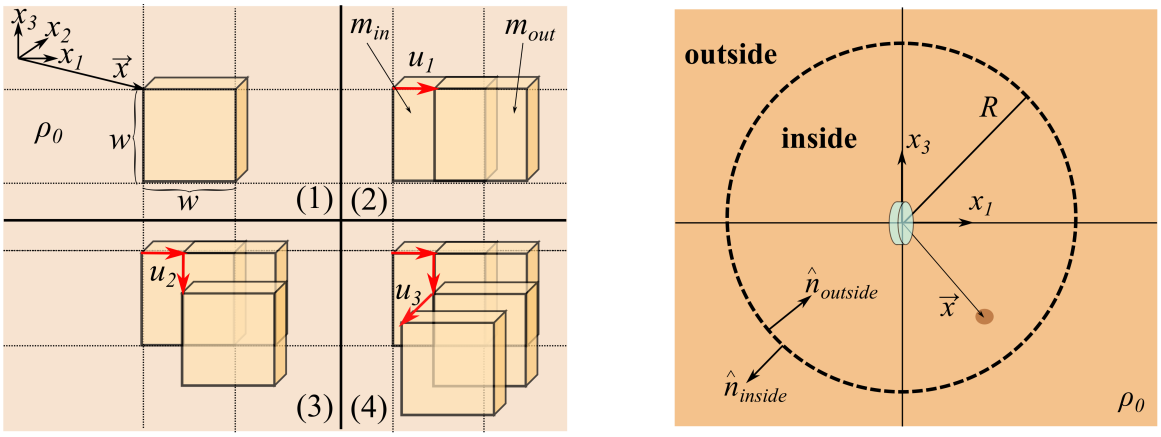

Figure 3.11: *Left: A cubic volume element with width w at location $\vec{x}$ in a medium of unperturbed density ρ_0 is displaced with $\vec{u}(\vec{x}, f) = (u_1, u_2, u_3)$. Right: Sketch of a test mass fully embedded in an unbound, homogeneous medium with unperturbed density ρ_0, where the test mass is located at the center of the coordinate frame with the x_2-axis pointing into the drawing. The integration area is separated in an area inside and outside a volume that is defined by the maximum integration radius R. The normal vectors on the interface that separates both areas are $\hat{n}_{inside}$ and $\hat{n}_{outside}$ and they are pointing outwards with respect to the part of the volume they correspond to.*

The sum of the individual fluctuations gives the total density fluctuation due to the displacement $\vec{u}(\vec{x}, f)$ as

$$\begin{aligned}\delta\rho(\vec{x}, f) &= \delta\rho_1 + \delta\rho_2 + \delta\rho_3 \\ &= -\rho_0\left(\frac{\partial u_1(\vec{x}, f)}{\partial x_1} + \frac{\partial u_2(\vec{x}, f)}{\partial x_2} + \frac{\partial u_3(\vec{x}, f)}{\partial x_3}\right) \\ &= -\rho_0\ \nabla \cdot \vec{u}(\vec{x}, f),\end{aligned} \tag{3.4.4}$$

where ∇ is the Nabla operator. This equation describes density fluctuations as a result of seismic motion and it is the basis of the following Newtonian noise derivation.

Newtonian acceleration in an unbound, homogeneous medium

Consider a test mass of a gravitational wave detector that is fully embedded in an unbound, homogeneous medium with unperturbed density ρ_0, where the center of the coordinate grid is placed at the location of the test mass (Fig. 3.11, right panel). The acceleration of the test mass due to density fluctuation $\delta\rho(\vec{x}, f)$ can then be obtained according to Newton's second law by integrating over the volume as

$$\delta\vec{a}(f) = G\int_V \delta\rho(\vec{x}, f)\frac{\vec{x}}{|\vec{x}|^3}\ dV, \tag{3.4.5}$$

where G represents the gravitational constant and $\vec{x}$ the vector pointing from the test mass in the direction of the density fluctuation. Substituting $\vec{k}(\vec{x}) \equiv \frac{\vec{x}}{|\vec{x}|^3}$ and with Eq. (3.4.4) the Newtonian acceleration of the test mass becomes

$$\begin{aligned}\delta\vec{a}(f) &= -G\int_V \rho_0\big(\nabla \cdot \vec{u}(\vec{x}, f)\big)\ \vec{k}(\vec{x})\ dV \\ &= -G\bigg(\int_V \rho_0 \nabla \cdot \big(\vec{u}\ \vec{k}\big)\ dV - \int_V \rho_0\big(\vec{u} \cdot \nabla\big)\vec{k}\ dV\bigg) \\ &= -G\bigg(\int_S \rho_0 u_1 n_1 \vec{k}\ dS_{23} + \int_S \rho_0(\vec{x}) u_2 n_2 \vec{k}\ dS_{13} + \int_S \rho_0(\vec{x}) u_3 n_3 \vec{k}\ dS_{12} \\ &\qquad - \int_V \rho_0\big(\frac{\partial\vec{k}}{\partial x_1}u_1 + \frac{\partial\vec{k}}{\partial x_2}u_2 + \frac{\partial\vec{k}}{\partial x_3}u_3\big)\ dV\bigg) \\ &= G\int_V \rho_0\big(\vec{u} \cdot \nabla\big)\vec{k}\ dV - G\int_S \rho_0\big(\vec{u} \cdot \hat{n}_S\big)\vec{k}\ dS,\end{aligned} \tag{3.4.6}$$

where for readability the arguments of the fields have been suppressed. In the third line Gauss's divergence theorem converts the volume to a surface integration and the integrals are given in Cartesian representation, where dS_{ij} refers to the surface integral across the $x_i x_j$-planes. In the last step the integral has been reformulated in terms of a coordinate independent representation, where $\hat{n}_S = (n_1, n_2, n_3)$ is the outward pointing vector normal to the surface that encloses the integration volume.

Next the integrals can be split into a region outside and inside a maximum integration area, that are separated by the integration radius R. The maximum integration radius R is defined such that 90 % of the Newtonian noise is derived from the spherical volume enclosed within this

radius. The acceleration of the test mass in the unbound, homogeneous medium then becomes

$$\begin{aligned}\delta\vec{a}(f) &= G\bigg(\int_V \rho_0\big(\vec{u}\cdot\nabla\big)\vec{k}\;dV_{inside} - \int_S \rho_0\big(\vec{u}\cdot\hat{n}_{inside}\big)\vec{k}\;dS \\ &\quad + \int_V \rho_0\big(\vec{u}\cdot\nabla\big)\vec{k}\;dV_{outside} - \int_S \rho_0\big(\vec{u}\cdot\hat{n}_{outside}\big)\vec{k}\;dS\bigg) \\ &= G\int_V \rho_0\big(\vec{u}\cdot\nabla\big)\vec{k}\;dV_{inside},\end{aligned} \tag{3.4.7}$$

where after the second step only the volume integral enclosed by R remains, because the contribution of the volume outside R to Newtonian noise is negligible. The surface integrals represent the mass flowing in and out of the integration volume, and since $-\hat{n}_{outside} = \hat{n}_{inside}$ both contributions cancel each other if the medium is continuous with constant density ρ_0. This means that in an unbound, homogeneous medium Newtonian noise is generated only by density fluctuations within the integration volume.

Newtonian noise in a layered medium

Consider now a test mass located at a depth h in a realistic, layered geology. It is instructive to first consider a geology with $M = 2$ layers of density ρ_m as depicted in Fig. 3.12. The Newtonian acceleration can then be derived from the contributions of the individual layers according to Eq. (3.4.6), where the part of the surface integral where seismic displacement occurs within the medium of the same density cancels out as derived in Eq. (3.4.7). The remaining part of the surface integral corresponds then to the interfaces between the layers and the resulting Newtonian acceleration can be expressed as

$$\begin{aligned}\delta\vec{a}(f) &= G\bigg(\int_V \rho_1\big(\vec{u}\cdot\nabla\big)\vec{k}\;dV_1 - \int_S \rho_1\big(\vec{u}\cdot\hat{n}_{1,up}\big)\vec{k}\;dS_1 - \int_S \rho_1\big(\vec{u}\cdot\hat{n}_{1,down}\big)\vec{k}\;dS_1 \\ &\quad + \int_V \rho_2\big(\vec{u}\cdot\nabla\big)\vec{k}\;dV_2 - \int_S \rho_2\big(\vec{u}\cdot\hat{n}_{2,up}\big)\vec{k}\;dS_2\bigg) \\ &= \sum_{m=1}^{M} G\bigg(\int_V \rho_m\big(\vec{u}\cdot\nabla\big)\vec{k}\;dV_m + (\rho_{m-1}-\rho_m)\int_S \big(\vec{u}\cdot\hat{n}_m\big)\vec{k}\;dS_m\bigg),\end{aligned} \tag{3.4.8}$$

where the volume and surface integral of the m^{th} layer are represented by dV_m and dS_m, and where $\hat{n}_{m+1,up} = -\hat{n}_{m,down} = \hat{n}_{m+1}$ holds for the normal vectors on the interface between the

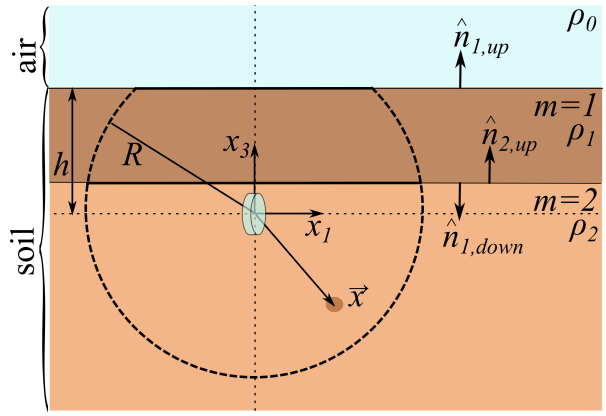

Figure 3.12: *Sketch of a test mass embedded at a depth h in a medium with $M = 2$ layers, where the density of each layer is indicated with ρ_m. Air has a density of $\rho_0 = 0$ and is not counted as layer. The vectors normal to the horizontal interfaces of the m^{th} layer are indicated with $\hat{n}_{m,up}$ and $\hat{n}_{m,down}$. The bottommost layer is unbound in the downward direction and therefore the normal vector $\hat{n}_{M,down}$ is not defined.*

m^{th} and the $(m+1)^{th}$ layer. The last line of Eq. (3.4.8) is then the general expression for the Newtonian acceleration of a test mass in a horizontally layered medium with M layers. Due to the dependence of Eq. (3.4.8) on the site-specific subsurface geology and the employment of a seismic field that depends on the local seismic source distribution and that encompasses the full solution of the wave equation in the characteristic geology (see Section 3.3), the Newtonian noise derived from this approach will be referred to as *site-based Newtonian noise*.

Following the approach in [45] the derivatives of the elements of the vector $\vec{k} = \frac{\vec{x}}{|\vec{x}|^3}$ can be expressed as

$$\frac{\partial k_i}{\partial x_j} = \frac{1}{|\vec{x}|^5}(\delta_{ij}|\vec{x}|^2 - 3x_i x_j), \tag{3.4.9}$$

where δ_{ij} is the Kronecker delta, which allows to reformulate the volume integral of the m^{th} layer in Eq. (3.4.8) as

$$\delta\vec{a}_{V_m}(f) = G\int_V \rho_m \frac{1}{|\vec{x}|^5}\begin{bmatrix} |\vec{x}|^2 - 3x_1^2 & -3x_1x_2 & -3x_1x_3 \\ -3x_2x_1 & |\vec{x}|^2 - 3x_2^2 & -3x_2x_3 \\ -3x_3x_1 & -3x_3x_2 & |\vec{x}|^2 - 3x_3^2 \end{bmatrix}\begin{bmatrix} u_1(\vec{x},f) \\ u_2(\vec{x},f) \\ u_3(\vec{x},f)\end{bmatrix} dV_m, \tag{3.4.10}$$

where a Cartesian representation has been chosen. Note that in special cases, such as a test mass surrounded by a spherical cavern on the surface of a homogeneous half-space surface with a constant displacement in only one horizontal direction, the volume contribution vanishes. This is however not true when the medium is not homogeneous or the mirror is surrounded by an asymmetric cavern. In this case constant displacements leads to an acceleration of the test mass that does not necessarily have to be in the direction of the displacement.

The Newtonian acceleration of a test mass due to a seismic field from N incoherent sources is calculated equivalently to Eq. (3.3.2). First the Newtonian acceleration is derived from the complex displacement field of each source individually (Eq. (3.4.8)), then these contributions are summed incoherently. By taking into account the previously derived relative and absolute scaling factors the i^{th} component of the *Newtonian noise* can be written as

$$\delta a_{i,NN}(f) = m(f)\cdot\sum_{n=1}^{N}\tilde{m}_n(f)\cdot|\delta a_{i,NN}^{(n)}(f)|^2\ [(\mathrm{m/s^2})^2/\mathrm{Hz}]. \tag{3.4.11}$$

In a broader sense, Newtonian noise is referred to as the output of a gravitational wave detector due to the seismically induced Newtonian acceleration at all four test masses. Assume a detector with distance L between two test masses. An interferometer arm is typically much longer than the seismic wavelengths for frequencies above 2 Hz. This implies that the forces on the test masses are uncorrelated and the total difference in separation is obtained by a sum over the individual test mass motions in power. The resulting Newtonian (strain) noise is then

$$h_{NN}(f) = \frac{1}{L(2\pi f)^2}\sqrt{\sum_{n=1}^{4}\delta a_{i,NN}^{(n)}(f)^2}, \tag{3.4.12}$$

where the index n labels the test masses. As the horizontal test mass motion parallel to the detector arms is of relevance for Newtonian noise, the index $i \in \{1,2\}$ labels the corresponding horizontal component of the Newtonian acceleration vector.

3.5 Going beyond analytical Newtonian noise models

Analytical surface models

Modeling Newtonian noise requires a description of the local seismic field and geology. The first model for Newtonian noise has been derived by Saulson in 1984 [124] and it is used until today for Newtonian noise estimates in the design sensitivity of gravitational wave detectors [52, 66]. Since numerical solving tools were not available at that time, Saulson based his model on an analytical derivation assuming a detector on the surface and a half-space geology with density ρ. Furthermore, it is assumed that the seismic field consists of independent regions, that are coherent across a length of $\lambda/2$, where λ is the wavelength. It is assumed that these regions fluctuate independently of each other, and that the Newtonian acceleration of the test mass can be formulated as an incoherent sum over the contribution from the individual patches. The horizontal component of the Newtonian acceleration parallel to the detector arm in the x_1-direction is then derived as

$$|\delta a_1(f)|^2 = \sum_i \left| \frac{F_{i,1}}{M} \right|^2 = G^2 \sum_i \left| \Delta m_i(f) \frac{\cos\theta_i}{|\vec{r}_i|^2} \right|^2, \tag{3.5.1}$$

where $F_{i,1}$ represents the horizontal component of the force between the i^{th} volume element at location $\vec{r}_i$ and the test mass with mass M, Δm_i is the mass fluctuation of the volume element, θ_i the angle between the volume element and the detector arm and G the gravitational constant. To facilitate the sum, it is converted to an integral where a lower cutoff radius of $\lambda/4$ is introduced to avoid a singularity as $|\vec{r}_i|$ approaches zero (see Appendix C for a summary of the derivation). Next, it is assumed that the fluctuation of mass $\delta m_i(f)$ in the volume element is directly proportional to the displacement amplitude $|\Delta X(f)|$ of the coherent region, which is in units $[\mathrm{m}/\sqrt{\mathrm{Hz}}]$ and a quantity that is measurable by seismometers. For simplicity it is assumed that the amplitude of the displacement is uniform across the entire half-space surrounding the test mass. The expression for the horizontal displacement Newtonian noise $|\delta x_1(f)|^2$ of four independent test masses can then be derived as

$$\begin{aligned} |\delta x_1(f)|^2 &= \frac{|\delta a_1(f)|^2}{(2\pi f)^4} \\ &= \frac{16\pi^2}{3} \frac{G^2\rho^2}{(2\pi f)^4} |\Delta X(f)|^2 \ \ [\mathrm{m}^2/\mathrm{Hz}]. \end{aligned} \tag{3.5.2}$$

It is important to understand that Saulson's result in Eq. (3.5.2) is only valid for a surface detector where the integration is carried out over a half-space, where no explicit assumption on a cavern shape, geology, source distribution, seismic waves, possible mode conversions, damping and amplitude attenuation with distance or depth have been made. Moreover, it needs to be understood that the cutoff condition of $\lambda/4$ leads to the factor $\frac{16\pi^2}{3}$ in Eq. (3.5.2). If the cutoff condition would be changed for example to $\lambda/2$, the factor in Eq. (3.5.2) would change to $\frac{2\pi^2}{3}$ and a smaller Newtonian noise level would be obtained. Note that this model has been used for Newtonian noise estimates in the Advanced Virgo design sensitivity curve [52, 53] and in the conceptual design study for the underground Einstein Telescope detector [66]. Moreover, numerous scientific papers have been written where event rates have been based on this Einstein Telescope sensitivity, see [125] and references within.

In an attempt to overcome some of the simplifications in the wavefield and geology in Eq. (3.5.2), the analytical model has been expanded by assuming plane Rayleigh waves, contributions from bulk and surface of a half-space and dispersive soil properties [126–128]. Combining these methods leads to an expression for the horizontal displacement Newtonian noise of a surface detector as [129]

$$|\delta x_1(f)|^2 = \beta^2 4\pi^2 \frac{G^2\rho^2}{(2\pi f)^4} |\Delta X(f)|^2 e^{-\frac{2\pi h}{\lambda}}, \tag{3.5.3}$$

where h is the height of the test mass above ground and the factor $\beta < 1$ is related to the dispersive properties of the detector geology. For the geology at the LIGO detectors, β has been estimated to be of the order $\beta \approx 0.35 - 0.6$ for quiet and $\beta \approx 0.15 - 1.4$ for noisy times [128].

All these models are confined to surface waves, since no detailed geological model of the subsurface at the detector sites nor a realistic distribution of noise sources and their spectral content was at hand. Together with finite element models of underground seismic fields in homogeneous media [45, 130], early studies stressed the necessity of a detailed seismic model, including the full solutions to the elastodynamic wave equation for a realistic geology of the detector site.

Site-based Newtonian noise model

To overcome the computational simplifications and assumptions about the seismic field and geology that were necessary to analytically derive the Newtonian noise expression in Eq. (3.5.2), Newtonian noise in this work is derived from Newton's second law, where the acceleration of a test mass is calculated from the integral over the density fluctuations across the entire volume as

$$\delta\vec{a}(f) = G \int_V \frac{\delta\rho(\vec{r}, f)}{|\vec{r}|^2} \hat{r}\, dV, \tag{3.5.4}$$

where density fluctuations $\delta\rho(\vec{r}, f)$ are connected to the seismic displacement through the continuity equation (see Eq. (3.4.4)). The seismic displacement is derived from the full solution of the elastodynamic wave equation in a detector-specific horizontal geology that takes the local noise source distribution into account (see Section 3.3) and in the following it is therefore referred to as *site-based Newtonian noise*. In its final expression the site-base Newtonian noise incorporates the coherent sum and difference of contributions from the bulk volume and the interfaces between media with different material properties (see Eq. (3.4.8)). Furthermore, the individual integrals are carried out with a Gaussian quadrature algorithm, a numerical integration method (see Appendix B).

Comparison of our site-based Newtonian noise to predictions from the analytical models for a constant wave field

A qualitative comparison between the analytical approach given by Eq. (3.5.2) and our site-based Newtonian noise is possible and assumes the same homogeneous half-space geology, lower cutoff radius and displacement field. For this comparison, a homogeneous half-space with a density of $\rho = 2000\ \frac{\mathrm{kg}}{\mathrm{m}^3}$, a Rayleigh wave speed of $v_R = 280\ \frac{\mathrm{m}}{\mathrm{s}}$ and a constant, horizontal displacement of $1\ \frac{\mathrm{nm}}{\sqrt{\mathrm{Hz}}}$ is assumed. Following Saulson's model, a minimum integration radius

of $\lambda_R/4$ has been used in Eq. (3.5.4), which corresponds to 280 m at 1 Hz and to 28 m at 10 Hz in this example.

First, the test mass in our site-based Newtonian noise is assumed to be at a height of $h = 0$ m, the same as in the analytical approach. For our numerical model the only contribution to Newtonian noise originates from the spherical soil-to-air interface. The contribution from the volume is zero, because of the absence of a density gradient in the horizontal direction of the half-space. With the above specified parameters and Eq. (3.4.8), the displacement power of the test mass can be analytically derived and deviates from Eq. (3.5.2) by a factor 3 (see Fig. 3.13 (a)). Note that this disagreement is coincidental and would not occur for a different cutoff condition. The prefactor attributed to the cutoff in the analytical approach leads to an increasing Newtonian noise for a decreasing cutoff radius and is singular for a cutoff radius of zero (see Eq. (C.4)). In contrast, the surface integral in our site-based approach represents a displacement flux through the spherical interface. As the integration radius decreases, the amount of mass being displaced on the interface decreases as well and as a result the site-based Newtonian noise is well behaved and the same for different cutoff conditions for a constant, horizontal displacement. Another contributing factor may originate from the fact that in the site-based approach, the cavern is taken into account by adjusting the integration bounds of the integral. However, the solving software is limited to a strictly horizontal soil profile, which does not allow to model seismic displacements between soil and air on arbitrary cavern walls. As a result, the Newtonian noise from Eq. (3.5.2) may be considered as upper bound of the Newtonian noise of a surface test mass under the given seismic conditions, which qualitatively agrees with the Newtonian noise from the site-based approach.

As the numerical evaluation of the integral of our site-based Newtonian noise allows for a minimum integration bound of zero, it is possible to evaluate the same integral without the lower cutoff radius. For a homogeneous, unbound medium without discontinuity in the horizontal direction, that is displaced horizontally, each moving volume element is replaced by a volume element with identical density and thus the total Newtonian noise of a test mass at $h = 0$ m vanishes. The same argument holds if the test mass is located above ground; for a pure horizontal displacement of the soil, the site-based Newtonian noise vanishes. Note that in both cases, the

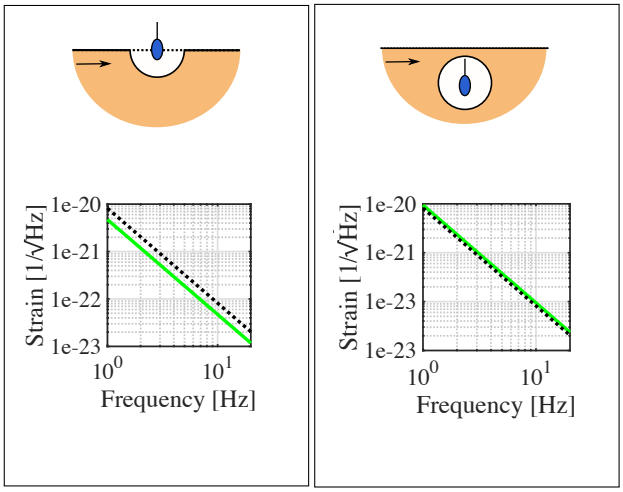

Figure 3.13: *The Newtonian noise derived with Saulson's analytical model, with a test mass height of $h = 0$ m and a frequency dependent cutoff radius of $\lambda/4$, is depicted in dashed black in both bottom panels. Our site-based Newtonian noise is depicted in green. In panel (a) it differs by a factor $\sqrt{3}$ from the Newtonian noise from the analytical model for a test mass height of $h = 0$ m and the same frequency dependent cutoff radius. In panel (b), the site-based Newtonian noise for a a test mass at arbitrary depth and a cavern radius of $\lambda/4$ is a factor two above the green curve in panel (a).*

Newtonian noise prediction from the analytical approach would diverge towards infinity, when such a variable cutoff condition would be applied.

Finally, the test mass is located underground at a depth of 500 m with a frequency dependent cavern radius of $\lambda/4$ (Fig. 3.13 (b)). As before, the contribution from the volume vanishes and only the spherical interface between soil and air contributes to the site-based Newtonian noise. This means that in that case the site-based Newtonian noise is the same for any arbitrary test mass depth when the cavern is spherical. The surface integral is a representation of the displacement flux through the surface and due to the absence of a density gradient, this surface integral is equal for all cavern radii. The site-based Newtonian noise from the underground cavern is then a factor 2 larger than what is expected for a hemispherical cavern on the surface.

Introducing realistic seismic fields Previously,constant horizontal displacement in a half-space geology was assumed. However, realistic seismic displacement is not constant in depth or distance.

The first step towards the evaluation of our site-based Newtonian noise with realistic seismic fields is to introduce the seismic displacement from a plane Rayleigh wave according to Eq. (3.1.26). The amplitudes of the Rayleigh waves are scaled such that the horizontal displacement on the surface amounts to $1\ \frac{\text{nm}}{\sqrt{\text{Hz}}}$. The geology model is as previously assumed to be a half-space with density $\rho = 2000\ \frac{\text{kg}}{\text{m}^3}$ and has a Rayleigh wave speed of $v_R = 280\ \frac{\text{m}}{\text{s}}$. To facilitate a comparison to the analytical approach, the test mass is located at $h = 0$ m and a frequency dependent, lower cutoff radius of $\lambda_R/4$ is used. The numerical integral is carried out up to a maximum radius of $2\lambda_R$, which is an integration range that comprises more than 90 % of the Newtonian noise on the test mass. For concrete examples of the determination of the integration radius, the reader is referred to Section 5.3 and Section 6.3.

The density gradient from the plane Rayleigh waves across the volume in horizontal and vertical direction results in a contribution of the volume and the soil-to-air interface to our site-based Newtonian noise. The volume contribution dominates the contribution from the interface (see Fig. 3.14 (a)). Since the amplitudes of the Rayleigh waves attenuate quickly with depth, the corresponding Newtonian noise is below Saulson's analytical expectation, which significantly overestimates seismic amplitudes underground.

Next, Newtonian noise is derived from a seismic field that is the response of a vertical excitation of the half-space. The site-based Newtonian noise expression in Eq. (3.4.11) is based on the incoherent sum of Newtonian noise from a large number of sources at various distances and angles with respect to the test mass. As the Newtonian noise on the test mass is calculated individually for each source, it is sufficient for the simplicity of this qualitative comparison to only consider Newtonian noise from excitations with a single source. The seismic field is then derived from the soil response from a vertical source and it therefore comprises surface and body waves, as well as attenuation of seismic amplitudes with distance from the source. As a result, the exact composition of the seismic field depends on the distance from the source.

If the source is at large distance, that is more than $7\lambda_R$ from the integration area, then body waves have mostly attenuated and the surface field consists dominantly of Rayleigh waves (see Fig. 3.14 (b)). Even though the seismic field at the test mass location consists mostly of Rayleigh waves, the amplitudes attenuate with $1/r$ as a function of distance r from the source in the entire integration area. Individual volume and interface Newtonian noise contributions are almost equivalent and are comparable to the analytical expectation. However, they are added coherently (see Eq. (3.4.8)) and our resulting site-based Newtonian noise is less than what is derived for a

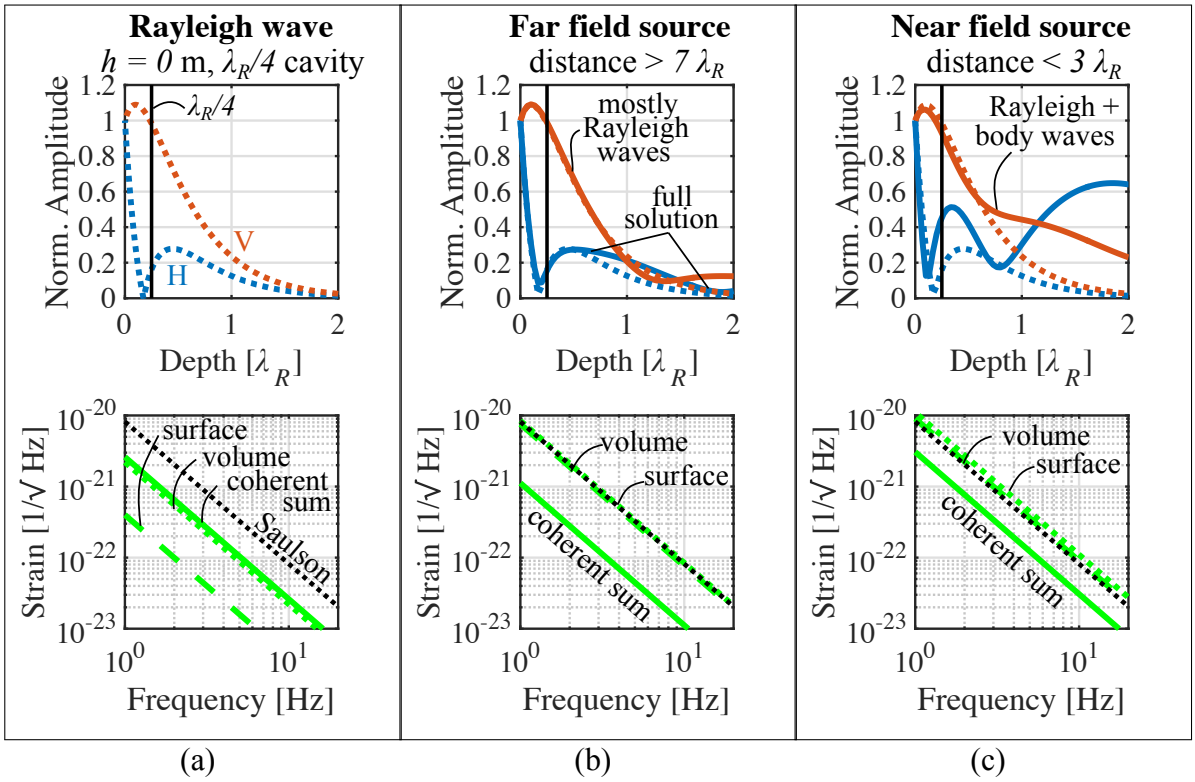

Figure 3.14: *The top panel of each column displays the horizontal (blue) and vertical (red) amplitudes of the seismic field, where the dotted curves indicate Rayleigh wave displacement and the full curves the seismic field from the full solution of the wave equation at* 3 Hz. *The vertical black line indicates* $\lambda_R/4$. *The bottom panel displays Saulson's analytical expectation by a black dashed curve and the horizontal, site-based Newtonian noise in green, where the volume contribution is represented by a dotted curve, the interface contribution by a dashed curve and the coherent sum by a full curve. Furthermore, the test mass is at* $h = 0$ m *and a cutoff radius of* $\lambda_R/4$ *is assumed. (a) For a seismic field that is comprised of plane Rayleigh waves, the contribution of the volume dominates our site-based Newtonian noise. It is less than the analytical expectation due to the attenuation of wave amplitudes with depth. (b) For a seismic field from a far field source excitation, the seismic field consists mainly of Rayleigh waves. As these waves also attenuate with distance from the source, our site-based Newtonian noise decreases with respect to the seismic field from a plane Rayleigh wave. Note that even though the individual volume and surface contributions are in the range of the analytical expectation, they are added coherently and thus can lead to a reduction in Newtonian noise. (c) For a seismic field from a near field source the seismic field comprises a superposition of body and surface waves. This leads to an increase of subsurface amplitudes in the seismic field and thus to a higher site-based Newtonian noise than from a far away source.*

plane Rayleigh wave.

A source close to the integration area, that is within a distance of $3\lambda_R$, leads to a more complex wave field with interfering body and Rayleigh waves and thus to higher subsurface amplitudes compared to the field from a source at large distance (Fig. 3.14 (c)). These higher amplitudes increase the individual contributions of the volume and interface to Newtonian noise. Even though they are added coherently, our site-based Newtonian noise from the nearby source is higher than the expectation from the far excitation due to the additional contribution of body

waves. The exact level of Newtonian noise is dependent on the distance between source and test mass position.

Varying the test mass height in a realistic seismic field It is of interest to qualitatively study site-based Newtonian noise depending on the height of the test mass with a fixed cavern radius in a geology that comprises a wave field with body and surface waves. For this comparison, a half-space geology with density $\rho = 2000\ \frac{\text{kg}}{\text{m}^3}$ and Rayleigh wave speed $v_R = 280\ \frac{\text{m}}{\text{s}}$ is assumed. The seismic field is obtained from a vertical excitation at $5\lambda_R$ from the test mass. The resulting displacement allows Rayleigh waves to be dominant on the surface, but also includes a significant contribution of body waves at shallow depths. The strength of the source is chosen such, that the horizontal displacement at the center of the integration area is $1\ \frac{\text{nm}}{\sqrt{\text{Hz}}}$ across the whole frequency range.

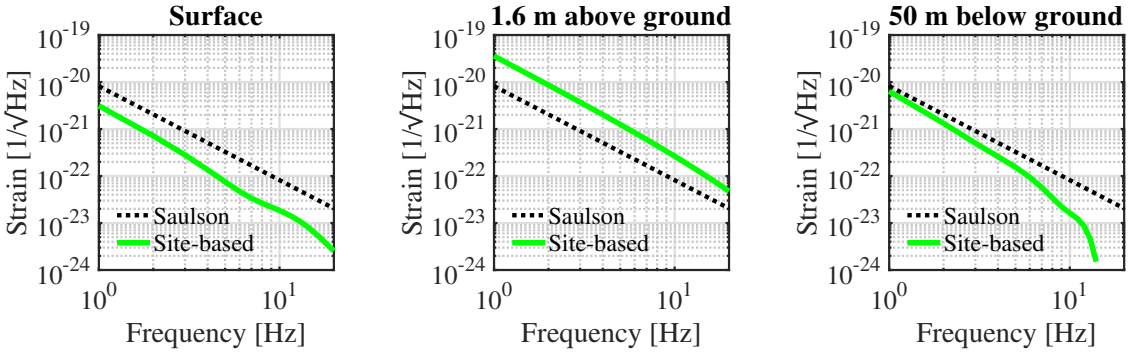

Figure 3.15: *Newtonian noise from Saulson's analytical model for $h = 0$ and $\lambda_R/4$ integration bound is displayed in all three panels with the same dashed black curve. Our site-based Newtonian noise prediction is indicated with a green curve. Left: For a test mass on the surface and a hemispherical cavern with fixed* 10 m *radius, our site-based Newtonian noise is lower than the expectation based on Saulson's model due to the incorporation of amplitude attenuation in the seismic field model. Center: For a test mass* 1.6 m *above ground our site-based Newtonian noise surpasses analytical surface expectations, as the wave field in close vicinity to the test mass is not neglected since in our calculation no spherical cutoff is applied. Right: For a test mass cavern* 50 m *below ground the dominant Rayleigh waves at low frequencies lead to a relatively high site-based Newtonian noise. At frequencies above about* 5 Hz *the Rayleigh waves have attenuated and therefore the site-based Newtonian noise decreases, and is derived from low amplitude body waves.*

For this comparison the test mass is located at three distinct locations. First, the test mass is located on the surface with $h = 0$ m, where a hemispherical cavern of constant radius of 10 m is created around the test mass. A larger fraction of the seismic field in the vicinity of the test mass is included in the volume integral of the site-based Newtonian noise for a fixed cavern radius in comparison to the virtual "cavern" that was created by the frequency dependent cutoff condition. However, the fast attenuation of seismic amplitudes with depth and distance ensures that the site-based Newtonian noise remains below the analytical expectation (Fig. 3.15, left panel). At high frequencies, where Rayleigh wavelengths become smaller than the cavern radius, our site-based Newtonian noise is more strongly suppressed than at low frequencies with respect to the Newtonian noise based on Saulson's analytical expectation.

Second, the test mass is placed at a height of 1.6 m above the ground, which is the same height as the test masses at Advanced Virgo. The test mass height serves as a natural lower cutoff radius for the numerical integral and no additional cutoff from a spherical cavern has been considered. The resulting site-based Newtonian noise therefore does not neglect any seismic displacement in the vicinity of the test mass and the result surpasses the surface Newtonian noise estimates (Fig. 3.15, central panel). The exact noise level depends on the test mass height and decreases with increasing distance from the surface.

The third location of the test mass is at a depth of 50 m, where a fixed cavern radius of 10 m serves as lower integration bound. At this depth the test mass is fully emerged in Rayleigh waves up to a frequency of about 5 Hz and as a result our corresponding site-based Newtonian noise almost reaches the analytical Newtonian noise expectations (Fig. 3.15, right panel). At higher frequencies the Rayleigh waves have attenuated at the depth of the test mass and the wave field consists of body waves. Therefore, our resulting site-based Newtonian noise decreases fast with increasing frequency. For a stronger overall attenuation of Newtonian noise the underground test mass has to be moved to greater depths, be located in a geology with short surface wavelengths or be located in a layered geology where a large fraction of the seismic amplitudes are confined to the surface.

Not only the seismic field and depth of the test mass, but also the cavern shape has influence on our site-based Newtonian noise estimate for an underground detector. For a qualitative study, that neglects scattering of seismic waves on cavity walls, the cavern radius of the test mass at 50 m depth has been successively increased from 5 m to 45 m (see Fig. 3.16). Even though the increasing cavern size suppresses Rayleigh wave amplitudes that would be within the cavern volume below 5 Hz, the higher amplitudes interacting with the larger cavern surface lead to a site-based Newtonian noise that increases with increasing cavern radius. A maximum is reached at 3 Hz, where the cavern diameter is equal to the Rayleigh wavelength. Here, the motion of the cavity wall is coherent in the same direction, which leads to a peak in Newtonian noise. At high frequencies, the waves in close vicinity to the test mass are low-amplitude body waves. Their slowly changing amplitudes cannot compensate for the increasing suppression of nearby seismic displacements as the cavern radius increases and as a result leads to a stronger suppression of our site-specific Newtonian noise at high frequencies. Similar to the maximum at 3 Hz, an increase in Newtonian noise is observed around 18 Hz. Here, the cavern radius is of the order of the P-wavelength, the largest underground wavelength. It is clear that all of these factors depend on

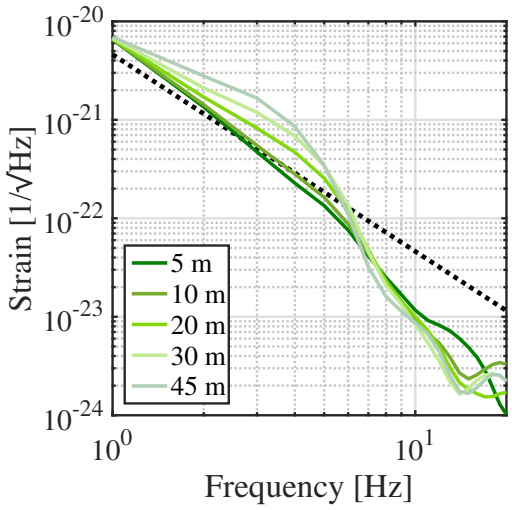

Figure 3.16: *Site-based Newtonian noise for a test mass at* 50 m *depth for a cavern radius that increases from* 5 *to* 45 m. *As the cavern radius increases, Newtonian noise below* 5 Hz *increases as well, while Newtonian noise at high frequencies decreases. The expectation derived from Saulson's analytical model is depicted with a dashed black curve.*

the local geology, source distribution, seismic field, test mass location and cavern shape and for more insight it will be necessary to study specific examples.

Limitations and possible improvements of the site-based model

Further improvements in the modeling approach of the site-based model are possible. First, a detailed seismic study of the detector site should be conducted to obtain knowledge of the three-dimensional subsurface structure, the mechanism and location of the main seismic sources, as well as PSD and correlation measurements on the surface and underground during longterm periods of at least one year. The geology in the site-based model can be improved by evolving the horizontally layered structure towards a more complex, three-dimensional subsurface composition that encompasses for example fault lines and inclining layers. This migration will require the use of alternative numerical solving software, for instance SOFI3D [131]. Furthermore, the current model derives seismic displacement only from vertical excitations. Including horizontal excitations will improve the agreement between measurement and model at low frequencies, especially if the seismic sources are near the test masses. Far away underground sources will allow to model the so called body wave background, which is not negligible at high frequencies at subsurface detectors sites. In addition, studies for subsurface detectors should move beyond spherical caverns and are advised to investigate the effect of arbitrary cavern shapes and sizes on the Newtonian noise level. It should be noted that in this work the cavern is considered by subtracting the Newtonian noise that is derived within a hypothetical cavern area from the Newtonian noise that is derived if no cavern would be present. Future studies are advised to dedicate time to the investigation of cavern wall motion and its effect on Newtonian noise. As this motion occurs on an interface between soil and air it is potentially non-negligible and its influence is yet to be understood. These factors will improve the agreement between measurement and model output and will lead to an enhanced understanding of site-based Newtonian noise.

Summary

The comparisons shown in this section demonstrate that it is necessary for improved, site-based Newtonian noise estimates at surface and underground detectors to move past a model that is based on Saulson's analytical approach model of Eq. (3.5.2). Our site-based Newtonian noise model is derived from a seismic field that comprises body and surface waves. This seismic field depends on the detector specific geology such as subsurface material composition and the local source distribution. Carrying out a numerical Newtonian noise integration that includes contributions from within the integration volume, from interfaces between subsurface layers and from the boundaries between soil and air is crucial for precise modeling. Furthermore, the test mass location needs to be taken into consideration as well as the cavern geometry. All these parameters depend on a specific detector site and therefore this approach can be used to derive site-based Newtonian noise at various locations of gravitational wave detectors. For our site-based Newtonian noise estimate for Advanced Virgo the reader is referred to Chapter 5 and for our site-based Newtonian noise estimate for an underground detector at the Belgian-German-Dutch Einstein Telescope candidate site in Limburg the reader is referred to Chapter 6.

Chapter 4

Seismic array studies

Seismology is a relatively young field of science that was born in the 1850s with the goal to study the origins and mechanisms of earthquakes [132]. This quickly led to the understanding of soil as an elastic medium, which allowed to identify the tectonic plates and Earth's structural composition as crust, mantel and core. Since then large efforts, also driven by the oil and gas industry, have been made to develop efficient methods to characterize Earth's typical vibrations and crustal composition.

One of the most prominent seismic measurement techniques, as it is non-invasive, cost-efficient and flexible in design choice, is the deployment of large surface arrays of seismic sensors. The following section will first explore how ambient noise, recorded with a dedicated network of seismic sensors, can lead to an understanding of local seismic noise sources and the composition of underground structures. The performance of a sensor network depends on the quality of its individual elements. The development of standalone seismic sensors by Nikhef's spinoff company Innoseis [133] has been motivated to facilitate the deployment of flexible array geometries for the seismic characterization of gravitational wave detector sites. In the course of this work the performance of these sensors has been validated and the results are presented in the second part of this section.

4.1 Ambient seismic noise

Ambient seismic noise is defined as ground motion which is continuously present irrespective of location. It therefore does not include abrupt motion such as earthquakes. During a seismic campaign of several years, Peterson aimed to characterize the ambient seismic noise level on a global scale [134]. During this study, seismic noise was simultaneously measured at in total 75 seismic stations all across the globe. The stations were situated in various types of rock geology with measurement locations at the surface, in subsurface caverns and in boreholes, reaching to depths of 340 m. From each measurement station a representative power spectral density during seismically quiet and noisy conditions has been selected (Fig. 4.1). The upper bound, the *new high noise model* (NHNM), represents an average of high background noise power, and the lower bound, the *new low noise model* (NLNM), represents an average of low background noise power. Both, the NHNM and the NLNM are up to today used as standard reference for the comparison of seismic spectra in the seismology and exploration geophysics community.

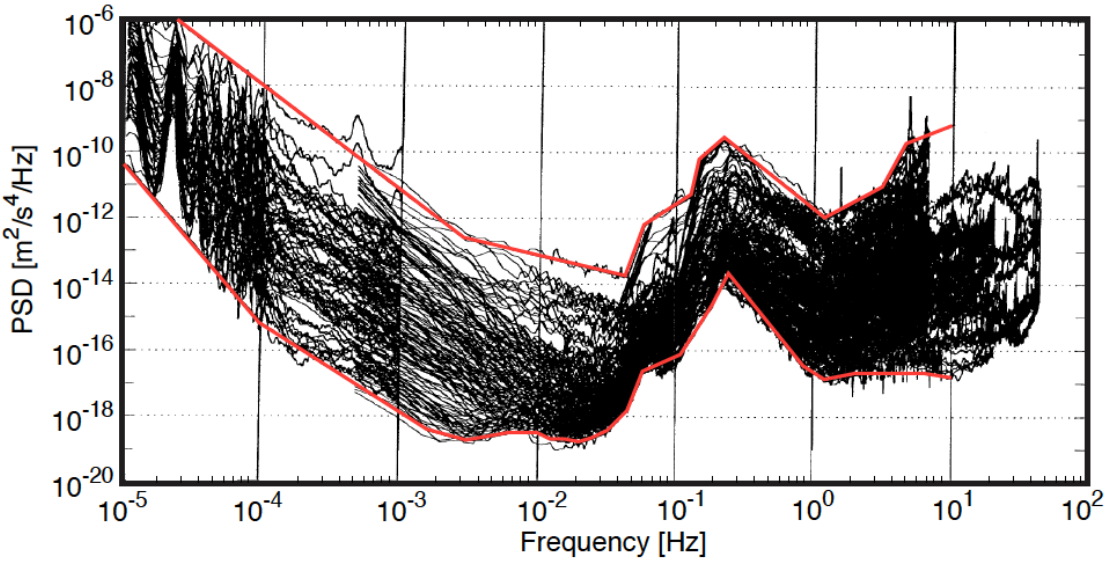

Figure 4.1: *Seismic spectra from* 75 m*easurement stations that were recorded during a world-wide, ambient noise measurement campaign. The upper and lower bound (red) correspond to the new high and low noise model, respectively, which are a standard reference for comparing seismic spectra. Figure taken from [45] and adapted from [134].*

The sources of ambient seismic noise can be grouped into three categories, depending on their frequency range:

- At frequencies below 1 mHz, seismic motion is attributed to tidal effects due to the Earth's rotation relative to the Moon with a period of 12 h. In a range between 2 and 7 mHz, noise originates from the free oscillation modes of the Earth, referred to as the *hum*. The origin of the hum is not fully understood, but current research points towards atmospheric turbulences [135] or ocean waves [136]. Between 7 to 30 mHz the noise consists of large wavelength Rayleigh waves that travel long distances across the globe. Their origin is not understood yet and a topic of ongoing research [137].

- In the low frequency range from 30 mHz to 1 Hz, seismic noise is attributed to interactions between oceanic waves and the ocean ground, referred to as *microseismic activity*. The primary peak around 60 mHz originates from ocean waves transferring energy to the soil in shallow waters close the shore line. The secondary peak at twice the frequency is due to the same interaction with the ground, but of incoming and outgoing waves that interfere to a standing wave at about 120 mHz. Microseismic activity from the ocean is dominant, but for measurement sites in the vicinity of large lakes or inland seas, waves generated by storms or even ship traffic can interact with the soil and contribute to local low frequency spectra. In Europe, microseismic activity is mainly attributed to the activity of the northern Atlantic Ocean [138]. However, spectra taken at Italian sites exhibit an additional peak at 0.5 Hz, which results from the activity of the Mediterranean Sea [139]. Even though these low frequencies are not part of the detection band of gravitational wave detectors, they influence the longterm stability of the detector. To achieve high duty cycles, large parts of the control of these detectors is therefore dedicated to keep the detector stable below 1 Hz.

- At frequencies above 1 Hz, seismic noise can be due to anthropogenic activity and atmospheric turbulences, which are local phenomena. Anthropogenic noise is created by human activity such as car traffic or agricultural activity. It shows characteristic, diurnal patterns with large spectral power during day- and low power during night time. Atmospheric conditions such as storms induce noise by shaking buildings or trees, which in turn transfer the vibrations into the soil. As the frequency band of interest for gravitational wave detectors lies above 1 Hz, local anthropogenic and atmospheric activity characterizes the seismic noise level of a detector site [140, 141].

4.2 Passive seismic arrays and beam forming

Large networks of seismic arrays that record ambient seismic noise allow to determine information about the local seismic source distribution and the characteristic subsurface composition of the soil. By measuring the velocity and angle of incidence of seismic waves, approximate source locations can be identified with beam forming. A byproduct of beam forming is the dispersion curve, which can be used to derive a model of the subsurface layer and material composition with an inversion algorithm. These techniques are briefly discussed in the following section.

Surface information: beam forming Surface waves are a result of body waves interacting with the surface of the soil (Fig. 4.2, left panel) [142]. If the body wave travels with a speed $v_{body} = \frac{\Delta s}{\Delta t}$, where $\Delta t = t_2 - t_1$, and if it is incident with an angle α with respect to the vertical axis such that $\Delta s = \Delta x \sin\alpha$, then

$$p = v_{surface}^{-1} = \frac{\Delta t}{\Delta x} = \frac{\sin\alpha}{v_{body}}, \tag{4.2.1}$$

where p denotes the magnitude of the *slowness*. The slowness corresponds to the horizontal component of the inverse body wave speed. It is parallel to the surface and therefore equivalent

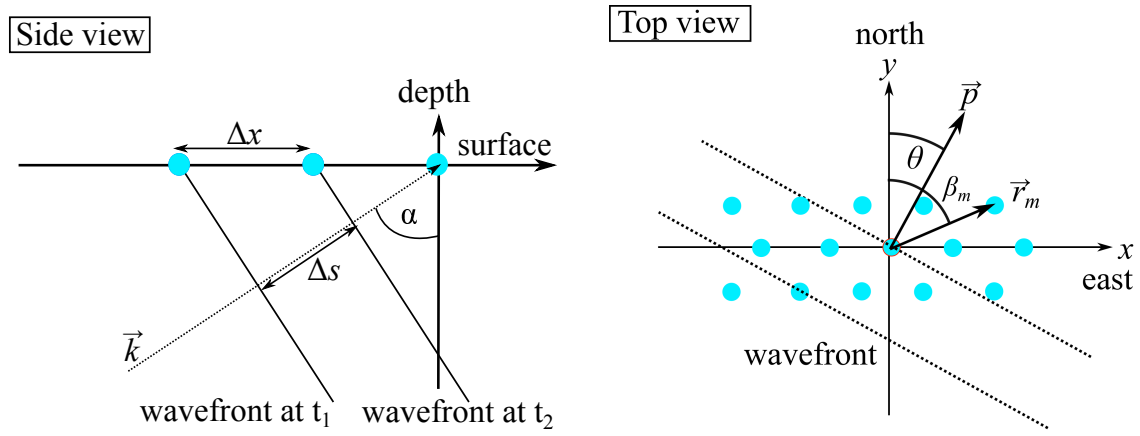

Figure 4.2: *Left: The body wave is incident on the surface at an angle α with respect to the vertical axis. Schematic seismic measurement stations are indicated with blue dots. Right: The back-azimuth angle θ is defined as the angle between north and the propagation direction, which is indicated by the slowness vector $\vec{p}$. The angle between north and the m^{th} seismometer at $\vec{r}_m$ is β_m.*

to the inverse speed of the surface wave that is generated by the body wave. The propagation direction of seismic amplitudes at the surface can then be characterized by two parameters: the *back-azimuth angle* θ which is the angle between north - the positive y-axis - and the propagation direction through the epicenter of the array, and the slowness p (Fig. 4.2, right panel). The slowness vector on the surface is then defined in terms of the back-azimuth angle as

$$\vec{p} = p\ (\sin\theta, \cos\theta). \tag{4.2.2}$$

Consider an array with M seismometers, where the m^{th} seismometer is located at $\vec{r}_m = (x_m, y_m)$ and has an angle β_m with respect to north, and where the center of the coordinate system is placed on the central seismometer of the array. If the central seismometer records a certain signal

$$s_{center}(t) = f(t) + n(t), \tag{4.2.3}$$

where $f(t)$ is the signal from a coherent seismic source and $n(t)$ denotes incoherent noise, then the m^{th} seismometer measures the signal

$$s_m(t) = f(t - \tau_m) + n_m(t),\ \text{with}\ \tau_m = |\vec{r}_m||\vec{p}|\cos(\beta_m - \theta), \tag{4.2.4}$$

where τ_m is the time between the arrival of the surface wave at the central and the m^{th} seismometer.

During data post-processing, the signal of the $M-1$ seismometers is compared to the signal of the central seismometer by applying a time delay τ_m as

$$s_m(t) \rightarrow \tilde{s}_m(t) = f(t) + n_m(t + \tau_m) \tag{4.2.5}$$

and then summing over the shifted signals from all sensors as

$$b(t) = \frac{1}{M}\sum_{m=1}^{M} \tilde{s}_m(t) = f(t) + \frac{1}{M}\sum_{m=1}^{M} n_m(t + \tau_m), \tag{4.2.6}$$

where $b(t)$ represents the average energy per seismometer and is called the beam of the array. Each τ_m and therefore (p, θ)-pair corresponds to a specified direction of incidence and slowness of the wave. By probing many beams, the direction of incidence and the phase velocity of the seismic wave can be identified from the beam that maximizes the signal with respect to the noise. This method of probing (p, θ)-pairs, time-shifting and summing data from M seismometers is called *beam forming*. Eq. (4.2.6) shows that beam forming suppresses incoherent noise, while it enhances the signal from coherent noise sources. The efficiency of noise suppression depends on the number of seismometers M and the signal-to-noise ratio improves with the square root of the number of seismometers as $\sqrt{M}$ [143].

To gain computational efficiency, it is desirable to perform the analysis in the frequency-wave number domain. In this case the time-shift translates to a phase-shift of the Fourier transformed signal as $s_m(\omega) \rightarrow \tilde{s}_m(\omega) = s_m(\omega)e^{-i\omega\tau_m}$. Assuming that after integrating over an sufficient amount of time the incoherent noise term is negligible in comparison to the coherent part of the signal, the total beam power BP of the array is defined as the integral of the array

output over time as

$$\begin{aligned} BP(\vec{k}(\omega,p,\theta)) &= \int_{-\infty}^{\infty} |b(t)|^2 dt \\ &= \frac{1}{2\pi}\int_{-\infty}^{\infty} |f(\omega)|^2 \cdot \left| \frac{1}{M}\sum_{m=1}^{M} e^{-i\omega\tau_m} \right|^2 d\omega \\ &= \frac{1}{2\pi}\int_{-\infty}^{\infty} |f(\omega)|^2 \cdot \left| \mathrm{ARF}(\vec{k}(\omega,p,\theta)) \right|^2 d\omega, \end{aligned} \tag{4.2.7}$$

where in the from the first to the second step Parseval's theorem has been used to move from the time-domain representation $f(t)$ to the frequency-domain representation $f(\omega)$ of the signal, and where

$$\mathrm{ARF}(\vec{k}(\omega,p,\theta)) = \frac{1}{M}\sum_{m=1}^{M} e^{-i\omega\tau_m} = \frac{1}{M}\sum_{m=1}^{M} e^{-i\omega|\vec{r}_m||\vec{p}|\sin\theta} \tag{4.2.8}$$

is the array response function in terms of the slowness p and the back-azimuth angle θ. By calculating the beam power at a fixed frequency ω in a range of slowness-azimuth pairs (p,θ), the maximum value of BP can be determined. It corresponds to the dominant direction of incidence and phase velocity of the seismic waves at frequency ω. Multiple maxima are possible and usually originate from different noise sources of similar relevance.

Underground information: seismic inversion With beam forming, the phase velocity of the surface wave is determined per frequency bin. The relation between velocity and frequency is called the *dispersion curve*, which is characteristic for the subsurface layer composition of the geology beneath the array [107]. In Section 3.1.2 the dispersion curve is obtained by solving the elastodynamic wave equation for a specific, multilayered geology. The inverse problem needs to be solved when analyzing data from a seismic sensor array: from the measured dispersion the subsurface layer composition and material properties have to be retrieved. The set of free parameters that needs to be determined in a horizontally layered geology are the number of layers, their thickness, the density of each layer, the P-and S-wave speeds, and the P- and S-wave damping ratios. In the *inversion analysis*, a theoretical dispersion curve is computed from a fixed set of free parameters with the propagator matrix method [114,115] or the computationally more efficient direct stiffness method [116]. Optimization algorithms then probe a large number of theoretical dispersion curves within the accepted range of the free parameters against the measured dispersion curve. Minimizing the difference between the measured and theoretical dispersion curves leads to an optimized parameter set, that constitutes the subsurface geology model.

As the mathematical details of the inversion analysis are not relevant for this work, the interested reader is referred to [107] for a more elaborate discussion. For the results of the inversion analysis from the Advanced Virgo site see Section 5.1 of this work or [75,144,145] and from the Belgian-German-Dutch Einstein Telescope candidate site in Limburg see Section 6.1 of this work or [74, 75, 146].

4.3 Seismic sensors for array studies

Passive seismic array studies require a large number of seismic sensors. For the sensor networks that are relevant for this work the standalone Innoseis Tremornet nodes (TN-1) shown in Fig. 4.3 have been used [133]. The performance of these sensors has been validated and the results are presented in the following.

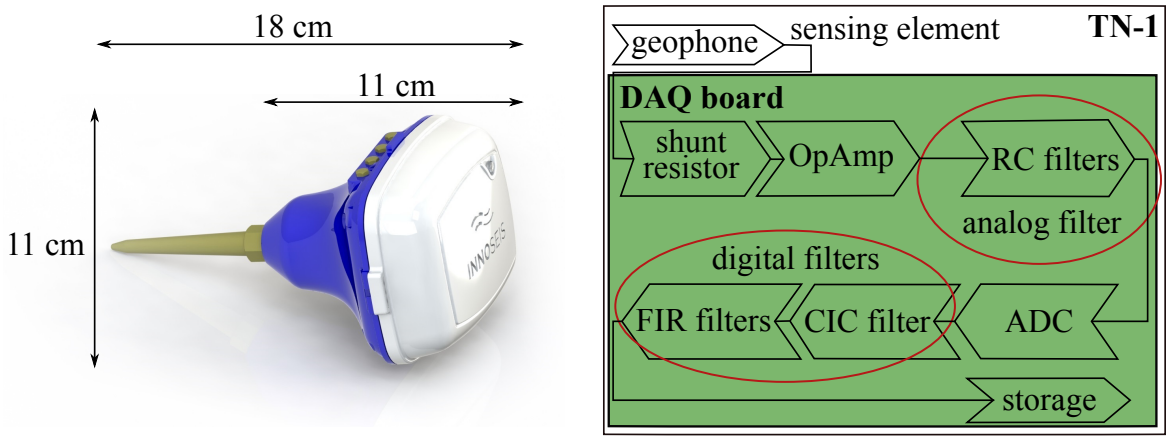

Figure 4.3: *Left: Picture of a TN-1 sensor. The* 7 cm *long spike makes the connection between ground and geophone. Geophone, data acquisition hardware and software as well as the battery are enclosed in the* 11×11 cm *large housing. Right: Schematic of the data acquisition chain of the TN-1 node. The signal from the geophone is amplified and low-pass filtered before it is digitized by the ADC with selectable sampling frequencies. Digital filters optimize storage space and computational effort and reduce signal noise before storing the data on a local storage unit.*

The TN-1 sensor consist of a one-axial, 5 Hz DTCC SOLO (HP305V) geophone, which senses vertical seismic motion. Geophones are standard devices used to measure ground velocity in scientific research, oil exploration, mining and engineering. Ground velocity is converted to a voltage and for optimal damping, the geophone is shunted with a parallel 40 kΩ resistor. The voltage from the geophone is amplified with an ADA4084-2 operational amplifier, where 5 different gain settings are available. Data are taken with an LTC-2378-20 ADC, which has a 20 bit resolution and a reference voltage range of 5 V. To increase the effective resolution of the ADC, the signal is oversampled, where input sampling rates are available from 64 kHz to 512 kHz. To optimize data storage resources, the data are averaged afterwards, where output sampling rates of 250 , 500 or 1000 sps are available. A storage space of 8 GB is available on flash memory, where the data can be read out after the completion of the seismic measurement campaign. Analog filters before and after the amplifier ensure that high frequency signals do not clip the amplifier and attenuate noise from the amplifier itself. Digital filters after the ADC low-pass filter and decimate the signal to reduce noise, optimize storage space and reduce the computational effort. Each TN-1 sensor is powered by a rechargeable 2S2P battery pack. Depending on the selected input and output sampling rate of the ADC, the Tremornet node runs in continuous, standalone operation between about 20 to 70 days.

4.3.1 Geophone performance

Vertical seismic motion is sensed by a geophone, an inertial mass-spring system, consisting of a moving mass m, a coil in a magnetic field B and a spring with stiffness k inside a case (Fig. 4.4,

left panel). The ground displacement is denoted as $x(t)$, while $y(t)$ is the absolute displacement of the mass. The relative displacement of the mass is then $z(t) = y(t) - x(t)$. The following forces are acting on the moving mass

- The weight of the mass $F_0 = mg$, where g is the gravitational acceleration
- The force from the spring with spring constant k, that is stretched under the weight m, is given by $F_1 = -kz(t) - mg$
- Friction and mechanical damping between the mass and the housing results in a force $F_2 = -b\dot{z}(t)$, where b represents the viscous damping factor and the dot denotes the derivative with respect to time
- When the housing moves with respect to the mass due to a ground displacement $x(t)$, the coil moves in the magnetic field B of a magnet that is mounted to the housing. This motion induces an electrical damping force $F_3 = -Bli(t) = -Gi(t)$ where l is the length of the coil wire in the magnetic field and $i(t)$ the current. $G = Bl$ is the sensitivity of the geophone in units $[V/(m/s)]$. It gives information on how the velocity of the ground is translated to a voltage.

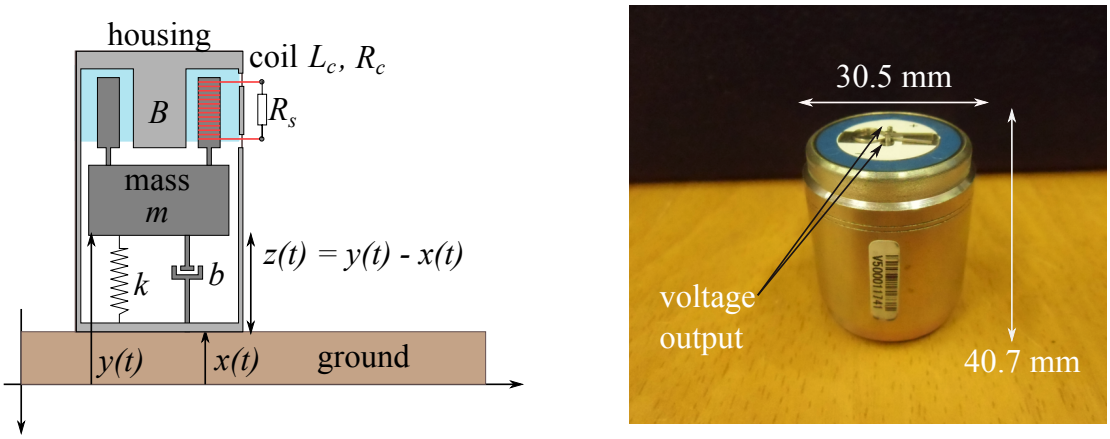

Figure 4.4: *Left: Schematic of a geophone as a mass-spring system with spring constant k, mechanical damping b and a coil with resistance R_c and inductance L_c in a magnetic field B. The absolute ground position is denoted with $x(t)$ and the absolute position of the moving mass with with $y(t)$. Right: DTCC SOLO* 5 Hz *geophone with width and height specification.*

The equation of motion of the moving mass can then be derived from the force equilibrium as

$$\begin{aligned} m\ddot{y}(t) &= \sum_{i=0}^{3} F_i \\ &= mg - (kz(t) + mg) - b\dot{z}(t) - Gi(t) \\ \rightarrow m\ddot{x}(t) &= -kz(t) - b\dot{z}(t) - m\ddot{z}(t) - Gi(t), \end{aligned} \tag{4.3.1}$$

where in the last step the absolute displacement has been replaced by the relative displacement of the mass.

Attached to the moving mass is a coil with resistance R_c and inductance L_c. When the coil is moving in the magnetic field a voltage $V_c = G\dot{z}(t)$ is induced, which is opposed by a voltage $V_{EMF} = -L_c\dot{i}(t)$ due to the electromotive force from the change in current in the system. Taking into account an external shunt resistance R_s the voltage equilibrium is expressed as

$$\begin{aligned}(R_c + R_s)i(t) &= V_c + V_{EMF} \\ &= G\dot{z}(t) - L_c\dot{i}(t),\end{aligned} \tag{4.3.2}$$

where $i(t)$ is the current that emerges from the induced voltage. Taking the Laplace transform (see Section 1.4.1) of Eq. (4.3.1) and Eq. (4.3.2) gives

$$\begin{aligned}ms^2X(s) &= (-k - bs - ms^2)Z(s) - GI(s) \\ GsZ(s) &= (R_c + R_s + L_cs)I(s)\end{aligned} \tag{4.3.3}$$

and solving for $Z(s)$ in the first equation and inserting it into the second gives the transfer function between ground velocity $\dot{X}(s) = sX(s)$ and output voltage $V_{out}(s) = R_sI(s)$ as

$$\begin{aligned}\frac{V_{out}(s)}{sX(s)} &= \left(\frac{-R_smG}{R_s + R_c + L_cs}\right) \cdot \left(\frac{s^2}{ms^2 + (b + \frac{G^2}{R_s+R_c+L_cs})s + k}\right) \\ &= \left(\frac{-R_sG}{R_s + R_c + L_cs}\right) \cdot \left(\frac{s^2}{s^2 + 2\omega_0\zeta s + \omega_0^2}\right),\end{aligned} \tag{4.3.4}$$

which is the transfer function of a damped harmonic oscillator with eigenfrequency $\omega_0^2 = \frac{k}{m}$, and damping $\zeta = \frac{1}{2m\omega_0}(b + \frac{G^2}{R_s+R_c+L_cs})$. By adjusting the external shunt resistance R_s the damping can be used to re-shape the frequency response of the sensor. A geophone with a high shunt resistance will oscillate for a certain amount of time when subjected to an impulse. The number of oscillations can be damped by decreasing the shunt resistance down to a critical damping after which the coil does not oscillate anymore. Figure 4.5, left panel, shows the geophone response depending on the damping. Above the resonance frequency the response is flat in

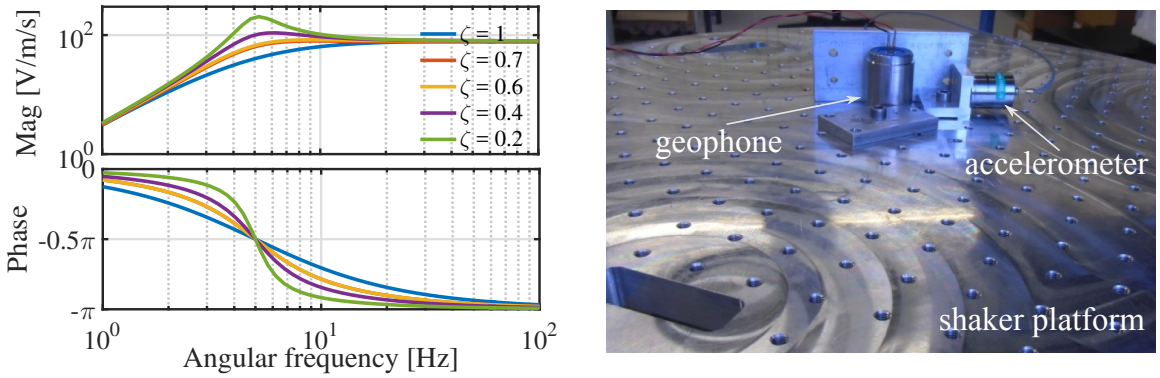

Figure 4.5: *Left: Frequency response in magnitude and phase of a geophone for a range of damping factors. The optimal working point in terms of flat frequency response and minimized amplitude distortion is for a damping close to $\zeta = 0.7$. Right: A vertical geophone is mounted on a horizontal shaker platform to measure the cross-axis coupling. The horizontal motion of the platform is recorded with an accelerometer.*

ground velocity. For a damping of $\zeta = 0.7$ the flat range of the response is slightly extended to lower frequencies. A damping in the range of 70 % of the critical damping is considered the optimal damping for a geophone in terms of frequency response and minimal amplitude distortion [147].

Parameter	Specification	Measurement ($R_s = \infty$)	Measurement ($R_s = 40\ k\Omega$)
Resonance frequency	(5.0 ± 0.4) Hz	(4.9 ± 0.1) Hz	(4.9 ± 0.1) Hz
Damping	0.60 ± 0.05 (open)	0.617 ± 0.01	0.730 ± 0.01
Coil resistance	$(1850 \pm 93)\ \Omega$	$(1873.3 \pm 9)\ \Omega$	$(1790.4 \pm 9)\ \Omega$
Sensitivity	$(80 \pm 4)\ \frac{\text{V}}{\text{m/s}}$	$(80.3 \pm 0.7)\ \frac{\text{V}}{\text{m/s}}$	$(77.1 \pm 0.7)\ \frac{\text{V}}{\text{m/s}}$
Moving mass	22.6 g	–	–

Table 4.3.1: *Selected specifications of the DTCC SOLO* 5 Hz *(HP305V) geophone [148] and the result of measurements averaged over* 60 *geophones in open circuit ($R_s = \infty$) and with a shunt resistor as installed in the Tremornet DAQ board ($R_s = 40\ k\Omega$). The measured parameters are in range with the specifications.*

For a list of selected specifications of the DTCC SOLO 5 Hz (HP305V) geophone employed in the Tremornet sensor, the reader is referred to Table 4.3.1. If not specified otherwise, it is usually assumed that the inductance L_c is small, in the order of a few Henry. This means that sL_c is very small in comparison to R_s in the frequency range of interest and therefore it can be neglected. To cross-check the performance of the geophones the Checkmate Geophone Tester from Infinity Seismic [149] was used. By applying a known voltage impulse to the geophone, the Tester measures geophone parameters such as resonance frequency, damping, coil resistance and sensitivity. These parameters were measured for 60 geophones with open circuit ($R_s = \infty$) and 60 geophones with a shunt resistor as installed in the Tremornet DAQ board ($R_s = 40\ k\Omega$). All geophone parameters were found to be within the range of specifications.

Another important specification is the cross-axis coupling which should not be larger than 1%. The cross-axis coupling specifies the amount by which horizontal motion excites the natural vertical motion of the geophone. The cross-axis coupling of 30 geophones has been measured by mounting them on a horizontal shaker platform, which has been driven with a 12 Hz sine wave at $5\ \text{V}_{\text{pp}}$ (Fig. 4.5, right panel). The horizontal motion of the platform has been recorded with a 731-207 Wilcoxon accelerometer [150]. Coincident data of the geophone and the accelerometer were acquired with a Keysight 35670A Signal Analyzer [151], where a Hanning window with 50 % overlap was used to calculate the power spectral density (PSD) of the signal, which was averaged over 81 measurements. The percentage of cross-axis coupling is calculated by dividing the PSD of the geophone by the PSD of the accelerometer at 12 Hz, where care has to be taken that the data in terms of ground acceleration from the accelerometer are converted to a velocity in order to be comparable to the geophone. The resulting cross-axis coupling is (0.5 ± 0.2) %, which is well below the requirement.

4.3.2 Electronic noise

Three main noise sources contribute to the electronic noise of the DAQ board of the Tremornet node: Johnson noise from the resistors in the circuit, noise from the operational amplifier (OpAmp) and ADC quantization noise.

Johnson noise

Johnson noise is attributed to thermal noise of resistors in the network. For the electronic noise measurements, the geophone is disconnected and replaced with a resistor of the same resistance R_c as the geophone. On the DAQ board, before the OpAmp, a shunt resistor of $R_s = 40\,\text{k}\Omega$ is installed in parallel to the geophone. The one sided noise power spectral density of the Johnson noise per 1 Hz bandwidth is then

$$J_n = 4k_BTR\ [\text{V}^2/\text{Hz}], \tag{4.3.5}$$

where k_B is the Boltzmann constant, T the temperature, and R the resistance. As the voltage of the geophone is measured across the shunt resistor, R_c and R_s are as if in parallel. Their combined resistance is $R = \frac{R_sR_c}{R_s+R_c}$, which results in a Johnson noise of $J_n = 2.8 \cdot 10^{-17}\ \text{V}^2/\text{Hz}$.

OpAmp noise

OpAmp noise consists of voltage and current noise, both being uncorrelated noise sources. These noise densities are flat in frequency and what needs to be taken into account at low frequencies is the additional $1/f$-noise. The cross-over between flat and $1/f$-noise, the so called corner frequency, varies between the noise sources. The flat voltage noise of the ADA4084-2 OpAmp amounts to $V_0 = 3.9\,\text{nV}/\sqrt{\text{Hz}}$ with a corner frequency at $f_{c,v} = 6$ Hz, while the current noise is specified as $I_0 = 0.55\,\text{pA}/\sqrt{\text{Hz}}$ and has its corner frequency at $f_{c,i} = 35$ Hz [152]. The individual noise powers of voltage and current noise are then [153]

$$\begin{aligned} \tilde{v}_n^2 &= V_0^2(\frac{f_{c,v}}{f} + 1)\ [\text{V}^2/\text{Hz}], \\ \tilde{i}_n^2 &= I_0^2(\frac{f_{c,i}}{f} + 1)\ [\text{A}^2/\text{Hz}]. \end{aligned} \tag{4.3.6}$$

Quantization noise

Digitizing a signal with an ADC adds quantization noise to the input signal. Quantization noise is information loss, as the ADC maps a continuous signal onto a discrete set of digital points. It is therefore connected to the properties of the ADC such as reference voltage V_{ref} and number of bits N. The *dynamic range* of an ADC, also called the signal-to-noise ratio, is defined as the ratio between largest and smallest signal that can be measured. The minimum signal change that can be recorded, the *least significant bit* (LSB), is calculated as

$$LSB = \frac{2V_{ref}}{2^N}, \tag{4.3.7}$$

where 2^N corresponds to the number of digitization levels the input signal is mapped on. The full scale of the ADC is calculated as

$$FS = LSB(2^N - 1), \tag{4.3.8}$$

and as a result the dynamic range (DR) is then

$$\begin{aligned} \text{DR} &= 20 \cdot \log_{10}\left(\frac{FS}{LSB}\right) = 20 \cdot \log_{10}\left(2^N - 1\right) \\ &= 20 \cdot \log_{10}\left(\frac{V_{in}}{e_{rms}}\right), \end{aligned} \tag{4.3.9}$$

where in the last line the signal-to-noise ratio is expressed in terms of the input voltage V_{in} and the mean square error of the quantization noise e_{rms}. The latter can be derived by integrating across one quantization level as [154]

$$e_{rms}^2 = \frac{1}{LSB}\int_{-LSB/2}^{LSB/2} e^2 de = \frac{LSB^2}{12}, \tag{4.3.10}$$

where e is the flat quantization noise. The one-sided quantization noise power spectral density is then defined as (see Section 3.2)

$$D_n = \frac{2e_{rms}^2}{f_s} = \left(\frac{2V_{ref}}{2^N}\right)^2 \frac{1}{6 \cdot f_s}\ [\mathrm{V^2/Hz}], \tag{4.3.11}$$

where f_s denotes the sampling rate of the ADC. Assuming a full scale sine wave that has an RMS amplitude of $V_{ref}/\sqrt{2}$ as input in Eq. (4.3.9), the dynamic range is reformulated as

$$\mathrm{DR} = 20 \cdot \log_{10}\left(\frac{V_{ref}/\sqrt{2}}{LSB \cdot /\sqrt{12}}\right) = 1.76 + N \cdot 6.02\ [\mathrm{dB}], \tag{4.3.12}$$

where the factor $1/\sqrt{2}$ originates from the average of the sine wave. This means that each bit increases the dynamic range by 6.02 dB, which corresponds to 2 digitization levels. The dynamic range can further be increased by oversampling and averaging [155]. If the highest frequency that is of interest is called the Nyquist frequency f_N, then to resolve a signal at this frequency without aliasing one needs to sample at least at twice the Nyquist frequency. Sampling with a rate higher than twice the Nyquist frequency is then referred to as oversampling. The noise power of quantization noise is flat in the frequency domain (see Eq. (4.3.10)) and hence the noise spectral density in Eq. (4.3.11) decreases as the sampling rate is increased (Fig. 4.6, left panel). As a result, the dynamic range increases as the quantization noise decreases. From Eq. (4.3.12) it further follows that oversampling increases the effective number of bits by one

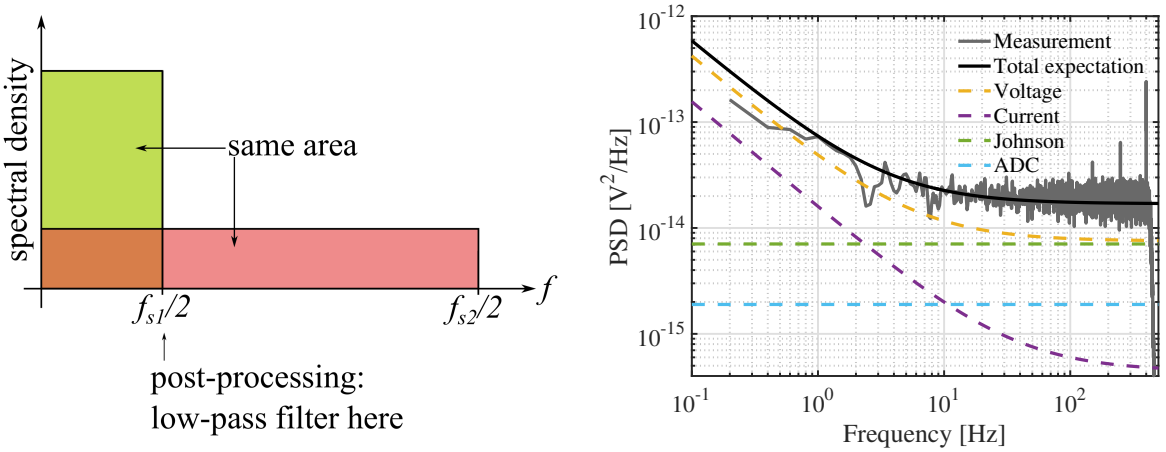

Figure 4.6: *Left: While the noise power is constant (area of the colored blocks), the noise power spectral density decreases when increasing the sampling frequency from f_{s1} to f_{s2}. Right: Expected and measured electronic noise of the TN-1 board for $f_{in} = 512$ kHz, $f_{out} = 1$ kHz and an amplitude gain factor of $G = 16$. Similar comparisons have been made for other output sampling rates and gain factors.*

for each factor of 4 in increased sampling frequency. To optimize storage space and remove unwanted data the signal is low-pass filtered and averaged during post-processing.

The total electronic noise power spectral density is then the incoherent sum of all noise sources as

$$PSD_{el} = G^2 \cdot \left(J_n + 2 \cdot \left((R\tilde{i}_n)^2 + \tilde{v}_n^2 \right) \right) + D_n \ [\mathrm{V}^2/\mathrm{Hz}], \tag{4.3.13}$$

where G represents the amplitude gain of the amplifier and where the current noise has been converted to a voltage via the internal resistance R. Since the noise from the OpAmp is input referred, it needs to be multiplied by the gain as well to obtain the noise at the output and the factor 2 accounts for the two OpAmps, each of them connected to one geophone.

For the electronic noise measurement, the geophone has been disconnected and replaced by a resistor with the same resistance as R_c. The electronic noise has been measured and compared to the expectation that is given by Eq. (4.3.13) for an input sample rate of $f_{in} = 512\,\mathrm{kHz}$ and a range of output sampling rates and gain parameters. It has been shown that expectation and measurement are in good agreement (Fig. 4.6, right panel).

4.3.3 Sensor self-noise

To determine the total noise performance of the TN-1 sensor the geophone needs to be connected to the DAQ board. Noise from the geophone is due to thermal noise of the mechanical system, like Brownian motion in the material of the geophone mass. Its corresponding one-sided noise power spectral density is [156]

$$S_n = 16\pi k_B T \frac{h f_0}{m} \ [(\mathrm{m/s^2})^2/\mathrm{Hz}], \tag{4.3.14}$$

where k_B represents the Boltzmann constant, T the temperature, h the geophone damping, f_0 the resonance frequency and m the moving mass of the geophone. For the expected self-noise of the TN-1 sensor this is added to Eq. (4.3.13) as

$$PSD_{self-noise} = PSD_{el} + G^2 \cdot S_n/(2\pi f)^2 \cdot TF^2(f) \ [\mathrm{V}^2/\mathrm{Hz}], \tag{4.3.15}$$

where the division by $(2\pi f)^2$ converts acceleration to velocity spectral density, and $TF(f)$ is the geophone transfer function as derived in Eq. (4.3.4).

The self-noise of the 5 Hz DTCC SOLO geophone is calculated with Eq. (4.3.14) to be $S_n = 3 \cdot 10^{-17}\ (\mathrm{m/s^2})^2/\mathrm{Hz}$, which is below the low noise level of Peterson's noise model. To measure the sensor self-noise a setup with high seismic isolation or dedicated analysis techniques are required.

High frequency self-noise on the MultiSAS

For frequencies above 5 Hz the self-noise can be measured on the multi-stage seismic attenuation system (MultiSAS) which has been developed at Nikhef for the seismic isolation of optical benches in vacuum for the Advanced Virgo detector [45, 157]. MultiSAS damps seismic motion between the ground and the optical bench, which is suspended from a set of mechanical, passive filters (Fig. 4.7, left panel). Vertical ground motion is attenuated with two cascaded geometric anti-spring systems, while horizontal motion is attenuated through an inverted pendulum followed by two pendulum stages. The angular and translational position of the bench with respect

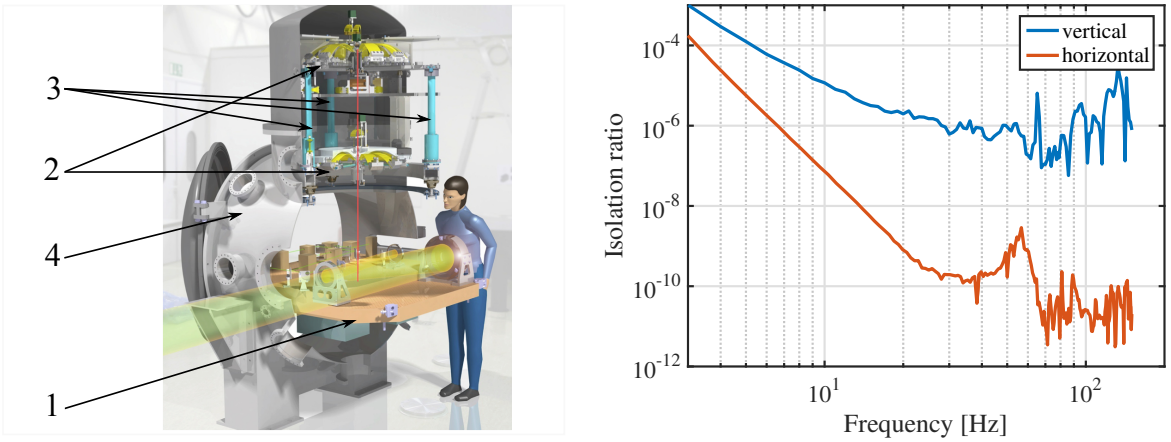

Figure 4.7: *Left: Impression MultiSAS with 1) the suspended optical bench, 2) the geometric anti-spring systems, 3) the (inverted) pendulum and 4) the vacuum chamber. Drawing by Nikhef. Right: MultiSAS transfer function between ground motion and the suspended optical bench. Above* 5 Hz *the amplitude of the ground motion is suppressed by more than four orders of magnitude [157].*

to the isolation system is controlled via an active control scheme [158]. The vertical seismic motion of the optical bench of MultiSAS is suppressed by more than four orders of magnitude in amplitude above 5 Hz (Fig.4.7, right panel). This suppresses local seismic motion efficiently and makes it suitable for the high-frequency measurement of the self-noise of the TN-1 node.

To measure the TN-1 self-noise the sensor has been mounted within a vacuum-tight box on the optical bench of a MultiSAS setup. The vacuum-tight enclosure is necessary as the system is evacuated to $3 \cdot 10^{-5}$ mbar to reduce acoustic coupling between MultiSAS and the suspended bench. The sensor was sampling with an input rate of 512 kHz, an output sampling rate of 500 Hz and with an OpAmp gain of 16. In total 600 s of data were analyzed in the frequency domain and have been averaged over stretches of 2 s length, which have been padded with a Hanning window of 50 % overlap. The self-noise of the TN-1 sensor measured on MultiSAS is compliant with noise expectations above 5 Hz (Fig. 4.8). The peaks at 50 Hz and 150 Hz are due to a pick-up signal from the power line, whereas the residual spikes above 100 Hz are modes of

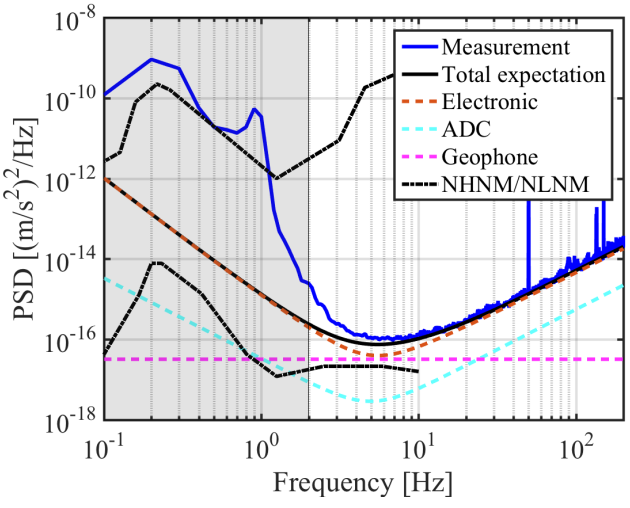

Figure 4.8: *The TN-1 self-noise as measured on MultiSAS for a sensor with* f_{in} = 512 kHz, f_{out} = 500 Hz *and a gain of* 16. *Above* 5 Hz *the measured self-noise is in agreement with the expectation. Spikes at high frequencies originate from power line pick-up and residual modes of elements of the MultiSAS installation.*

the MultiSAS keystone that feeds through the isolation. Below 5 Hz the residual ground motion is not suppressed sufficiently and is therefore present in the sensor.

Low frequency self-noise with a three-channel correlation analysis

To measure the TN-1 self-noise at low frequencies, a seismically more quiet location is required. With a three-channel correlation analysis technique the sensor self-noise can then be estimated without the necessity of an additional seismic isolation system [159]. The three-channel correlation analysis is based on a coherence analysis of the output of three sensors with a common input signal. If three sensors are placed sufficiently close to each other, then it can be assumed that at low frequencies, where wavelengths are large, the sensors record the same ground motion. Assuming that the sensor's in- and output are linearly related, the output Y_i of the i^{th}-sensor can be expressed in the frequency domain as

$$Y_i = X \cdot H_i + N_i, \tag{4.3.16}$$

where X is the common input signal, H_i the transfer function and N_i the internal noise of the sensor. The internal noise between any two sensors, as well as the internal noise and the input signal of each single sensor are uncorrelated. The cross-power spectral density of the i^{th} and the j^{th} sensor is then calculated as

$$P_{ij} = Y_i \cdot Y_j^* = P_{xx} \cdot H_i \cdot H_j^* + N_{ij}, \tag{4.3.17}$$

where $*$ denotes complex conjugation, $P_{xx} = X_i \cdot X_j^*$ is the auto-power spectral density of the input signal and N_{ij} the noise cross-power spectral density (see Section 3.2), which is zero if $i = j$. From the ratio of auto- and cross-power spectral density P_{ii}/P_{ij} of the i^{th} sensor, the noise auto-power spectral density N_{ii} - the self-noise of the sensors- can be derived as

$$N_{ii} = P_{ii} - P_{ij}\frac{P_{ik}}{P_{jk}}, \tag{4.3.18}$$

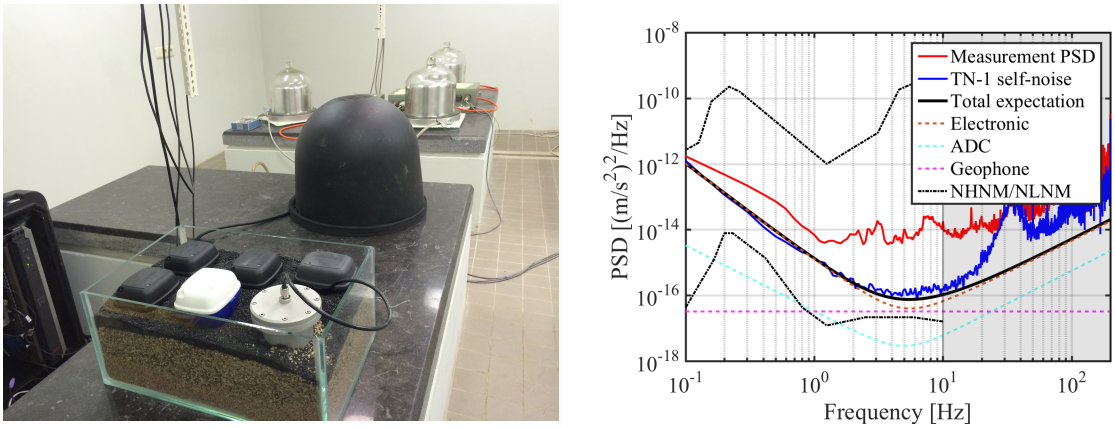

Figure 4.9: *Left: Seismic sensors at the KNMI station at Heimansgroeve in the Netherlands. In the front the TN-1 sensors in the container are visible, in the middle a Trillium 240 broadband seismometer with the black housing for thermal isolation is installed and in the back three permanent KNMI STS-1 seismometers can be seen. Right: The self-noise of the TN-1, deduced from the three-channel correlation analysis, is valid up to about* 10 Hz*, where it is in good agreement with expectations.*

where P_{ii} is the auto-spectral density of the seismic signal measured with the i^{th} sensor. The last term is the same signal, but estimated from the cross-correlations between the sensors. It does not contain information about the individual sensor self-noise, which is what remains after the subtraction.

Selecting a seismically quiet site to perform the measurement for the three-channel correlation analysis ensures that the sensor self-noise does not become negligible in comparison to the ground motion. Due to its quiet conditions the 10 m deep underground laboratory of the Royal Dutch Meteorological Institute (KNMI) at Heimansgroeve in the Netherlands has been selected for the measurement [73, 160]. Here, the floor in the laboratory is directly connected to the underlying bedrock. Three sensors have been placed in a container filled with gravel for ideal transfer of the seismic motion between ground to the geophones (Fig. 4.9, left panel). The sensors sampled data with an output rate of 500 Hz and an OpAmp gain of 16. For the analysis, stretches of 400 s long coincident data were averaged over 10 s long segments, which have been padded with a Hanning window and an overlap of 50 %. The three-channel correlation analysis recovers the TN-1 self-noise from coherent seismic noise that is up to two orders of magnitude higher that the expected self-noise up to about 10 Hz (Fig. 4.9, right panel). For higher frequencies the data of the sensors are not correlated anymore, which prohibits meaningful results.

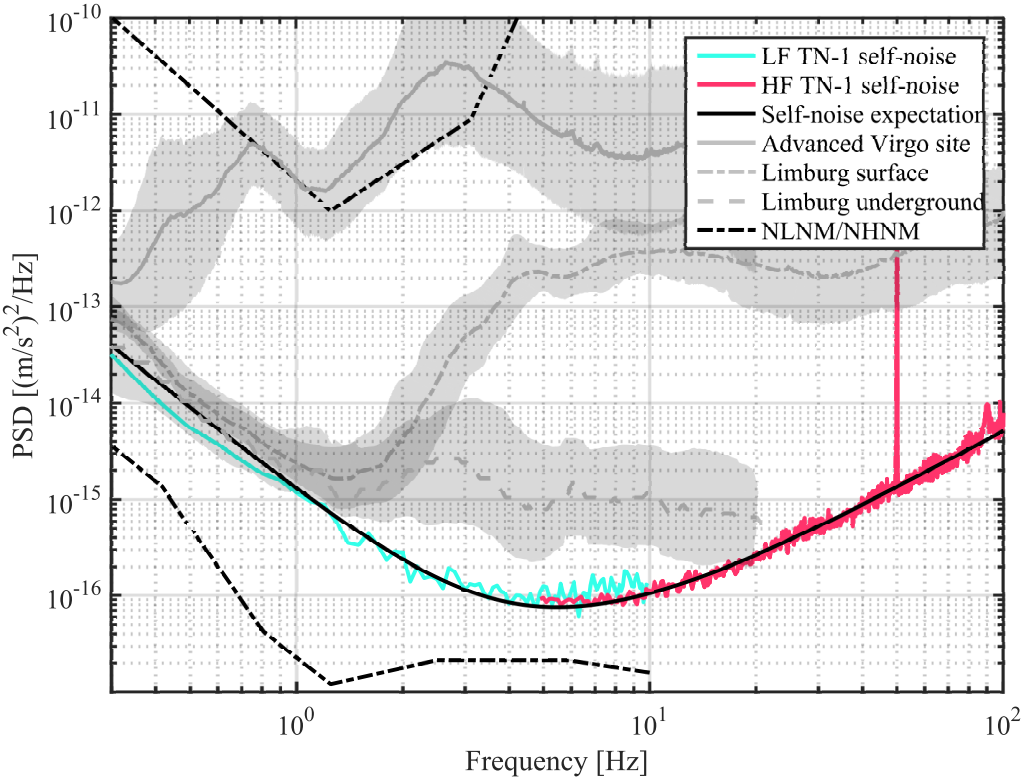

Figure 4.10: *TN-1 low (LF) and high frequency (HF) self-noise together with the site characteristic spectra of the Advanced Virgo site and the surface and underground spectra of the Einstein Telescope candidate site in Limburg. In the frequency band of interest for Newtonian noise above* 1 Hz *the sensor self-noise is well below the site characteristic PSD.*

4.4 Summary

Information about surface and subsurface composition of a site is gained through measurement campaigns with large networks of seismic sensors. Beam forming and inversion of array data allows to retrieve information about subsurface geology and seismic source distribution at the site under investigation. Standalone seismic sensors, such as the TN-1 node, are flexible in use and can be deployed in array structures. However, the sensitivity of the network is only as good as the sensitivity of each single element. The main noise sources in a TN-1 node are electronic noise, ADC noise and the thermal noise of the geophone. The total self-noise of the whole system has been measured for high frequencies at the MultiSAS setup at Nikhef and determined with three-channel correlation analysis at low frequencies. These sensors have been used for seismic characterization studies at the Advanced Virgo site in Italy and the Belgian-German-Dutch Einstein Telescope candidate site in the Netherlands (Fig. 4.10). The sensor self-noise is several orders of magnitude below the characteristic site PSDs in the frequency band of interest for Newtonian noise (>1 Hz) at the Advanced Virgo site and above 2 Hz also at the ET candidate site. This makes the sensor data from these locations suitable for site characterization measurements and Newtonian noise estimates.

Chapter 5

Newtonian noise at Advanced Virgo

Newtonian noise is one of the fundamental noise sources that limit the design sensitivity of ground based gravitational wave detectors below 20 Hz. State of the art seismic and Newtonian noise models rely on simplified geological and seismic conditions. As detectors such as Advanced Virgo and Advanced LIGO are constantly improving their performance and are moving towards their final sensitivity goals, the need for an improved understanding of Newtonian noise contributions at low frequencies arises. This ultimately means that more realistic seismic and Newtonian noise models are required.

This section focuses on the derivation of a seismic and Newtonian noise model that takes into account a wave field from a complete solution of the elastodynamic wave equation together with the characteristic geology and source distribution at EGO, the Advanced Virgo detector site. The first part of the section will describe the seismic study from which all relevant soil parameters, such as subsurface layer composition, layer densities, wave speeds and local distribution of seismic noise sources have been obtained. In the second part of this section, these parameters are used to obtain a solution of the wave equation in such a Virgo-like, horizontally layered geology. By combining the fields of several seismic sources, a model of an ambient seismic field is derived. In the third section, Newtonian noise at the Advanced Virgo detector is calculated from this realistic seismic field model.

5.1 Seismic characterization of the Advanced Virgo site

A passive seismic array study has been performed at the EGO site of the Advanced Virgo gravitational wave detector in Italy between 13 and 29 August 2016 [144, 145]. An array of 64 geophone based TN-1 sensors (see Section 4.3) was deployed in concentric circles, distributed within the 3 km long arms of the Advanced Virgo interferometer with the aim to continuously record ambient seismic noise (Fig. 5.1, left panel). This specific design choice for the network geometry allowed to maximize the array sensitivity at low frequencies and to avoid spatial aliasing at the same time. With a minimum inter-sensor spacing of 6 m in the center of the array and a maximum aperture of 3000 m, the array resolved low frequencies down to 0.2 Hz and high frequencies up to 8 Hz.

The PSD measurement of the array corresponds to the average over the PSDs from all sensors and for the full measurement period. It is referred to as site-characteristic PSD and it represents the average seismic noise level that can ultimately be achieved at the site. Due to high anthropogenic activity, seismic noise at the Virgo site is high in the frequency band of interest for

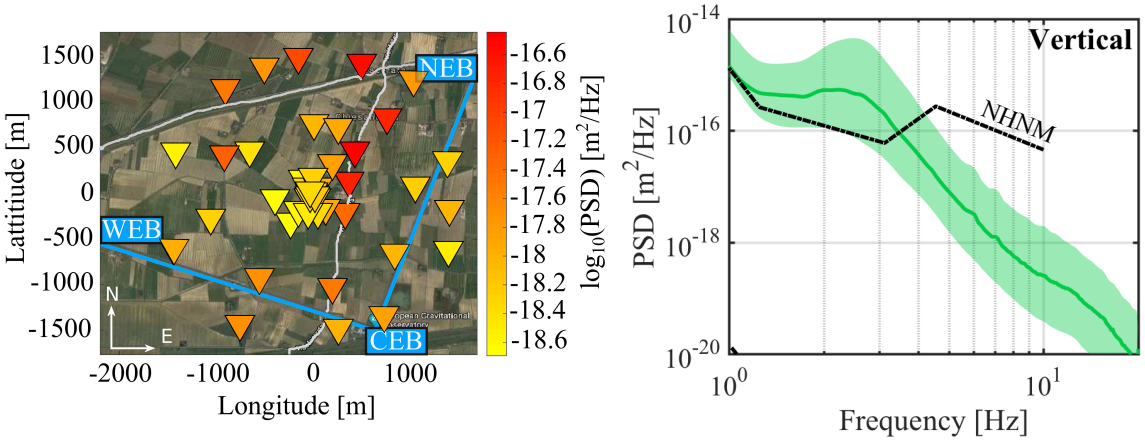

Figure 5.1: *Left: Seismic sensor array layout (triangular markers) within the* 3 km *long Advanced Virgo interferometer arms (blue). The color of the markers displays the average from* 2 *to* 20 Hz *over the mean PSD from the full measurement period of the corresponding sensor. Sensors that record a high PSD are in the vicinity of streets (light grey), bridges and buildings. Right: Vertical mean power spectral density of the site-characteristic PSD. The transparent band indicates the* 10^{th} *and* 90^{th} *percentiles. High anthropogenic activity leads to a high seismic noise level above* 1 Hz.

Newtonian noise below 20 Hz; it even surpasses Peterson's new high noise model below 4 Hz.

Beam forming analysis of the ambient seismic noise at the Virgo site showed that the main noise sources can be grouped into three categories (see Fig. 5.2). At frequencies between 0.2 and 1.5 Hz the seismic noise originates from oceanic microseismic activity of the Mediter-

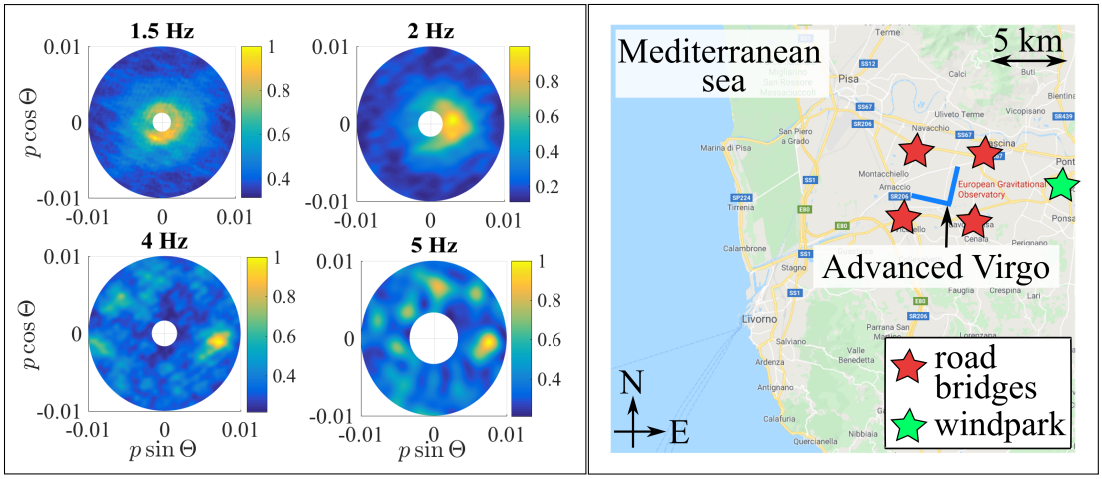

Figure 5.2: *Left: Surface wave direction of incidence for four representative frequencies, where the inverse surface wave velocity is denoted with* p*, the incident angle with* Θ*, measured from the positive* y*-axis (north). The color scale indicates the normalized beam power and the peak corresponds to the dominant noise sources at the given frequency. Below* 1.5 Hz *the noise originates from the Mediterranean sea in the western direction (not shown), from* 1.5 - 4 Hz *noise from road bridges and a wind park is dominant and above* 4 Hz *noise originates from local sources such as a road through the sensor array. Right: Geographical locations of the noise sources in the area of the Advanced Virgo detector.*

ranean Sea, which is located in the western direction from the sensor array. For this analysis the seismic data of the sensor array were correlated to oceanic swell, that has been measured with a buoy that is anchored about 200 km off the coast of Pisa in the north-western direction in the Ligurian sea. As this frequency range is not relevant for Newtonian noise, the corresponding analysis results are not shown here and the reader is referred to [75, 145].

In the frequency band from 1.5 to 4 Hz seismic noise originates from traffic on road bridges and streets of the nearby highway surrounding the sensor array at distances between 1 and 3 km. Correlation between seismic noise at the Advanced Virgo site and traffic on nearby roads has been measured during a dedicated study, where seismic sensors have been placed at the Advanced Virgo Central Building and at five bridge locations in the area [75, 145]. Furthermore, a nearby wind park in the eastern direction has previously been identified as additional noise source in this frequency range [161].

Due to the fast attenuation of surface waves at high frequencies, typically after a few hundred meters, seismic noise above 4 Hz corresponds to human activity and local disturbances such as shaking of buildings during times of high wind activity or traffic on roads through or nearby the sensor array.

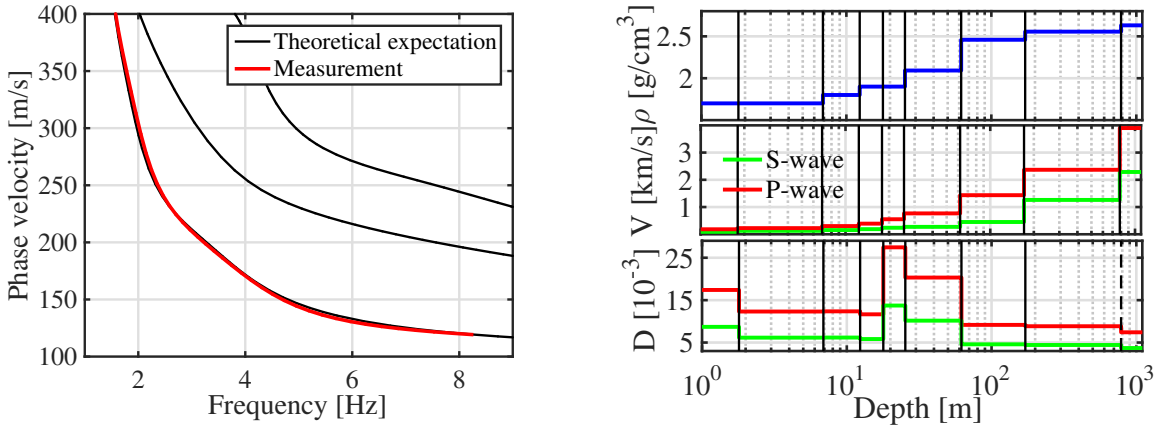

Figure 5.3: *Left: Measured dispersion curve (red) of the surface waves is obtained from the beam forming analysis [75]. The theoretically expected fundamental and higher order mode dispersion curves, based on the soil parameters in the right panel, are depicted in black. Right: From top to bottom, a visualization of density ρ, P- and S-wave speeds V and material damping D for P- and S-waves for the nine layers derived with the inversion method.*

In addition to the identification of local noise sources, the surface wave velocities in terms of the fundamental mode dispersion curve were derived from the beam forming analysis (Fig. 5.3, left panel). This dispersion curve was used to conduct the inversion analysis to a depth greater than 1 km, whereas the subsurface parameter space was confined with results from previous borehole, gravimetric and inversion studies at the Virgo site to shallow depths of 70 m [162]. The inversion was carried out for a nine layer model and the densities of these layers were fixed. In total 60 000 theoretical subsurface models and their corresponding dispersion curves were explored. The damping parameters of each layer were obtained by a similar analysis, where a frequency dependent attenuation coefficient of surface waves has been derived. This attenuation coefficient has been inverted to derive P- and S-wave material damping factors for each layer [75]. The subsurface model that minimizes the misfit between measured and theoretical dispersion is displayed in Fig. 5.3, right panel, and the corresponding parameters are listed in Table 5.1.

Thickness [m]	ρ [kg/m^3]	V_p [m/s]	V_s [m/s]	D_p [10^{-3}]	D_s [10^{-3}]
1.8	1700	183	90	8.7	17.4
5.1	1700	226	127	6.2	12.3
5.5	1800	301	155	6.2	12.4
5.5	1900	390	188	5.8	11.7
7.5	1900	552	240	13.7	27.5
36.6	2092	767	272	10.2	20.3
109.2	2459	1435	451	4.6	9.2
613.8	2556	2368	1261	4.4	8.8
∞	2631	3900	2287	3.7	7.4

Table 5.1: *Material parameters for the nine-layer subsurface model of the geology at the Advanced Virgo site derived with the inversion of the dispersion curve. The parameters are the layer thickness, density ρ, P- and S-wave speed and material damping.*

5.2 Ambient seismic field model

To recreate a representation of the local seismic field that reproduces data as measured with the sensor array at Advanced Virgo in the Newtonian noise integration range, we calculate the response of the Virgo geology given in Table 5.1 to vertical source excitations. The full solution of the wave equation (see Section 3.3) is derived with the direct stiffness method. The corresponding algorithm that solves the elastodynamic wave equation is part of the Matlab Elastodynamics toolbox [117].

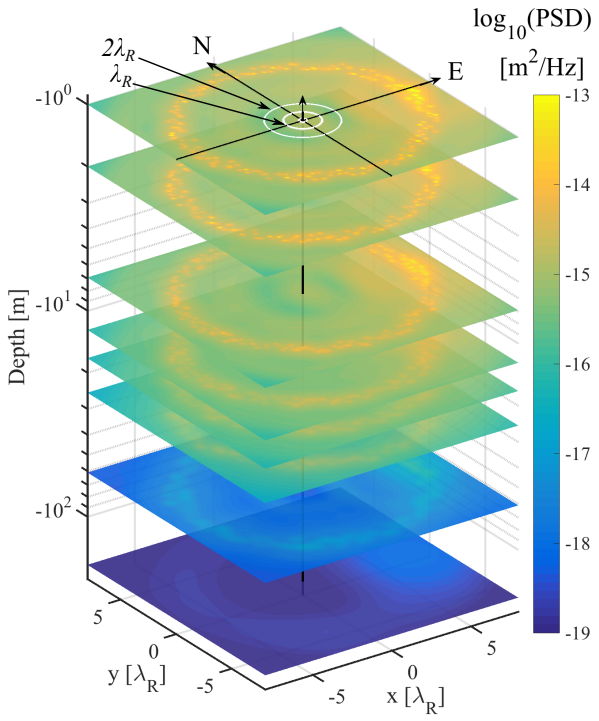

Figure 5.4: *Displacement PSD response to seismic disturbances at the Virgo site down to* 200 m *depth. The local geology has been excited by* 180 *vertical* 3 Hz *sources, which are distributed in a λ_R wide ring about $6\lambda_R$ from the center. Note that the Rayleigh wavelength is* 70 m *at* 3 Hz*. The relative strength of the sources is scaled according to the measured beam power at* 3 Hz *(see Fig. 5.5) and the absolute strength is such that at the center of the coordinate grid the PSD at the Virgo Central Building is reproduced. Each sheet corresponds to the top surface of a new layer and the color scale indicates the PSD. The Newtonian noise integration range around the test mass is indicated in white. It is about λ_R for low and $2\lambda_R$ for high frequencies.*

The ambient seismic field within the Newtonian noise integration range (see Fig. 5.4) is then modeled by incoherently summing over the seismic displacement fields from sources at 180 excitation points (see Eq. (3.3.1)). These excitation points are distributed in a ring of thickness λ_R, which has a radius of several λ_R from the test mass. The distance of the excitation points depends on the frequency and is aimed to reproduce measured horizontal and vertical surface spectra, while remaining consistent with source locations as obtained by beam forming, where sources are at distances greater than 1 km for low and within a few hundred meter of the test mass at high frequencies. Furthermore, the distance of the sources from the receiver grid is sufficiently large for the plane wave assumption to be valid. Each excitation point is randomly placed within a 2° wide segment of the ring.

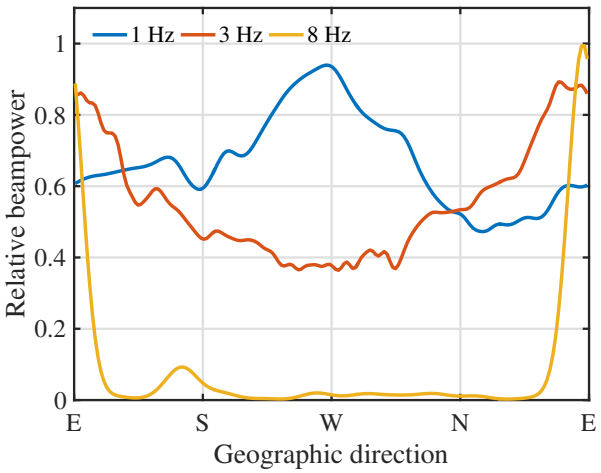

Figure 5.5: *Measured beam power distribution of representative frequencies as used to derive the relative scaling factor. At low frequencies the noise originates from a broad western direction, whereas it moves towards a peak in the eastern direction for high frequencies.*

The frequency band of interest for Newtonian noise is from 1 to 20 Hz. The relative strength of the sources is frequency dependent and has been scaled with the measured beam power in each frequency bin (see Fig. 5.5). Below 1 Hz the noise originates from activity of the Tyrrhenian Sea in the west. In the intermediate frequency band the noise peaks in north-eastern, south-eastern and north-western direction, pointing towards road-bridges at the close-by highway crossings and the wind farm. For frequencies above 4 Hz the noise is very local and originates from the road passing through the sensor array, which is located east of the center of the array. For simulation frequencies above 8 Hz, the maximum frequency the array can resolve, a uniform relative scaling in all azimuth directions has been assumed.

The surface PSD that has been simulated is based on the characteristic PSD of the site, which corresponds to the average of the vertical spectra measured with all sensors from the array study in 2016 during the full measurement period (Fig. 5.1, right panel).

5.2.1 Coherence and correlation

To simulate an ambient seismic field the soil response to 180 source excitations has been calculated. It is assumed that these excitations are incoherent, meaning that the total field is calculated by summing incoherently over the PSD and Newtonian noise contributions of the individual sources (see Section 3.3). For a qualitative test of the response of the geology, the modeled coherence and correlation between two points is compared to measurement results.

The sources are placed at large distances from the test mass, and for simplicity it is assumed that their strength is uniform. The coherence is then obtained from the absolute value and the correlation from the real part of the normalized cross-correlation spectral density as derived in

Section 3.2. A pair of test receivers, with a separation of 35 m and of 800 m, are placed at the center of the geometry. Figure 5.6 shows that the expected correlation and coherence are high at low frequencies and decreases strongly above 1 Hz for a 35 m separation and already above 0.1 Hz for a 800 m separation of the sensors. This behavior is consistent with what has been previously observed at the Virgo site [45]. Due to the nearly uniform distribution and strength of the sources, the correlation of the synthetic data between two receivers is in reasonable agreement with the expected behavior of the Bessel function given in Eq. (3.2.8).

In reality, the assumption of a uniform source distribution is invalid, as the strength of the sources depends on their geographic location and the measured cross-correlation, thus on the orientation of the receiver pair with respect to the source. To reduce this directionality in the measurement, the correlation and coherence have been averaged over all receiver pairs within a 10 % range of the predefined distance of 35 m and 800 m.

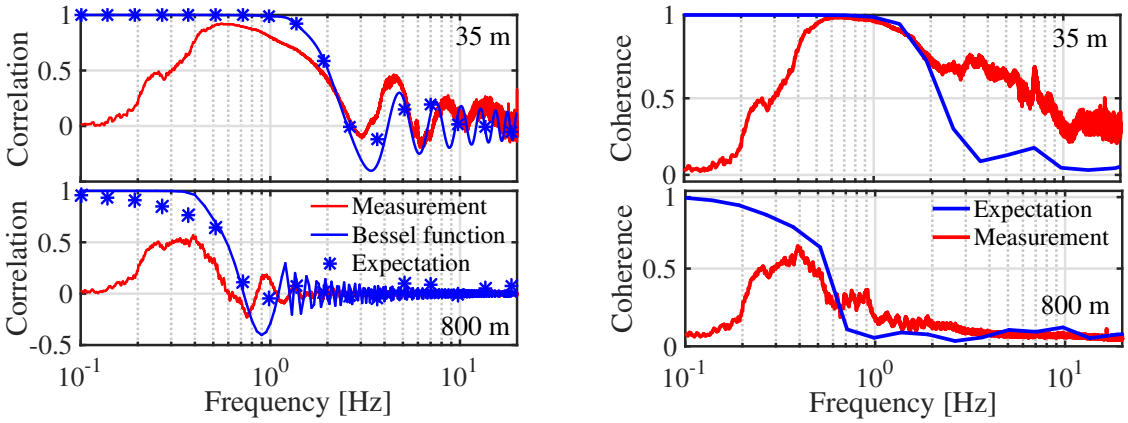

Figure 5.6: *Simulated and measured correlation (left) and coherence (right) between two receivers at short (*35 m*) and long (*800 m*) distance. Qualitatively, measurement and simulation are in good agreement. Deviations below* 0.3 Hz *originate from uncorrelated instrument noise that is not taken into account in the simulation. For short receiver distances the measured result surpasses the simulated coherence due to the presence of local noise sources within the sensor array, which have not been considered in the simulation.*

Qualitatively, measured and expected correlation are in reasonable agreement with each other for short and long receiver distances above 0.3 Hz (Fig. 5.6, left panels). Disagreement below 0.3 Hz is due to uncorrelated instrument noise between the sensors (see Section 4.3). At short distances, the characteristic Bessel function behavior of the correlation is visible and in good agreement with expectations. Deviations may originate from the fact that in reality, noise sources are not uniformly distributed, not of equal strength or may even be located within the sensor array - all factors that lead to a degradation of the Bessel function behavior. For short distances, the coherence from 0.3 to 2 Hz is in good agreement with the measurement results (Fig. 5.6, right panels). Above 2 Hz local seismic noise from a road through the sensor array (see Fig. 5.1, left panel) leads to an enhanced coherence with respect to the expectation from the simulation, where the noise sources are located at great distances outside the sensor array. Previous measurements along the interferometer arms show a short-distance coherence that is comparable to the expectations of this simulation [45] . For large sensor distances, the measured and expected coherence are in reasonable agreement above 0.3 Hz, where seismic noise dominates over uncorrelated sensor noise.

As simulated and measured coherence and correlation are in reasonable agreement, it can be concluded that the modeled geology is a reasonable approximation of the conditions at the Virgo site.

5.2.2 Beam power and dispersion

For an additional validation of the simulated geology and source distribution, the beam forming analysis has been performed on data from the model. For this analysis the soil has been excited with 180 incoherent sources, where the relative strength of each source was selected according to the measured beam power. The left panel in Fig. 5.7 shows the beam forming of the simulated vertical surface displacement across the whole frequency band. The direction of incidence and the beam power of the modeled source distribution are in reasonable agreement with the measurement, shown in the left panel of Fig. 5.2. As measured, the noise at low frequencies originates from a more uniform direction from west over south to east, while at higher frequencies the main noise contribution originates from the eastern direction.

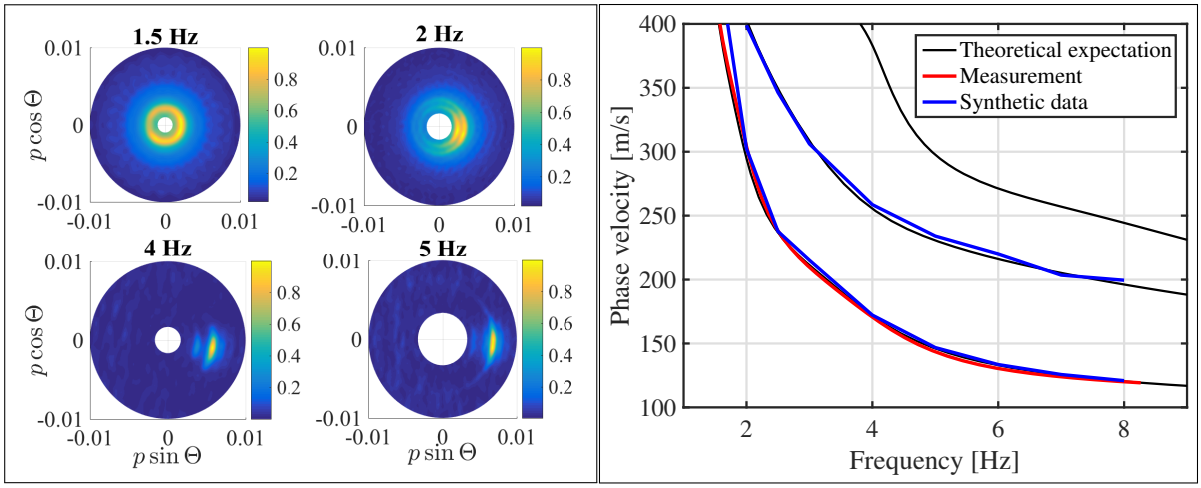

Figure 5.7: *Left: Results from beam forming of simulated surface waves for four representative frequencies, where the inverse velocity is denoted with p, the direction of incidence with θ, measured from the positive y-axis which represents north. The colorbar shows the normalized beam power. Direction of incidence and beam power from beam forming of synthetic data are in fair agreement with the measurement (Fig. 5.2, left panel), except for* 5 Hz *where the sensor array also records local noise sources within the array, which have been neglected in the simulation. Right: Comparison of dispersion curves derived from measured and synthetic data for selected frequencies. Both are in good agreement with the theoretical expectations for the subsurface geology.*

Both data sets, measured and synthetic, recover well the slowness peaks of the fundamental Rayleigh wave mode. Due to the possibility to design the synthetic grid denser and larger than the sensor array, the beam forming of the synthetic data also allowed to recover the first higher order Rayleigh wave mode, which is characterized by a higher velocity than the fundamental mode. Higher order modes can be understood as the constructive interference of transmitted and reflected waves in the layered medium [109]. The specific geometry of the sensor array of the study described in Section 5.1 did not record the higher order mode for two reasons. At frequencies below 4 Hz, the large wavelength of the higher order mode could not be recorded

as the array was limited by its specific aperture and inter-sensor spacing. A different sensor array geometry might have allowed the measurement of the higher order mode, which would have given additional constraints on the soil model during the inversion analysis. At frequencies above 4 Hz the dominant noise sources were in the close vicinity of the array. The short travel distance of the waves to the receivers prohibited a noticeable separation between fundamental and higher order mode in the array data. Finally, overtones will be high in amplitude on the surface in case the subsurface geology exhibits a high velocity contrast at shallow depths - a condition that is not valid in the geology at the Virgo site. This means that even with a suitable array geometry, the amplitude of the overtone may be simply too small to be measured with the seismic sensors at hand.

The dispersion curve has been retrieved from beam forming of the synthetic data. The velocities of the fundamental mode derived from synthetic data are in good agreement with the measured fundamental mode dispersion curve (Fig. 5.7, right panel). Since the first order surface wave velocities agree as well with the expected theoretical dispersion curve for this type of medium it can be concluded that the horizontally layered geology model with the corresponding source distribution is a valid representation of the seismic conditions at the Advanced Virgo detector site.

5.2.3 Power spectral density

To reproduce the seismic spectra at the Virgo site, the source strengths are scaled individually with the relative scaling factor according to Eq. (3.3.1) to reproduce the measured beam power of the array and with the absolute scaling factor according to Eq. (3.3.2) such that the measured horizontal and vertical surface PSDs are reproduced by the simulation. Due to the TN-1 sensor characteristics, only data of vertical ground motion have been acquired during the seismic cam-

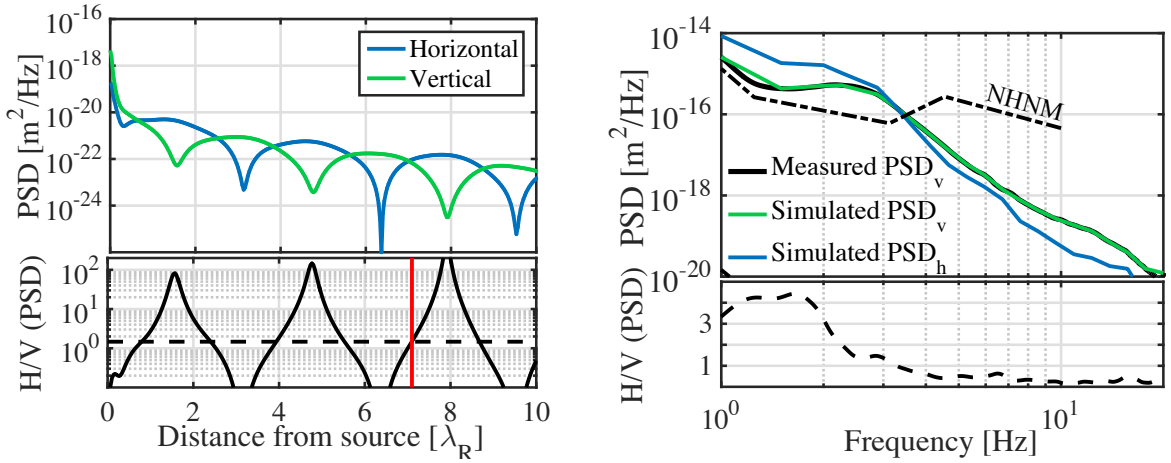

Figure 5.8: *Left: Horizontal and vertical unscaled, simulated displacement PSD of a single* 3 Hz *source together with the expected H/V ratio (black) as a function of distance. The value of the measured H/V ratio at* 3 Hz *is indicated by the horizontal dashed black line and the optimized distance is marked in red. Right: Simulated horizontal and vertical site-characteristic PSD at Advanced Virgo from* 180 *sources that are scaled according to the measured beam power and are located such that the measured H/V ratio [163], see bottom panel, is reproduced at the test mass location. The absolute scaling factor is chosen such that the simulated vertical PSD reproduces the measured vertical PSD. The horizontal PSD follows then from the simulation.*

paign. However, horizontal Newtonian noise, which is the most relevant for Advanced Virgo, is generated by horizontal seismic displacements and therefore knowledge of horizontal seismic spectra at the site is needed to design a model that is a valid representation of the local conditions. This information can be inferred from the ratio of horizontal to vertical PSD. This so called *H/V ratio* is characteristic for a given site, as it depends on the local geology, source mechanisms and distance between source and receiver [113]. Coincident horizontal and vertical spectra of the Virgo site are available from a one year long measurement campaign in 2014 with a single Episensor FBA-EST seismometer [163] and the H/V ratio obtained from these data can be used to reproduce representative horizontal spectra in the simulation.

The expected H/V ratio for a single source can be computed from the simulation and it depends strongly on the distance to the source (Fig. 5.8, left panels). These fluctuations are characteristic for a single source and average out, if many sources are placed in a ring, that varies in thickness, around the test mass. The radius of the ring is then chosen such that at each frequency the measured H/V ratio is reproduced by the model at the location of the test mass. For a given frequency several source distances may reproduce the measured H/V ratio. In this case a distance that is compatible with the noise source locations as indicated by the beam forming analysis is chosen. At low frequencies this is at distances of 1 km or larger, while sources at high frequencies are within a few hundred meters of the test mass. Once the radius of the ring is determined for a given frequency, the distance of the individual sources is allowed to vary within $\lambda_R/2$, thus producing a ring of thickness λ_R of sources around the test mass.

After deriving the optimized distance from the measured H/V ratio for each frequency and scaling the strength of each source according to the beam power distribution with the relative scaling factor according to Eq. (3.3.1), the absolute scaling factor is then derived from the measured vertical PSD, denoted with $\mathrm{PSD_V}$, following Eq. (3.3.2) as

$$m(f) = \mathrm{PSD_V}/|u_v(\vec{x}, f)|^2, \tag{5.2.1}$$

where $|u_v(\vec{x}, f)|^2$ denotes the vertical component of the quadratic sum of the individual responses. The horizontal PSD can then be reconstructed from the measured H/V ratio as

$$|u_H(\vec{x}, f)|^2 = (\mathrm{H/V\ ratio})(f) \cdot |u_v(\vec{x}, f)|^2, \tag{5.2.2}$$

where $|u_h(\vec{x}, f)|^2$ refers to the mean horizontal component of the unscaled PSD. The horizontal and vertical PSDs in the seismic model that have been derived with the measured H/V ratio and vertical PSD are displayed in Fig 5.8, right panel.

5.3 Newtonian noise

Our site-based Newtonian noise at Advanced Virgo is calculated from the full solution of the wave equation according to Eq. (3.4.8), Eq. (3.4.11) and Eq. (3.4.12) in the horizontally layered geology with nine subsurface layers as listed in Table. 5.1. The ambient seismic field model comprises surface and body waves, reflection, transmission and mode conversion of waves at interfaces as well as damping of seismic amplitudes with distance from the source. The strength of the seismic sources is scaled according to the measured beam power distribution and their distance from the test mass is optimized such that the measured ratio of horizontal over vertical PSDs is reproduced by the simulation. The absolute strength of the sources is scaled such that the simulated PSD at the test mass follows the site-characteristic PSD at EGO (see Fig. 5.9,

left panel). The test mass height in the simulation is 1.6 m above the ground, which is the same height as the Virgo test masses [37]. The test mass height further serves as a natural, lower cutoff radius in the Newtonian noise integral. The integral is carried out through Gaussian quadrature, a numerical integration method (see Appendix B).

To increase the computational efficiency, a maximum integration radius is calculated for each frequency. The integration radius is the integration distance after which the cumulative Newtonian noise remains within 10 % from its asymptotic value. Previous studies in homogeneous half-space geologies with Rayleigh waves and surface detectors have shown that an integration radius of $\lambda_R/2$ is sufficient to reach a stable Newtonian noise level [45]. In this model Newtonian noise is calculated as the incoherent sum of the Newtonian noise contributions from the individual seismic sources (see Eq. (3.4.11)). The maximum integration radius at each frequency is then determined from the contribution of a single source by subsequently increasing the integration radius, starting from $0.5\lambda_R$ and reaching up to a distance where fluctuations stay within a small percentage of the asymptotic value. Figure 5.9, right panel, shows that at low frequencies an integration radius of λ_R or even less is sufficient. Higher frequencies require a larger integration radius of up to $2\lambda_R$, because at these high frequencies the wavelengths of the Rayleigh waves are short and therefore they attenuate fast. As a result, nearby body waves contribute to Newtonian noise as well and their larger wavelengths lead to a higher maximum integration radius.

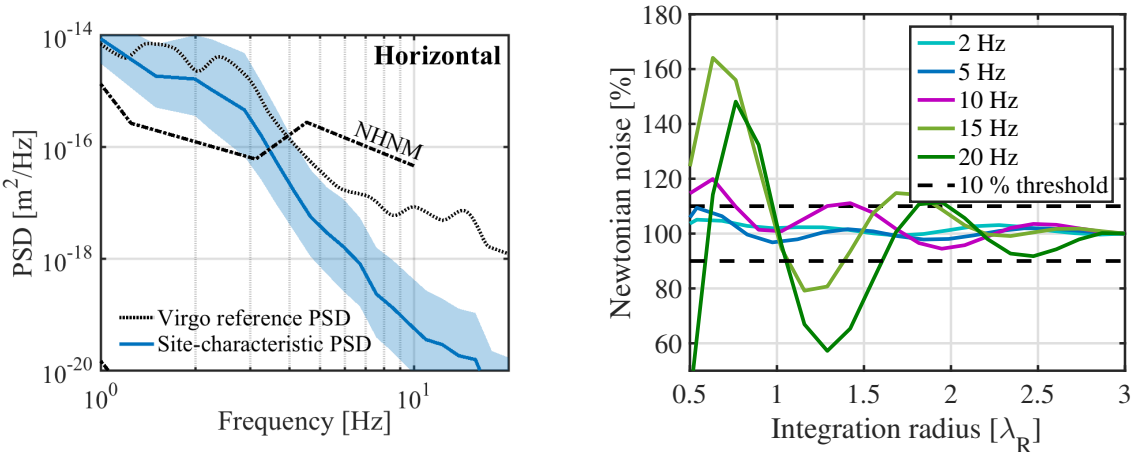

Figure 5.9: *Left: Horizontal site-characteristic PSD at EGO as obtained from the simulation, based on data from the array study in* 2016. *This PSD is used to derive the site-based Newtonian noise. For reference the PSD of the Newtonian noise in the design sensitivity is shown by the black dotted curve. Right: Newtonian noise from a single source on a* 1.6 m *high test mass as a function of increasing integration radius as percentage of the Newtonian noise obtained with the largest integration radius for various frequencies. At low frequencies (*< 10 Hz*) an integration radius of* λ_R *is sufficient whereas at high frequencies (*$10 - 20$ Hz*) a radius of* $2\lambda_R$ *is required.*

The resulting site-based Newtonian noise estimate at Advanced Virgo is displayed in Fig. 5.10. The characteristic Newtonian noise is derived from the site-characteristic PSD measured at EGO and it represents the ultimate noise limit that can be reached due to the seismic properties of the detector location. The mode, that is the most common value during the measurement period, of the site-characteristic Newtonian noise is compliant with the Advanced Virgo design sensitivity curve at low frequencies and it reaches several orders of magnitude below the analytical estimate at frequencies above 6 Hz. However, considering the Newtonian noise that corresponds to the

90^{th} percentile, that is the curve below which the Newtonian noise will reside 90% of the time, it surpasses the Advanced Virgo sensitivity below 6 Hz. Even though the detector performance during O3 has not been limited by site-based Newtonian noise, it will prohibit reaching sensitivity goals during future science runs. The installation of permanents seismic sensor arrays at the Virgo central and end buildings to integrate online Newtonian noise cancellation schemes in the context of the Advanced Virgo Plus upgrade is aimed to measure and overcome these limitations [55].

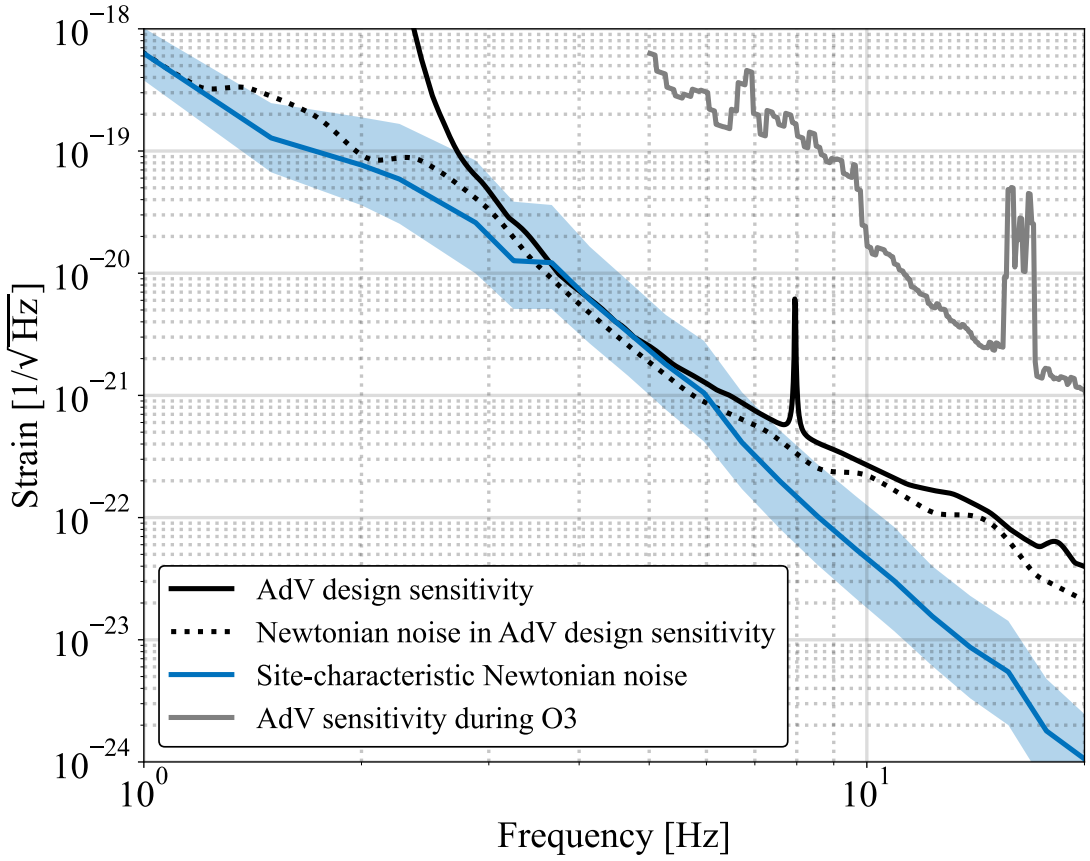

Figure 5.10: *Mode of our site-based Newtonian noise estimate at Advanced Virgo, derived for a test mass height of* 1.6 m *above the ground. The full solution of the wave equation in a layered geology is taken into account. The lower and upper bounds of the transparent band correspond to the* 10^{th} *and* 90^{th} *percentile of the Newtonian noise, respectively. Site-based Newtonian noise is a factor* 2 *below the design sensitivity above* 8 Hz *and the* 90^{th} *percentile surpasses the Advanced Virgo sensitivity curve only below* 8 Hz*. This site-based Newtonian noise represents the ultimate limit that can be reached at the EGO site due to the properties of the local geology and the ambient seismic noise level. Furthermore, site-based Newtonian noise is more than a factor* 10 *below the O3 sensitivity and did not limit the detector performance. The Newtonian noise estimate of the design sensitivity, that is based on Saulson's expression, deviates from our site-based Newtonian noise as it neglects seismic displacements in the vicinity of the test mass at low frequencies and overestimates seismic wave amplitudes at high frequencies.*

Our site-based Newtonian noise estimate can be compared to the Newtonian noise that is used in the derivation of the Advanced Virgo design sensitivity. This Newtonian noise is evaluated according to Eq. (3.5.2) and based on Saulson's analytical model of a half-space geology with density $\rho = 1800\ \frac{\text{kg}}{\text{m}^3}$, and a test mass on the surface that is surrounded by a cavern with a frequency dependent radius of $\lambda/4$. Moreover, a constant displacement without wave attenuation, that follows the 90^{th}-percentile spectrum of the horizontal PSD measured at the Central Building of the detector as shown in Fig. 5.9, left panel, is assumed [52, 53].

As elaborated in Section 3.5, the height of a test mass above the ground and the absence of a frequency dependent lower cutoff radius in the our site-based Newtonian noise integral lead to an increase with respect to the analytical Newtonian noise derived with Eq. (3.5.2). As a result the 90^{th} percentile of the site-based Newtonian noise surpasses the analytical estimate below about 8 Hz. At higher frequencies, the dispersive wave speed properties and the fast attenuation of surface waves that are incorporated in the realistic seismic field model lead to a site-based Newtonian noise that is significantly below the analytical expectation at high frequencies. This underlines the necessity that in order to develop realistic, site-based Newtonian noise estimates it is important to consider a seismic model that incorporates a seismic field with surface and body waves in a geology model that encompasses a realistic subsurface composition, seismic source distribution and seismic spectrum that is representative of the detector location, without the necessity to neglect seismic displacement in the vicinity of the test mass due to computational limitations.

Furthermore, the PSDs that are used in our site-based Newtonian noise estimate are more quiet than the PSD used in the analytical estimate of the design sensitivity curve above 4 Hz (see Fig. 5.9, left panel). The seismic noise at the Central Building surpasses the site-characteristic PSD at high frequencies, due to higher anthropogenic activity and noise through local infrastructure at the detector site like vacuum pumps, ventilation fans and the air conditioning system. To improve the Newtonian noise level at the detector site in order to reach the ultimate site-characteristic limit that has been derived with our site-based approach, the anthropogenic contributions of each building need to be reduced and smart infrastructure needs to be installed. First steps towards a noise characterization of each building and the installation of a new air conditioning system have been taken in 2019 [164].

5.4 Summary and conclusion

In August 2016 a seismic sensor array study has been performed at the site of Advanced Virgo, that allowed to identify the main seismic noise sources and to set up a horizontally layered subsurface geology model. This information has been used to derive a seismic wave model, which incorporates the full solution of the wave equation and reproduces the dispersion curve and power spectral densities measured at the detector site. This realistic, geology-based method overcomes the limitations of the analytical Newtonian noise model which is up to today used for Newtonian noise estimates at the Advanced Virgo detector. Our site-based Newtonian noise estimate, derived from the full model, shows that the analytical model based on Saulson's expression underestimates Newtonian noise at low and overestimates Newtonian noise at high frequencies. Furthermore, anthropogenic and infrastructure noise lead to a noise level at high frequencies which is higher than the sensitivity that can in principle be achieved at the EGO site. To overcome these limitations, mitigation and noise subtraction schemes based on permanent sensor arrays at the detector site will be of importance.

Chapter 6

Newtonian noise at the Einstein Telescope candidate site in Limburg

In the conceptual design report for Einstein Telescope the Belgian-German-Dutch (BGN) border region of South Limburg has been identified as a candidate site for this next generation gravitational wave observatory [37]. A candidate site is required to be seismically quiet in order to minimize the coupling of ground vibrations and detector test masses. The interaction may be due to residual seismic motion, but mainly originates from direct Newtonian coupling, the so called *Newtonian noise* (see Section 3.4). Newtonian noise depends on the local seismic field which is in turn dependent on the local geology and seismic source distribution. The BGN candidate site has been characterized in terms of seismic noise and geology with a set of seismic measurement campaigns. A realistic seismic field model has been derived, based on the results of these campaigns in combination with a complete solution of the elastodynamic wave equation for horizontally layered media. This seismic field model has been used to estimate Newtonian noise in the characteristic geology of South Limburg for an underground Einstein Telescope detector.

6.1 Seismic site characterization studies

The Belgian-German-Dutch Einstein Telescope candidate site is located near the village Terziet in Limburg, the southernmost province of the Netherlands (Fig. 6.1). The site is located in a rural area, which is known for agricultural activity and tourism. Despite its rural location, the BGN site is in the heart of the Leuven-Aachen-Eindhoven triangle, a European top technology area with numerous universities, established high-tech companies and all necessary infrastructure for the area to be easily accessible, and where nearby cities like Aachen in Germany and Maastricht in the Netherlands, with population densities ten times larger than the population density in Terziet, are within a range of 20 km. The BGN site has been characterized between 2017 to 2019 by means of several active and passive seismic array studies and two borehole campaigns. These studies allowed to obtain a detailed understanding of the local noise source distribution. Moreover, they allowed to characterize the subsurface geology in terms of thickness, densities and wave speeds of subsurface layers, a 2D subsurface model imaging a fault line, rock samples to depths of 140 m, and ongoing coincident power spectral density measurements on the surface and at 250 m depth. The following will list the outcomes of the first passive sensor array study and the results of both borehole studies that are most relevant for the context of this work. For

a complete list of all seismic studies and their results the reader is referred to [75, 165].

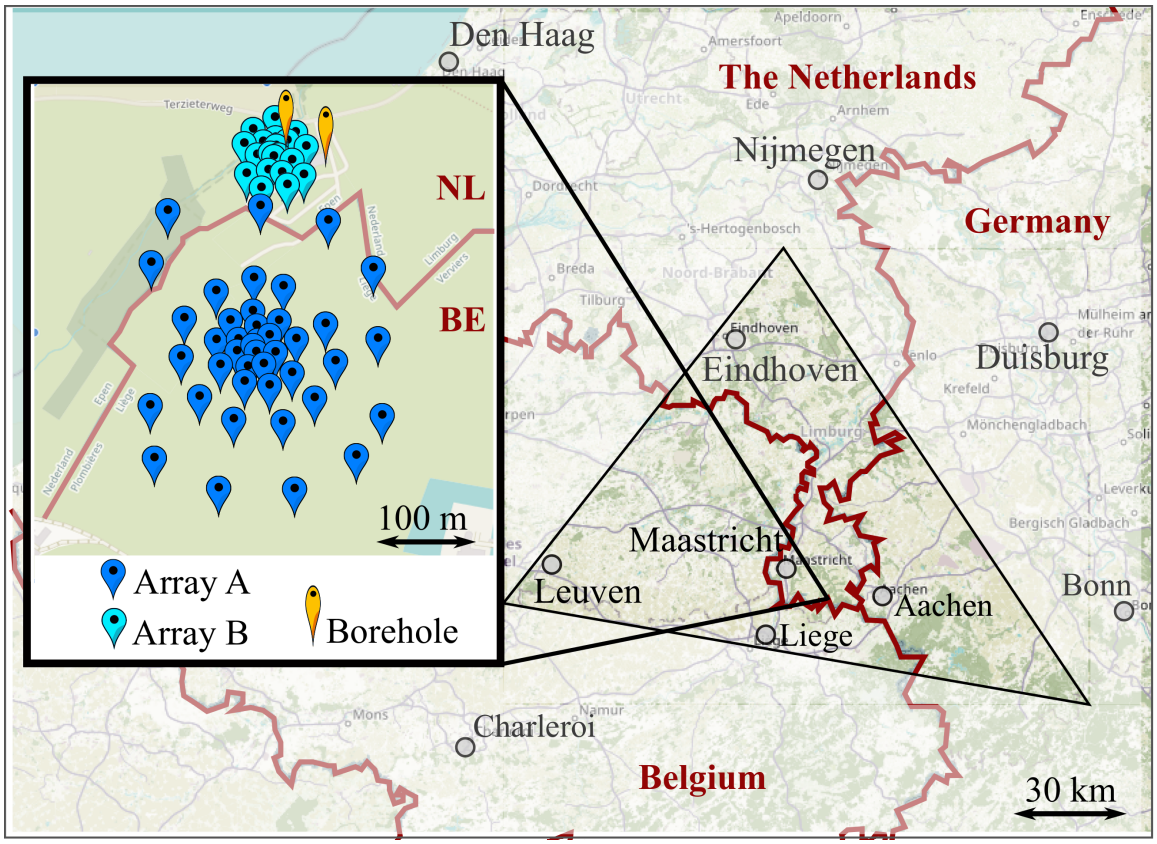

Figure 6.1: *The Belgian-German-Dutch Einstein Telescope candidate site is located in the south of the Netherlands at the heart of the so called Leuven-Aachen-Eindhoven technology triangle. The inset indicates the location of the two sensor arrays employed during the first passive array study and the locations of the two boreholes at the candidate site near the village Terziet.*

6.1.1 Borehole campaign in March 2017

In March 2017 a borehole with a diameter of 270 mm and a depth of 135 m has been drilled near the village Terziet in South Limburg, the Netherlands at $50°45'22.6''$ latitude and $5°54'24.2''$ longitude. To plan and execute this large-scale project, Nikhef has collaborated with industrial partners such as Shell, Innoseis, Deltares, TNO, Antea and EBN. During the drilling process, standard borehole logging techniques of exploration geophysics [166] have been applied to gain information about the subsurface geology and lithology [167]:

- *Resistivity logging*: With the Short and Long Normal measurement, SONO and LONO respectively, the resistivity along the borehole is measured in units Ωm by determining the potential between electrodes. The first electrode is at a fixed position while the second electrode is moved upwards in the borehole. With a so called Multi-tool, the SONO measurement allows a maximum distance of 0.5 m between the electrodes, whereas the LONO measurement allows a spacing of 0.8 to 1.6 m. From the potential difference the resistivity can be determined. The resistivity gives information about the porosity of the rock formation along the borehole, as saline water leaks from pores in the rock into the

borehole water. The higher the porosity of the material, the higher the conductivity of the water in the borehole between the electrodes and the lower the resistivity [168]. A similar method is called Single Point Resistivity (SPR) measurement. Here the electrical resistance from points within the borehole to an electrical ground on the surface is determined.

- *Gamma-ray logging*: With gamma-ray (GR) logging the natural gamma radiation emitted by the subsurface rock along the borehole is measured. GR logs are typically measured in units gAPI (gamma-ray American Petroleum Industry), which is a scale that is defined in a calibration borehole at the University of Houston [166]. High gAPI values from about 75 to 200 gAPI indicate the presence of clay-rich rock formations such as shale, claystone or mudstone, whereas low values around 20 gAPI are an indicator for clean or coarse-grained sandstone and carbonate rock such, as dolomite and limestone. The general gamma ray spectrum can only serve as an indicator for the clay content of a rock formation and has to be combined with other logs to make more precise statements about the subsurface lithology. For example, the gAPI value of sandstone containing clay or micas is higher than the value for clean sandstone, which may lead to a confusion of sandstone with shale material. To avoid this confusion, distinguishing the contribution of potassium (K), uranium (U) and thorium (Th) to the gamma-ray spectrum is a powerful tool. Thorium is typically combined with shales and heavy minerals containing zinc and lead, potassium is present mainly in shale rock and stabilizes clay minerals, and uranium can be linked to organic matter content in the rock [169, 170].

- *Sonic logging*: The Sonic logging tool has a length of 3.5 m and consists of a sonic pulse emitter at the top, one receiver nearby the emitter and one receiver at the bottom of the tool. When a short, high amplitude sonic pulse is emitted, it excites seismic waves in the surrounding rock structure which are measured by the receivers. No distinction between the type of waves that arrive are made, hence the measured velocity is not a direct measurement of the wave speeds in the rock material. Velocities smaller than $1500\,\mathrm{m\,s^{-1}}$ indicate non-saturated, soft materials while velocities higher than $2000\,\mathrm{m\,s^{-1}}$ indicate hard rock material. Even though the receivers are isolated from the emitter, direct sonic waves may arrive through the thick liquid in the borehole and deteriorate the quality of the measurement. In this case the velocities at the first receiver are lower than at the second receiver and the measurements at the second receiver are closer to the real velocities in the rock.

- *Orientation logging*: The Acoustic Borehole Imager (ABI) tool measures the reflection of acoustic waves from the borehole walls, which allows to determine the slope and the direction of a possible deviation from the vertical depth of the borehole [171].

During the drilling process, rock samples have been collected every 5 m and stored (see Fig. 6.4). Together with the results from the borehole logging (Fig. 6.2 and Fig. 6.3) the following lithographic interpretation can be made:

- $0-5$ m: Surface rock samples collected during the preparation of the borehole site revealed a thin surface layer of pure clay material until a depth of about 5 m. Slight variations in the gamma-ray spectrum peaks and in the velocity spectrum after 5 m indicate a new material layer.

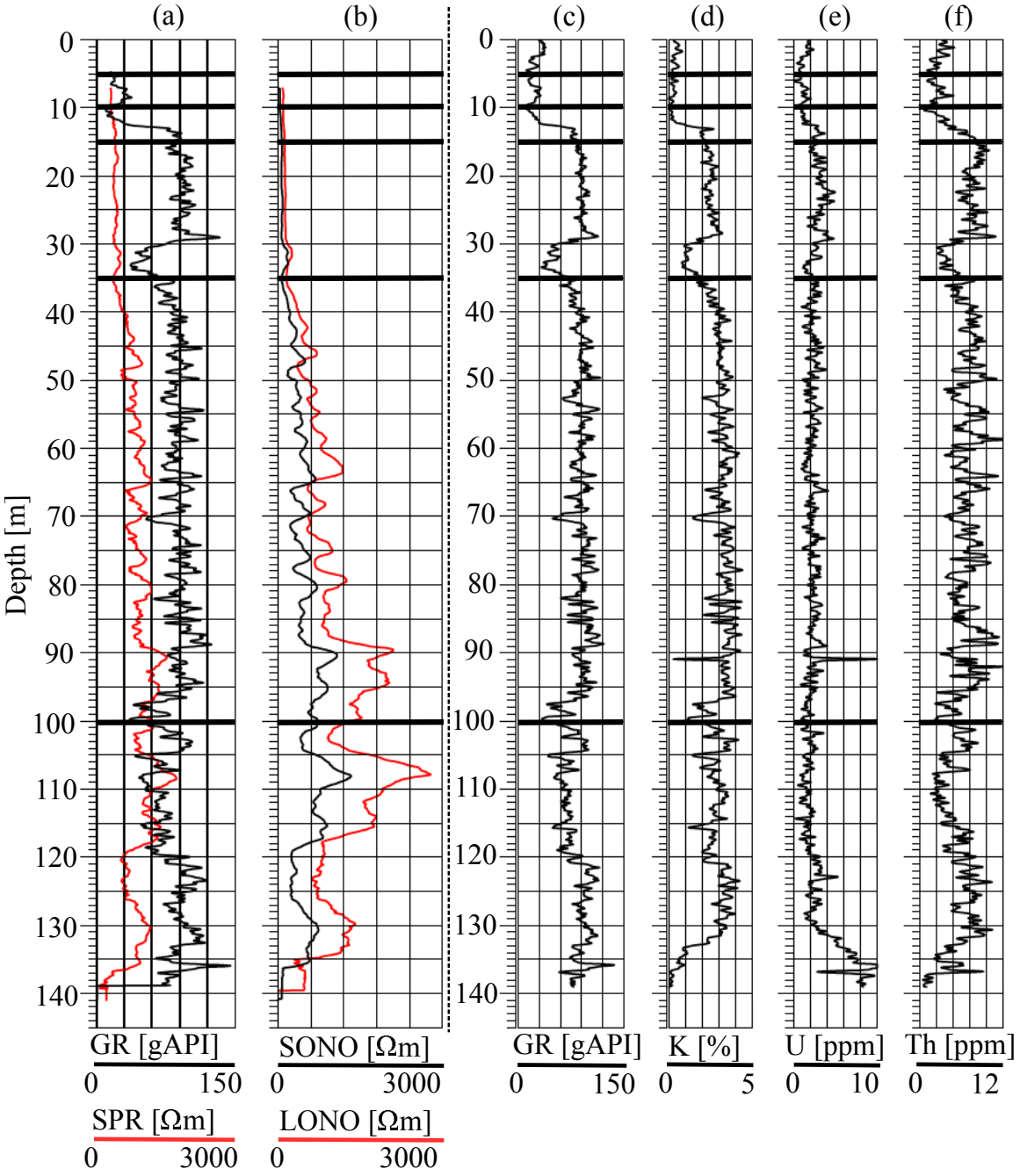

Figure 6.2: *Borehole logging to a depth of* 140 m *has been carried out by Deltares and TNO [167], showing (a) the gamma-ray (GR) and Single Point Resistivity (SPR) measurement with the Multi-tool, (b) the resistivity log from the Slow (SONO), Long Normal (LONO) with the Multi-tool, and the (c) the gamma-ray measurement with a so called Spectral tool, that have been decomposed into contributions from (d) potassium (K), (e) uranium (U) and (f) thorium (Th). The thickened horizontal bars indicate the stratification of the subsurface layers that is based on the lithographic interpretation of the borehole logging (see also Fig. 6.3). The GR measurements in (a) and (c) have been measured with different tools, but show the same result. The increase in the GR spectrum after* 10 m *and the decrease after* 35 m*, as well as the change in resistivity at* 100 m *indicate the beginning of new layers.*

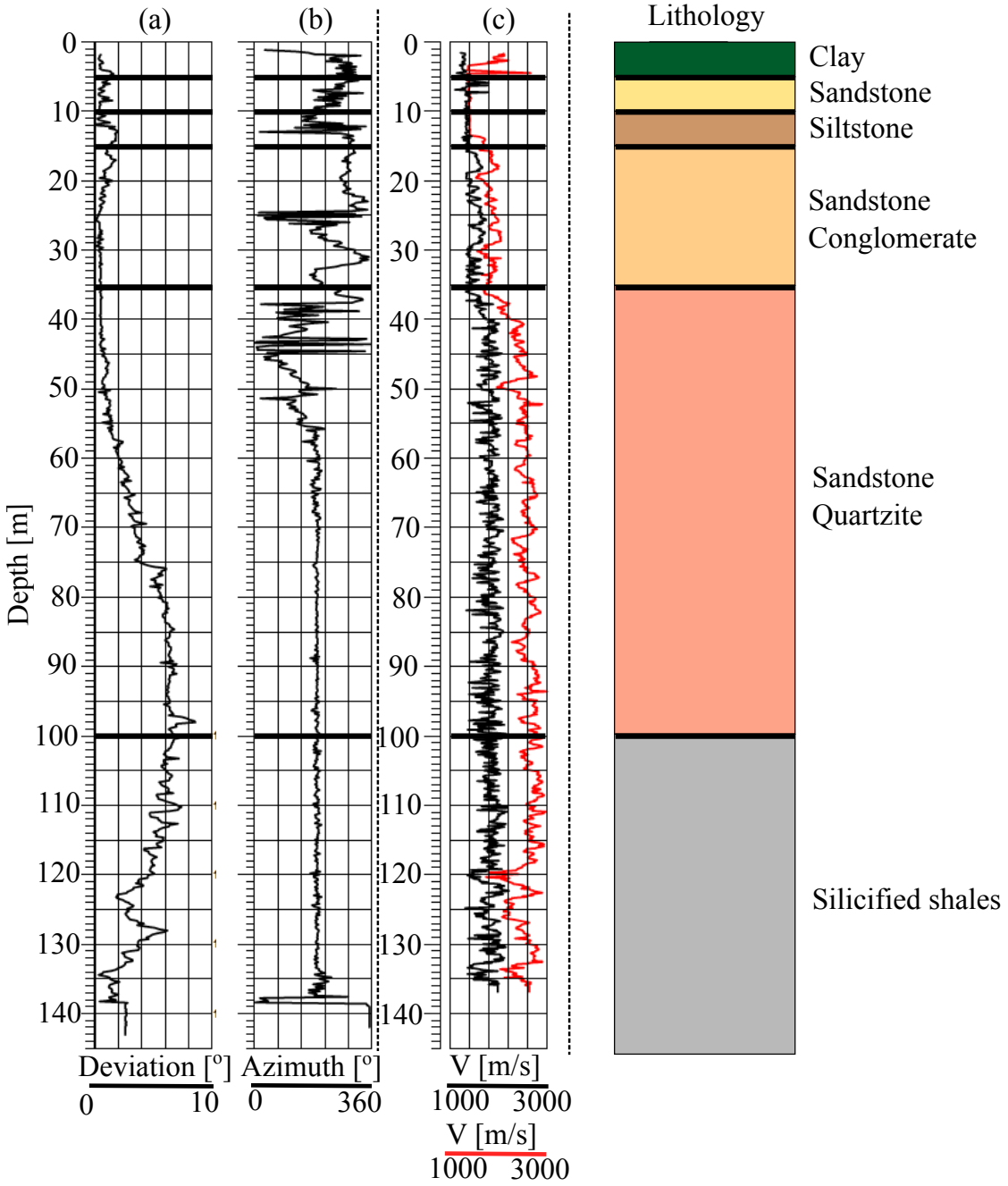

Figure 6.3: *Borehole logging to a depth of* 140 m *showing (a) the deviation of the drill from the vertical drill axis with depth and (b) in the horizontal plane. Strong fluctuations in the azimuth angle up to about* 45 m *depth occur where the subsurface is composed of gravel and conglomerate, whereas a steady angle occurs in more compact material. The deviation from the vertical axis at great depths prohibited a continuation of the drilling beyond* 140 m. *(c) The sonic log shows the wave speeds measured with a receiver far (red) and nearby (black) the emitter of the sonic pulse. The far receiver measures the speed of waves traveling through surrounding rock, while the measurement of the nearby receiver is deteriorated by waves propagating through the borehole fluid. The right column shows the lithographic interpretation of the subsurface that has been made, based on the logging data [167].*

Figure 6.4: *Scientists inspecting the rock samples that have been collected every* 5 m *during the drilling of the first borehole in 2017 at the Belgian-German-Dutch Einstein Telescope candidate site. The rock samples have been analyzed by TNO to facilitate a lithographic interpretation of the subsurface composition [167].*

- 5 – 10 m: Changes in the thorium and uranium gamma-ray log indicate a new material layer, and the lower gamma-ray spectrum shows that the clay content in this layer is reduced. The low resistivity indicates a highly porous, soft rock material. However, high velocity spikes in the wave speeds measured with the sonic tool also hint to hard rock gravel materials. Soft material at these shallow depths typically originate from the Cretaceous, a geological period that lasted from about 145 to 66 million years ago. The main material of this layer consists of lightweight sandstone, which is formed as a result of pressure from surface sediments.

- 10 – 15 m: The wave speed and resistivity in this layer are still low, which indicates a soft material. At about 12 m the gamma ray spectrum and its potassium and thorium contribution drastically increase, which means that a change of material is occurring at greater depth. In this layer the transition from soft to hard rock material manifests itself as a fine, grainy mix of different material types. These types of formations are called siltstone.

- 15 – 35 m: The overall increasing, but yet fluctuating wave speed of this layer indicates a large amount of gravel and hard rock material. Nevertheless, the material shows little resistivity, indicating the presence of soft material and rough gravel. The high amount of gamma-radiation means that the soft material in this layer is clay whereas the thorium and potassium contents are typical for sandstone. This layer is a coarse-grained rock conglomerate, consisting of various sandstone and clay materials.

- 35 – 100 m: This layer is characterized by a clear change in the gamma-ray spectrum at 35 m, the increase in resistivity, meaning a decrease of rock porosity and an increase in wave speeds to velocities above 2000 m s^{-1}; all indicating a hard-rock material. At the location of the Heimansgroeve, a former query which is now used as a seismic measurement location of the Royal Dutch Metrological Institute (KNMI) about 1 km north-east from the drilling location, this hard-rock formation breaks through to the surface [73]. It consists of many 0.1 m to 0.5 m thin, strongly folded and faulted layers. The fault structure is also indicated by the strongly fluctuating thorium spectrum. Thorium is often combined with heavy minerals such as lead and zinc, which are components of the formations present in this area. Each thin layer consists of different amounts of minerals, leading to a fluctuation

in the thorium spectrum. At a depth of 92 m a strong peak in the uranium and potassium layer indicates the folding of a layer with shale content, originating from greater depths.

- 100 – 140 m: At a depth of 100 m the resistivity drastically increases, which indicates the presence of a hard rock formation. The reduction of the gamma-ray spectrum indicates the presence of shale.

It is important to note that the lithological interpretation is not trivial and can often be ambiguous, as the indications from different measurements can be contradicting or vague. It is therefore indispensable to collaborate with local geology experts to obtain an overall understanding of the factors that contribute to the interpretation of a subsurface composition and to bring practical observations in agreement with the local conditions. The interpretation of the lithology at the first borehole location of the BGN candidate site allows to group the subsurface stratification into three zones: a soft material layer on the surface (0 m to 15 m), laying on a hard rock bedrock (35 m to at least 140 m) with a mostly soft, thin transition area in between (15 m to 35 m).

The orientation of the borehole starts to deviate from the vertical axis at a depth of 45 m towards the south-western direction, reaching a maximum of 7° at about 90 m depth (see Fig. 6.5). This deviation caused a rupture of the drill and prohibited drilling activities beyond 140 m depth. It was caused by the borehole drill moving along a large, underground fault formation that was unknown at the time of the site study. For an image of the fault migration underground, seismic imaging techniques such as active seismic studies with large seismic sensor arrays have been carried out and the interested reader can study the results in [165].

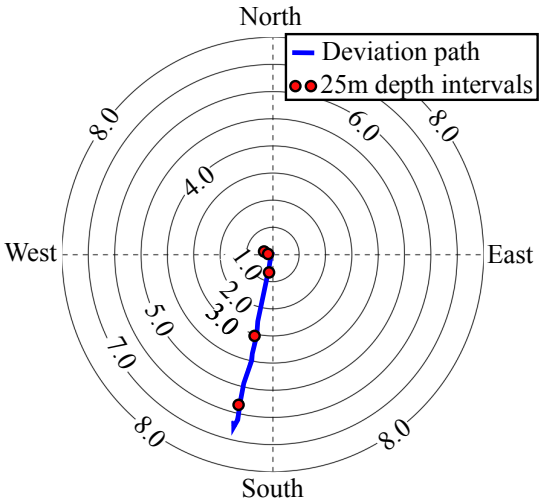

Figure 6.5: *Vertical deviation of the drill orientation during the drilling of the first borehole [167]. At a depth of about* 45 m *the orientation of the drill starts to deviate from the vertical axis as it moves along a subsurface fault line. The drill reaches a maximum deviation of* 7° *at about* 90 m *depth, which corresponds to a horizontal deviation from the original location of* 11 m. *This deviation prohibited a continuation of the drilling process beyond* 140 m.

6.1.2 Passive seismic array study in November 2017

From 3 to 16 November 2017 a network of 74 seismic sensors has been deployed near the village of Terziet in Limburg, the Netherlands [74, 146]. The second generation of the geophone-based Innoseis Tremornet nodes were used, which have the same characteristic as the sensors described in Section 4.3. The network was split into two subarrays, where each array consists of several concentric rings (see Fig. 6.6, left panel). The radius of the n^{th} ring is $r_n = r_0 2^{n-1}$ with $r_0 = 3.5$ m and each ring consisted of $2n - 1$ sensors. The circular symmetric design of the array

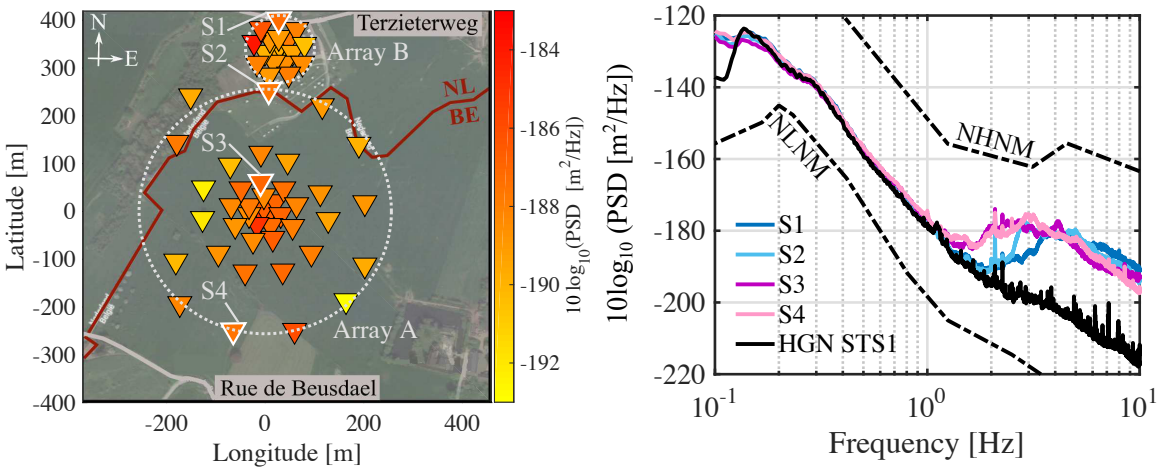

Figure 6.6: *Left: Layout of the passive sensor array. Each triangular marker indicates the location of a seismometer, its color is the PSD of the corresponding seismometer averaged over the full measurement period and frequency range from* 1 *to* 10 Hz*. The PSDs of the four highlighted sensors are displayed in the right panel. Right: PSD mode of four sensors of the array during one full day of measurement, where the two sensors in array A (S3 and S4) exhibit a higher noise level between* 1 Hz *and* 3 Hz *than the two sensors in array B (S1 and S2). For comparison, the PSD* 10 m *underground at the nearby KNMI Heimansgroeve underground observatory (HGN) is shown in black. Above about* 3 Hz *underground spectra are suppressed by up to two orders of magnitude with respect to surface data.*

allowed to equally resolve seismic waves arriving from all directions. The frequency resolution of the array is determined by the number of rings and their radius. The theoretical response of the array can be calculated with the array response function (Eq. (4.2.8)). It can be shown that for simple and regular array geometries the resolving power is related to the minimum and maximum inter-sensor spacing [172]. Array A had a maximum aperture of 456 m and consisted of 7 rings with 49 sensors in total. Its sensitive frequency range for beam forming was from 2.5 to 8.0 Hz. Array B was smaller with a maximum aperture of 112 m and was comprised of 5 rings with 25 sensors. Due to its smaller diameter, array B was sensitive for beam forming in the frequency range of $3.4 - 8.0$ Hz.

Figure 6.6, right panel, shows four representative PSDs from individual sensors of the array during one full day of measurement. Due to the remote location, the surface spectra are quiet. For the same period, data at 10 m depth from a permanent STS1 seismometer are publicly available from the seismic station of the Royal Dutch Meteorological Institute (KNMI) at Heimansgroeve, located 1 km to the north-east of the sensor array [73]. Below 1 Hz, where microseismic activity is dominant, the vertical spectra from the array and the STS1 are in excellent agreement. Above 1 Hz, where noise is created by anthropogenic activity, subsurface PSDs are already suppressed at 10 m depth by up to two orders of magnitude with respect to surface data. This is because the local geology consists of a soft soil layer on hard rock and seismic waves attenuate fast when they travel in soft material. These short wavelength can then lead to a strong attenuation of seismic amplitudes at shallow depths. The distinctive attenuation of seismic amplitudes at depth near the BGN candidate site motivated the realization of a second borehole study down to a depth of 250 m (see Section 6.1.3). More insight for the site characterization is gained here with two permanent seismometers that allow the continuous measurement

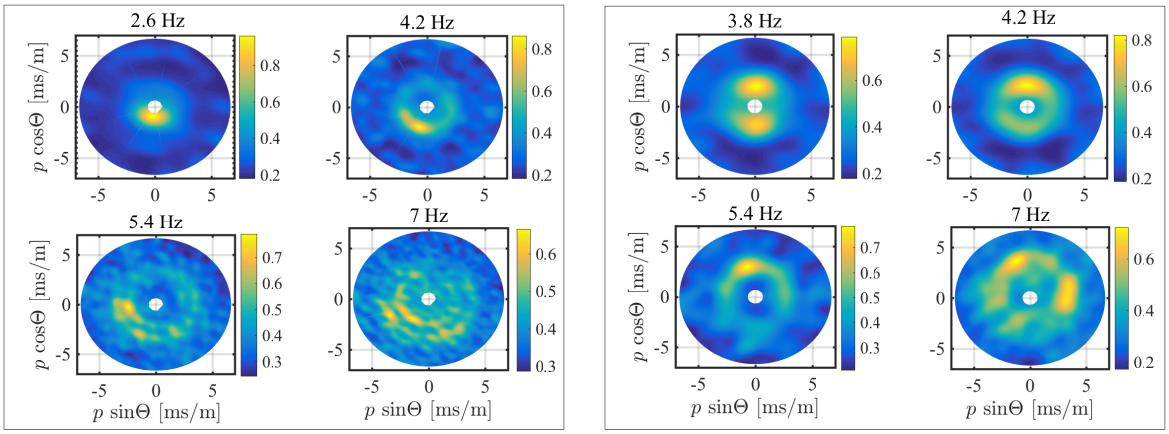

array A array B

Figure 6.7: *Selection of beam forming plots from array A (left panel) and array B (right panel), analyzed during the same period. The radial axis displays the slowness p, which is increasing in the outward direction and the azimuth angle θ is measured clockwise from the positive y-axis such that $x = p \cdot \sin\theta$ and $y = p \cdot \cos\theta$. The color scale indicates the normalized beam power (see Eq. (4.2.7)). East is towards the positive x-axis, north towards the positive y-axis. For array A, the noise at low frequencies originates from the south-western direction, while it is less localized at high frequencies. For array B, noise mainly originates from north at low frequencies, while a second peak in the eastern direction emerges at high frequencies.*

of surface and underground PSDs.

With beam forming the direction of incidence of the surface waves and their velocities has been determined. Beam forming shows that the main seismic noise sources for both subarrays are extremely local and in close vicinity of the sensor array (Fig. 6.7). For array A, the main noise in the whole frequency band originates from the south-western direction, from traffic on the Rue de Beusdael. For increasing frequency the incoming noise is not as localized and spreads of a large angle anticlockwise from the western to the eastern direction, where a farm is located about 500 m from the center of the array. At low frequencies, array B picks up noise from Rue de Beusdael as well, but is dominated by noise from the northern direction. As the frequency increases, the noise keeps originating from the northern direction and in addition starts to spread towards east. Possible noise sources are the Terzieterweg and the nearby camping ground.

The peak of the beam power distribution in the radial direction indicates for each frequency the surface wave velocity. Array A has the larger aperture, which means that it resolves a larger frequency range. It was therefore used to determine the dispersion curve (Fig. 6.8, left panel). An additional advantage of the large aperture of array A is that it allows to record not only the fundamental Rayleigh wave mode, but also reveals the first overtone mode above 5 Hz, visible as two slowness rings in the bottom plots of Fig. 6.7, left panel. The presence of the first overtone can be understood by considering a medium with high, non-continuous velocity contrast in the subsurface composition, for example a thin, soft soil layer on hard rock as in Limburg. In this case P-and S-waves, which form the Rayleigh waves and that originate from surface excitations, are almost entirely reflected back and forth inside the soft soil layer. This leads to observable interference effects in terms of higher order modes on the surface [109]. In principle overtones of surface waves also exist in more homogenous media. However their amplitude is then very low, which makes it difficult to distinguish them from uncorrelated surface noise.

Layer number	Thickness [m]	ρ [kg/m^3]	V_p [m/s]	V_s [m/s]
1	5.7	1950	385	163
2	10.2	2250	444	270
3	18.9	2500	687	336
4	58.2	2800	2805	1240
5	∞	2800	4054	2432

Table 6.1.2: *List of material properties for the five-layer subsurface model of the geology at the Dutch-Belgian-German Einstein Telescope candidate site derived from the inversion of the dispersion curve measured with array A. The parameters are the layer thickness, layer density ρ, and the P- and the S-wave speeds, V_p and V_s, respectively.*

The fundamental and first order Rayleigh wave dispersion curves from array A have been used in the inversion to obtain a 1D-model of the subsurface lithology [173]. This model is therefore most accurate at the center of array A. The inversion has been carried out with a stochastic direct search method, where the parameter space contained the number of subsurface layers, as well as their thickness, density, P- and S-wave speed. With the subsurface information from the first borehole study the inversion has been based on six subsurface layers with the thickness and the densities from the lithological interpretation displayed in Fig. 6.3 as starting values [146]. The resulting velocity model shows a steep velocity contrast at a depth of about 35 m, where the interface between soft soil and hard rock is located (Fig. 6.8, right panel). Furthermore, the parameters of the two layers from 5 to 10 m depth were found to be almost identical, making it more efficient to combine these layers. The numerical values of the P- and S-wave speed, the density and the thickness of each layer are summarized in Table 6.1.2. The theoretical dispersion curve from these soil parameters is in good agreement with the measured dispersion curve (Fig. 6.8, left panel). To reduce the complexity of the analysis, the amplitude attenuation

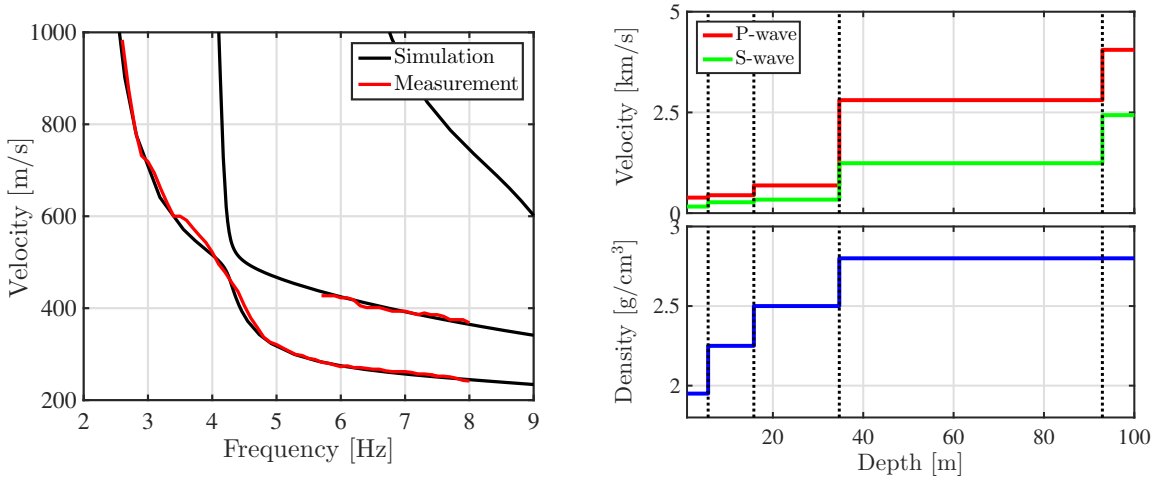

Figure 6.8: *Left: Dispersion curve of fundamental and first overtone Rayleigh wave as obtained from beam forming of array A. It is compared to theoretical dispersion curves that are calculated from the results of the inversion analysis. They are both in excellent agreement. Right: Subsurface velocity and density model as obtained from the inversion analysis. A steep velocity contrast at* 35 m *indicates the interface between soft soil and hard rock.*

factors have not been derived.

6.1.3 Borehole campaign in April 2019

A second borehole campaign to a depth of 250 m has been carried out from November 2018 until April 2019 at the Einstein Telescope candidate site near the village of Terziet in the Netherlands. The aim of the campaign was to install a surface and a borehole seismometer underground to simultaneously measure long-term seismic spectra. Since June 2019 a three-axial Trillium T240 seismometer measures surface spectra, and a three-axial STS-5 broadband borehole seismometer measures spectra at a depth of 250 m. Long term measurement periods will give information about yearly variations of the surface and underground seismic conditions, which will allow to estimate yearly variations in Newtonian noise.

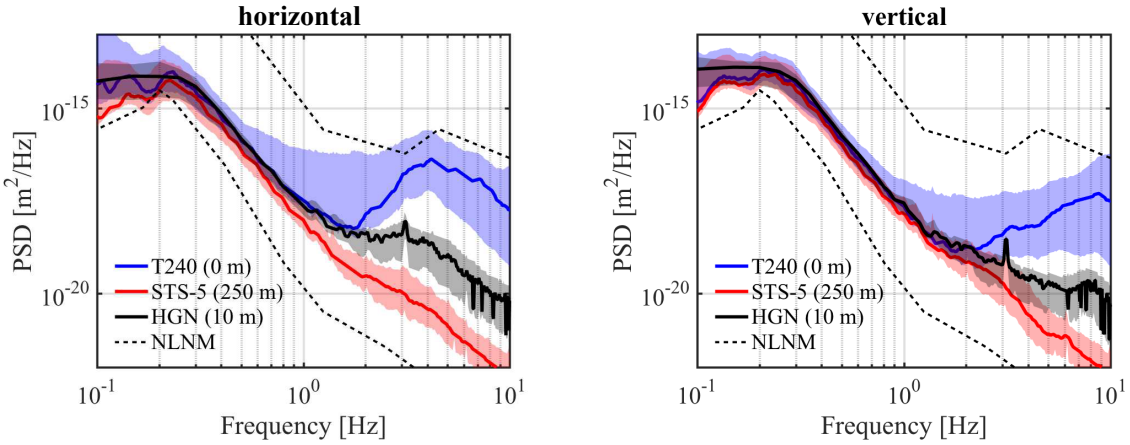

Figure 6.9: *Horizontal (left) and vertical (right) displacement PSD mode in Terziet. The PSD in eastern and western direction are the same. The transparent band encloses the 10^{th} and 90^{th} percentile of the PSD from the 27 day long measurement campaign. Above* 1 Hz *the underground PSDs are strongly suppressed with respect to surface values. The PSD from the KNMI measurement station at Heimansgroeve (HGN)* 1 km *east of the borehole location is shown for comparison.*

The first set of coincident surface and underground data were taken in the period from June 25^{th} to July 21^{th} 2019 (Fig. 6.9). At frequencies below 1 Hz noise originates from microseismic activity. At these frequencies the wavelengths are larger than 1 km, which means that measurements at a depth of 250 m mainly encompass Rayleigh waves with little attenuation. Therefore, low frequency surface and underground PSDs are the same. As the frequency increases, horizontal and vertical displacements attenuate fast with depth. Rayleigh wavelengths above 4 Hz are shorter than 125 m, and therefore surface waves have already attenuated at the depth of the underground seismometer. Hence, the attenuation in power between surface and underground reaches a peak of more than four orders of magnitude above 4 Hz for horizontal and above 7 Hz for vertical PSDs (see Fig. 6.10, left panel). At these frequencies, body waves become the more dominant contribution to the underground wave field. Furthermore, it can be observed that horizontal PSDs attenuate already at lower frequencies than vertical PSDs, which is characteristic for Rayleigh waves. As Newtonian noise is driven by horizontal seismic displacement, the strong increase of suppression between 1 and 20 Hz and the attenuation of

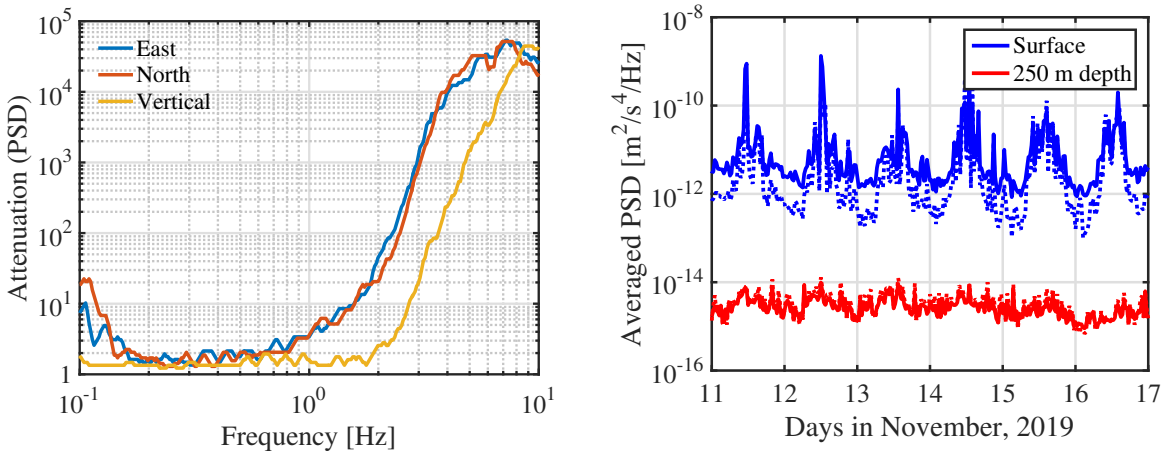

Figure 6.10: *Left: Attenuation of PSD between surface and* 250 m *depth. Horizontal attenuation starts at lower frequency than the vertical one. Right: Temporal variation of surface and underground PSDs at the BGN candidate site, averaged between* 2 *to* 10 Hz*, where the horizontal spectrum is depicted with a full, the vertical with a dotted curve. The almost constant noise level underground in both displacement directions, while simultaneously measuring high temporal fluctuations on the surface, indicates the dominance of the body wave background at the subsurface seismometer.*

horizontal PSDs at lower frequencies are beneficial for Einstein Telescope at the BGN candidate site.

The reason for the strong attenuation of seismic waves at the BGN site lies in the local geology, where a layer of soft soil is resting on hard rock (see Fig. 6.3). Seismic waves above about 1 Hz are generated by anthropogenic surface sources. As the waves travel through the subsurface, they are confined to the soft surface layer by multiple reflections and only a small fraction of the waves penetrate into the hard rock layer. This means that at these frequencies, Rayleigh waves do not reach the borehole seismometer anymore and it measures purely body waves. The presence of this *body wave background*, a superposition of body waves from un-

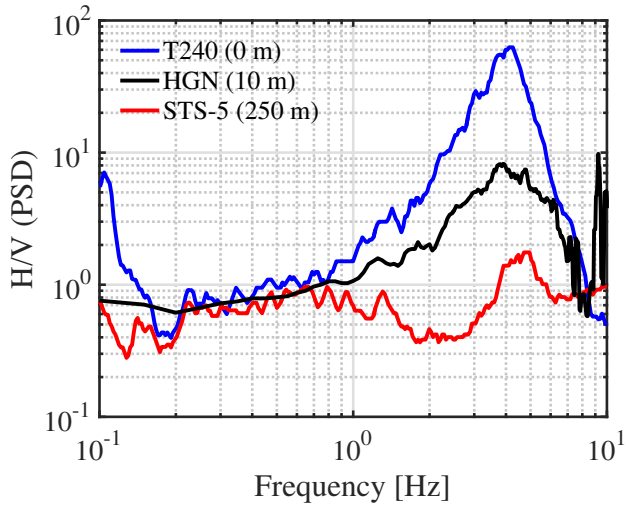

Figure 6.11: *Ratio of horizontal and vertical PSDs at the surface and underground at the borehole location. Below* 1 Hz *the ratio is equivalent for surface and underground measurements. The maximum ratio on the surface, where anthropogenic noise sources dominate, is reached at about* 4 Hz*. This peak at high frequencies is characteristic for geologies where a soft soil layer is resting on hard rock [174]. The H/V ratio at the KNMI measurement station (HGN) is shown for reference.*

known surface and underground sources, has further been shown by investigating the temporal variation of surface and underground PSDs (see Fig. 6.10, right panel) [165]. The day-night acceleration PSD ratio, averaged over the frequency range from 2 to 10 Hz, as measured on the surface surpasses two orders of magnitude, while the underground day-night ratio is about a factor 3. As the high daily variation in excess power on the surface is due to the anthropogenic activity in the region, the amount of suppressed power at depth is higher during the day than at night. Due to the reduced power of surface waves at night, the underground is quiet enough for the station at 250 m depth to measure the body wave background. It has been shown that below 4 Hz, the body wave background is about half an order of magnitude below the total underground noise and that above 4 Hz, the contribution of the body wave background gradually increases and makes a more significant contribution to the underground noise [165].

The three-axial nature of the borehole seismometers allowed to determine the characteristic ratio of horizontal to vertical PSDs at the BGN site (see Fig. 6.11). This H/V ratio is characteristic for each site as it depends on the geology, source mechanism, source depth and distance [113]. Up to about 1 Hz the ratio at the borehole site is comparable for all sensors. Above 1 Hz anthropogenic activity, which is connected to surface excitations, is the dominant seismic noise source. Due to the high impedance contrast in the local geology of soft soil resting on hard rock, the seismic amplitudes are confined to the surface layers and mode conversion is favored. As a result the horizontal amplitudes significantly surpass vertical amplitudes on the surface at high frequencies [174]. For increasing depth and frequency, the surface amplitudes are attenuated more efficiently and the ratio approaches a nearly constant level across all frequencies.

6.1.4 Summary

The seismic site studies of the BGN candidate site presented in this section resulted in the identification of five distinct subsurface layers, where the last layer started at a depth of about 90 m. The geology of the site is characterized by a thin soft soil formation on the surface of about 35 m thickness, resting on hard rock material (see Section 6.1.1). This information was used to derive the thickness of the five subsurface layers, their wave speeds and densities as well as the surface wave speeds of fundamental and first overtone. Together with PSD measurements on the surface, the mostly local seismic noise sources were determined in the frequency range from 2.5 to 8.0 Hz (see Section 6.1.2). Three-axial, simultaneous measurements of seismic spectra on the surface and at 250 m depth lead to the identification of a significant reduction of underground PSDs with respect to the surface as a result of the local geology, to the measurement of a body wave background at frequencies above about 4 Hz and the identification of the site-characteristic H/V ratio. The surface and underground PSD measurements are ongoing and will reveal annual variations in the spectra at the BGN candidate site for Einstein Telescope [165].

6.2 Ambient seismic field model

To model an ambient seismic field, the seismic displacement field is calculated from vertical surface excitations of a geology model that has been derived from a passive array study (see Section 6.1.2). As the derivation of material damping factors was excluded from the inversion analysis, a uniform damping factor of 1% was chosen for all layers. Material damping is the inverse of the Q-factor and represents the loss of energy per oscillation cycle due to inelastic processes in the medium during wave propagation. The chosen value represents an estimated

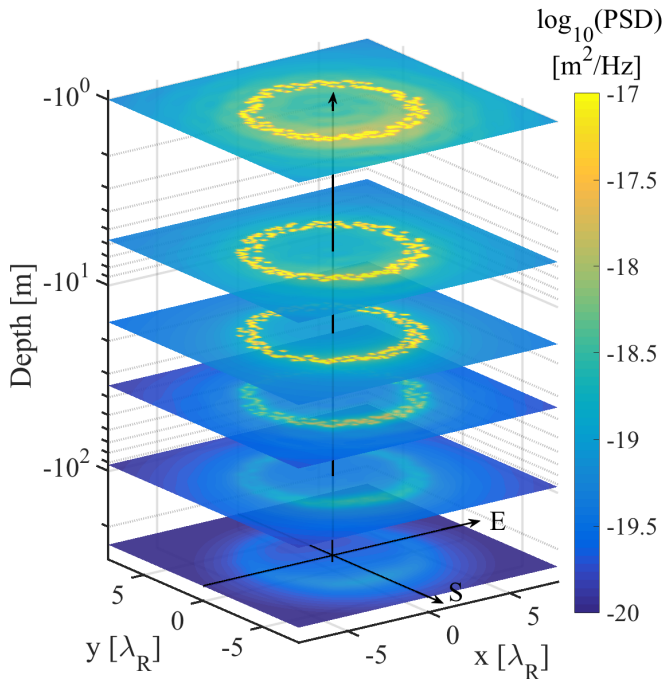

Figure 6.12: *Simulation of the Limburg geology at* 2.6 Hz *that has been excited by* 180 *vertical sources, which are distributed in a* $\lambda_R \approx 240$ m *wide ring of radius* $R \approx 1$ km. *The relative strength is selected according to the measured beam power at* 2.6 Hz *and the absolute strength to reproduce the measured surface PSD at the center of the ring. The first five sheets show the PSD across the top surface of each new layer. The last sheet at* 250 m *depth does not correspond to a new layer, but shows the PSD at the depth of the test mass. Note the strong reduction of amplitude at depths greater than* 35 m, *where the hard rock layer begins.*

average over the high damping values found in clay structures and the low damping of rock formations [175]. The test mass is located underground at a distance of 250 m from the surface and in the center of the coordinate frame.

In this model the soil is excited for each frequency at 180 locations, which are distributed in a ring symmetrically around the vertical axis of the coordinate frame (Fig. 6.12). The excitation points are uniformly distributed within a ring of central radius R and width λ_R, where λ_R denotes the Rayleigh wavelength. The distance R is selected such that the surface horizontal over vertical ratio of the simulated surface PSDs reproduces the measured ratio at the center of the ring (see Section 6.2.1). In addition, the source locations are required to be compatible with source locations as predicted by beam forming, that is at several kilometer distance at low and at a few tens of meter at high frequencies.

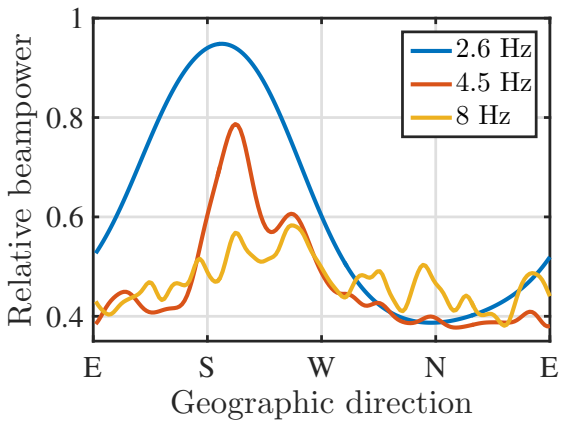

Figure 6.13: *Beam power distribution depending on the geographic direction measured with array A for three discrete frequencies. The noise at low frequencies is maximum and originates from the south-western direction, where an agricultural farm is located. At high frequency the noise is more local and evenly distributed across all azimuthal directions.*

With 180 excitation points, each of the sources is located in a segment of 2° width. The relative strength of the sources is selected according to the beam power as measured with array A (see Fig. 6.13). Due to the sensitivity of the array, beam power values are available in the frequency range from 2.6 to 8 Hz. Note that the Newtonian noise frequency band of interest is from 1 to 20 Hz, which exceeds the beam power frequency band. Hence, for frequencies smaller than 2.6 Hz the same beam power distribution in azimuthal angle as for 2.6 Hz is assumed, whereas for frequencies larger than 8 Hz a uniform distribution is assumed.

The PSD that is used to derive the absolute scaling factor is obtained from the surface seismometer at the location of the second borehole (see Section 6.1.3). With a second sensor at 250 m depth simultaneous surface and underground data are taken. Both sensors offer three-axial measurements of the seismic field which is of paramount importance for the determination of the horizontal over vertical PSD ratio. Note that the borehole sensors are located at a distance of 300 m towards the north-eastern direction from the center of array A (Fig. 6.1).

6.2.1 Surface horizontal over vertical PSD ratio

For a given distance R from the source on the surface, the body waves decay in amplitude with $1/R$ and attenuate faster than Rayleigh waves, which decay with $1/\sqrt{R}$. This means that within a few Rayleigh wavelengths from the source the wave field consists of a superposition of surface and body waves, whereas far away from the source the wave field mostly consists of surface waves. Hence, for a given source mechanism and frequency, the amplitudes of the horizontal and vertical components of the displacement field are distance dependent (Fig. 6.14).

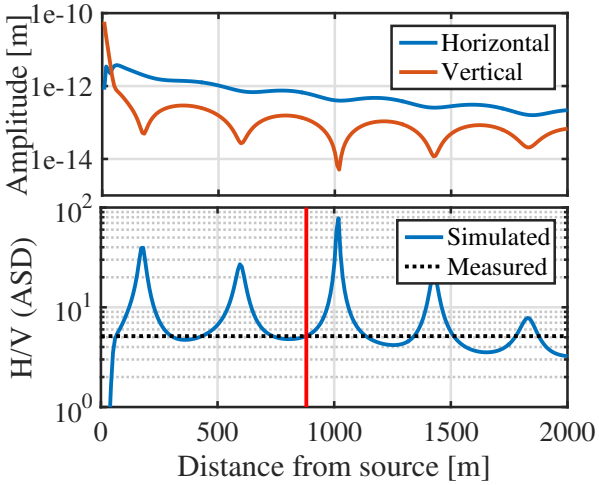

Figure 6.14: *Top: Horizontal and vertical amplitude on the surface from a single* 2.8 Hz *source exciting the soil. The Rayleigh and the reflected body waves interfere on the surface, leading to a rich structure. These structures disappear in the final representation of the ambient wave field from* 180 *sources. Bottom: Simulated H/V ratio as a function of distance from the source (blue) together with the value measured at one point at the site (dotted black). A working point of the model is marked with a red bar.*

For this model to approximate the real situation at the site, we require the horizontal to vertical PSD ratio on the surface to reproduce the conditions measured with the T240 surface sensor near to top of the borehole. To achieve this, the sources are placed at a distance from the vertical coordinate axis that is derived at each frequency individually by comparing the measured and expected ratio as a function of distance from the source (see Fig. 6.15). In addition, the distance is required to agree with source distances as indicated by beam forming of the Array A data. This means that for low frequencies the sources may be several km away, whereas at high frequencies the sources are very local and may be a few hundreds of meters from the test mass.

For most frequencies in the range of interest, that is from 1 to 20 Hz, a source distance can be determined within the desired length preferences. However, between about 3 and 5 Hz the

measured ratio can either not be reached at all or only if the source is assumed to be directly next to the surface receiver. This deviation indicates that the soil model that is used at the location of the borehole sensor - the model which is most precise in the center of array A - may not be the best representation of the geology at the borehole in this frequency range. Even though both only lie about 300 m apart, the area is known to exhibit changes in the thickness of the soft soil layer [176]. Further results of this section will substantiate the suspicion that the soil response from this model in the 3 to 5 Hz range does not lead to satisfactory agreement with the measurement results. The central radius in this frequency band is then derived according to the fit in Fig. 6.15.

The selection of the source distance is not unique. To allow for a variation in distance the sources for an individual frequency are placed within a ring of minimum radius $r_{min} = R - \lambda_R/2$ and maximum radius $r_{max} = R + \lambda_R$, where λ_R is the Rayleigh wavelength.

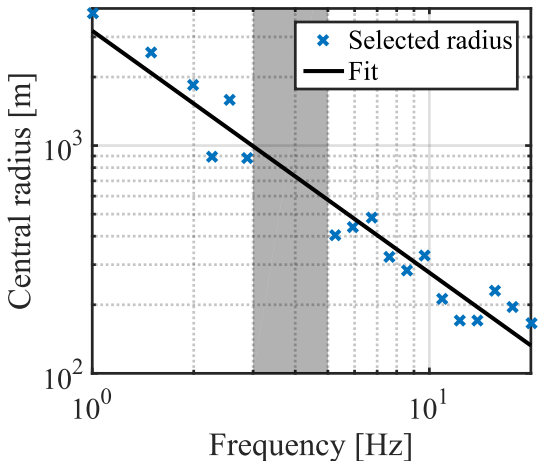

Figure 6.15: *Central radii of the source ring depending on the frequency. For each frequency, the radius has been chosen such that the H/V ratio of a single source reproduces the measurement at the center of the ring. Furthermore, the radius is required to be in agreement with beam forming results. Between about* 3 Hz *and* 5 Hz *no source distance allowed to reproduce the measured H/V ratio. This may indicate that the soil model obtained from Array A might not be an ideal representation of the subsurface composition at the location of the borehole.*

6.2.2 Beam forming and dispersion curve

The energy distribution between the fundamental and higher order modes depends on many factors: material properties of the layer such as wave speeds and attenuation factors, source mechanism and distance between source and receiver [113]. As some of these parameters cannot be obtained by the seismic studies, beam forming of synthetic data is used as an independent method to verify if the applied soil model and source distribution are a good approximation of the real situation at the site.

For the beam forming of synthetic data the soil has been excited with a ring of vertical sources as described in Section 6.2.1. The radius of the ring allows to reproduce the measured H/V ratio at the center and the ring has a width of λ_R. Inside the ring the sources are placed uniformly and their relative strength is set according to the measured beam power distribution. Beam forming and dispersion curve data are available from array A, which was sensitive to a frequency range between 2.5 and 8 Hz. As the data from the sensor array only encompass vertical displacements, the beam forming analysis was carried out on the vertical synthetic data.

Fig. 6.16, left panels, shows that beam forming of synthetic data allows to reproduce the measured beam power distribution for frequencies above 4.5 Hz. The surface wave velocity that corresponds to the beam power maximum, can be either attributed to the fundamental mode

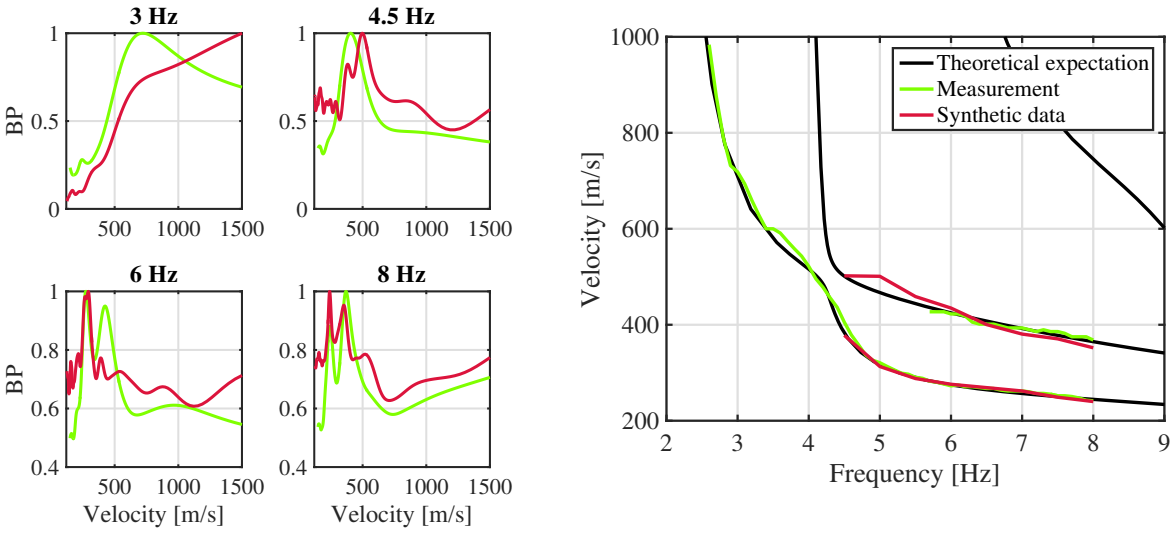

Figure 6.16: *Left: Surface wave speed and corresponding beam power (BP) of measured data (green) and synthetic data (red) for representative frequencies. Above* 4.5 Hz *the results of beam forming of measured and synthetic data are in fair agreement while for lower frequencies uncertainties in the geology model lead to deviations. Future studies that allow to include various source mechanisms and specified damping factors may lead to a better agreement. Right: The fundamental mode and first overtone dispersion curve that have been derived from beam forming of measured and synthetic data are in good agreement and follow the expected dispersion curve of the soil model.*

or to the first overtone. In the modeled data the velocity peaks of the first overtone are visible already above 4 Hz. However, the energy distribution between fundamental and higher order mode deviates from the measured value. This deviation can be attributed to unknown material damping ratios in the model and the uncertainty in the source distance. Below 4.5 Hz the beam power peak is not well recovered from the synthetic data, which can be attributed to uncertainties in the geology model for this frequency range (see Section 6.2.1).

The dispersion curve (Fig. 6.16, right panel) can be obtained by selecting the velocities corresponding to the beam power peaks of each individual frequency. Fundamental mode and first order overtone are recovered well by the source distribution of this model and are in good agreement with the theoretical expectation of the soil model. Deviations below 5 Hz in the overtone can be attributed to the uncertainties in the geology model. Since the limitations of the model only encompass a small part of the frequency range of interest for Newtonian noise, it can be concluded that the model and the applied source distribution are a realistic approximation of the actual situation at the site. In summary, we have derived a layered model that sufficiently reproduces the angular and beam power distribution of seismic sources on site, the fundamental mode and the first overtone dispersion curve and the H/V ratio.

6.2.3 Surface and underground spectra

With the source distribution obtained in the previous section, an ambient seismic field is derived with relative and absolute scaling factors as described in Section 3.3. To determine the absolute scaling factor, the horizontal PSD from synthetic data is scaled to the measured horizontal PSD of the surface borehole sensor. The model then allows to predict the vertical PSD on the sur-

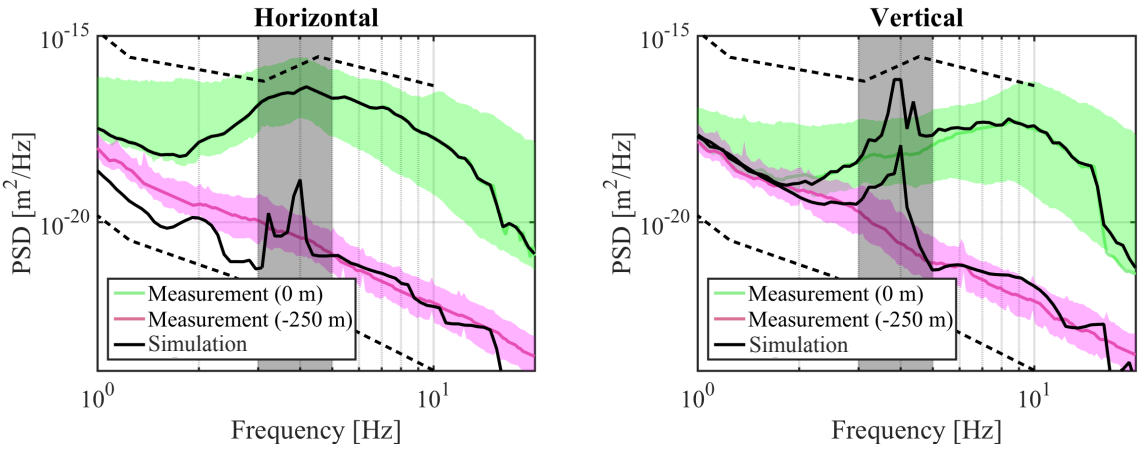

Figure 6.17: *Mode of horizontal (left panel) and vertical (right panel) PSD of simulated data in comparison to surface and subsurface data of the borehole seismometers. The transparent regions enclose the* 10^{th} *and* 90^{th} *percentiles. The absolute source strength has been set so that the simulated horizontal surface PSD exactly reproduces the measurement. The resulting simulated surface and subsurface PSDs are in good agreement with the measurement, except between* 3 *and* 5 Hz *(shaded grey). This deviation may originate from uncertainties in the subsurface geology at the borehole location. Note that the horizontal subsurface PSD exhibits an additional deviation below* 3 Hz*, which may indicate that another source mechanism may be more representative at these low frequencies.*

face and the underground PSDs for horizontal and vertical directions at 250 m depth (Fig. 6.17). Due to the location of the sources, that has been determined such that the measured H/V ratio is reproduced at the center, the simulated vertical surface and underground spectra are in good agreement with the measurement in the full frequency range except from about 3 to 5 Hz. Between 3 and 5 Hz, the model predicts an increase of PSD around 4 Hz which is not observed in

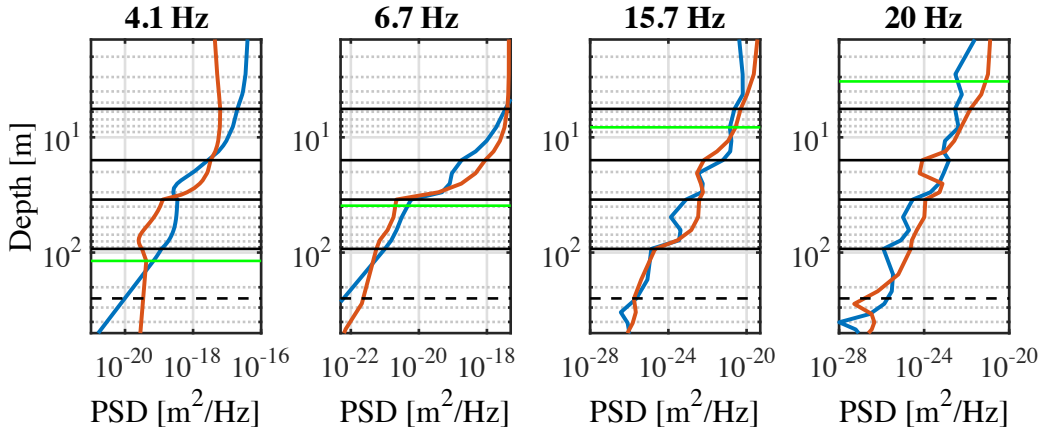

Figure 6.18: *Horizontal (blue) and vertical (red) PSD as a function of depth for representative frequencies, where the figure axes have been inverted. The subsurface layers are indicated in black and the Rayleigh wavelength in green. The depth of the test mass is indicated with a dashed black curve. At all frequencies, the displacement noise PSD difference between surface and at the depth of the test mass is several orders of magnitude. The energy of the surface waves is mostly confined to the shallow subsurface layers.*

the data. As derived in the previous discussion, this may be attributed to uncertainties in the geology model. With results from active array studies that identify the underground fault lines and a fast variation in the thickness of the soft soil layer [165] this indicates that the assumption that the horizontally layered subsurface composition at the center of the sensor array is representative for the lithology at the borehole only holds to first order. For the Newtonian noise analysis of the following section, interpolation between 3 and 5 Hz will be used to obtain a Newtonian noise result that matches the measured PSD.

The predicted horizontal underground PSD is in good agreement with the measurement above 5 Hz, where the same uncertainty in the geology leads to deviations between 3 and 5 Hz. Note that the simulated horizontal PSD exhibits an additional deviation from the measurement below 3 Hz. It has been shown that this deviation is not present for horizontal source excitations. However, the inclusion of horizontal excitations into the analysis framework was beyond the scope of this thesis, but is recommended to be pursued in future studies.

Above 15 Hz the simulated spectra drop below the measurement and surface excitations do not sufficiently reproduce the measurements anymore. This is because Rayleigh waves, which are generated on the surface, attenuate fast at these high frequencies and do not reach to a depth of 250 m and what remains are body waves (see Fig. 6.18). Body waves have large wavelengths, can be generated by surface as well as underground sources and can travel across large distances in solid rock. The underground sensor is sensitive to a superposition of body waves from nearby surface, and far way subsurface sources, all together called the body wave background. As the nature of the far away subsurface sources is not determined, they are not taken into consideration in this analysis. It is recommended to dedicate future studies on the origin, composition and modeling of this background noise, since the seismic field from the body wave background represents the baseline seismic noise in close vicinity of the test mass at high frequencies.

In summary, our model comprises a horizontally layered geology as well as a source distribution as measured at the BGN candidate site. This model is excited with vertical surface sources with a relative strength according to the measured beam power. The model reproduces fundamental mode and first over tone dispersion curve, H/V ratio as well as surface and subsurface PSDs of the borehole. Deviations between the simulation and the measurement between 3 and 5 Hz, where the measured H/V ratio cannot be reproduced, suggest that it is essential in future geology models to expand the subsurface to a complex, three-dimensional medium that encompasses a detailed study of local material damping factors. Deviations between measured and simulated underground PSDs below 3 Hz suggest that other source mechanisms than vertical excitations may be more representative at certain frequencies, deviations above 15 Hz allow for the recommendation that future models need to take a realistic contribution of the body wave background into account. To achieve this, additional seismic array and borehole studies that reveal a more complex image of the subsurface and allow for the exact identification of the location and nature of the seismic sources at the site will be necessary.

6.3 Newtonian noise

Newtonian noise is calculated by integrating over the seismic displacements in the vicinity of the test mass as derived in Eq. (3.4.8). Previous studies relied on carrying out the Newtonian noise integral in terms of finite element modeling (FEM) in homogeneous media [45, 127, 130]. This FEM approach has strict requirements in terms of grid symmetry and requires a dense spacing between the volume elements in the grid in order to calculate Newtonian noise to the

required precision. This approach may still be feasible for surface detectors, where the largest wavelength to consider is the Rayleigh wavelength. However, for underground detectors like Einstein Telescope much larger integration areas have to be considered and an evaluation of the integral via finite element modeling is computationally challenging. Compared to previous studies [45, 127], this work provides an alternative approach which yields high accuracy and an improvement in computation time of several orders of magnitude. The computation of the integral is carried out with Gaussian quadrature (see Appendix B), a numerical integration method where the integrand is approximated at n points by a set of orthonormal polynomials. If the set of polynomials is of the order $2n-1$, then the approximated integral is exact [177].

The previous section introduced the design of the seismic model, the source distribution and the determination of the relative and absolute scaling factors. Newtonian noise is then calculated with Eq. (3.4.11). The Einstein Telescope detector will be located underground at a depth between 100 and 300 m, depending on the site and the infrastructure [66]. As the final depth is not defined yet, a detector location of 250 m underground, equivalent to the depth of the borehole seismometer, has been chosen. To approximate the effect of a spherical cavern around the test mass, a minimum integration radius of 10 m is chosen. Note, that it is of importance for future work to consider arbitrary cavern sizes and shapes as well as scattering effects of seismic waves on cavern walls. Next, a maximum integration radius for the integrals in Eq. (3.4.8) needs to be determined.

Integration radius

The maximum integration radius r_{NN}^{max} is the integration distance after which Newtonian noise does not significantly change when the integration volume is increased further. Previous studies in homogeneous half-space geologies with Rayleigh waves and surface detectors have shown that an integration radius of $r_{NN}^{max} \approx \lambda_R/2$ is sufficient to reach a stable Newtonian noise level within 10 % [45]. This generalization is not evident anymore for test masses in layered geologies with realistic wave fields and for underground caverns. It is therefore derived in the following for a test mass at 250 m depth, with a spherical cavern of radius 10 m in the Limburg geology. In this model Newtonian noise is calculated as the incoherent sum of the Newtonian noise contributions from the individual seismic sources (see Eq. (3.4.11)). The r_{NN}^{max} in each frequency bin is then determined from the contribution of a single source by subsequently increasing the integration radius, starting with 250 m and reaching up to a distance where fluctuations stay within 10 % of the asymptotic value.

The maximum integration radius r_{NN}^{max} for each frequency bin for the underground test mass is displayed in Fig. 6.19. The r_{NN}^{max} exceeds λ_R across the full frequency band by at least one order of magnitude and is always larger than 250 m. This means that at all frequencies the seismic surface displacement contributes to the underground Newtonian noise, even though the Rayleigh wavelengths may be much shorter than the distance between surface and test mass.

Note, that r_{NN}^{max} also surpasses the central radius of the source ring, which means that the sources are included in the integration volume. This is a reasonable assumption, as beam forming analysis has shown that the noise sources are very local and in the close vicinity of the sensor array. Increasing the source distances to remove them from the Newtonian noise integration area is in principle possible, but will not allow to reproduce the measured H/V PSD ratio at the central part of the model, which is in turn crucial to reproduce the measured PSDs near the test mass.

Newtonian noise is derived from the incoherent sum of the contributions of the individual

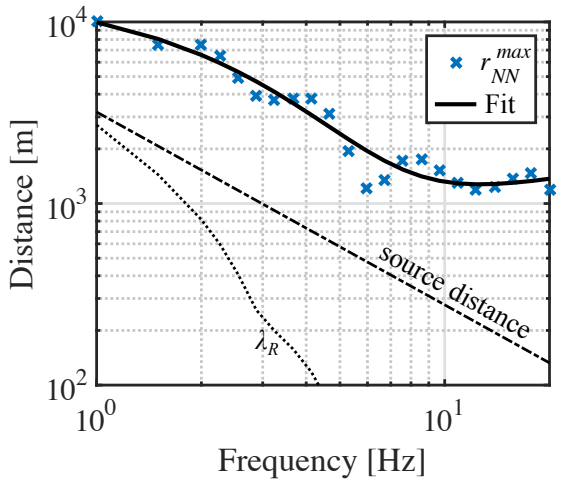

Figure 6.19: *Maximum integration radius r_{NN}^{max} for a test mass located at 250 m depth in the Limburg geology depending on the frequency. The r_{NN}^{max} exceeds the central radius of the source ring, which means that the sources are included within the integration volume. To avoid a bias from high displacements near the source, an area with radius $\lambda_R/2$ around the test mass is padded with a linear interpolation in the Newtonian noise integral.*

sources where each individual numerical integral is approximated by a weighted sum over a discrete number of points within the integration volume (see Eq. (B.6) in Appendix B). Less than 2 % of these discrete points are within an area of radius $\lambda_R/2$ from the source. To avoid a bias due to the excess displacement in the vicinity of the source, all seismic displacements within $\lambda_R/2$ are excluded. If a discrete integration point is located in this area, its displacement is determined by a linear interpolation based on the displacement field outside the excluded source area. For example, for a 3 Hz source located at about 1 km from the center, seismic displacements are excluded in an area of radius 100 m, which contains less than 1 % of the integration points. Due to the small percentage of discrete points within the $\lambda_R/2$ area, the resulting Newtonian noise differs less than a factor 2 from the Newtonian noise that is derived without the exclusion area

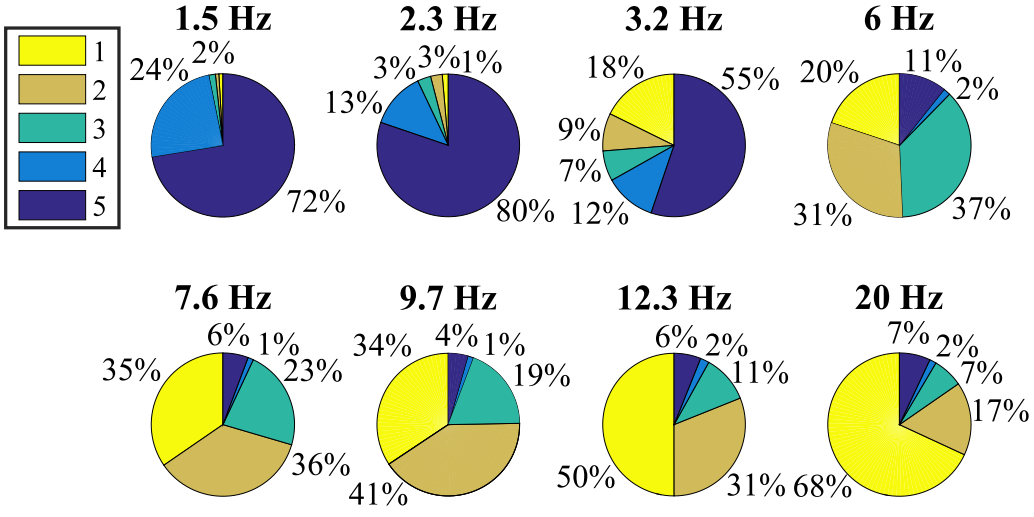

Figure 6.20: *Relative Newtonian noise contribution of each individual layer to the total Newtonian noise for selected frequencies from 1 to 20 Hz. In the color scale, 1 denotes the top layer and 5 the bottommost layer (see Table 6.1.2). Percentages below 1% have been omitted. At low frequencies the Newtonian noise originates mostly from the bottom layer in which the test mass is emerged, while at high frequencies surface layers dominate.*

around the test mass.

As r_{NN}^{max} depends on the frequency, so does the Newtonian noise contribution from each individual layer (see Fig. 6.20). At low frequencies, Newtonian noise from the bottommost layer, in which the test mass is located, is dominant. At these frequencies the wavelength of the Rayleigh waves are of the order of 1 km and only attenuate well significantly below the test mass. Their amplitudes dominate the wave field, even at the depth of the test mass, and thus the Newtonian noise from the bottommost layer is most significant. As the frequency increases, the Rayleigh wave amplitudes attenuate faster with depth and become less important for the wave field at the test mass. Thus the contribution of the bottommost layer to the Newtonian noise gradually decreases. For frequencies above about 5 Hz Rayleigh waves do not reach the test mass. The nearby wave field then consists of body waves with amplitudes that are several

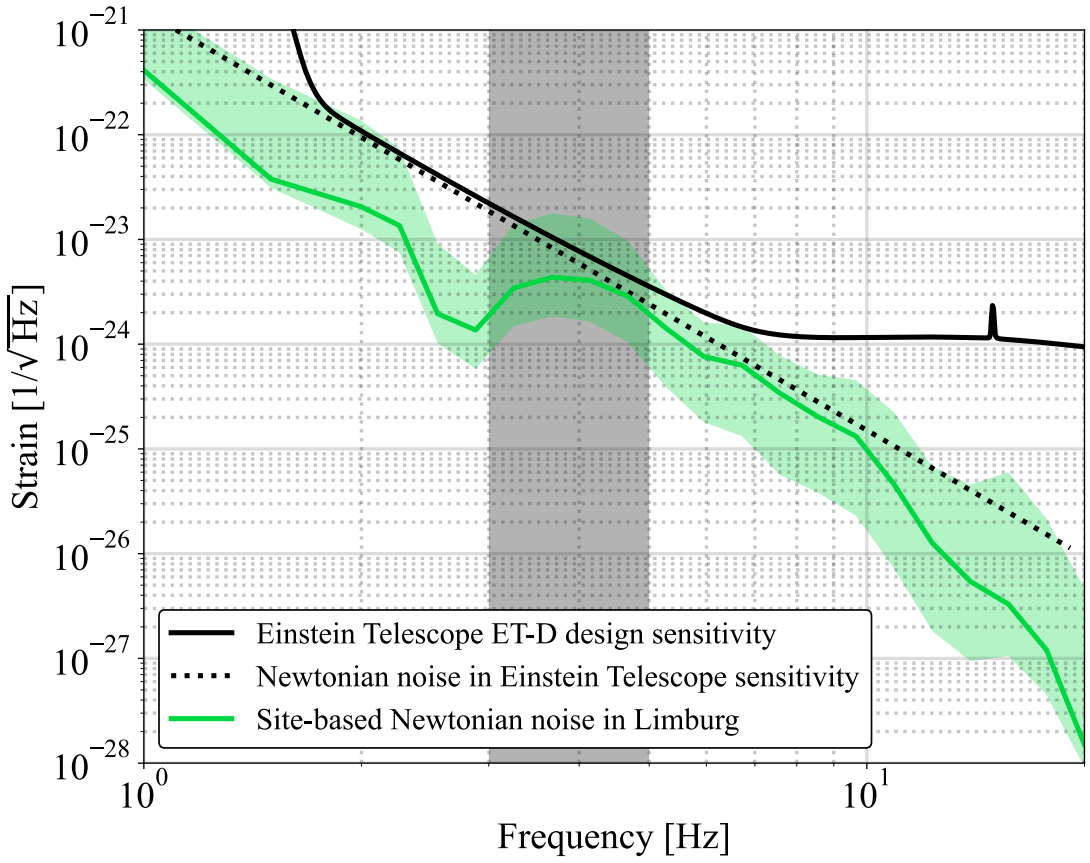

Figure 6.21: *Site-based Newtonian noise at the BGN candidate site in Limburg for a test mass at* 250 m *depth with a cavern radius of* 10 m*. It is within its* 90^{th} *percentile compatible with the Einstein Telescope ET-D sensitivity curve across the full frequency range. In the frequency band from* 3 *to* 5 Hz *it represents an upper limit to the Newtonian noise estimate due to uncertainties in the geology model in this frequency range. At frequencies above* 5 Hz *the site-based Newtonian noise rapidly decreases due to the decreasing wavelength of the waves in the dominant surface layer. From the viewpoint of Newtonian noise, the conditions at the BGN candidate site offer suitable conditions to host the Einstein Telescope detector.*

orders of magnitude lower than the amplitudes of the far away surface waves (see Fig. 6.18). Even though the surface layers are at great distance from the test mass, their contribution to the total Newtonian noise gains increasingly in significance with increasing frequency, due to the high amplitudes of the waves confined in them. This means that if Newtonian noise is to be suppressed at frequencies above about 6 Hz, the distance to the surface needs to be increased.

Site-based Newtonian noise at the BGN candidate site in Limburg

We have estimated the site-based Newtonian noise for Einstein Telescope at the BGN candidate site in Limburg (see Fig. 6.21) in a realistic, horizontally layered geology that is excited with 180 vertical seismic noise sources. The Newtonian noise has been calculated according to Eq. (3.4.12) and using Gaussian quadrature to perform the numerical integral. This calculation was based on an ambient seismic field that reproduces the beam power as well as the surface and underground PSDs that have been measured during the field studies described in Section 6.1. The test mass was placed at a depth of 250 m underground and surrounded by a spherical cavern of radius 10 m.

Fig. 6.21 shows that the overall site-based Newtonian noise in Limburg, including the 90^{th} percentile, is compatible with the ET-D Einstein Telescope sensitivity curve as in [66, 69]. At frequencies below 3 Hz the site-based Newtonian noise of the 90^{th} percentile is predicted to be approximately equal to the Einstein Telescope design sensitivity curve. Here, Rayleigh wavelengths are large and the seismic waves in the bottommost layer give the dominant contribution to Newtonian noise estimates. The dip just before 3 Hz is an artifact of the underestimated horizontal underground displacement in the seismic model at low frequencies (see Fig. 6.17). In the intermediate band from 3 Hz to 5 Hz, seismic amplitudes are highly uncertain due to the ambivalence in the geology model and as a result the Newtonian noise in this area can be considered as lower limit. At frequencies above about 5 Hz, surface waves in the top layers are the main contributor to the total Newtonian noise level. Their wavelength decreases with increasing frequency, and thus the ratio of test mass depth and wavelength increases. As a result Newtonian noise decreases with increasing frequency.

The Newtonian noise curve that enters the Einstein Telescope sensitivity has been derived from Eq. (3.5.3), where $\beta = 0.58$, $\rho = 5000\ \frac{\text{kg}}{\text{m}^3}$ and where the expone ntial term containing the test mass height has been omitted [66]. This model has been derived for a surface detector that is surrounded by a half-spherical cavern of a frequency dependent radius of $\lambda/4$, where λ

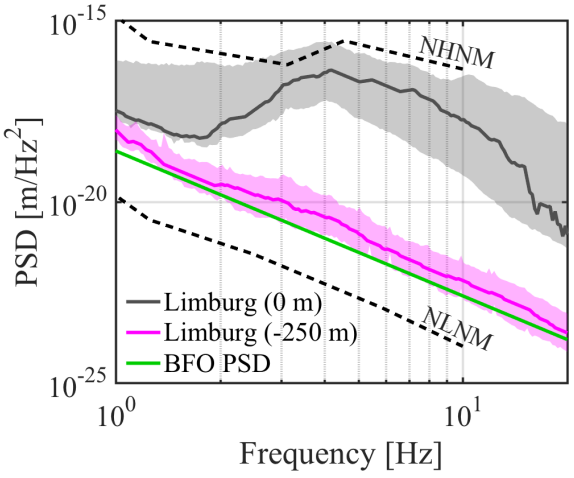

Figure 6.22: *Horizontal PSD at* 250 m *depth measured at the BGN candidate site in Limburg in comparison to the* 10^{th} *percentile of the PSD measured underground during night times at* 95 m *depth at the Black Forest Observatory (BFO). This BFO PSD was used to derive the Newtonian noise estimate in the ET-D Einstein Telescope sensitivity. The* 10^{th} *percentile of the underground PSD in Limburg is compatible with the BFO PSD.*

represents the wavelength of the constant seismic field. Even though this model does not apply for an underground detector it has been used in the Einstein Telescope sensitivity curve and makes out the basis of numerous scientific studies [69, 127, 129, 178]. Therefore it is shown here as reference.

The seismic displacement that is used in this Newtonian noise reference curve corresponds to $5 \times 10^{-10} \frac{1}{f^2} \frac{\mathrm{m}}{\sqrt{\mathrm{Hz}}}$ and it corresponds to a fit of the 10^{th} percentile of the ambient seismic noise spectrum measured during night time at 95 m depth at the Black Forest underground observatory (BFO) in Germany [45, 69]. Note that even though the 10^{th} percentile of the underground PSD at the BGN candidate site is compatible with the BFO PSD (see Fig. 6.22), the 10^{th} percentile of the site-based Newtonian noise is about one order of magnitude below the Newtonian noise of the Einstein Telescope sensitivity. This shows that it is not enough to only consider PSDs in a comparison between candidate sites for Einstein Telescope, but that it is highly significant to derive Newtonian noise estimates that take into consideration the geological and seismic conditions that are characteristic to the candidate site.

6.4 Summary and conclusion

Einstein Telescope aims to extend the low frequency limit of gravitational wave detectors to as low as 2 Hz and simultaneously increase the strain sensitivity by one order of magnitude. The consequential increase in sensitivity will lead to a significant improvement of the detection distance and rate of gravitational wave events. Probing the dark ages of the Universe, Einstein Telescope at its design sensitivity will allow measuring BNS events at redshifts higher than 10 and stellar-mass BBH events to a redshift of up to 100 [67].

To fulfil these ambitious sensitivity goals at low frequencies, it is of highest importance that Newtonian noise at the prospective candidate site, which represents the dominant noise source below 20 Hz, is well understood and modeled. Therefore, the site-based Newtonian noise for the BGN Einstein Telescope candidate site in Limburg has been derived from a full solution of the wave equation in a horizontally layered geology. The ambient seismic field model for this estimate has been derived from a model that comprises the five-layered subsurface geology, seismic source distribution and PSDs, that have been measured during a series of seismic array and borehole studies at the candidate site. Future models are recommended to be expanded to a three-dimensional subsurface geology to account for structures that deviate from horizontal layers such as fault lines, to include horizontal in addition to vertical source excitations and to include a mechanism that accounts for the body wave background at high frequencies. This method leads to a Newtonian noise estimate, which is compatible with the design sensitivity reported in the Einstein Telescope Conceptual Design Report [66]. From the perspective of Newtonian noise, this makes the region in Limburg suitable to host Einstein Telescope.

It has further been shown that in order to compare candidate sites in their adequacy to host Einstein Telescope, it is not sufficient to compare PSD measurements. A suitable comparison requires deriving Newtonian noise based on a realistic seismic field that includes all solutions of the wave equation and is derived from a geology that includes subsurface structures and seismic noise sources that are characteristic for each detector site. In addition to these prerequisites, future Newtonian noise models are recommended to encompass complex, three-dimensional subsurface structures, damping factors derived from measurements, a variety of source mechanisms, and studies showing the influence of a variety of cavern shapes on the site-based Newtonian noise.

Chapter 7

Conclusion and outlook

Gravitational waves are ripples in the curvature of spacetime, a phenomenon that has been predicted as a consequence of Einstein's theory of general relativity in 1915. Even though their effects have long been believed to be extremely difficult to observe, the LIGO-Virgo Collaboration achieved the first, direct detection of gravitational waves in 2015, one hundred years after the formulation of general relativity. Since then, weekly detections of gravitational waves from binary black hole merger systems have become the standard. These detections are complemented by the rare measurement of a few gravitational wave events per year from neutron star merger systems.

The measurement of gravitational waves is facilitated by a global network of ground-based laser interferometers. This network consists of three detectors which are close to reaching their final upgrade phase within the advanced detector generation, one detector that recently joined the network and one test facility that contributes though its Astrowatch program. Optimizing these detectors such that their operational sensitivity matches their design goal is achieved by identifying, measuring and mitigating technical noise sources like electronic or control noise. At present, the sensitivity of Advanced Virgo is only limited by fundamental noise sources at high frequencies, whereas technical noise sources still remain to be identified and eliminated at low and mid frequencies (see Chapter 2).

With the advanced detectors reaching their design sensitivity, a comprehensive understanding of the fundamental limitations gains increasing importance. Newtonian noise, a direct coupling between fluctuations in the gravitational field surrounding the detector and the test masses, places a strict bound on the low frequency sensitivity of any ground-based gravitational wave detector. In this thesis we considered seismic noise as the source of these fluctuations. As the seismic field is characterized by a location's geology and anthropogenic noise source distribution, the associated Newtonian noise estimate depends on a detailed insight into these site specific properties. With these parameters at hand, a model of the ambient seismic field of a given detector site, comprising surface and body waves, can be derived from the solution of the elastodynamic wave equation - a differential equation that can be solved numerically for any complex geology. Using numerical integration, Newtonian noise can then be derived for any test mass location within this seismic field (see Chapter 3). The corresponding knowledge of subsurface composition and source distribution at a given site can be obtained with minimal intrusion through the deployment of large surface arrays of seismic sensors (see Chapter 4).

A dedicated seismic array study at the Advanced Virgo site in Cascina, Italy, revealed nine distinct subsurface layers and seismic noise sources related to road-bridges on the nearby high-

ways and a nearby wind park. With this information, a seismic model was derived that reproduces the characteristic spectra of the wider area around the detector. This site-based Newtonian noise estimates shows that below 8 Hz Newtonian noise is underestimated and above 10 Hz it is overestimated by the existing Newtonian noise reference curve in the design sensitivity of Advanced Virgo (see Chapter 5). This disagreement is attributed to the simplified geology, seismic field and Newtonian noise calculation routine that has been used to derive the reference Newtonian noise. Furthermore, it is shown that anthropogenic activity on the detector site leads to an increase in seismic and hence Newtonian noise at frequencies above 5 Hz. It is thus necessary to mitigate noise from for example heating, ventilation and air conditioning systems in order to reach the ultimate detector performance that is possible at EGO, the site of the Advanced Virgo detector.

Site selection for the European Einstein Telescope underground gravitational wave observatory is an ongoing process and the scientific arguments which speak for a specific site are affected by its Newtonian noise level. The Belgian-German-Dutch (BGN) candidate site in Limburg has been characterized by several surface array studies, which revealed five distinct subsurface layers and identified nearby farm populations as the main seismic noise sources of the area. A borehole study with a depth of 135 m led to a detailed understanding of the local geology and a borehole to 250 m allows for simultaneous measurement of surface and underground seismic spectra. This information resulted in a seismic model of the site and in a Newtonian noise estimate which shows that the BGN site is compatible with the Newtonian noise specification set for the sensitivity of Einstein Telescope (see Chapter 6).

In this dissertation it has been shown that Newtonian noise depends on the seismic conditions which are unique to each detector site. A model that derives this so called site-based Newtonian noise for a given detector site should encompass local geology, seismic sources and spectral measurements for the site under investigation. If all these parameters are taken into consideration, then a realistic Newtonian noise estimate for surface and underground detectors can be obtained.

In this work, geologies have been assumed to be horizontally layered, neglecting the presence of more complex underground structures. Future work should evolve this geology model and determine the influence of additional parameters such as fault lines, underground rock structures, water levels and source mechanisms on the Newtonian noise level. This analysis also showed that the inclusion of a body wave background to the seismic field model will be of relevance for future studies. Additional focus should be given to the size and shape of the caverns hosting underground detectors - as their boundary between soil and air is closest to the test mass and comprises the largest density gradient - as well as to the inclusion of scattering of seismic waves on the cavern walls.

Finally, it will not be feasible to completely mitigate anthropogenic noise at any detector site. To reach a site specific minimum Newtonian noise level, permanent seismic sensor arrays will need to be in place around the test mass and on the surface for an online subtraction of Newtonian noise from the output signal of the gravitational wave interferometer. For maximum information about the surrounding wave field the sensors deployed in the network should furthermore comprise sensing elements in horizontal as well as vertical direction. The development of this technology and software is ongoing research and will be tested within the upgrade of Advanced Virgo.

Appendix

A The elastodynamic wave equation in the fk-domain

Here the conversion of the representation of the elastodynamic wave equation from the time-space domain to the frequency-wave number (fk) domain is derived for the example of a plane wave that is propagating in the x_1x_3-plane in Cartesian coordinates. It is based on the argumentation found in [118]; similar derivations hold for spherical coordinates and for arbitrary wave propagation.

The elastodynamic wave equation in the time-space domain (Eq. (3.1.11)) is

$$\sum_{j=1}^{3}\left((\lambda+\mu)\frac{\partial^2 u_j}{\partial x_i \partial x_j}+\mu\frac{\partial^2 u_i}{\partial x_j \partial x_j}\right)=\rho\frac{\partial^2 u_i}{\partial t^2}, \tag{A.1}$$

where $\vec{u}=(u_1,u_2,u_3)$ denotes the displacement field. For a wave vector in the x_1x_3-plane and a displacement field that is constant in x_2, this corresponds to three equations

$$\begin{bmatrix}(\lambda+2\mu)\frac{\partial^2 u_1}{\partial x_1^2}+(\lambda+\mu)\frac{\partial^2 u_3}{\partial x_1 \partial x_3}+\mu\frac{\partial^2 u_1}{\partial x_3^2}\\ \mu\frac{\partial^2 u_2}{\partial x_1^2}+\mu\frac{\partial^2 u_2}{\partial x_3^2}\\ \mu\frac{\partial^2 u_3}{\partial x_1^2}+(\lambda+\mu)\frac{\partial^2 u_1}{\partial x_1 \partial x_3}+(\lambda+2\mu)\frac{\partial^2 u_3}{\partial x_3^2}\end{bmatrix}=\rho\begin{bmatrix}\frac{\partial^2 u_1}{\partial t^2}\\ 0\\ \frac{\partial^2 u_3}{\partial t^2}\end{bmatrix}. \tag{A.2}$$

As a next step it is common to modify the displacement vector to $\vec{u}\rightarrow\vec{\mathfrak{u}}(u_1,u_2,-iu_3)$ so that $u_1=\mathfrak{u}_1,\ u_2=\mathfrak{u}_2,\ u_3=i\mathfrak{u}_3$. This will ensure in the later calculations that the stiffness matrix is symmetric. As a result Eq. (A.2) becomes

$$\begin{bmatrix}(\lambda+2\mu)\frac{\partial^2 \mathfrak{u}_1}{\partial x_1^2}+i(\lambda+\mu)\frac{\partial^2 \mathfrak{u}_3}{\partial x_1 \partial x_3}+\mu\frac{\partial^2 \mathfrak{u}_1}{\partial x_3^2}\\ \mu\frac{\partial^2 \mathfrak{u}_2}{\partial x_1^2}+\mu\frac{\partial^2 \mathfrak{u}_2}{\partial x_3^2}\\ \mu\frac{\partial^2 \mathfrak{u}_3}{\partial x_1^2}-i(\lambda+\mu)\frac{\partial^2 \mathfrak{u}_1}{\partial x_3 \partial x_1}+(\lambda+2\mu)\frac{\partial^2 \mathfrak{u}_3}{\partial x_3^2}\end{bmatrix}=\rho\begin{bmatrix}\frac{\partial^2 \mathfrak{u}_1}{\partial t^2}\\ 0\\ \frac{\partial^2 \mathfrak{u}_3}{\partial t^2}\end{bmatrix}. \tag{A.3}$$

In the next step Eq. (A.3) is transformed from the space-time domain to the wave number-frequency domain, making use of Eq. (3.1.32) and Eq. (3.1.34). This means that every derivative with respect to time is replaced by a factor $i\omega$ and every derivative with respect to x_1 is replaced by a factor $-ik_{x_1}$. For simplicity, the same letter $\vec{\mathfrak{u}}$ for the displacement is used in the following, but now it refers to the frequency-wave number representation of the displacement. Equation (A.3) then becomes

$$\begin{bmatrix}-k_{x_1}^2(\lambda+2\mu)\mathfrak{u}_1-k_{x_1}(\lambda+\mu)\frac{\partial \mathfrak{u}_3}{\partial x_3}+\mu\frac{\partial^2 \mathfrak{u}_1}{\partial x_3 \partial x_3}\\ -k_{x_1}^2\mu\mathfrak{u}_2+\mu\frac{\partial \mathfrak{u}_2}{\partial x_3 \partial x_3}\\ -k_{x_1}^2\mu\mathfrak{u}_3+k_{x_1}(\lambda+\mu)\frac{\partial \mathfrak{u}_1}{\partial x_3}+(\lambda+2\mu)\frac{\partial^2 \mathfrak{u}_3}{\partial x_3 \partial x_3}\end{bmatrix}=-\omega^2\rho\begin{bmatrix}\mathfrak{u}_1\\ 0\\ \mathfrak{u}_3\end{bmatrix}. \tag{A.4}$$

And this can be further re-expressed in matrix notation as

$$-k_{x_1}^2\mathbf{A}\vec{\mathfrak{u}}-k_{x_1}\mathbf{B}\frac{\partial\vec{\mathfrak{u}}}{\partial x_3}+\mathbf{C}\frac{\partial^2\vec{\mathfrak{u}}}{\partial x_3^2}=-\omega^2\rho\vec{\mathfrak{u}},\ \text{where} \tag{A.5}$$

$$\mathbf{A}=\begin{bmatrix}\lambda+2\mu & 0 & 0\\ 0 & \mu & 0\\ 0 & 0 & \mu\end{bmatrix},\ \mathbf{B}=\begin{bmatrix}0 & 0 & -(\lambda+\mu)\\ 0 & 0 & 0\\ \lambda+\mu & 0 & 0\end{bmatrix},\ \mathbf{C}=\begin{bmatrix}\mu & 0 & 0\\ 0 & \mu & 0\\ 0 & 0 & \lambda+2\mu\end{bmatrix}.$$

B Numerical integration with Gaussian quadrature

The numerical integration method employed of this work approximates the solution to the definite integral

$$\int_{-1}^{1} f(x)\ dx \approx \sum_{j=0}^{N-1} w_j f(x_j), \tag{B.1}$$

where $f(x)$ is a continuous function across the interval $[-1, 1]$, as a weighted sum of N values of $f(x_j)$, evaluated at the abscissas x_j and multiplied with the corresponding weights w_j. In the literature, this method is referred to as *Gaussian quadrature* [177]. The abscissa values $x_0, .., x_{N-1}$ in Eq. (B.1) can be understood as the zero-crossings of a polynomial of order N, that is part of a set of orthonormal polynomials $p_0, .., p_N$ in the interval $[a, b]$. When the polynomial is known, then first zero-crossings can are calculated and in the next step the weights are derived by solving

$$\int_{-1}^{1} p_j(x)\ dx = \sum_{i=0}^{N-1} w_i p_j(x_i) \tag{B.2}$$

for the $j = 0, ..N$ polynomials. These weights and abscissa values can now be used to approximate any function $f(x)$ with Eq. (B.1). It can be shown that with those values Eq. (B.1) is exact for all polynomials of degree $2N - 1$ or lower [177]. Furthermore, this numerical integration method converges exponentially with the order N.

A standard method utilizes Gauss-Legendre polynomials for the Gaussian quadrature routine, where a polynomial of order j is defined recursively as

$$\begin{gathered}(j+1) \cdot p_{j+1} = (2j+1) \cdot x \cdot p_j - j \cdot p_{j-1}, \\ \text{where } p_0(x) = 1 \text{ and } p_1(x) = x,\end{gathered} \tag{B.3}$$

and where $-1 \leq x \leq 1$. The polynomial of order j has j zero-crossings which are labeled with x_j and the corresponding weights are then calculated as

$$w_j = \frac{2}{(1 - x_j^2) \cdot p'_N(x_j)}, \tag{B.4}$$

where $p'_N(x_j)$ is the derivative of the polynomial at its zero-crossing x_j. For an integral over $[a, b]$ Eq. (B.1) can be rewritten as

$$\int_a^b f(x)\ dx \approx \frac{b-a}{2} \sum_{j=0}^{N-1} w_j f(\frac{b-a}{2} x_j + \frac{b+a}{2}). \tag{B.5}$$

Multi-dimensional integrals, like surface or volume integrals with $f(r, \theta, \phi)$, can be evaluated as nested loops over several dimensions as

$$\int_V r^2 \sin\theta f(r, \theta, \phi)\ \ dV = \sum_k w_k \left(\sum_i w_i r_i^2 \ \big(\sum_j w_j \sin(\theta_j) f(r_i, \theta_j, \phi_k) \big) \right) \tag{B.6}$$

where (r, θ, ϕ) are the variables of spherical coordinate representations and where corresponding i, j, k are the indices of the Gauss-Legendre polynomials.

C Saulson's analytic seismic Newtonian noise model

This section summarizes the derivation of Saulson's analytical model for seismic Newtonian noise as presented in [124], based on remarks elaborated in [179].

Volume contribution

A test mass at $h = 0$ is assumed to be located on the surface of a homogeneous half-space with density ρ. According to Newton's second law, a density fluctuation ΔM near the test mass translates to a force on the test mass as

$$\frac{\vec{F}}{m} = G\frac{\Delta M}{r^2}\hat{r}. \tag{C.1}$$

The component parallel to one detector arm is expressed as

$$\frac{F_x}{m} = G\frac{\Delta M}{r^2}\cos\theta = G\frac{\Delta M}{r^2}\cos\phi\sin\gamma, \tag{C.2}$$

where θ is is the angle between $\hat{r}$ and the x-axis, ϕ is the azimuth angle of the orthogonal projection of $\hat{r}$ in the xy-plane and γ is the polar angle (see Fig. 1).

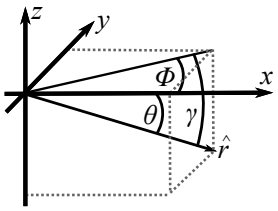

Figure 1: *Schematic of the geometry. The angle θ is between $\hat{r}$ and the x-axis, ϕ is the azimuth angle of the orthogonal projection of $\hat{r}$ in the xy-plane and γ is the polar angle.*

The half-space is assumed to be filled with patches of size $\lambda/2$ that are fluctuating independent of each other as a result of constant P-waves. The force on the test mass from all these patches is then expressed by the quadratic sum over the individual contributions as

$$\left((\omega_0^2-\omega^2)^2+\frac{\omega}{\tau^2}\right)|\Delta x|^2 = G^2\big|\Delta M\big|^2\sum_i \frac{\cos^2\phi_i\sin^2\gamma_i}{r_i^4}, \tag{C.3}$$

where the force on the test mass m on the left side of the equation has been replaced by the equation of motion of a harmonic oscillator with resonant frequency ω_0, damping time τ and displacement $|\Delta x|$ of the test mass. The sum in Eq. (C.3) can be evaluated by approximating it as an integral, with a lower cutoff radius of $\lambda/4$ to avoid a singularity, as

$$\begin{aligned}\sum_i \frac{\cos^2\phi_i\sin^2\gamma_i}{r_i^4}\frac{dV_i}{dV_i} &\simeq \int_V dV\ \frac{\cos^2\phi\sin^2\gamma}{r^4}\frac{1}{(\lambda/2)^3}\\ &= \frac{8}{\lambda^3}\int_{r=\lambda/4}^{R}\int_{\phi=0}^{2\pi}\int_{\gamma=0}^{\pi/2}\ \frac{\cos^2\phi\sin^2\gamma}{r^4}r^2\sin\gamma\ dr d\phi d\gamma\\ &= \frac{64\pi}{3\lambda^4} = \frac{64\pi}{3v^4}\left(\frac{\omega}{2\pi}\right)^4\end{aligned} \tag{C.4}$$

where $\lambda = 2\pi v/\omega$, with v being the velocity of the wave, and Eq. (5) in [124] deviates from the last expression by a factor π.

Next, we would like to find the connection between mass fluctuation ΔM and seismic displacement ΔX. Assuming that the displacement corresponds to the maximum amplitude of the wave, the total amount of mass flowing in- and out of the volume element can be expressed as

$$|\Delta M|^2 = \left|2\Delta X \left(\frac{\lambda}{2}\right)^2 \rho\right|^2 = \rho^2 \frac{\lambda^2}{4} |\Delta X|^2, \tag{C.5}$$

which differs by a factor $\frac{\pi}{4} \approx 0.79$ from Eq. (11) in [124]. Other assumptions such as ΔX corresponding to the RMS value or to the average displacement across the patch result in an even larger difference by a factor $\frac{\pi}{2} \approx 1.57$ and $\frac{\pi^3}{16} \approx 1.94$. In the following we will therefore assume that Eq. (C.5) and Eq. (11) are sufficiently equivalent and continue with the expression for ΔM as in [124].

Since the seismic wavelength is short in comparison to the baseline of the interferometer we can approximate

$$\left((\omega_0^2 - \omega^2)^2 + \frac{\omega}{\tau^2}\right) |\Delta x|^2 \approx \omega^4 |\Delta x|^2, \tag{C.6}$$

and using this in Eq. (C.3) together with Eq. (C.4) and multiplying an additional factor 4 to account for the four independent test masses, then allows to express the displacement Newtonian noise due seismic density fluctuations as

$$|\Delta x|^2 = \frac{16\pi^2}{3} \frac{G^2 \rho^2}{\omega^4} |\Delta X|^2 \ \ [\mathrm{m}^2/\mathrm{Hz}], \tag{C.7}$$

which is equivalent to Eq. (21) in [124].

Remark concerning the surface contribution

Furthermore, vertical displacement ΔZ is assumed to have an effect on horizontal displacement at the interface between soil and air. It is derived by casting the sum to an integral over the surface as

$$\begin{aligned} \sum_i \frac{\cos^2\phi_i \sin^2\gamma_i}{r_i^4} \frac{dA_i}{dA_i} &\simeq \int_A dA \, \frac{\cos^2\phi}{r^4} \frac{1}{(\lambda/2)^2} \\ &= \frac{4}{\lambda^2} \int_{r=\lambda/4}^{R} \int_{\phi=0}^{2\pi} \frac{\cos^2\phi}{r^4} r \, dr d\phi \\ &= \frac{32\pi}{\lambda^4} \end{aligned} \tag{C.8}$$

where $\sin\gamma_i = 1$ and which differs by a factor 4 from Eq. (13) in [124]. The resulting displacement of the test mass is then calculated as previously and is obtained to be

$$|\Delta x|^2 = 2\pi^2 \frac{G^2 \rho^2}{\omega^4} |\Delta Z|^2. \tag{C.9}$$

Due to the additional factor π in comparison to Eq. (16) in [124], Eq. C.9 is only about a factor 3 smaller than Eq. (C.7) instead of an order of magnitude, as estimated in [124]. This means that the Newtonian noise due to density fluctuations on the interface between soil and air may be underestimated in [124].

Bibliography

[1] J. Weisberg, J. Taylor, and L. Fowler. Gravitational waves from an orbiting pulsar. *Scientific American*, 245, 1981.

[2] B. P. Abbott et al. (The LIGO Scientific Collaboration and the Virgo Collaboration). Observation of Gravitational Waves from a Binary Black Hole Merger. *Phys. Rev. Lett.*, 116(061102), 2016.

[3] *Philosophiae Naturalis Principia Mathematica*. I. Newton, 1687.

[4] A. Einstein. Die Feldgleichungen der Gravitation. *Sitzungberichte der Preussischen Akademie der Wissenschaften zu Berlin*, pages 844–847, 1915.

[5] A. Einstein. Zur Elektrodynamik bewegter Körper. *Annalen der Physik*, 322(10):981–921, 1905.

[6] A. Michelson and E. Moreley. On the Relative Motion of the Earth and the Luminiferous Ether. *American Journal of Science*, 34:333–345, 1887.

[7] M. Maggiore. *Gravitational waves. Volume 1: Theory and experiments*. Oxford University Press, 2008.

[8] T. Baumgarte et al. Learning about compact binary merger: The interplay between numerical relativity and gravitational-wave astronomy. *Phys. Rev. D*, 2007.

[9] J. K. Taylor and J. M. Weisberg. Further Experimental Tests of Relativistic Gravity Using the Binary Pulsar PSR 1913+16. *Astrophysical Journal*, 345:434, 1989.

[10] R. Prix. *Gravitational Waves from Spinning Neutron Stars*, volume 357. Astrophysics and Space Science Library, 2009.

[11] D. R. Lorimer. The Galactic population and birth rate of radio pulsars. In *Young Neutron Stars and Their Environments (IAU Symposium 218, ASP Conference Proceedings)*, 2004.

[12] B. P. Abbott et al. (The LIGO Scientific Collaboration and the Virgo Collaboration). Upper limits on gravitational wave emission from 78 radio pulsars. *Phys. Rev. D*, 76(04200), 2008.

[13] S. E. Woosley. Gamma-ray bursts from stellar mass accretion disks around black holes. *The Astrophysical Journal*, 405:273, 1993.

[14] S. E. Woosley and J. S. Bloom. The Supernova Gamma-Ray Burst Connection. *Annual Review of Astronomy & Astrophysics*, 44(1):507–556, 2006.

[15] B. Giacomazzo et al. Compact binary progenitors of short gamma-ray bursts. *The Astrophysical Journal Letters*, 762(2), 2012.

[16] N. Christensen. Stochastic gravitational wave backgrounds. *Reports on Progress in Physics*, 82(1), 2018.

[17] B. P. Abbott et al. (The LIGO Scientific Collaboration and the Virgo Collaboration). GWTC-1: A Gravitational-Wave Transient Catalog of Compact Binary Mergers Observed by LIGO and Virgo during the First and Second Observing Runs. *Phys. Rev. X*, 9(031040), September 2019.

[18] S. A. Usman et al. The PyCBC search for gravitational waves from compact binary coalescence. *Classical and Quantum Gravity*, 33(21), October 2016.

[19] S. Sachdev et al. The GstLAL Search Analysis Methods for Compact Binary Mergers in Advanced LIGO's Second and Advanced Virgo's First Observing Runs. *https://arxiv.org/abs/1901.08580*, 2019.

[20] S. Klimenko et al. Method for detection and reconstruction of gravitational wave transients with networks of advanced detectors. *Phys. Rev. D*, 93(042004), 2016.

[21] A. H. Nitz et al. Detecting binary compact-object mergers with gravitational waves: Understanding and Improving the sensitivity of the PyCBC search. *The Astrophysical Journal*, 849(2), 2017.

[22] R. Meyer and M. Russel. *Bayesian Analysis of Gravitational Wave Data*. Wiley StatsRef: Statistics Reference Online, 2018.

[23] S. Fairhurst. Source localization with an advanced gravitational wave detector network. *Classical and Quantum Gravity*, 28(10), 2011.

[24] B. F. Schutz. Networks of gravitational wave detectors and three figures of merit. *Classical and Quantum Gravity*, 28(12), 2011.

[25] LIGO-Virgo Gravitational Wave Candidate Event Database. `https://gracedb.ligo.org/latest/` and `http://chirp.sr.bham.ac.uk/`. Last checked: 09.03.2020.

[26] T. Adams. Low latency search for compact binary coalescences using MBTA. *https://arxiv.org/abs/1507.01787*, 2015.

[27] A. H. Nitz et al. 1-OGC: The first open gravitational-wave catalog of binary mergers from analysis of public Advanced LIGO data. *The Astrophysical Journal*, 872(2), 2019.

[28] B. P. Abbott et al. (The LIGO Scientific Collaboration and the Virgo Collaboration). Gw151226: Observation of Gravitational Waves from a 22-Solar-Mass Binary Black Hole Coalescence. *Phys. Rev. Lett.*, 116(241103), 2016.

[29] B. P. Abbott et al. (The LIGO Scientific Collaboration and the Virgo Collaboration). GW170104: Observation of a 50-Solar-Mass Binary Black Hole Coalescence at Redshift 0.2. *Phys. Rev. Lett.*, 121(129901), 2018.

[30] B. P. Abbott et al. (The LIGO Scientific Collaboration and the Virgo Collaboration). A Three-Detector Observation of Gravitational Waves from a Binary Black Hole Coalescence. *Phys. Rev. Lett.*, 119(141101), 2017.

[31] B. P. Abbott et al. (The LIGO Scientific Collaboration and the Virgo Collaboration). GW170608: Observation of a 19 Solar-mass Binary Black Hole Coalescence. *The Astrophysical Journal Letters*, 851(2), 2017.

[32] B. P. Abbott et al. (The LIGO Scientific Collaboration and the Virgo Collaboration). GW170817: Observation of Gravitational Waves from a Binary Neutron Star Inspiral. *Phys. Rev. Lett.*, 119(161101), 2017.

[33] B. P. Abbott et al. Multi-messenger Observations of a Binary Neutron Star Merger. *The Astrophysical Journal Letters*, 848(12), 2017.

[34] Gravitational wave network summary. `https://ldas-jobs.ligo.caltech.edu/~detchar/summary/day/20200306/`. Last checked: 06.03.2020.

[35] B. P. Abbott et al. (The LIGO Scientific Collaboration and the Virgo Collaboration). GW190425: Observation of a Compact Binary Coalescence with Total Mass 3.4 m. *Astrophysical Journal Letters*, 892(1), 2020.

[36] Caltech Office of Strategic Communications. `https://www.ligo.caltech.edu/news/ligo20191004`. Last checked: 10.03.2020.

[37] The Virgo Collaboration. Advanced Virgo Technical Design Report. VIR–0128A–12, April 2012.

[38] The Virgo Collaboration. Optics and related topics. The VIRGO Physics Book, Vol. II, 2010.

[39] M. Bassan, editor. *Advanced Interferometers and the Search for Gravitational Waves*. Springer Verlag, 2014.

[40] B. J. Meers. Recycling in laser-interferometric gravitational-wave detectors. *Phys. Rev. D*, 38(8):2317–2326, 1988.

[41] D. Bersanetti. *Development of a new lock acquisition strategy for the arm cavities of Advanced VIRGO*. PhD thesis, Università di Genova, 2015.

[42] T. Accadia et al. Virgo: A laser interferometer to detect gravitational waves. *Journal of Instrumentation*, 7(03), 2012.

[43] F. Acernese et al. Measurements of Superattenuator seismic isolation by Virgo interferometer. *Astroparticle Physics*, 33(3), 2010.

[44] P. Meyers et al. Direct Observations of Surface-Wave Eigenfunctions at the Homestake 3D Array. *Bulletin of the Seismological Society of America*, 109(4):1194–1202, 2009.

[45] M. G. Beker. *Low-frequency sensitivity of next generation gravitational wave detectors*. PhD thesis, Vrije Universiteit Amsterdam, 2013.

[46] J. Harms and H. J. Paik. Newtonian-noise cancellation in full-tensor gravitational-wave detectors. *Phys. Rev. D*, 92(022001), 2015.

[47] D. Fiorucci, J. Harms, M. Barsuglia, I. Fiori, and F. Paoletti. Impact of infrasound atmospheric noise on gravity detectors used for astrophysical and geophysical application. *Phys. Rev. D*, 97(062003), March 2018.

[48] S. D. Penn et al. Frequency and surface dependence of the mechanical loss in fused silica. *Phys. Lett. A*, 352, 2006.

[49] M. G. Harry et al. Titania-doped tantala/silica coatings for gravitational-wave detection. *Classical and Quantum Gravity*, 24(2), 2006.

[50] S. Ballmer and V. Mandic. New Technologies in Gravitational-Wave Detectors. *Annual Review of Nuclear and Particle Science*, 65, 2015.

[51] F. Piergiovanni, M. Punturo, and P. Puppo. The thermal noise of the Virgo+ and Virgo Advanced Last Stage Suspension (The PPP effect). Internal Virgo note VIR-015E-09, 2009.

[52] M. Punturo. Advanced Virgo sensitivity curve study. Internal Virgo note VIR-0073D-12, November 2012.

[53] F. Acernese et al. Advanced Virgo: a second-generation interferometric gravitational wave detector. *Classical and Quantum Gravity*, 32(2), 2014.

[54] L. van der Schaaf. *The Phase Cameras of Advanced Virgo*. PhD thesis, Vrije Universiteit Amsterdam, 2020.

[55] The Virgo Collaboration. Advanced Virgo Plus (AdV+) - Design Report for Phase I (PRELIMINARY). Internal Virgo note VIR-0568A-19, June 2019.

[56] The Virgo Collaboration. Overview of Advanced Virgo Plus Phase II. Internal Virgo note VIR-1179B-19, November 2016.

[57] S. Dwyer (for the LIGO Scientific Collaboration). Advanced LIGO status. *Journal of Physics: Conference Series*, 610(012013), 2015.

[58] LIGO Caltech. `https://www.ligo.caltech.edu/page/ligo-india`. Last checked: 08.04.2020.

[59] B. P. Abbott et al. (The LIGO Scientific Collaboration, the Virgo Collaboration, and the KAGRA Collaboration). Prospects for Observing and Localizing Gravitational-Wave Transients with Advanced LIGO, Advanced Virgo and KAGRA. arXiv: 1304.0670v10, January 2020.

[60] F. Acernese et al. (The Virgo Collaboration). Status of Advanced Virgo. *EPJ Web of Conferences*, 182(02003), 2018.

[61] KAGRA observatory. https://gwcenter.icrr.u-tokyo.ac.jp/en/archives/1352. Last checked: 08.04.2020.

[62] K. Somiya (for the KAGRA Collaboration). Detector configuration of KAGRA - the Japanese cryogenic gravitational-wave detector. *Classical and Quantum Gravity*, 29(12), 2011.

[63] K. L. Dooley (for the LIGO Scientific Collaboration). Status of GEO600. *Journal of Physics: Conference Series*, 610(012015), 2015.

[64] P. Barriga et al. Optical design of the proposed Australian International Gravitational Observatory. *Optics Express*, 2009.

[65] Maastricht University. https://www.maastrichtuniversity.nl/news/prototype-einstein-telescope-will-be-housed-randwyck. Last checked: 08.04.2020.

[66] M. Abernathy et al. Einstein gravitational wave telescope conceptual design study. ET-0106C-10, June 2011.

[67] J. M. Ezquiaga and D. E. Holz. Jumping the gap: searching for LIGO's biggest black holes. arXiv: 2006.02211, May 2020.

[68] A. Freise, S. Chelkowski, Hild S., W. Del Posso, A. Perreca, and Vecchio A. Triple Michelson interferometer for a third-generation gravitational wave detector. *Classical and Quantum Gravity*, 26(8), April 2009.

[69] S. Hild et al. Sensitivity studies for third-generation gravitational wave observatories. *Classical and Quantum Gravity*, 28(094013):13pp, 2011.

[70] ET steering committee. Et design report update 2020. Internal ET docuemten ET-0007A-20, March 2020.

[71] A. Paoli et al. Some considerations on the ET infrastructure - The case for the Sardinia site. 9th Einstein Telescope Symposium, April 2018.

[72] L. Naticchioni et al. Microseismic studies of an underground site for a new interferometric gravitational wave detector. *Classical and Quantum Gravity*, 31(105016):20pp, 2014.

[73] KNMI Royal Dutch Meteorological Institute webpage. http://www.knmi.nl. Last checked: 26.08.2020.

[74] S. Koley et al. Characteristics of surface wave Green's function for anisotropic ambient seismic noise field — a case study in Limburg, The Netherlands. *First Break*, 37(4):83–90, April 2019.

[75] S. Koley. *Sensor networks to measure environmental noise at gravitational wave detector sites*. PhD thesis, Vrije Universiteit Amsterdam, 2020.

[76] A. E. Siegman. *Lasers*. University Science Books, 1986.

[77] E. Hecht. *Optics*. Pearson, 2012.

[78] Bas Swinkels. Requirements on sensing noise for the Pound-Drever-Hall technique for the lock of the arm-cavities. *Internal Virgo note VIR-0467A-12*, 2012.

[79] R. W. P. Drever, J. L. Hall, F. V. Kowalski, J. Hough, G. M. Ford, A. J. Munley, and H. Ward. Laser Phase and Frequency Stabilization Using an Optical Resonator. *Appl. Phys. B*, 31(2):97–105, June 1983.

[80] Eric D. Black. An introduction to Pound–Drever–Hall laser frequency stabilization. *American Journal of Physics*, 69(1):79–87, 2001.

[81] Dana Z. Anderson. Alignment of resonant optical cavities. *Appl. Opt.*, 23(17):2944–2949, Sep 1984.

[82] E. Morris, B. J. Meers, Robertson D. I., and H. Ward. Automatic alignment of optical interferometers. *Applied Optics*, 33(22):5041–5049, 1994.

[83] A. Freise. *The Next Generation of Interferometry: Multi-Frequency Optical Modelling, Control Concepts and Implementation*. PhD thesis, Universität Hannover, 2003.

[84] J. Smith. *Formulation of Instrument Noise Analysis Techniques and Their Use in the Commissioning of the Gravitational Wave Observatory, GEO600*. PhD thesis, Universität Hannover, 2006.

[85] J. Smith, P. Ajith, H. Grote, M. Hewitson, S. Hild, H. Lück, K. Strain, B. Willke, J. Hough, and K. Danzmann. Linear projection of technical noise for interferometric gravitational-wave detectors. *Classical and Quantum Gravity*, 23(2):527–537, 2006.

[86] J. Casanueva Diaz. *Control of the gravitational wave interferometric detector Advanced Virgo*. PhD thesis, Université Paris-Saclay, 2017.

[87] T. Corbitt, D. Ottaway, E. Innerhofer, K. Pelc, and N. Mavalvala. Measurement of radiation-pressure-induced optomechanical dynamics in a suspended Fabry-Perot cavity. *Phys. Rev A*, 74(021802(R)), August 2006.

[88] L. Sidles and D. Sigg. Optical torques in suspended Fabry-Perot interferometers. *Phys. Rev A*, 354(3):167–172, May 2006.

[89] Sigg. D. Angular Instabilities in High Power Fabry-Perot Cavities. Internal LIGO note LIGO-T030120-00, June 2003.

[90] E. Hirose, K. Kawabe, D. Sigg, R. Adhikari, and P. Saulson. Angular instability due to radiation pressure in the LIGO gravitational wave detector. *Applied Optics*, 49(18):3474–3484, 2009.

[91] J. Liu et al. Angular instability in high optical power suspended cavities. *Review of Scientific Instruments*, 89(124503), 2018.

[92] S. Solimeno, F. Barone, C. de Lisio, D. Fiore, L. Milano, and G. Russo. Fabry-Pérot resonators with oscillating mirrors. *Phys. Rev A*, 43(6227), June 1991.

[93] F. Acernese et al. A local control system for the test masses of the Virgo gravitational wave detector. *Astroparticle Physics*, 20(6):617–628, March 2004.

[94] T. Accadia et al. Automatic Alignment system during the second science run of the Virgo interferometer. *Astroparticle Physics*, 34:327–332, 2011.

[95] F. Acernese et al. Automatic Alignment for the first science run of the Virgo interferometer. *Astroparticle Physics*, 33(3):131–139, April 2010.

[96] F. Acernese et al. The Virgo automatic alignment system. *Classical and Quantum Gravity*, 23(8):S91, March 2006.

[97] E. Majorana. SUSP comissioning status. Internal Virgo note VIR-0155A-17, March 2017.

[98] Advanced Virgo online noise budget. `https://scientists.virgo-gw.eu/commissioning/plots/nested/NoiseBudget/`. Last checked: 14.04.2020.

[99] M. Mantovani. ISC status and plans. Internal Virgo note VIR-0838A-17.

[100] P. Ruggi. UGF measurement of angular control loops. Virgo logbook entry 45499, April 2019.

[101] Michal Was. The noise budget in September 2019 - STAC report. Internal Virgo note VIR-1023B-19, November 2019.

[102] M. Mantovani and J. Casanueva. Virgo logbook entry 45351.

[103] P. Ruggi. Virgo logbook entry 46845.

[104] Advanced Virgo noise budget documentation. `https://wiki.virgo-gw.eu/Commissioning/NoiseBudget/WebHome?validation_key=8b4046ffbb6a803103d829d30bd6ca1e`. Last checked: 14.05.2020.

[105] E. Robinson and D. Clark. Elasticity: Stress and strain. *The Leading Edge*, 7(2):1–64, February 1988.

[106] P. M. Shearer. *Introduction to Seismology*. Cambridge University Press, 2009.

[107] K. Aki and P. Richards. *Quantitative Seismology*. University Science Books, Sausalito, CA, second edition edition, 2002.

[108] W. M. Ewing, W. S. Jardetzky, and F. Press. *Elastic Waves in Layered Media*. New York: McGraw-Hill Book Company, Inc., 1957.

[109] J. Achenbach. *Wave Propagation in Elastic Solids*. North-Holland Series in Applied Mathematics and Mechanics, 1984.

[110] J. Rayleigh. On Waves Propagated along the Plane Surface of an Elastic Solid. *Proceedings of the London Mathematical Society*, s1-17(1):4–11, November 1885.

[111] K. Visser, J. Trampert, and Kennet B. L. N. Global anisotropic phase velocity maps for higher mode Love and Rayleigh waves. *Geophysical Journal International*, 172(3):1016–1032, 2007.

[112] D. Forsyth. Higher-mode Rayleigh waves as an aid to seismic discrimination. *Bulletin of the Seismological Society of America*, 66(3):827–841, 1976.

[113] S. Foti et al. Guidelines for the good practice of surface wave analysis: a product of the InterPACIFIC project. *Bulletin of Earthquake Engineering*, 16(16), 2018.

[114] N. A. Haskell. The Dispersion of Surface Waves on Mulitlayered Media. *Bulletin of the Seismological Society of America*, 43:17–34, 1964.

[115] W. T. Thomson. Transmission of Elastic Waves through a Stratified Solid Medium. *Journal of Applied Physics*, 21:98–93, 1950.

[116] E. Kausel and J. M. Roësset. Stiffness matrices for layered soils. *Bulletin of the Seismological Society of America*, 71(6):1743–1761, 1981.

[117] M. Schevenels, G. Degrande, and S. François. EDT: An ElastoDynamics Toolbox for MATLAB. *Computers & Geoscience*, 35(8):1752–1754, 2009.

[118] E. Kausel. *Fundamental Solutions in Elastodynamics - A Compendium*. Cambridge University Press, 2006.

[119] M. Schevenels. *The impact of uncertain dynamic soil characteristics on the prediction of ground vibrations*. PhD thesis, Katholieke Universiteit Leuven, 2007.

[120] G. Heinzel, A. Rüdiger, and R. Schilling. Spectrum and spectral density estimation by the Discrete Fourier transform (DFT), including a comprehensive list of window functions and some new flat-top windows. Max-Planck-Institut fur Gravitationsphysik Max-Planck-Institut für Gravitationsphysik (Albert-Einstein-Institut), February 2015.

[121] C. E. Shannon. Communication in the Presence of Noise. *Proceedings of the Institute of Radio Engineers*, 37(1):10–21, 1949.

[122] A. Zerva and Zervas V. Spatial variation of seismic ground motions: An overview. *Appl. Mech. Rev.*, 55(3):271–297, 2002.

[123] R. N. Bracewell. *The Fourier Transform and Its Applications*. McGraw-Hill Higher Education, 2000.

[124] P. Saulson. Terrestrial gravitational noise on a gravitational wave antenna. *Phys. Rev. D*, 30(732), 1984.

[125] M. Maggiore et al. Science case for the Einstein telescope. *Journal of Cosmology and Astroparticle Physics*, 2020, March 2020.

[126] M. Beccaria et al. Relevance of Newtonian seismic noise for the VIRGO interferometer sensitivity. *Classical and Quantum Gravity*, 15(3339-3362), 1998.

[127] M. Beker, G. Cella, et al. Improving the sensitivity of future GW observatories in the 1–10 Hz band: Newtonian and seismic noise. *General Relativity and Gravitation*, 43(2):623–656, 2011.

[128] S. Hughes and K. Thorne. Seismic gravity-gradient noise in interferometric gravitational-wave detectors. *Phys. Rev. D*, 58(122022), 1998.

[129] J. Harms and S. Hild. Passive Newtonian noise suppression for gravitational-wave observatories based on shaping of the local topography. *Classical and Quantum Gravity*, 31(18), 2014.

[130] J. van den Brand. *100 Years of General Relativity: Advanced Interferometeric Gravitational-Wave Detectors*, volume 5, chapter 6. World Scientific, 2019.

[131] SOFI3D project. `https://git.scc.kit.edu/GPIAG-Software/SOFI3D/`. Last checked: 29.10.2020.

[132] D. Agnew. History of seismology. *International Handbook of Earthquake and Engineering Seismology, Part A*, 2020.

[133] Innoseis webpage. `http://www.innoseis.com`. Last checked: 26.08.2020.

[134] J. Peterson. Observations and modeling of seismic background noise. Open-file report 93-322, U.S. Department of Interior Geological Survey, 1993.

[135] J. Rhie and B. Romanowicz. Excitation of Earth's continuous free oscillations by atmosphere–ocean–seafloor coupling. *Nature*, 431:552–556, 2004.

[136] S. Webb. The Earth's 'hum' is driven by ocean waves over the continental shelves. *Nature*, 445:784–756, 2007.

[137] R. Sleeman. Ambient Earth noise and instrumental noise. KNMI background information (www.knmi.nl), 2006.

[138] S. Kedar et al. The origin of deep ocean microseisms in the North Atlantic Ocean. *Proceedings of The Royal Society A Mathematical Physical and Engineering Sciences*, 464(2091):1–35, 2007.

[139] E. Marcetti and M. Mazzoni. Evidence of oceanic microseism as a source of low frequency seismic signal recorded at Virgo. Internal Virgo note VIR-NOT-FIR-1390-261, 2014.

[140] S. Schofield et al. Source and propagation of the predominant 1-50 Hz seismic signal from off-site at LIGO-Handford. LIGO Collaboration Meeting, 2000.

[141] I. Fiori et al. Studies of the 1-4 Hz seismics. Internal Virgo note VIR-NOT-FIR-1390-251, 2003.

[142] R.T. Lacoss, E.J. Kelly, and M.N. Toksöz. Estimation of seismic noise structure using arrays. *Geophysics*, 34(1):21–38, February 1969.

[143] H. P. Harjes and M. Henger. Array-seismologie. *Zeitschrift für Geophysik*, 39:865–905, 1073.

[144] S. Koley et al. Rayleigh wave phase velocity models for gravitational wave detectors using an array of nodal sensors. *First Break*, 35(6):71–78, 2017.

[145] S. Koley et al. S-wave velocity model estimation using ambient seismic noise at virgo, italy. In *Technical Program Expanded Abstracts 2017*, pages 2946–2950, 2017.

[146] S. Koley et al. Seismic Noise Characterization at a Potential Site for the Einstein Telescope Underground Gravitational Wave detector. In *80th EAGE Conference and Exhibition*, 2018.

[147] W. M. Telford, L. P. Geldart, and R. E. Sheriff. *Applied Geophysics*. Cambridge University Press, 1990.

[148] DTCC Dynamic Technologies. *DT-SOLO 5Hz (HP305V) specification sheet*, 08 2016.

[149] Checkmate webpage. `http://www.mitchamindustries.com/products-for-lease/land-seismic/peripherals/infinity-checkmate/`. Last checked: 26.08.2020.

[150] Wilcoxon Sensing Technologies. *Compact, ultra low-frequency accelerometer specifications (Model 731-207)*, 09 2018.

[151] Keysight Technologies. *35670A FFT Dynamic Signal Analyzer, DC-102.4 kHz*, 2017.

[152] Analog Devices Inc. *ADA4084-1/ADA4084-2/ADA4084-4 data sheet*, 2017.

[153] Analog Devices Inc. *Op Amp Noise tutorial MT-047*, 2008.

[154] C. Man. *Qantization Noise: An Expanded Derivation of the Equation (Mini Tutorial MT-229)*. Analog Devices Inc., 2012.

[155] Silicon Laboratories. *Improving ADC resolution by Oversampling and Averaging (Tutorial AN118)*, 2013.

[156] C. Collette et al. Review of sensors for low frequency seismic vibration measurement. CERN technical note, 2011.

[157] J. van Heijningen et al. A multistage vibration isolation system for Advanced Virgo suspended optical benches. *Classical and Quantum Gravity*, 2019.

[158] J. van Heijningen. *Turn up the bass - Low-frequency performance imporvement of seismic attenuation systems and vibration sensors for next generation gravitational wave detectors*. PhD thesis, Vrije Universiteit Amsterdam, 2018.

[159] R. Sleeman, A. van Wettum, and J. Trampert. Three-Channel Correlation Analysis: A New Technique to Measure Instrumental Noise of Digitizers and Seismic Sensors. *Bulletin of the Seismological Society of America*, 96(1):258–271, 2006.

[160] M. Beker et al. Innovations in seismic sensors driven by the search for gravitational waves. *Leading Edge*, 35(7):590–593, 2016.

[161] D. Saccorotti et al. Seismic noise by wind farms: a case study from the Virgo gravitational wave observaotry, Italy. *Bulletin of the Seismological Society of America*, 101(2):568, 578 2011.

[162] S. Stefanelli et al. Microgravity vertical gradient measurement in the site of VIRGO interferometric antenna (Pisa plain, Italy). *Annals of Geophysics*, 51(5/6), 2008.

[163] I. Fiori. Reference seismic data for Virgo. Internal Virgo note VIR-00390A-15, 2015.

[164] M. Tringali et al. Seismic array measurements at Virgo's West End Building for the configuration of a Newtonian-noise cancellation system. Internal Virgo note VIR-0504A-19, May 2019.

[165] S. Koley et al. Surface and underground seismic noise characterization at a candidate site for Einstein Telescope. Publication in preparation, 2020.

[166] R. E. Chapman. *Petroleum geology (Developments in Petroleum Science; 16)*. Elsevier Science Publishers B.V., 1938.

[167] P. Doornenbal. Uitwerkingen boorgatmetingen Terziet. Internal report by Deltares, May 2017.

[168] C. Schlumberger, M. Schlumberger, and E. G. Leonardon. Electrical coring: A method of determining bottom-hole data. *A.I.M.E Technical Publication 462*, 1932.

[169] P. Glover. `http://homepages.see.leeds.ac.uk/~earpwjg/PG_EN/CD%20Contents/GGL-66565%20Petrophysics%20English/`. Petrophysics MSc Course Notes, University of Leeds.

[170] J. Klaja and L. Dudek. Geological interpretation of spectral gamma ray (SGR) logging in selected boreholes. *NAFTA-GAZ*, 72(1):3–14, 2016.

[171] Advanced Logic Technology, Bat A, Route de Niederpallen, L8506 Redange sur Attert, Luxembourg. *QL40 ABI - Acoustic Borehole Imager - User Guide*.

[172] J. W. Woods and P. R. Lintz. Plane waves at small arrays. *Society of Exploration Geophysicists*, 1973.

[173] Private conversation with Soumen Koley, 2016.

[174] P. Bard et al. Guidelines for the implementation of the H/V spectral ratio technique on ambient vibrations measurements, processing and interpretation. *Bulletin of Earthquake Engineering*, 5((4)), 2008.

[175] D. Lo Presti et al. Seismic Behaviour of Ground and Geotechnical Structures. In *Conference: Proceedings of the 14th International Conference on Soil Mechanics and Foundations Engineering*, 1997.

[176] Private conversation with Björn Vink, 2019.

[177] W. H. Press et al. *Numerical recipies - the art of scientific computing*. Cambridge University Press, 2007.

[178] M. Beker, J. van den Brand, E. Hennes, and D. Rabeling. Newtonian noise and ambient ground motion for gravitational wave detectors. *Journal of Physics: Conference Series*, 363, 2011.

[179] E. Hennes. Comments on Saulson's: "Terrestrial gravitational noise on a gravitational wave antenne" Phys. Rev. D, 30, 4, p.732-736 (1984). Internal Nikhef document, 2009.

Academic summaries

English summary

For centuries, humans have been curious to understand the nature of the Cosmos surrounding us. Not only do we aspire to understand the underlaying laws that hold the Universe together, even more so do we hope to reveal the mystery behind its origin. The quest that gravitational wave science is set upon is nothing less than gaining deeper understanding of the composition of the Universe.

What are gravitational waves?

Gravitational waves have been predicted as a consequence of Einstein's Theory of general relativity, that has been formulated in 1916. General relativity describes how mass, such as planets, stars or black boles, curves spacetime in our Universe and how this curvature in turn affects the motion of the masses. Masses that are accelerated induce "ripples" in the fabric of spacetime (see Fig. 2). These ripples are called gravitational waves. In general, all kinds of accelerated masses can produce gravitational waves. However, the fabric of spacetime is very stiff and only the most violent events in the Universe emit waves that are large enough to be measurable with our detectors on earth. Such events are for example the collision of heavy objects such as stel-

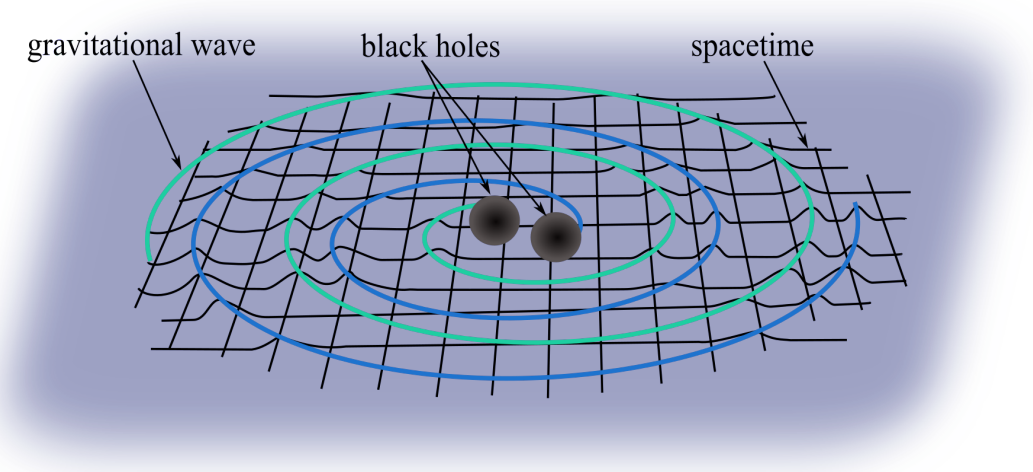

Figure 2: *Spacetime can be imagined like a rubber band. Heavy objects that move in an accelerated motion, such as colliding black holes, cause ripples in spacetimes. These ripples are called gravitational waves and they travel through the Universe at the speed of light.*

lar mass black holes, asymmetric rotating neutron stars or burst events of new, undiscovered objects. Numerous events from colliding black holes and two events from binary neutron star mergers have been reported since the very first detection of gravitational waves in 2015. Gravitational wave measurements of neutron star mergers complement electromagnetic observations from telescopes and give new information on the structure of neutron stars and on cosmological parameters such as the Hubble parameter.

How do we measure gravitational waves?

On Earth gravitational waves are measured with laser interferometers, which are based on the design of a Michelson interferometer. Advanced Virgo is a laser interferometer in Italy, where a laser beam is split with a beam splitter into two 3 km long paths (see Fig. 3, left panel). At the end of each arm the laser beam is reflected back towards the center and both beams are recombined at the beam splitter. The intensity of the resulting laser beam is then investigated with a photo diode.

If no gravitational wave is present, the lengths of both arms are almost the same and are tuned such that the recombined beams interfere destructively. As a result, almost no light is detected at the photo diode. If a gravitational wave passes, it stretches one arm, while the other one is compressed. Now one laser beam travels a longer distance than the other one and they are out of phase when they are recombined. As a result a time dependent signal can be measured with the photo diode (see Fig. 3, right panel). The strength, duration and shape of this signal depends on the type of source that emitted the gravitational wave. It allows to distinguish between different

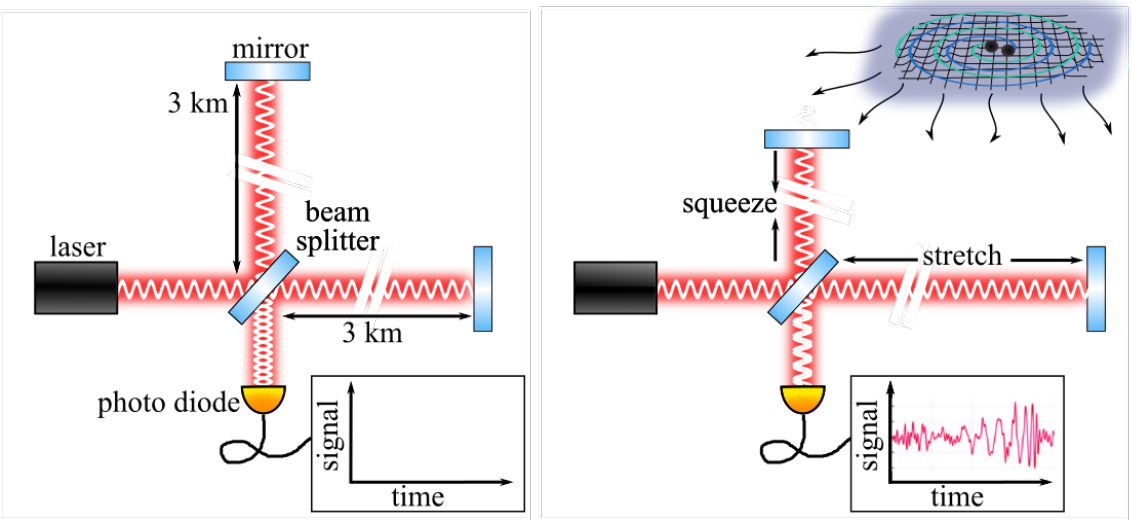

Figure 3: *Left: Gravitational waves are measured with laser interferometers, where a laser beam is split into two arms of several kilometers length. At the end of the arms, mirrors reflect the laser beam back towards the center, where both beams are recombined and measured with a photo diode. If no gravitational wave is present, then the arm lengths are tuned such that the laser beams interfere destructively and no signal is visible at the photo diode. Right: If a gravitational wave passes, one arm is compressed and the other one is stretched. The recombined laser beams do not interfere destructively anymore and as a result a signal is measured at the photo diode. The shape is characteristic for each gravitational wave source type. Note that in reality this effect is much smaller than depicted here.*

types of events and gives valuable information on the mass composition and distance of the gravitational wave source.

Performance limitations of gravitational wave detectors

Gravitational wave signals are very faint, for instance the loudest event measured so far only lead to a variation in arm length of about 0.000 000 000 000 000 01 m, which is a small fraction of the radius of the atomic nucleus. On Earth, many noise sources disturb the detector and thereby limit its performance. Seismic motion, driven by oceanic and human activity, couples directly and indirectly to the mirror motion and is the main cause of the noise sources discussed in this dissertation. The interaction of the mirrors with the seismic motion of the soil is suppressed by suspending the mirrors from a system of springs and pendula such that they can be assumed to be freely floating across almost the full frequency range of the detector (see Fig. 4, left panel). However, at very low frequencies, the suspension system is not sufficient anymore, and an active feedback control loop is in place to correct the mirror motion (see Fig. 4, central panel). In this work the performance of the angular control system that is in place at Advanced Virgo is briefly discussed and its performance during the third observation run is evaluated. Another important aspect is that seismic motion couples directly to the mirrors, which are attracted to denser regions in the seismic field via gravitational attraction (see Fig. 4, right panel). Modeling this so called *Newtonian noise*, depending on seismic fields that are characteristic for the detector site, is the main topic of this thesis.

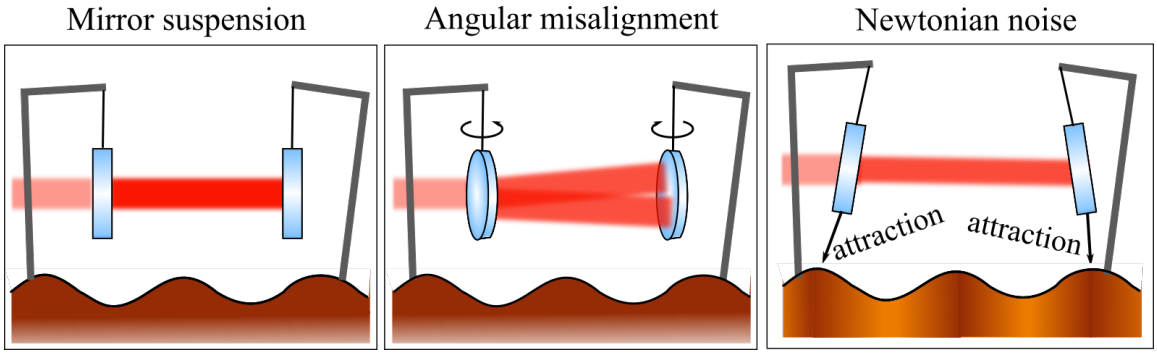

Figure 4: *Left: To reduce the interaction between the mirror and the ground motion, the mirrors are suspended by a system of pendula. They can be assumed to be freely floating across almost the full frequency range. Center: At low frequencies, the seismic motion is not sufficiently suppressed by the suspension system and the mirrors suffer from residual angular motion. Active angular feedback control loops are in place at Advanced Virgo to keep the mirrors aligned during operation. Right: Direct interaction between the mirrors and density fluctuations in the seismic field induce the so called Newtonian noise.*

Seismic models for site-based Newtonian noise

Current models that estimate Newtonian noise at gravitational wave detectors assume surface detectors and rely on a soil that consists of a single material in which only one specific wave type propagates. However, realistic geologies are multilayered and the seismic field consists of a complex composition of surface and body waves, which are excited by seismic sources. Such sources can for example be traffic on roads or over bridges or wind shaking buildings. In

addition, the prospective construction of Einstein Telescope, a next generation European gravitational wave detector that will be installed 100 to 300 m underground, gives rise to the necessity for realistic seismic and Newtonian noise models. From a scientific point of view, the selection of the location for Einstein Telescope will be set in an area that favors low Newtonian noise levels.

Recently, the subsurface composition at Advanced Virgo in Italy and at the Belgian-German-Dutch (BGN) Einstein Telescope candidate site in the Netherlands have been determined by using large arrays of seismic surface sensors. The geology at Advanced Virgo has been found to consists of nine soft soil layers. The most dominant seismic sources are more than 1 km away and originate from road bridges of a nearby highway and a distant wind park. The geology at the BGN site has been found to consist of five subsurface layers, which consist of soft soil down to about 35 m laying on a thick layer of hard rock. Noise sources in this region are local and within a few hundred meters up to 1 km distance from the sensor array. For both detectors a seismic model that is based on the measured geology and that reproduces seismic conditions such as

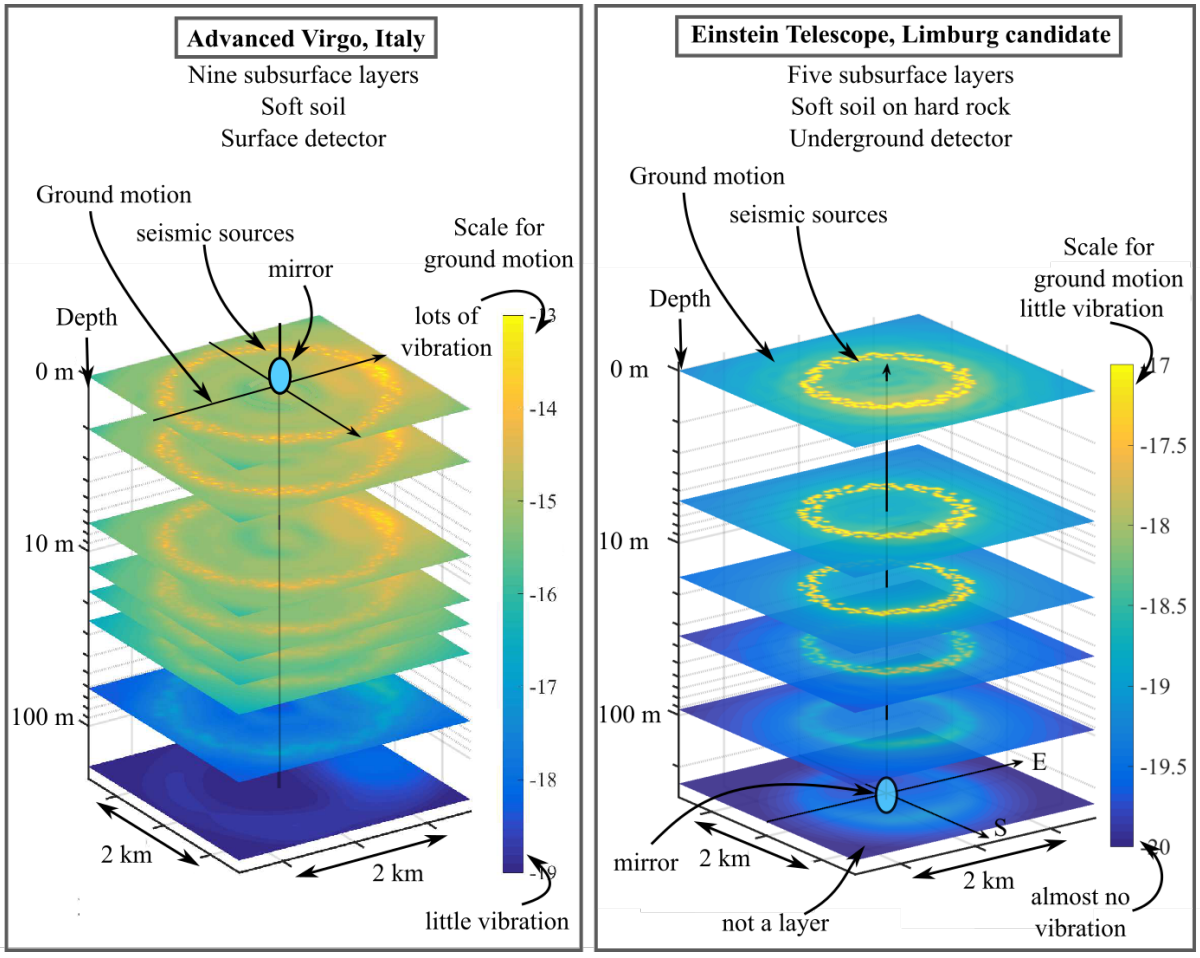

Figure 5: *Schematic drawing of the seismic model that is based on the geology and source locations as measured at the Advanced Virgo detector in Italy (left) and at the Einstein Telescope candidate site in Limburg (right). The color indicates the strength of the ground motion and each colored sheet represents the seismic motion at the start of a new subsurface layer. It is visible that the seismic motion is strongest on the surface and attenuates further underground. Note that at Advanced Virgo the mirror is on the surface while for Einstein Telescope it is* 250 m *underground.*

surface wave speeds and seismic spectra has been derived (see Fig. 5). From these seismic models, site-based Newtonian noise has been calculated for both detector sites by numerically integrating the seismic field in the vicinity of the mirrors.

Where do we go from here?

The research that has been presented in this dissertation has lead to a better understanding of how local seismic conditions such as the geology and the seismic field affect Newtonian noise at a given gravitational wave detector. We have also learned that additional factors such as the detector depth as well as the shape and size of the cavern have a strong influence on Newtonian noise. Future research is therefore recommended to elaborate on the one hand on the geology models, for example by including complex three-dimensional subsurface structures, and on the other hand on a detailed understanding of the influence of cavern geometries on the Newtonian noise of underground gravitational wave detectors.

In this work a detailed understanding of the site-based Newtonian noise at a given detector site is obtained. However, Newtonian noise cannot be suppressed and at times it may limit the detector performance during operation. It is therefore of the utmost importance that future research encompasses the development of online subtraction schemes based on permanent seismic sensor arrays that constantly monitor the seismic field around the detector and cross-correlate it to the detector output. First steps towards the development of an online subtraction scheme are taken at Advanced Virgo, where a permanent sensor array is currently being installed and integrated into Virgo's online-monitoring system for environmental noise.

Nederlandse samenvatting

Eeuwenlang is de mensheid al nieuwsgierig naar de samenstelling van de kosmos om ons heen. Wij streven niet alleen naar het begrijpen van de onderliggende wetten die het universum bijeenhouden, maar wij hopen ook het mysterie achter zijn oorsprong te onthullen. De zwaartekrachtsgolfwetenschap levert een belangrijke bijdrage aan om het heelal vanuit een geheel nieuw perspectief te kunnen zien.

Wat zijn zwaartekrachtgolven?

Zwaartekrachtgolven zijn voorspeld als gevolg van Einsteins algemene relativiteitstheorie, die in 1916 geformuleerd is. De algemene relativiteitstheorie beschrijft de interactie tussen massa en ruimtetijd in ons heelal. Als massa's worden versneld, veroorzaakt dit "rimpelingen" in het weefsel van ruimtetijd (zie Fig. 6). Deze rimpelingen worden zwaartekrachtgolven genoemd. Over het algemeen kunnen allerlei versnelde massa's zwaartekrachtgolven produceren. Het weefsel van ruimtetijd is echter erg stijf en alleen de meest gewelddadige gebeurtenissen in het heelal zenden golven uit die groot genoeg zijn om meetbaar te zijn met onze detectoren op aarde. Dergelijke gebeurtenissen zijn bijvoorbeeld botsingen tussen objecten zo zwaar als zwarte gaten,

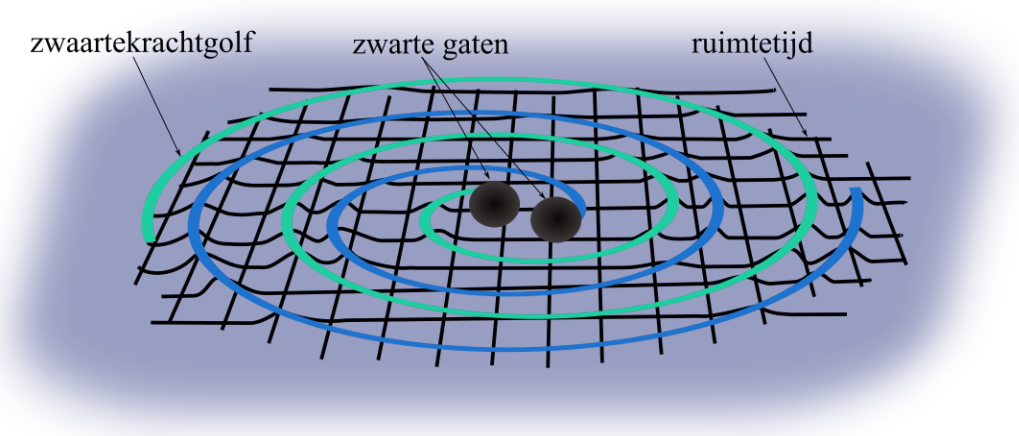

Figuur 6: *Ruimtetijd kan worden voorgesteld als een elastiek. Zware objecten die in een versnellende beweging bewegen, zoals botsende zwarte gaten, veroorzaken rimpelingen in de ruimtetijd. Deze rimpelingen worden zwaartekrachtgolven genoemd en zij reizen door het heelal met de snelheid van het licht.*

asymmetrisch roterende neutronensterren, burst-gebeurtenissen of van nieuwe, onontdekte objecten. Sinds de allereerste detectie van zwaartekrachtgolven in 2015 zijn er talloze gebeurtenissen gemeld die zijn veroorzaakt door botsende zwarte gaten en twee gebeurtenissen door samenvoegingen van binaire neutronensterren. Metingen van zwaartekrachtgolven van versmeltingen van neutronensterren vormen een aanvulling op elektromagnetische waarnemingen van telescopen en geven nieuwe informatie over de structuur van neutronensterren en over kosmologische parameters zoals de Hubble-parameter.

Hoe meten wij gravitatiegolven?

Op aarde worden gravitatiegolven gemeten met laser interferometers, die zijn gebaseerd op het ontwerp van een Michelson-interferometer. De Advanced Virgo detector is een laser interferometer in Italië, waar een laserbundel met een bundelsplitser wordt opgesplitst in twee 3 km lange paden (zie Fig. 7, linker paneel). Aan het uiteinde van elke arm wordt de laserbundel teruggekaatst naar het midden en worden beide bundels weer gecombineerd bij de bundelsplitser. De intensiteit van het uitgaande bundel wordt vervolgens onderzocht met een fotodiode.

Als er geen zwaartekrachtgolf aanwezig is, zijn de lengtes van beide armen bijna hetzelfde en zo afgestemd dat de gerecombineerde bundels destructief interfereren. Hierdoor is er geen licht zichtbaar bij de fotodiode. Als een zwaartekrachtgolf passeert, strekt deze één arm uit, terwijl de andere wordt gecomprimeerd. Nu legt de ene laserbundel een grotere afstand af dan de andere en zijn zij uit fase wanneer zij opnieuw worden gecombineerd. Hierdoor kan een tijdsafhankelijk

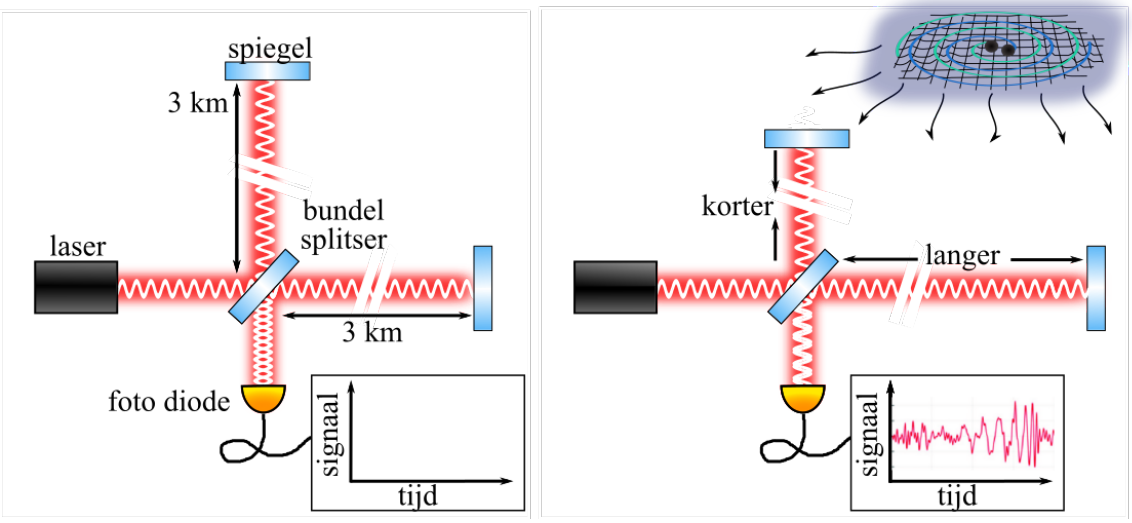

Figuur 7: *Links: Gravitatiegolven worden gemeten met laser interferometers, waarbij een laserbundel wordt opgesplitst in twee armen van enkele kilometers lengte. Aan het uiteinde van de armen reflecteren spiegels de laserbundels naar het midden, waar beide bundels worden gecombineerd en gemeten met een fotodiode. Als er geen zwaartekrachtgolf aanwezig is, dan zijn de armlengtes zo afgestemd dat de laserbundels destructief interfereren en er geen signaal zichtbaar is bij de fotodiode. Rechts: Als een zwaartekrachtgolf passeert, wordt één arm samengedrukt en de andere uitgerekt. De gerecombineerde laserbundels interferen niet meer destructief en daardoor wordt een signaal gemeten bij de fotodiode. De vorm is kenmerkend voor elk type bron van gravitatiegolf. Merk op dat dit effect in werkelijkheid veel kleiner is dan hier afgebeeld.*

signaal worden gemeten met de fotodiode (zie Fig. 7, rechter paneel). De sterkte, duur en vorm van dit signaal is afhankelijk van het type bron dat de zwaartekrachtgolf heeft uitgezonden. Het maakt het mogelijk om onderscheid te maken tussen verschillende soorten gebeurtenissen en geeft waardevolle informatie over de massasamenstelling en afstand van de bron van de zwaartekrachtgolven.

Limitaties van gravitatiegolfdetectoren

Signalen van zwaartekrachtgolven zijn erg zwak. Zo leidt de luidste gebeurtenis die tot nu toe is gemeten slechts tot een variatie in armlengte van ongeveer 0.000 000 000 000 000 01 m, veel kleiner dan een atoomkern. Op aarde verstoren veel ruisbronnen de detector en beperken daardoor zijn prestaties. Seismische trillingen, gedreven door oceanische en menselijke activiteit, koppelen direct en indirect aan de spiegelbeweging en zijn de hoofdoorzaak van de ruis die in dit proefschrift worden besproken. De interactie van de spiegels met de seismische trillingen van de grond wordt onderdrukt door de spiegels op te hangen aan een systeem van veren en slingers zodat kan worden aangenomen dat zij vrij zweven over bijna het volledige frequentiebereik van de detector (zie Fig. 8, linker paneel). Bij zeer lage frequenties is het veersysteem niet meer adequaat en is er een actief terugkoppelsysteem om de spiegelbeweging te corrigeren (zie Fig. 8, middenpaneel). In dit werk worden de prestaties van het hoek controle systeem dat aanwezig is bij Advanced Virgo besproken en zijn de prestaties tijdens de derde observatierun geëvalueerd. Een ander belangrijk aspect is dat seismische trillingen direct aan de spiegel koppelen, die via de zwaartekracht wordt aangetrokken door dichtere gebieden in het seismische veld (zie Fig. 8, rechter paneel). Het modelleren van deze zogenaamde *Newtoniaanse ruis*, die afhankelijk is van seismische velden die kenmerkend zijn voor de detectorlocatie, is de zoektocht waar dit proefschrift zich op richt.

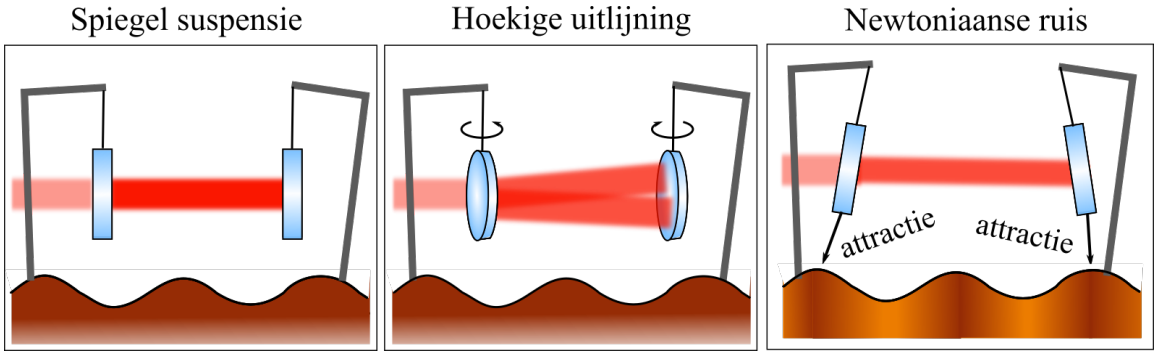

Figuur 8: *Links: Om de interactie tussen de spiegel en grondbeweging te verminderen, worden de spiegels opgehangen met behulp van een pendelsysteem. Het kan worden aangenomen dat zij vrij zweven over bijna het volledige frequentiebereik. Midden: Bij lage frequenties worden de seismische trillingen niet voldoende onderdrukt door het ophangsysteem en hebben de spiegels last van een resterende hoekbeweging. Actieve terugkoppelsystemen zijn aanwezig bij Advanced Virgo om de spiegels tijdens het gebruik uitgelijnd te houden. Rechts: Directe interactie tussen de spiegels en schommelingen in de dichtheid in het seismische veld veroorzaken de zogenaamde Newtoniaanse ruis.*

Seismische modellen voor Newtoniaanse ruis

Huidige modellen die Newtoniaanse ruis bij gravitatiegolf detectoren schatten gaan uit van oppervlaktedetectoren en vertrouwen op een bodem die uit slechts één materiaal bestaat waarin slechts één specifiek golftype zich voortplant. Realistische geologieën zijn echter meerlagig en het seismische veld bestaat uit een complexe samenstelling van oppervlakte- en ruimtegolven, die worden aangeslagen door seismische bronnen. Dergelijke bronnen kunnen bijvoorbeeld verkeer op wegen of over bruggen of door de wind schuddende gebouwen zijn. Bovendien geeft de toekomstige constructie van de Einstein Telescope, een nieuwe Europese gravitatiegolf detector die 100 tot 300 m ondergronds zal worden geïnstalleerd, aanleiding tot de noodzaak van realistische modellen voor seismische en Newtoniaanse ruis. Wetenschappelijk gezien zal de selectie van de locatie voor Einstein Telescope plaatsvinden in een gebied dat een laag Newtoniaanse ruis niveau bevordert.

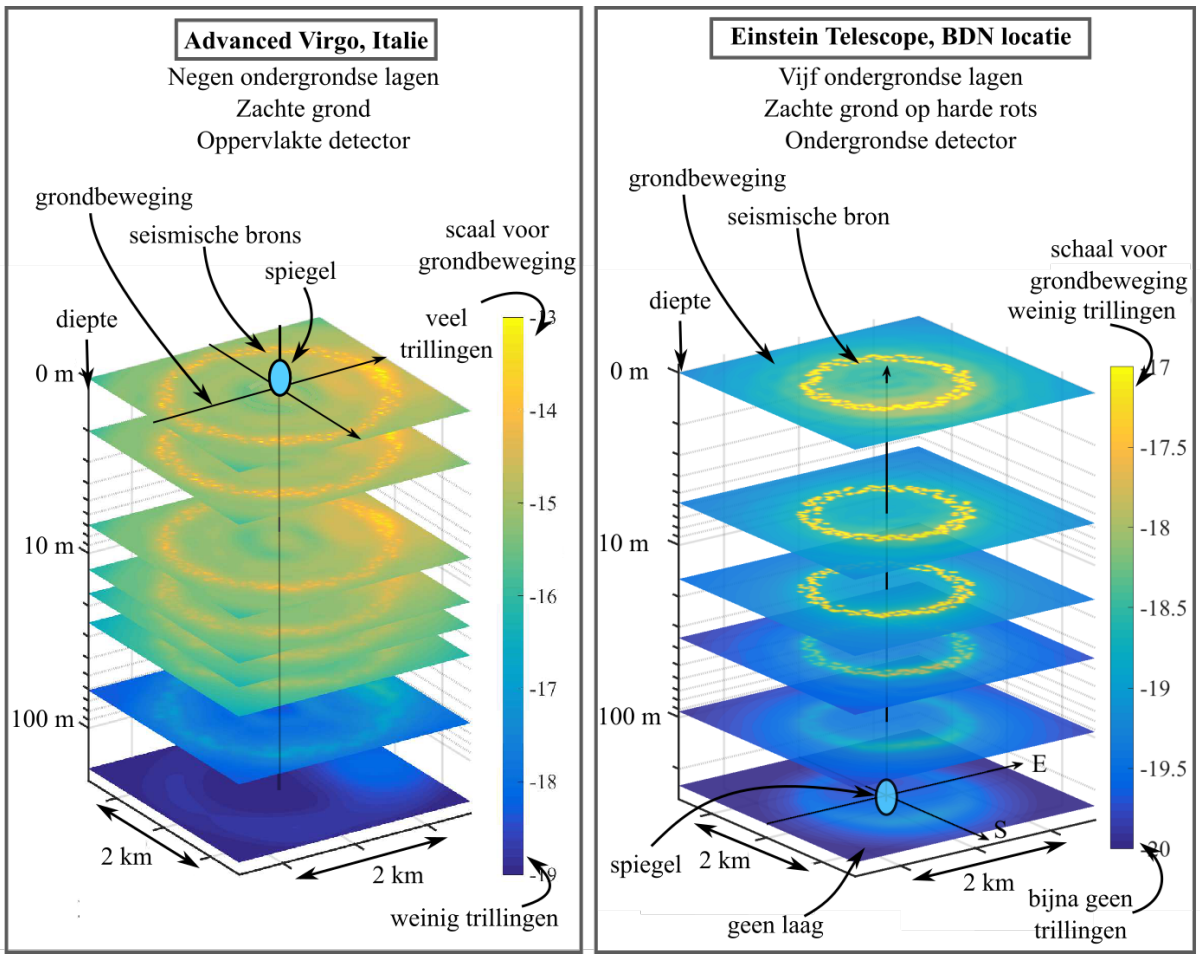

Figuur 9: *Schematische weergave van het model dat is gebaseerd op de geologie en bronlocaties zoals gemeten bij de Advanced Virgo detector in Italië (links) en bij de kandidaat locatie voor Einstein Telescope in Limburg (rechts). De kleur geeft de kracht van de trillingen aan en elk gekleurd veld vertegenwoordigt de seismische trillingen aan het begin van een nieuwe ondergrondse laag. Het is zichtbaar dat de seismische beweging het sterkst is aan de oppervlakte en verder onder de grond afzwakt. Merk op dat bij Advanced Virgo de spiegel zich aan de oppervlakte bevindt, terwijl hij zich bij Einstein Telescope* 250 m *ondergronds bevindt.*

Onlangs is de samenstelling van de ondergrond bij Advanced Virgo in Italië en op de Belgisch-Duits-Nederlandse (BDN) Einstein Telescope kandidaat-locatie in Nederland bepaald met behulp van grote arrays van seismische sensoren. De geologie bij Advanced Virgo blijkt uit negen zachte grondlagen te bestaan, waarbij de belangrijkste bronnen op meer dan 1 km afstand verwijderd zijn en afkomstig zijn van bruggen, een nabijgelegen snelweg en een wind park. De geologie op de BGN locatie blijkt uit vijf ondergrondse lagen te bestaan, die tot op ongeveer 35 m diepte uit een zachte ondergrond bestaan en op een dikke harde steenlaag liggen. Belangrijke ruisbronnen in deze regio zijn lokaal en bevinden zich op afstanden van een paar honderd meter tot een kilometer Voor beide detectoren is een seismisch model afgeleid dat seismische omstandigheden zoals oppervlaktgolfsnelheden en seismische spectra reproduceert voor de specifieke geologie (zie Fig. 9). Voor beide detector locaties is met deze seismische modellen een locatie-specifieke Newtoniaanse ruis berekend door het seismische veld in de nabijheid van de spiegels numeriek te integreren.

Waar gaan wij nu naartoe?

Het onderzoek dat in dit proefschrift is gepresenteerd, heeft geleid tot een beter begrip van hoe de lokale seismische omstandigheden, zoals de geologie en het seismische veld, de Newtoniaanse ruis beïnvloeden bij een bepaalde detector voor gravitatiegolven. Wij hebben ook geleerd dat aanvullende factoren, zoals de detectordiepte en de grootte van de hal rond de spiegels, een sterke invloed hebben op Newtoniaanse ruis. Toekomstig onderzoek wordt daarom aanbevolen om enerzijds de geologische modellen uit te werken, bijvoorbeeld door complexe driedimensionale ondergrondse structuren op te nemen, en anderzijds een gedetailleerd begrip van de invloed van hal-geometrieën op de Newtoniaanse ruis van ondergrondse zwaartkrachtgolfdetectoren te krijgen.

In dit werk een gedetailleerd begrip is verkregen van de locatie-gebaseerde Newtoniaanse ruis op een specifike detector. Newtoniaanse ruis kan echter niet worden onderdrukt en kan de prestaties van de detector tijdens het gebruik soms beperken. Het is daarom van het grootste belang dat toekomstig onderzoek de ontwikkeling van online compensatieschemas omvat, gebaseerd op permanente seismische sensor arrays die constant het seismische veld rond de detector in kaart brengen en dit correleren met het detector signaal. De eerste stappen voor de ontwikkeling van een online compensatieschemas worden gezet bij Advanced Virgo, waar momenteel een permanente sensor array wordt geïnstalleerd en geïntegreerd in Virgo's online monitor-systeem van de omgevingsfactoren.

Deutsche Zusammenfassung

Seit Jahrhunderten treibt uns die menschliche Neugier dazu, die Zusammensetzung des Kosmos genauer verstehen zu wollen. Wir streben nicht nur danach die Gesetze zu enthüllen, die das Universum zusammenhalten, sondern hoffen auch darauf, das Geheimnis hinter seinem Ursprung aufzudecken. Einen wichtigen Beitrag dazu leistet die Gravitationswellenwissenschaft, die es uns ermöglicht, das Universum aus einem völlig neuen Blickwinkel zu betrachten.

Was sind Gravitationswellen?

Gravitationswellen wurden als eine Folgeerscheinung der Allgemeinen Relativitätstheorie vorhergesagt, die 1916 von Einstein formuliert wurde. Die Allgemeine Relativitätstheorie beschreibt wie Masse, also etwa Planeten, die Raumzeit unseres Universums krümmt und wie diese Krümmung sich auf die Bewegung der Masse auswirkt. Wenn besonders schwere Objekte wie beispielsweise schwarze Löcher beschleunigt werden, dann werden dadurch Wellen in der Raumzeit erzeugt (siehe Abb. 10). Diese Wellen breiten sich durch das ganze Universum aus und werden Gravitationswellen genannt. Im Allgemeinen können alle Arten von beschleunigter Masse Gravitationswellen erzeugen. Allerdings ist die Raumzeit sehr „steif"

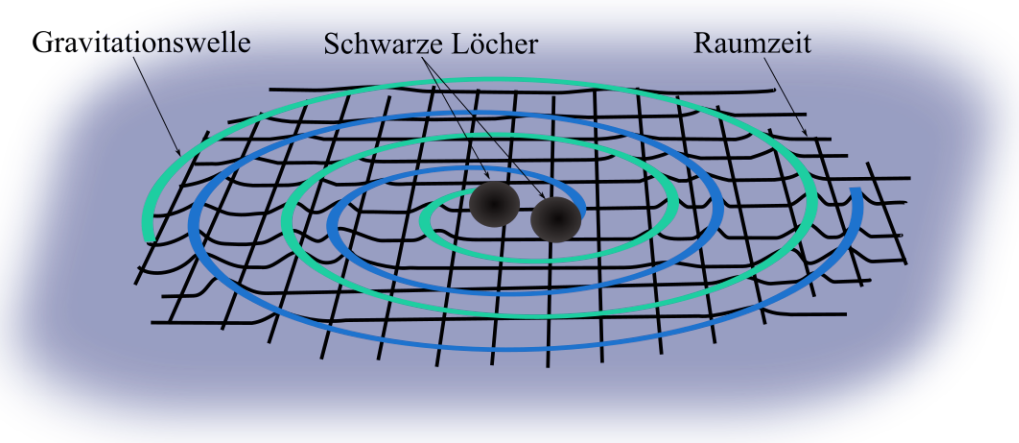

Abbildung 10: *Raumzeit kann man sich wie ein Trampolin vorstellen. Schwere Objekte wie beispielsweise schwarze Löcher, die einander umkreisen und dabei immer schneller werden, erzeugen Wellen in der Raumzeit. Diese sogenannten Gravitationswellen breiten sich mit Lichtgeschwindigkeit im Universum aus und können dadurch auf der Erde gemessen werden.*

und dadurch erzeugen nur die energiereichsten Vorgänge im Universum Gravitationswellen, die wir mit unseren Detektoren auf der Erde messen können. Solche Vorgänge sind etwa die Kollision zweier schwarzer Löcher, rotierende Neutronensterne oder Gammastrahlenexplosionen. Seit der allerersten Messung von Gravitationswellen im Jahr 2015 wurden unzählige Gravitationswellen durch Kollisionen schwarzer Löcher und zweimal das Phänomen von kollidierenden Neutronensternen gemessen. Im Gegensatz zu Messungen mit elektromagnetischen Teleskopen erlauben uns Gravitationswellen Rückschlüsse über Phänomene wie die Struktur von verschmelzenden Neutronensternen zu machen und kosmologische Parameter, wie etwa den Hubble-Parameter, genauer zu spezifizieren.

Wie werden Gravitationswellen gemessen?

Gravitationswellen werden auf der Erde mit Laserinterferometrie gemessen. Laserinterferometrie ist eine Technik, die auf dem sogenannten Michelson-Morley Experiment von 1887 basiert. Am Advanced Virgo Detektor, einem Laserinterferometer in Italien, wird ein Laserstrahl mit einem Strahlteiler in zwei 3 km lange Strecken aufgeteilt (siehe Abb. 11, linkes Bild). Am Ende dieser Strecken wird der Laserstrahl zurück zur Mitte reflektiert, wo beide Strahlen wieder miteinander kombiniert werden. Der sich daraus ergebende Laserstrahl wird mit einer Photodiode gemessen.

Wenn keine Gravitationswelle den Detektor passiert, dann sind beide Arme etwa gleich lang. Die Längen werden so abgestimmt, dass sich die beiden Laserstrahlen destruktiv überlagern und

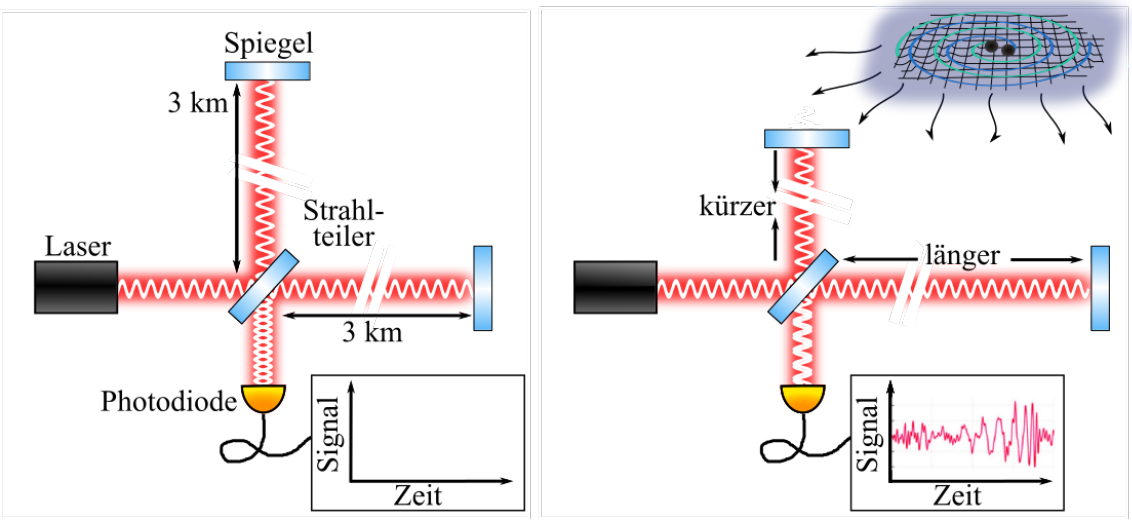

Abbildung 11: *links: Gravitationswellen werden mit Laserinterferometrie gemessen. Hierbei wird ein Laserstrahl mit einem Strahlteiler in zwei, mehrere Kilometer lange Detektorarme aufgeteilt. Am Ende der Arme wird der Strahl durch Spiegel zurück zur Mitte reflektiert, wo beide Strahlen überlagert und mit einer Photodiode gemessen werden. Wenn keine Gravitationswelle den Detektor passiert, dann ist die Länge beider Arme so eingestellt, dass die Strahlen destruktiv interferieren und kein Signal an der Photodiode messbar ist. Rechts: Wenn eine Gravitationswelle den Detektor passiert wird ein Arm verkürzt, während der andere verlängert wird (dieser Effekt ist in Wirklichkeit viel kleiner als hier dargestellt). Der rekombinierte Laserstrahl interferiert nun nicht mehr destruktiv und die Photodiode misst ein Signal. Die Form dieses Signals ist charakteristisch für das Gravitationswellenphänomen.*

kein Licht auf der Photodiode sichtbar ist. Wenn eine Gravitationswelle den Detektor passiert, dann verlängert sie den einen Detektorarm, während der andere Arm verkürzt wird. Das bedeutet, dass ein Laserstrahl nun einen weiteren Weg zurücklegt als der andere. Die Wellenformen beider Strahlen sind nun im Vergleich zum ungestörten Signal zueinander Verschoben, wenn sie überlagert werden. Daraus ergibt sich dann ein zeitabhängiges Signal, das durch die Photodiode gemessen wird (siehe Abb. 11, rechtes Bild). Die Stärke, Dauer und Form dieses Signals hängt von dem Vorgang ab, der das Signal erzeugt hat. Diese Eigenschaften geben uns Aufschluss über die Massenzusammensetzung und Distanz des Geschehens, das die Wellen erzeugt hat, und erlauben uns, verschiedenen Vorkommnisse zu unterscheiden.

Leistungsgrenzen von Gravitationswellendetektoren

Gravitationswellen sind sehr schwach. Beispielsweise hat das bisher stärkste Phänomen, das je gemessen wurde, nur zu einer Variation von 0.000 000 000 000 000 01 m in der Armlänge geführt. Das ist kleiner als der Durchmesser eines Atoms! Auf der Erde gibt es viele Rauschquellen, die den Detektor stören und dadurch seine Fähigkeit Gravitationswellen zu messen, einschränken. Seismische Schwingungen, die durch ozeanische oder menschliche Aktivität hervorgerufen werden, beeinflussen die Position der Spiegel im Detektor auf direkte und indirekte Weise. Die Verschiebung der Spiegel durch seismische Aktivität ist die Hauptquelle für das Detektorrauschen, das in dieser Dissertation behandelt wird.

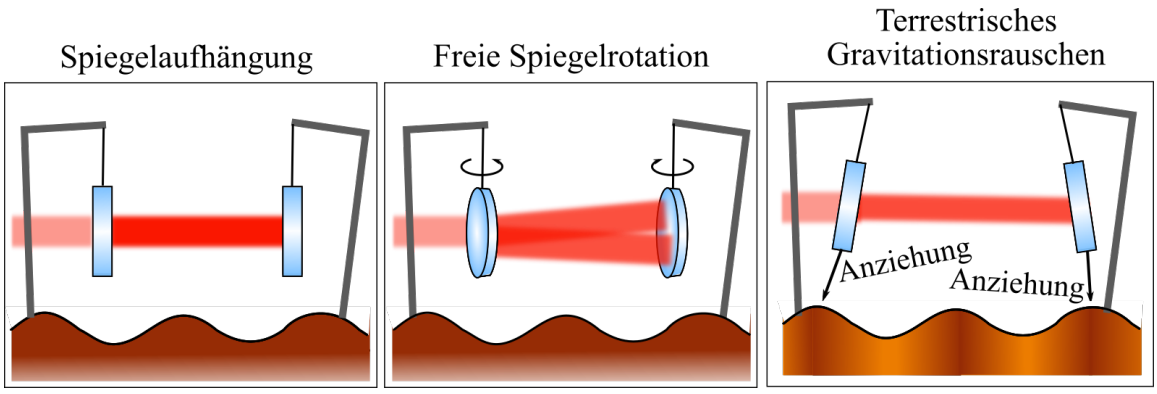

Abbildung 12: *Links: Um die Wechselwirkung zwischen den Spiegeln und seismischen Schwingungen zu reduzieren, werden die Spiegel an einem System von Federn und Pendeln aufgehängt. So kann angenommen werden, dass sich die Spiegel so verhalten, als ob sie sich im freien Fall befänden. Mitte: Im Niedrigfrequenzbereich wird die seismische Aktivität nicht mehr ausreichend durch das Pendelsystem unterdrückt, was zu einer freien Rotation der Spiegel führt. Am Advanced Virgo Detektor sorgt ein aktives Feedback-Kontrollsystem dafür, dass die Spiegel weiterhin stabil ausgerichtet bleiben. Rechts: Die Wechselwirkung zwischen den Spiegeln und den Schwankungen in der Materialdichte der Bodenstruktur, die mit der seismischen Aktivität verknüpft sind, wird terrestrisches Gravitationsrauschen genannt.*

Die Wechselwirkung zwischen den Spiegeln und der seismischen Bewegung des Bodens kann unterdrückt werden, wenn die Spiegel an einem System aus Federn und Pendeln aufgehängt werden. So kann angenommen werden, dass sich die Spiegel fast im gesamten Frequenzbereich des Detektors wie im freien Fall verhalten (siehe Abb. 12, linkes Bild). Im unteren Frequenzbereich isoliert dieses Aufhängungssystem die Spiegel jedoch nicht mehr ausreichend. Dort korrigiert ein aktives Feedback-Kontrollsystem die freie Spiegelrotation und garantiert damit

die korrekte Spiegelposition (siehe Abb. 12, mittleres Bild). Ein Teilaspekt dieser Dissertation ist die Analyse der Fähigkeit des Feedback-Kontrollsystems des Advanced Virgo Detektors, die dort anwesenden Spiegelrotationen zu korrigieren. Außerdem ist zu beachten, dass die seismische Aktivität im direkten Zusammenhang mit schwankender Materialdichte in der Bodenstruktur steht. Diese Variation erzeugt ein schwankendes Gravitationsfeld, durch das die Spiegel zusätzlich bewegt werden (siehe Abb. 12, rechtes Bild). Der Hauptfokus dieser Dissertation liegt auf der mathematischen Modellierung und der Vorhersage dieses sogenannten *terrestrischen Gravitationsrauschens*, das charakteristisch für das seismische Feld jedes Detektorstandortes ist.

Modelle für standortbasiertes terrestrisches Gravitationsrauschen

Bisher haben die Modelle für das terrestrische Gravitationsrauschen von Gravitationswellendetektoren angenommen, dass sich die Detektoren direkt auf der Erdoberfläche befinden. Außerdem wurde angenommen, dass die Geologie am Detektorstandort nur aus einem einzigen Bodenmaterial besteht, in dem sich nur eine spezielle seismische Schwingung ausbreiten kann. In Wirklichkeit weist die Bodenzusammensetzung jedoch verschiedene Materialschichten auf, in welchen sich Oberflächen- und Raumwellen unterschiedlich ausbreiten. Des Weiteren werden seismische Schwingungen von seismischen Quellen erzeugt. Quellen können etwa Ozeanwellen sein, die sich an der Küste brechen, oder Autoverkehr auf nahegelegenen Straßen und Brücken. Der bevorstehende Bau des Einstein Teleskop Detektors, einem zukünftigen Gravitationswellendetektor in Europa, der sich 100 bis 300 m unter der Erdoberfläche befinden wird, motiviert deshalb den Bedarf nach einem realistischen Modell für seismische Schwingungen und terrestrisches Gravitationsrauschen. Ein geringes terrestrisches Gravitationsrauschen ist aus wissenschaftlicher Sicht der entscheidende Faktor, nach dem der Standort des Einstein Teleskop Detektors gewählt wird.

Vor kurzem wurde die Untergrundzusammensetzung am Advanced Virgo Detektor in Italien und am Belgisch-Deutsch-Niederländischen (BDN) Bewerberstandort für den Einstein Teleskop Detektor in der niederländischen Provinz Limburg mit einem Netzwerk aus seismischen Oberflächensensoren untersucht. Es wurde festgestellt, dass sich die Untergrundgeologie am Advanced Virgo Detektor aus neun verschiedenen weichen Materialschichten zusammensetzt und das seismische Quellen auf Straßen- und Brücken einer nahegelegenen Autobahn zurückzuführen sind. Am BDN Standort konnte eine Geologie aus fünf verschiedenen Schichten festgestellt werden, wobei die ersten 35 m aus weichen Materialien und die darunter liegenden Schichten aus harten Steinmaterialien bestehen. Seismische Quellen sind in dieser Region sehr lokal und in einer Entfernung von einigen hundert Metern bis zu 1 km vorzufinden. In dieser Dissertation wurde für beide Detektorstandorte ein horizontal geschichtetes, seismisches Modell entwickelt, das auf der charakteristischen Standortgeologie beruht und das die gemessenen Geschwindigkeiten der Oberflächenwellen und lokale seismischen Spektren reproduziert (siehe Abb. 13). Diese seismischen Modelle wurden dann genutzt, um das standortbasierte terrestrisches Gravitationsrauschen zu berechnen.

Wohin führt die Zukunft?

Die Forschungsarbeit, die für diese Dissertation ausgeführt wurde, hat zu einem besseren Verständnis darüber geführt, wie sich lokale seismische Bedingungen, wie die Geologie und seismische Schwingungen, auf das terrestrische Gravitationsrauschen an Gravitationswellendetektoren

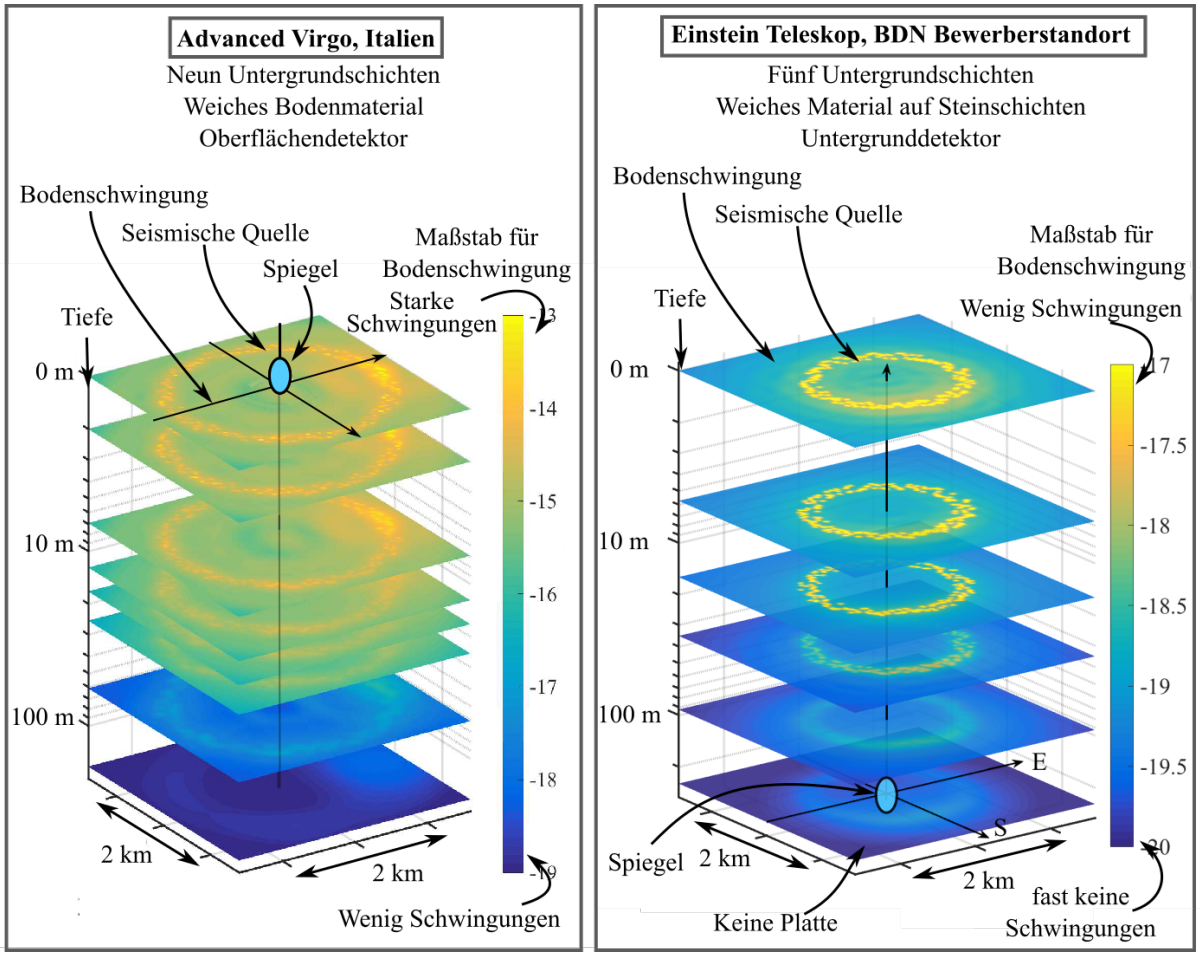

Abbildung 13: *Schematische Abbildung der Modelle für die Geologie am Advanced Virgo Detektor in Italien (links) und dem Einstein Teleskop Bewerberstandort in Limburg (rechts). Die Farbgebung indiziert die Stärke der seismischen Schwingungen und jede Platte repräsentiert die seismischen Schwingungen zu Beginn einer neuen Untergrundschicht. Seismische Schwingungen sind am stärksten an der Oberfläche und schwachen ab, je mehr sie sich unter der Erde ausbreiten. Die Spiegel des Advanced Virgo Detektors befinden sich auf der Oberfläche, während sich die Spiegel des Einstein Teleskop Detektors in einer Tiefe von* 250 m *unter der Erde befinden.*

auswirken. Es konnte außerdem festgestellt werden, dass zusätzliche Faktoren, wie die Tiefe des Detektors unter der Erde, sowie die Form und Größe der Kaverne, die den Detektor umgibt, Einfluss auf das terrestrische Gravitationsrauschen haben. Es wird deshalb empfohlen, dass sich die Forschung für terrestrisches Gravitationsrauschen an Untergrunddetektoren in den kommenden Jahren auf die Weiterentwicklung von geologischen Modellen fokussiert. Das beinhaltet das Modellieren von komplexen, dreidimensionalen Strukturen, die Analyse von Kavernengeometrien und die Weiterentwicklung von Quellmechanismen.

Auch wenn die Modellierung des standortbasierten terrestrischen Gravitationsrauschens das Verständnis von seismischen Detektorrauschen erhöht, so kann es doch nicht unterdrückt werden. Es stellt damit eine fundamentale Leistungsbegrenzung für Gravitationswellendetektoren dar. Aus diesem Grund ist es von höchster Wichtigkeit, dass die Forschung der kommenden Jahre die Entwicklung von Online-Rauschsubtraktionsmethoden mit einschließt. Diese Metho-

den basieren auf Messungen von fest installierten Sensornetzwerken, die permanent das seismische Feld in der Nähe des Detektors analysieren und mit dem Detektorsignal vergleichen. Erste Schritte dieser Entwicklung am Advanced Virgo Detektor werden zurzeit mit der Installation des Sensornetzwerkes gemacht. Dessen Datenströme werden nach Abschluss der Installation in die Online-Überwachungskanäle für Umgebungsrauschen am Advanced Virgo Detektor integriert, was eine Entwicklung von Online-Rauschsubtraktionsmethoden ermöglichen wird.

Acknowledgements

During my time at Nikhef and in the Virgo Collaboration, my paths crossed with those of many enthusiastic people. Without their support in my endeavor to track down my research questions to the utmost detail, I would not have completed this dissertation. I would like to thank all of them for their efforts to bring out the best version of the scientist in me.

Thank you, **Jo van den Brand**, for supplying me with fantastic research opportunities that were always on the frontier of gravitational wave science, for giving me the opportunity to promote our ideas during countless workshops, national and international conferences, and for bringing my thesis to a level of perfection with the help of your hawk eyes. Thank you, **Henk Jan Bulten**, for your inspirational ideas on optimizing our analysis and being a huge asset in revising the details of my methods. I would also like to express my deep gratitude to **Frank Linde**, who is an incredible supportive group leader when it comes to new research ideas and all other matters that a PhD student may encounter during their career.

I would further like to thank my colleagues at Virgo: **Julia Casanueva**, for your enthusiastic explanations on how to run *the machine* and for inviting me to your garden to cut olive trees and plant strawberries during my time in Tuscany. **Diego Bersanetti, Paolo Ruggi, Maddalena Mantovani** and **Bas Swinkels**, who answered my endless questions about control strategies, error signals and laser beams with great patience and who made a great effort to make me feel at home in the Virgo control room. **Michal Was**, for providing kind, smart and immediate support on all my questions related to the noise budget. **Pasquale Popolizio**, for helping us realize the seismic sensor study at Virgo. **Frederic Richard** and **Fabrizio Rossi**, for spending two weeks in the fields with us to stick tiny sensors in the ground and meticulously combing through farmland to retrieve all but two. **Irene Fiori**, for your kindness and for sharing all your insight on seismic noise at Virgo.

From my colleagues at Nikhef I would like to thank: **Robert Fleischer**, thank you for your advice in times of crisis and for our lunch discussions on CERN research, art, and German culture. I value your efforts as my external C3 advisor and I hope you will inspire many more students in- and outside of physics to excel. **Niels van Bakel**, for listening when I needed an open ear and for constantly re-inventing group structures, meetings, and conference outlines. You are a true experimentalist! **Martin van Beuzekom**, for the time you took to provide me with insight on QPDs and the lab-time we shared, for your detailed and patient explanations, and the fun Whiskey tasting in Alaska! **Guido Visser**, for shedding light on electronic circuits, noise measurements and joining the research trip to Annecy. **Eric Hennes**, for your eagerness to share your insights on Newtonian noise and for being most enthusiastic when it came to seismic sensor studies in Limburg. Who else would have biked all the way from Maastricht to

Terziet? **Alessandro Bertolini**, for sharing your detailed insights into matters of seismic noise, seismic sensors and detector controls. **Fred Schimmel**, for bringing a data acquisition setup to a state of absolute perfection. Even though time did not allow to bring my project on parameter estimates with the Fisher matrix to a state where it could be represented in this thesis, I'd like to thank **Chris van den Broek** and **Gideon Koekoek** for their enthusiasm to teach me all about gravitational wave data analysis.

My gratitude also further extends to **Mark Beker** and **Jules van Oven**, for trusting me with their brand new sensors (the tumbler test not only broke my heart) and for giving me insight into the work environment at Innoseis, to **Xander Campman**, for inviting us to Shell and sharing detailed knowledge of seismic field modeling, and to **Björn Vink**, for sharing all his knowledge of Limburg's geology, being passionate about bringing Einstein Telescope to the Netherlands and reaching out to his network at TU Delft.

A big shoutout also goes to all my colleagues, who became dear friends along the way: **Laura**, for taking care of me even before I arrived as your new office mate, you gave me the warmest welcome I could have wished for. For being our plant doctor, for making the office green, for being the social glue, sharing advice on books, notes and lectures, for countless table soccer matches and for showing us that it is possible to completely renovate a house while doing a PhD (it's not recommended though). **Archisman**, for being so fun! When you were at the lunch table, we could be sure that only fun topics would be discussed and no one could resist your contagious laugh ("Come ooooon!"). And we rocked the organization of the Texel outing. **Soumen**, our discussions on seismic and Newtonian noise were a huge inspiration, sparked many exciting ideas and I absolutely enjoyed working side by side with you to carry them out till the end. And more than that you became my dear friend along the way. I am grateful for every concert we went on, every song we shared and every story that was told over yet another Ijwit. There is no dark side of the moon, in fact, everything is dark! **Erik**, thank you for inspiring me to embark upon this quest to pursue a PhD. During all these years we've stayed in touch and you have witnessed all the big achievements in my scientific career from master's degree to doctorate! It was a pleasure to share our various experiences along the way, be your paranymph and to revive the PhD council together. You are an inspiration and I am very grateful for the friendship we forged in the last years. **Zhanna**, for becoming a friend, for not being afraid to share your personal PhD experience with me and for inspiring me to become a dancer! **Donatella**, for being my steady Newtonian noise fellow and long-distance friend - we had a blast at all these GWADW and LVC meetings. **Matteo**, the most dedicated postdoc that I know, for being honest, caring and sharing and for having a great taste in wine and music. **Tim**, for being the most chill housemate, and the most relaxed postdoc with the least average hours of sleep per day (4h). Sharing gossip with you was amazing and I hope we can continue this legacy in the future. **Ka Wa**, for being honest, fun and keeping your curious spirit. Always ready to invite us into your living room (sorry.. office) for some chat and gossip. **Anuradha**, for giving me the opportunity to be a carpenter (so much fun) and exchanging all the travel advice. **Boris**, for being a great officemate, who was always ready to join social events, but also never missed the train at 5:15pm. Not to forget the R&D folks such as **Sander**, **Felix**, **Elena**, **Ester**, **Enzo**, **Daniela**, **Yuefan** and **Rob**, my colleagues in the gravitational wave group **Joris**, **Jeroen**, **Reinier**, **Haris**, **Otto** and **Anna**, and other friends at Nikhef such as **Shi**, **Goran** and **Dimitra**. Finally, I am very grateful for having been a part of the **PhD council**, for getting the opportunity to make a change and to raise a voice for the needs of PhD students. Keep it up guys!

As rarely one challenge comes by itself, I've experienced a lot of personal growth in the years as PhD researcher. I am eternally grateful to my friends as they stayed by my side, who

always believed in me and who did not allow me to neglect them too much. I love you all very much! **Hamda**, thank you for having been a pure inspiration for growth for so many years. Your courage inspired me and I am glad you are a precious part of my life since that day in Utrecht when we sang ”Time of my life” together. Danke dir, liebe **Alice**, dass wir über so lange Zeit und trotz solch einer Distanz immer in Kontakt geblieben sind, dass du mich mit nach Hongkong genommen hast, für die vielen Karten und Care Paket, dass du immer für mich da warst und für deine Expertise im Thema Kommasetzung! **Nadja**, du warst die beste Reisebegleitung nach New York und Berlin, die ich mir je wünschen konnte, und ich freu mich schon darauf weitere Städte mit dir zu erkunden. Danke auch für deinen kreativen Input zum Coverdesign. **Rosalinde**, who became a valuable asset at the end of this journey, hang in there girl! (Italian) **Maria**, for your dark humor, your unique style and your honest and realistic view of the world... and for the poetry! **Iris**, from climbing buddy to best friend. I loved discovering Amsterdam from the Dutch side with you and I hope that we can share many more memories, but this time of your PhD journey please. **Dani** and **Aneta**, who joined me in the unique experience of writing a thesis during Corona. **Marilen** and **Shahin**, for keeping that Salsa spirit alive - Croatia 2021, here we come!

Mit mir gefiebert auf meiner Reise in die Welt der Forschung haben auch meine Lieben daheim: **Mama, Papa, Josefine, Oma Margi, Erwin**, ich danke euch dafür, dass ihr diese Reise mit mir unternommen habt, dass ihr immer für mich da wart, immer ein offenes Ohr für mich hattet, mich so oft besucht habt und während all dieser Zeit immer an mich geglaubt habt. Ich bin euch für eure Unterstützung und eurer Vertrauen in mich dankbar und freue mich, dass wir dieses Ereignis zusammen feiern können!

My last words belong to you, **Akash**. My gratitude and my respect for you to jump into this adventure with me goes beyond words. Thank you for all the midnight walks, the bike trips, the treasure hunt, Candyville, Idli, for celebrating my accomplishments with me and for making me a better person. ”All iz well now” and I can’t wait for our next adventures to start!